Dissertation zur Erlangung des Doktorgrades der Fakultät für Mathematik und Physik der Albert-Ludwigs-Universität Freiburg im Breisgau

Search for Supersymmetry in Events with Missing Transverse Energy and b-Jets with the ATLAS Detector

Stefan Winkelmann

November 2012

Betreut von Prof. Dr. Karl Jakobs

Dekan:	Prof. Dr. Michael Ruzicka
Referent:	Prof. Dr. Karl Jakobs
Koreferent:	Prof. Dr. Thomas Filk
Prüfer (Experiment):	Prof. Dr. Gregor Herten
Prüfer (Theorie):	JProf. Dr. Harald Ita
Datum der mündlichen Prüfung:	19.12.2012

Contents

List of Acronyms

AMSB	Anomaly Mediated SUSY Breaking
BR	Branching Ratio
BSM	Beyond the Standard Model
CERN	Conseil Européen pour la Recherche Nucléaire
CMSSM	Constrained Minimal Supersymmetric Standard Model
DCS	Detector Control System
DDV	DCS Data Viewer
FCNC	Flavor-Changing Neutral Current
FSR	Final State Radiation
GMSB	Gauge Mediated SUSY Breaking
GUT	Grand Unified Theory
ISR	Initial State Radiation
JER	Jet Energy Resolution
JES	Jet Energy Scale
LAr	Liquid Argon
LEP	Large Electron Positron Collider
LHC	Large Hadron Collider
LSP	Lightest Supersymmetric Particle
MC	Monte Carlo
MSSM	Minimal Supersymmetric Standard Model
MSUGRA	Minimal Supergravity
NLL	Next to Leading Logarithm
NLO	Next to Leading Order
PDF	Parton Distribution Function
QCD	Quantum Chromodynamics

QED	Quantum Electrodynamics
RPV	R Parity Violation
SCADA	Supervisory Control and Data Acquisition
SCT	Semiconductor Tracker
SM	Standard Model of Particle Physics
SUSY	Supersymmetry
TRT	Transition Radiation Tracker
UED	Universal Extra Dimensions
VEV	Vacuum Expectation Value
WIMP	Weakly Interacting Massive Particle

1 Introduction

The Standard Model of Particle Physics (SM) has been extremely successful in the description of nature for the last decades. The discovery of the W and Z bosons at CERN in 1983 [1–4] and the top quark at Fermilab in 1995 [5,6] provided experimental confirmation of the validity of the SM. Prior to the experiments at the Large Hadron Collider (LHC), the last missing piece has been the Higgs particle, which remained undetected. Its detection and the possibility to reach physics beyond the SM were the major motivations for the LHC to be built. The latest measurements, based on data taken by the ATLAS and CMS experiments in 2011 and 2012, confirm the observation of a new particle state, which is consistent with the SM Higgs boson with a mass of about 125 GeV [7, 8]. With the further progress of the experiments the properties of this new particle state will be studied in detail. The results of these studies will show if indeed the observed particle remains consistent with all SM predictions or if physics beyond the SM is needed to understand its properties.

Despite its great success, the SM does not answer all questions, e.g. the masses of the leptons and quarks and their hierarchies are not explained, the question why there are three generations of them is not answered. The SM contains 18 parameters that are not explained by theory but have to be measured with experiments. Furthermore, not all forces of nature are included in the SM. While it unifies the electromagnetic, weak and strong interactions, gravity is not included. There are many theoretical efforts to find a way of unifying all known forces. There are also experimental results, for which the SM does not provide answers, e.g. neutrino oscillation experiments give clear evidence for non-zero neutrino masses; observations in astrophysics lead to the postulation of dark matter and dark energy. There are many experimental and theoretical arguments, which motivate the expectation that the SM is not the final answer, but rather an approximation (or "effective theory") for the underlying, fundamental theory.

There are two important frontiers in today's experimental particle physics, namely the precision frontier and the energy frontier. At the former, there is a rich set of dedicated precision measurements, e.g. the experiments BaBar and BELLE, which measure CP violations and the CKM quark mixing parameters. Mainly at the latter, there is today the LHC with unprecedentedly high energy. At both frontiers, hints for physics beyond the Standard Model could be found. Precision measurements can be seen as indirect searches for new particles, contributing to low energy observables through higher order effects. In high energy searches at the LHC, new particles could be produced directly. Figuratively, the two approaches can be viewed as "shaking" the box of unknown content, inferring what may lie inside, or actually "opening" it. This study tries to do the latter.

Theoretical considerations suggest that new physics has to lie at the TeV scale, which would then be accessible by the LHC. New particles, so far unknown, might be produced and measured with the ATLAS detector. Supersymmetry (SUSY) is a well motivated theory beyond the SM that predicts the existence of many such yet undiscovered particles: One SUSY particle for every SM particle, as well as an enlarged Higgs sector.

One phenomenologically important class of SUSY models contains a new conserved quantum number, named R parity, which is motivated by proton stability bounds. As a consequence of R parity conservation, SUSY particles are always produced in pairs. The Lightest Supersymmetric Particle (LSP) is stable, does not interact with the detector material and therefore leaves the ATLAS detector undetected. If this particle is electrically neutral, it could contribute to the dark matter abundance in the universe. The experimental signature contains an imbalance of the measured momenta in the transverse plane, denoted as missing transverse momentum.

In many scenarios, the SUSY partners of the third generation quarks are lighter than their first and second generation counterparts, due to a mixing effect that is proportional to the SM quark mass. As a result, the partners of the third generation quarks can be produced with large cross sections and their decay products include t and b-quarks. The experimental signatures in these scenarios contain b-jets. Depending on the particular SUSY model, the final state can become complex, possibly including the production of leptons. The experimental signature considered in this thesis consists of several high energetic hadronic jets, including at least one b-jet, leptons and missing transverse momentum.

This thesis is structured as follows. The theoretical foundations of particle physics are described in Chapter 2. It includes an account of the Standard Model (SM) and an introduction to Supersymmetry (SUSY), as well as a description of the statistical methods used. In Chapter 3, the phenomenology of hadron-hadron collisions in general and for SUSY processes in particular are presented, including an account of the specific phenomenological SUSY models used. Chapter 4 gives an overview of the LHC and the ATLAS detector, including a description of the individual subdetectors and their respective performance. The last section of this chapter is dedicated to a discussion of the Monte Carlo simulations used for the SUSY signal and the SM background processes. Two main analyses are performed. The first analysis is presented in Chapter 5 and deals with the search for sbottom and stop particles, which are mainly produced from pair-produced gluinos and their subsequent decays. The second analysis is presented in Chapter 6 and is concerned with the direct production of stop pairs, assuming the stop to be lighter than the top quark, or very close in mass. The summary is given in Chapter 7.

2 Theory of Particle Physics

This chapter serves as an introduction to the theoretical foundations of this study, namely the Standard Model of particle physics (SM) and Supersymmetry (SUSY). In Section 2.3, the statistical methods used in the interpretation of the experimental data are presented.

2.1. Standard Model of Particle Physics

The SM contains all known elementary particles and their interactions, except gravity[1]. It consists of spin 1/2 fermions ("matter particles") and spin 1 gauge bosons ("force carriers"). The former are subdivided in quarks and leptons, and exist in three generations. It is a quantum field theory based on the gauge group $SU(3)_C \times SU(2)_L \times U(1)_Y$. The first part of the gauge group $SU(3)_C$ represents the strong interactions of quarks and gluons, which carry the color degree of freedom. The second part of the gauge group $SU(2)_L \times U(1)_Y$ represents unified electroweak interactions, where L stands for the left-handed weak isospin and Y for hypercharge. Table 2.1 lists all particles with their respective representations under the gauge groups.

2.1.1. Electroweak Theory

The electroweak theory as part of the SM was developed in the 1960s and 1970s and is also called GWS theory named after its main contributors Glashow [9], Weinberg [10] and Salam [11]. There are numerous textbooks and reviews of the SM, e.g. Ref. [12]. The Lagrangian reads as follows

$$\mathcal{L} = -\frac{1}{4} B^{\mu\nu} B_{\mu\nu} - \frac{1}{4} W_a^{\mu\nu} W^a_{\mu\nu} + \bar{\psi}\gamma^\mu D_\mu \psi + \mathcal{L}_{\text{Higgs}} \tag{2.1}$$

with the field strength tensors $B_{\mu\nu} = \partial_\mu B_\nu - \partial_\nu B_\mu$ and $W^a_{\mu\nu} = \partial_\mu W^a_\nu - \partial_\nu W^a_\mu - g\varepsilon^{abc} W^b_\mu W^c_\nu$ and the covariant derivative D_μ

$$D_\mu = \left(\partial_\mu + igW^a_\mu T^a + iYg' B_\mu\right), \tag{2.2}$$

with the $SU(2)$ and $U(1)$ gauge couplings g and g', Y denotes the hypercharge and the matrices T represent the $SU(2)$ algebra.

The gauge fields W^i_μ, $i = 1, 2, 3$ and B_μ are mixed to form the physical W boson fields $W^\pm_\mu$, the Z boson field Z_μ and the photon field A_μ

$$W^\pm_\mu = (W^1_\mu \mp iW^2_\mu)/\sqrt{2} \tag{2.3}$$

$$\begin{pmatrix} Z_\mu \\ A_\mu \end{pmatrix} = \begin{pmatrix} \cos\theta_W & -\sin\theta_W \\ \sin\theta_W & \cos\theta_W \end{pmatrix} \begin{pmatrix} W^3_\mu \\ B_\mu \end{pmatrix} \tag{2.4}$$

[1] At present, gravity cannot be described with a quantum field theory and for the purpose of elementary particle physics it does not play an important role due to the small particle masses and can be safely neglected.

Name					$SU(3)_C$	$SU(2)_L$	$U(1)_Y$
Quarks	Q_L	$\begin{pmatrix} u \\ d' \end{pmatrix}_L$	$\begin{pmatrix} c \\ s' \end{pmatrix}_L$	$\begin{pmatrix} t \\ b' \end{pmatrix}_L$	**3**	**2**	1/3
	q_R	u_R	c_R	t_R	**3**	**1**	4/3
		d_R	s_R	b_R	**3**	**1**	-2/3
Leptons	L_L	$\begin{pmatrix} \nu_e \\ e \end{pmatrix}_L$	$\begin{pmatrix} \nu_\mu \\ \mu \end{pmatrix}_L$	$\begin{pmatrix} \nu_\tau \\ \tau \end{pmatrix}_L$	**1**	**2**	-1
	ℓ_R	e_R	μ_R	τ_R	**1**	**1**	-2
Bosons		Hypercharge Gauge Field B_μ			**1**	**1**	0
		Isospin Gauge Field W_μ			**1**	**3**	0
		Gluon g_μ			**8**	**1**	0
		Higgs h			**1**	**2**	1

Table 2.1.: SM particles and their respective representation under the components of the SM gauge group. The down-type quarks d', s' and b' denote the electroweak eigenstates consisting of a mixture of mass eigenstates via the CKM mixing matrix. All listed particles have been measured experimentally. Only recently, a particle state consistent with the Higgs boson has been found [7,8]. Right-handed neutrinos can be added to account for non-zero neutrino masses.

with the weak mixing angle θ_W.

The Lagrangian in Eq. 2.1 does not contain explicit mass terms (quadratic terms in the fields), since these terms would break the gauge symmetry and the theory would become non-renormalizable. The masses of the W and Z bosons and the fermions, which can be measured experimentally, have to be generated by a mechanism without explicitly breaking the gauge symmetry. The standard way to achieve this is the so-called spontaneous symmetry breaking and the Higgs mechanism[2].

2.1.2. Higgs Mechanism

The Higgs field is introduced as a complex scalar doublet

$$\phi = \begin{pmatrix} \phi^+ \\ \phi^0 \end{pmatrix}. \tag{2.5}$$

The Lagrangian $\mathcal{L}_{\text{Higgs}}$ is written as

$$\mathcal{L}_{\text{Higgs}} = (D_\mu \phi)^\dagger D^\mu \phi + V\left(\phi^\dagger \phi\right) \tag{2.6}$$

[2] In recent literature, it is also called Englert-Brout-Higgs-Guralnik-Hagen-Kibble-Mechanism, to acknowledge the important contributions from these authors [13–18]. For the sake of brevity, this thesis uses the term Higgs only.

with the Higgs potential[3]

$$V\left(\phi^\dagger\phi\right) = -\mu^2\phi^\dagger\phi + \frac{\lambda}{4}(\phi^\dagger\phi)^2. \tag{2.7}$$

If the minimum of the potential is different from $\phi = 0$ (λ, $\mu^2 > 0$)

$$|\phi| = \sqrt{2}\mu/\sqrt{\lambda} \equiv v/\sqrt{2}, \tag{2.8}$$

the Higgs field can be expanded around this minimum, which yields

$$\phi = \frac{1}{\sqrt{2}}\begin{pmatrix} 0 \\ h+v \end{pmatrix}. \tag{2.9}$$

The underlying symmetry is now hidden or "spontaneously broken". One physical Higgs field h remains with mass $m_h = \sqrt{2}\mu \equiv \sqrt{\frac{\lambda}{2}}v$, which can be read off the quadratic term in the Lagrangian

$$\mathcal{L}_{\text{Higgs}} = \frac{1}{2}\partial_\mu h \partial^\mu h + \mu^2 h^2 + \frac{1}{4}\lambda v h^3 - \frac{1}{16}\lambda h^4. \tag{2.10}$$

Inserting the expansion Eq. 2.9 into Eq. 2.6 yields also the couplings and masses of the W and Z bosons. The masses of the W and Z bosons can be written as

$$m_W = \frac{1}{2}vg \tag{2.11}$$

$$m_Z = \frac{1}{2}v\sqrt{g^2+g'^2} \equiv \frac{m_W}{\cos\theta_W}, \tag{2.12}$$

while the photon remains massless.

The mass of a fermion f is generated by a Yukawa coupling g_f to the Higgs field. The term of the form $g_f\bar{\psi}_f\psi_f\phi$ results in a mass $m_f = g_f v/\sqrt{2}$. The physical Higgs field h couples to the fermions via $g_f\bar{\psi}_f\psi_f h$, proportional to the mass of the fermion.

2.1.3. Quantum Chromodynamics

The Lagrangian of Quantum Chromodynamics (QCD) reads

$$\mathcal{L} = -\frac{1}{4}F_a^{\mu\nu}F^a_{\mu\nu} + i\bar{\psi}\gamma^\mu D_\mu\psi, \tag{2.13}$$

with the field strength tensor $F_a^{\mu\nu} = \partial^\mu A_a^\nu - \partial^\nu A_a^\mu - g_s f_{abc} A_b^\mu A_c^\nu$, the strong coupling constant $g_s \equiv \sqrt{4\pi\alpha_s}$ and the structure constants f_{abc} of $SU(3)$. The covariant derivative D_μ is

$$D_\mu = \left(\partial_\mu - ig_s A_\mu^a T^a\right), \tag{2.14}$$

where T denotes matrices of the fundamental or adjoint representation of $SU(3)$.

The dependence ("running") of the coupling on the scale Q^2 is determined by the renormalization group equation

$$Q^2\frac{\partial\alpha_s}{\partial Q^2} = \beta(\alpha_s), \tag{2.15}$$

[3]There are different conventions in the literature for the parameter λ in the Higgs potential. Many authors omit the factor 1/4 of the quartic term in ϕ, which is equivalent to a trivial redefinition of the parameter $\lambda \to \lambda' = \lambda/4$.

where β is the so-called β function. It can be written in a perturbative expansion as

$$\beta = -b\alpha_s^2 \left(1 + b'\alpha_s + b''\alpha_s^2 + \dots\right), \tag{2.16}$$

with the leading order parameter

$$b = \frac{33 - 2n_f}{12\pi}, \tag{2.17}$$

where n_f denotes the number of quark flavors included. In the SM, the parameter b is always positive.

The differential equation 2.15 can be solved in leading order (neglecting the b' and b'') by

$$\alpha_s(Q^2) = \frac{12\pi}{(33 - 2n_f)\log(Q^2/\Lambda^2)}, \tag{2.18}$$

introducing a cutoff scale Λ. For large scales $Q^2 \gg \Lambda^2$, the coupling becomes small ("asymptotic freedom") and perturbative methods can be applied. For lower scales $Q^2 \leq \Lambda^2$, the coupling diverges and perturbation theory cannot be used. The quarks and gluons as fundamental degrees of freedom of QCD are "confined" and bound in hadrons. The value of Λ is a free parameter and experimentally measured to be $\Lambda \sim 200\,\text{MeV}$, which is the typical scale of hadron masses.

This situation in QCD is in contrast to Quantum Electrodynamics (QED), where confinement and asymptotic freedom are not observed. In QED, the analogous expression to Eq. 2.16 has a leading order parameter $b = -\frac{1}{3\pi} < 0$. The leading order β function therefore has a different sign and the running of the coupling shows a different behavior

$$\alpha(Q^2) = \frac{\alpha(\mu^2)}{1 - \frac{\alpha(\mu^2)}{3\pi}\log\left(\frac{Q^2}{\mu^2}\right)}, \tag{2.19}$$

with reference scale μ. For low scales $Q^2 \to 0$, the coupling is $\alpha \approx \frac{1}{137}$, for $Q^2 = m_Z^2$, it reaches $\alpha \approx \frac{1}{128}$. It increases only slowly with the scale and remains in the perturbative regime $\alpha \ll 1$ for all practical purposes.

2.1.4. Experimental Status

The experimental measurements performed so far are in excellent agreement with the SM expectation. A variety of quantities are obtained from electroweak precision measurements and no evidence of physics beyond the SM has been found.[4]

There is, however, a $\sim 3\sigma$ tension and therefore a possible hint to new physics, observed in the measurement of the muon anomalous magnetic moment

$$a_\mu = \frac{g_\mu - 2}{2}. \tag{2.20}$$

The present experimental and theoretical values are [19]

$$a_\mu^{\text{exp}} = (1165920.80 \pm 0.63)\,10^{-9} \tag{2.21}$$

$$a_\mu^{\text{theo}} = (1165918.41 \pm 0.48)\,10^{-9}. \tag{2.22}$$

[4] A review of electroweak precision measurements can be found in Ref. [19].

Although it is not clear at the moment, if the observed discrepancy is due to statistical fluctuations, an underestimation of the uncertainty or indeed a genuine effect resulting from physics beyond the SM, there are already theoretical studies, evaluating a_μ in several Beyond the Standard Model (BSM) scenarios[5].

Further indirect searches for BSM physics can be performed, e.g. for Flavor-Changing Neutral Current (FCNC) reactions with CP violation. The reaction $b \to s\gamma$ is forbidden at tree level in the SM. At present, the discrepancy of the experimentally measured branching ratio $BR(B \to X_s\gamma)$ and the SM value is at the 2σ level [21]. Theoretical studies evaluate the additional contributions from loops in BSM physics scenarios, such as supersymmetry. These studies can contribute to constrain the parameter space of BSM models or even lead to indirect observations.

In summary, there are numerous quantities measured with high precision, which are in agreement with the SM predictions. These measurements can be used both to indirectly search for new physics effects and to constrain BSM models. Results from direct and indirect searches are often interconnected and both are essential for a complete understanding.

2.2. Supersymmetry

Supersymmetry (SUSY) introduces a transformation between bosonic and fermionic particles. This means there must be an operator[6] Q with

$$Q\,|\text{boson}\rangle \;\propto\; |\text{fermion}\rangle \tag{2.23}$$
$$Q\,|\text{fermion}\rangle \;\propto\; |\text{boson}\rangle\,, \tag{2.24}$$

where Q itself has to be fermionic. It follows the (anti-)commutator relations

$$\left\{Q, Q^\dagger\right\} = P^\mu, \tag{2.25}$$
$$\{Q, Q\} = \left\{Q^\dagger, Q^\dagger\right\} = 0, \tag{2.26}$$
$$[P^\mu, Q] = \left[P^\mu, Q^\dagger\right] = 0. \tag{2.27}$$

Besides the SM particles, SUSY postulates new particles: bosons get fermionic counterparts and vice versa. Besides having different spins, the partner particles have the same properties, such as electric charge, weak isospin, color degrees of freedom and mass. The SM particles and their postulated SUSY particles, also referred to as superpartners, form supermultiplets.

Supersymmetry in its unbroken form leads to exactly identical masses for the SM particles and their superpartners. Since no equal mass superpartners are observed, SUSY must be broken, if it is realized in nature.

[5] Recent studies can be found in Ref. [20] and references therein.

[6] In the context of this thesis only the phenomenologically most interesting case of only one operator Q is considered. Theoretically one can assume N copies of such an operator, or supersymmetries. In this notation only $N = 1$ supersymmetry is covered here.

2.2.1. Minimal Supersymmetric Standard Model

The Minimal Supersymmetric Standard Model (MSSM)[7] is a supersymmetric extension of the SM with the minimal numbers of parameters and particles added[8]. With the exception of the physical Higgs particles, of which there are five in the MSSM (see below), the particle content is doubled. Every boson gets a fermionic SUSY partner, and vice versa.

In the literature there is a commonly adopted naming scheme for SUSY particles. Scalar SUSY particles are denoted by their SM partner name with an extra "s-" in front. The superpartners of the SM fermions are hence referred to as sfermions (squarks, sleptons). The superpartners of SM bosons acquire an extra "-ino" at the end of their respective SM partner name. Table 2.2 lists the particle content of the MSSM and the representations under the gauge groups.

For the masses of the particles in the MSSM, both mass terms of the unbroken supersymmetric theory and SUSY-breaking contributions[9] have to be taken into account. Additionally, particles with identical quantum numbers (electric charge, color and spin), will mix to form mass eigenstates. Table 2.3 presents a summary of the MSSM particles in gauge eigenstates and in mass eigenstates. The gluino as a color octet fermion cannot mix with any other particles in the MSSM.

In the following the MSSM Higgs sector and the mixing effects are discussed.

MSSM Higgs Sector

Two complex scalar Higgs doublets need to be introduced in the MSSM to generate masses for "up"-type and "down"-type quarks and charged leptons

$$H_u = \begin{pmatrix} H_u^+ \\ H_u^0 \end{pmatrix}, \quad H_d = \begin{pmatrix} H_d^0 \\ H_d^- \end{pmatrix}. \tag{2.28}$$

Now both H_u^0 and H_d^0 acquire vacuum expectation values called v_u and v_d, respectively, with

$$v_u^2 + v_d^2 = v^2 \approx (174\,\mathrm{GeV})^2. \tag{2.29}$$

The masses of the SM gauge bosons are then given by

$$m_W^2 = \frac{g^2}{2}(v_u^2 + v_d^2), \tag{2.30}$$

$$m_Z^2 = \frac{1}{2}(g^2 + g'^2)(v_u^2 + v_d^2). \tag{2.31}$$

The ratio of the two vacuum expectation values is usually written as

$$\tan\beta \equiv \frac{v_u}{v_d}. \tag{2.32}$$

Five physical Higgs bosons remain after electroweak symmetry breaking out of the original eight degrees of freedom. There are three neutral and two oppositely charged Higgs particles.

[7] A comprehensive review of the MSSM can be found in Refs. [22–25].
[8] The total number of physical parameters in the MSSM is 124 [26], including all SM parameters.
[9] The mechanisms of SUSY-breaking are discussed in Section 2.2.2.

Name	Fermions	Bosons	$SU(3)_C$	$SU(2)_L$	$U(1)_Y$
squarks/squarks					
first generation	$\begin{pmatrix} u \\ d \end{pmatrix}_L$	$\begin{pmatrix} \tilde{u}_L \\ \tilde{d}_L \end{pmatrix}$	**3**	**2**	1/3
	u_R	$\tilde{u}_R$	**3**	**1**	4/3
	d_R	$\tilde{d}_R$	**3**	**1**	-2/3
second generation	$\begin{pmatrix} c \\ s \end{pmatrix}_L$	$\begin{pmatrix} \tilde{c}_L \\ \tilde{s}_L \end{pmatrix}$	**3**	**2**	1/3
	c_R	$\tilde{c}_R$	**3**	**1**	4/3
	s_R	$\tilde{s}_R$	**3**	**1**	-2/3
third generation	$\begin{pmatrix} t \\ b \end{pmatrix}_L$	$\begin{pmatrix} \tilde{t}_L \\ \tilde{b}_L \end{pmatrix}$	**3**	**2**	1/3
	t_R	$\tilde{t}_R$	**3**	**1**	4/3
	b_R	$\tilde{b}_R$	**3**	**1**	-2/3
lepton/slepton					
first generation	$\begin{pmatrix} \nu_e \\ e \end{pmatrix}_L$	$\begin{pmatrix} \tilde{\nu}_{eL} \\ \tilde{e}_L \end{pmatrix}$	**1**	**2**	-1
	e_R	$\tilde{e}_R$	**1**	**1**	-2
second generation	$\begin{pmatrix} \nu_\mu \\ \mu \end{pmatrix}_L$	$\begin{pmatrix} \tilde{\nu}_{\mu L} \\ \tilde{\mu}_L \end{pmatrix}$	**1**	**2**	-1
	μ_R	$\tilde{\mu}_R$	**1**	**1**	-2
third generation	$\begin{pmatrix} \nu_\tau \\ \tau \end{pmatrix}_L$	$\begin{pmatrix} \tilde{\nu}_{\tau L} \\ \tilde{\tau}_L \end{pmatrix}$	**1**	**2**	-1
	τ_R	$\tilde{\tau}_R$	**1**	**1**	-2
gauge/gaugino	$\tilde{B}^0$	B^0	**1**	**1**	0
	$\tilde{W}^\pm$, $\tilde{W}^0$	$W^\pm$, W^0	**1**	**3**	0
gluon/gluino	$\tilde{g}$	g	**8**	**1**	0
Higgs/higgsino	$\tilde{H}_u^+$, $\tilde{H}_u^0$	H_u^+, H_u^0	**1**	**2**	1
	$\tilde{H}_d^0$, $\tilde{H}_d^-$	H_d^0, H_d^-	**1**	**2**	-1

Table 2.2.: List of MSSM particles (before electroweak symmetry breaking) and representations under the gauge groups.

The two neutral Higgs particles, which are even under CP transformation, are denoted as h^0 and H^0 (where conventionally $m_h \leq m_H$). The Higgs particle h can be similar to the SM Higgs particle. The neutral Higgs particle, which is CP odd, is denoted as A^0, the charged Higgs particles are referred to as $H^\pm$. At tree-level there are theoretical constraints[10] of the

[10]For a comprehensive review of the Higgs sector in the MSSM, see Ref. [27].

particle	gauge eigenstates	mass eigenstates
third generation squarks	$\tilde{t}_L$, $\tilde{t}_R$, $\tilde{b}_L$, $\tilde{b}_R$	$\tilde{t}_1$, $\tilde{t}_2$, $\tilde{b}_1$, $\tilde{b}_2$
third generation sleptons	$\tilde{\tau}_L$, $\tilde{\tau}_R$, $\tilde{\nu}_\tau$	$\tilde{\tau}_1$, $\tilde{\tau}_2$, $\tilde{\nu}_\tau$
Higgs bosons	H_u^+, H_u^0, H_d^0, H_d^-	h, H_0, A_0, $H^\pm$
neutralinos	$\tilde{W}^0$, $\tilde{B}^0$, $\tilde{H}_u^0$, $\tilde{H}_d^0$	$\tilde{\chi}_1^0$, $\tilde{\chi}_2^0$, $\tilde{\chi}_3^0$, $\tilde{\chi}_4^0$
charginos	$\tilde{W}^\pm$, $\tilde{H}_u^+$, $\tilde{H}_d^-$	$\tilde{\chi}_1^\pm$, $\tilde{\chi}_2^\pm$
gluino	$\tilde{g}$	$\tilde{g}$

Table 2.3.: List of MSSM particles, gauge and mass eigenstates [23]. The mixings of the first and second generation squarks and sleptons is expected to be small and omitted from the table.

Higgs particle spectrum, leaving only two free parameters, usually taken to be m_A and $\tan\beta$. The mass m_h of the light neutral Higgs boson is (at tree-level) constraint to be

$$m_h \leq \min(m_A, m_Z)|\cos 2\beta| \leq m_Z. \tag{2.33}$$

If one-loop corrections are taken into account, this constraint is loosened, but, in contrast to the SM, an upper bound of less than 150 GeV [27] remains [11], consistent with the new particle state observed by ATLAS and CMS with mass of ~ 125 GeV.

Charginos and Neutralinos

The bino $\tilde{B}^0$ mixes with the neutral higgsinos $\tilde{H}_{u,d}^0$ and wino $\tilde{W}^0$. This results in states called neutralinos, which are generally denoted as $\tilde{\chi}_1^0$ to $\tilde{\chi}_4^0$ and by definition ordered in their masses: $m_{\tilde{\chi}_1^0} < m_{\tilde{\chi}_2^0} < m_{\tilde{\chi}_3^0} < m_{\tilde{\chi}_4^0}$. Similar to the neutral states the positively and negatively charged winos $\tilde{W}^\pm$ and higgsinos $\tilde{H}_u^+$ and $\tilde{H}_d^-$ also mix among themselves and form the charginos $\tilde{\chi}_1^\pm$ and $\tilde{\chi}_2^\pm$.

As discussed in Section 2.2.2, the gauge couplings unify at a high scale, therefore, it is often assumed that also the gaugino masses unify at that scale ("gaugino universality"). As a consequence, this leads to a mass relation of the lightest neutralino and the lightest chargino at the electroweak scale

$$m_{\tilde{\chi}_1^\pm} \approx 2m_{\tilde{\chi}_1^0}. \tag{2.34}$$

Squarks and Sleptons

For the masses of the squarks and sleptons, different contributions have to be taken into account. The first contribution from the unbroken supersymmetry yields mass terms analogous

[11] The upper bound on m_h obtained in Ref. [27] is "most conservative". In the calculation, theoretical uncertainties (renormalization scheme dependence, variation of the renormalization scale, uncertainties due to the two-loop correction approximation) and experimental uncertainties due to the uncertainties on the measurements of the top quark mass are taken into account. The authors of Refs. [28, 29] quote a tighter upper limit of $m_h < 135$ GeV.

to the SM partners and one additional bilinear term.

For the partner of the quark q, the Lagrangian contains the terms

$$\mathcal{L} = -m_q^2 \tilde{q}_L^\dagger \tilde{q}_L - m_q^2 \tilde{q}_R^\dagger \tilde{q}_R - (\mu m_q \cot\beta)\left(\tilde{q}_L^\dagger \tilde{q}_R + \tilde{q}_R^\dagger \tilde{q}_L\right) + \ldots, \tag{2.35}$$

where m_q is the mass of the quark and μ the Higgs mass scale parameter.

Since the mechanism to break supersymmetry is unknown, the effects of this breaking are parametrized by explicitly adding SUSY-breaking terms to the Lagrangian. This results in additional bilinear and trilinear terms with a coupling to the Higgs boson. For the quark q, these additional terms are given by

$$\begin{aligned}
\mathcal{L}_{\tilde{q}}^{\text{SUSY-breaking}} = \; & - \; m_{\tilde{q}_L}^2 \tilde{q}_L^\dagger \tilde{q}_L - m_{\tilde{q}_R}^2 \tilde{q}_R^\dagger \tilde{q}_R & (2.36)\\
& - \; A_q f_q \tilde{q}_L h_u^0 \tilde{q}_R^\dagger + \text{h.c.} & (2.37)\\
& + \; A_q m_q \left(\tilde{q}_L^\dagger \tilde{q}_R + \tilde{q}_R^\dagger \tilde{q}_L\right) & (2.38)
\end{aligned}$$

with the SUSY-breaking masses $m_{\tilde{q}_L}$ and $m_{\tilde{q}_R}$, the trilinear coupling A_q and the Yukawa coupling f_q. The last SUSY-breaking contribution to the mass is the so-called D-term contribution [25]. It introduces a mass squared matrix $m^2_{\text{D-term}}$, which can be written as

$$m^2_{\text{D-term}} = m_Z^2 \cos 2\beta (T_3 - Q \sin^2\theta_w), \tag{2.39}$$

where T_3 is the third generator of $SU(2)$, Q is the electric charge and θ_W the weak mixing angle.

Since particles with the same quantum numbers (electric charge, color and spin) can mix with each other, the resulting expressions for the masses of squarks and sleptons can in general be very complex. Both L-R and flavor mixing can occur. Motivated by strong experimental constraints on CP violation and flavor-changing neutral currents, the mixings can be simplified, assuming that the breaking of supersymmetry is "flavor-blind" [23].

The first and second generation mixing is expected to be very small compared to the mixing in the third generation. In the following, the mixings of the third generation are discussed in detail.

The mass eigenstates $\tilde{b}_1$ and $\tilde{b}_2$ are obtained from the chiral eigenstates $\tilde{b}_L$ and $\tilde{b}_R$ by the following relation [24]

$$\begin{pmatrix} \tilde{b}_1 \\ \tilde{b}_2 \end{pmatrix} = \begin{pmatrix} m^2_{\tilde{t}_L,\tilde{b}_L} + m_b^2 + \Delta_{\tilde{d}_L} & m_b(A_0 - \mu\tan\beta) \\ m_b(A_0 - \mu\tan\beta) & m^2_{\tilde{b}_R} + m_b^2 + \Delta_{\tilde{d}_R} \end{pmatrix} \begin{pmatrix} \tilde{b}_L \\ \tilde{b}_R \end{pmatrix} \tag{2.40}$$

with

$$\begin{aligned}
\Delta_{\tilde{d}_L} &= \left(-\frac{1}{2} + \frac{1}{3}\sin^2\theta_W\right) m_Z^2 \cos 2\beta, & (2.41)\\
\Delta_{\tilde{d}_R} &= \frac{1}{3}\sin^2\theta_W m_Z^2 \cos 2\beta, & (2.42)
\end{aligned}$$

where a unified trilinear coupling A_0 is assumed.

The analogous expressions can be written down for the partner of the top quark and the third generation leptons, by replacing the isospin, charge and mass parameters, appropriately[12]:

$$\begin{pmatrix} \tilde{t}_1 \\ \tilde{t}_2 \end{pmatrix} = \begin{pmatrix} m^2_{\tilde{t}_L,\tilde{b}_L} + m_t^2 + \Delta_{\tilde{u}_L} & m_t(A_0 - \mu\cot\beta) \\ m_t(A_0 - \mu\cot\beta) & m^2_{\tilde{t}_R} + m_t^2 + \Delta_{\tilde{u}_R} \end{pmatrix} \begin{pmatrix} \tilde{t}_L \\ \tilde{t}_R \end{pmatrix}, \tag{2.43}$$

with

$$\Delta_{\tilde{u}_L} = \left(\frac{1}{2} - \frac{2}{3}\sin^2\theta_W\right) m_Z^2 \cos 2\beta, \tag{2.44}$$

$$\Delta_{\tilde{u}_R} = \frac{2}{3}\sin^2\theta_W m_Z^2 \cos 2\beta. \tag{2.45}$$

Since $m_t \gg m_b$ the mixing of the stop case is enhanced compared to the sbottom. This means that for high values of $(A_0 - \mu\tan\beta)$, there is large mixing and the lighter mass eigenstate $\tilde{t}_1$ can become light, even comparable to or lighter than m_t. The phenomenological consequences of these mixing effects for experimental searches at the LHC are discussed in Section 3.2.

2.2.2. Theoretical Aspects of Supersymmetry

Supersymmetry is the only known way of combining space-time symmetries and inner symmetries, which was shown in Ref. [30]. This might be considered as appealing from a theoretical point of view, since the exploration of possible symmetries as well as the concept of symmetries itself has lead to tremendous success in the field of particle physics. Besides this theoretical argument, there are also many other physical motivations in favor of supersymmetry, some of the important ones are mentioned in this section (see also Ref. [23]).

Hierarchy Problem and Fine-Tuning

The SM is a renormalizable theory, which means that every divergence that arises through loop diagrams can be cured by replacing the so-called bare parameters of the theory (masses, coupling constants) by their renormalized counterparts. For a renormalizable theory, there is no apparent scale at which the theory must fail, as it is the case for example in the Fermi theory with a four fermion coupling with the dimensionful parameter G_F. Nevertheless, it is clear that there exists an upper bound Λ for the validity of the SM, namely the Planck scale M_P, at which quantum gravity effects become important

$$M_P = 1.22 \times 10^{19}\,\text{GeV}. \tag{2.46}$$

The Higgs field is known to have a Vacuum Expectation Value (VEV), commonly written [24] as $\langle 0\,|\,\phi|0\rangle = v/\sqrt{2}$, which is related to all masses in the SM and experimentally fixed (electroweak scale). This VEV corresponds to the minimum of the Higgs potential

$$V = -\mu^2\phi^\dagger\phi + \frac{\lambda}{4}(\phi^\dagger\phi)^2 \tag{2.47}$$

with $|\phi| = \sqrt{2}\mu/\sqrt{\lambda} = v/\sqrt{2}$. The second term in Eq. 2.47 introduces a Higgs self-coupling and therefore loop corrections to the parameter μ which is related to the Higgs mass

$$\mu^2_{\text{phys}} = \mu^2 - \lambda\Lambda^2. \tag{2.48}$$

[12] It must be noted, that all given expressions are at tree level and can be modified when higher order loop corrections are included.

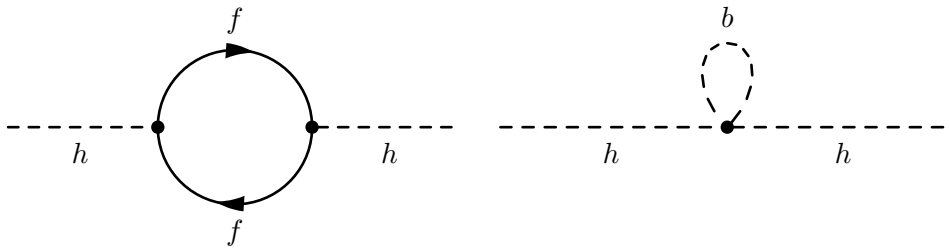

Figure 2.1.: Feynman diagrams of the one-loop contributions from a fermion f (left) and a boson b (right) to the Higgs propagator.

This means that if the Planck scale is considered as the cutoff scale Λ then the bare parameter μ must be of the same order. Both extremely high values must cancel to a high precision to produce a value of μ_{phys} at the electroweak scale, the difference in scales between the electroweak scale and the Planck scale being of 16 orders of magnitude. Mathematically, this could well be the case and there is no logical flaw in this cancellation. Nevertheless, many physicists do consider this as "unnatural". The presented hierarchy problem is even exacerbated by the fact that not only the particles known today, but all states that might exist with masses between the electroweak scale and the Planck scale can contribute to loop diagrams in the Higgs propagator.

If the coupling of the Higgs h to a fermion f is described by a term

$$\mathcal{L}^f_{\text{int}} = -\lambda_f h \bar{f} f \tag{2.49}$$

in the Lagrangian[13], the corresponding contribution to the Higgs squared mass in leading order is given by

$$\Delta\mu^f_{\text{phys}} = -\frac{|\lambda_f|^2}{8\pi^2}\Lambda^2, \tag{2.50}$$

which is quadratically dependent on the cutoff scale Λ. If the existence of two complex scalars b for every fermion f is assumed, which couple to the Higgs according to the term

$$\mathcal{L}^b_{\text{int}} = -\lambda_b |h|^2 |b|^2 \tag{2.51}$$

in the Lagrangian, the one-loop correction of the scalars

$$\Delta\mu^b_{\text{phys}} = \frac{\lambda_b}{8\pi^2}\Lambda^2, \tag{2.52}$$

cancels the contribution of the fermion in case of $\lambda_b = |\lambda_f|^2$. This correspondence of bosons and fermions is the essence of supersymmetry. The Feynman diagrams of the one-loop contributions to the Higgs propagator are shown in Fig. 2.1 for a fermion (left) and for a boson (right). The cancellation is exact for unbroken supersymmetry, which implies equal masses of the fermion and the corresponding boson.

As a result, assuming supersymmetry solves the hierarchy problem, since every fermion loop contribution is canceled by the corresponding boson loop contribution. This solution of the hierarchy problem can be preserved even for broken supersymmetry, as discussed below ("soft" SUSY breaking).

[13]This argument follows the discussion in Ref. [23].

R Parity and Dark Matter

There are astrophysics observations of gravitational effects, like the properties of rotational curves of spiral galaxies [31] or the collision of galaxies [32], that cannot be explained by the observed matter distribution. Therefore, the existence of large amounts of so-called dark matter is inferred. Particles contributing to the dark matter abundance should be massive, neutral (with respect to electric charge and color) and only weakly interacting. There is a number of experiments, in operation or planned, searching directly for Weakly Interacting Massive Particles (WIMPs). The present status of these direct search experiments is summarized in Ref. [33].

Supersymmetry provides a candidate particle for dark matter, in many models the lightest neutralino $\tilde{\chi}_1^0$, under the assumption of a conserved new quantum number named R parity[14]

$$R = (-1)^{3(B-L)+2S} \tag{2.53}$$

with the baryon number B, lepton number L and spin S. Every SM particle is assigned to an R parity of $R = +1$ and every SUSY particle $R = -1$. The postulation of R parity seems quite ad-hoc in this context, but besides giving a dark matter candidate R parity also forbids decays which would violate baryon and lepton number conservation and therefore the proton decay[15]. Although R parity is postulated in the MSSM, there are extensions under study that contain R parity as a remnant of a spontaneously broken gauge symmetry[16].

As a result, SUSY particles are always produced in pairs, and decay eventually to SM particles and the LSP, which is stable due to R parity conservation. The produced LSP then leaves the experiment undetected. Depending on the specific model, in particular the mass hierarchy of the SUSY particles, the decay can occur in short or long cascades. The phenomenology of R parity conserving SUSY is treated in more detail in Section 3.2. One common phenomenological aspect is an experimental signature of missing transverse energy ($E_{\mathrm{T}}^{\mathrm{miss}}$) due to the non-detection of the LSP.

Grand Unification

Already since the 1970s, there have been many efforts to unify the gauge groups $SU(3)_C \times SU(2)_L \times U(1)_Y$ of the SM in one common gauge group (e.g. $SU(5)$ [35], $SO(10)$ [36], E_6). If this succeeded, the SM could be seen as an effective theory, valid for low energy scales. Without SUSY the gauge coupling unification cannot be achieved: Figure 2.2 shows the running of the (inverse) coupling constants in the SM and the MSSM. In contrast to the SM, a supersymmetric extension could be the valid low energy effective theory[17].

[14] Often an alternative (but equivalent) formulation is found in the literature called "matter parity" $P_M = (-1)^{B-L}$ and $P_M = 1$ for $B = 0$ and $L = 0$.

[15] The conservation of R parity is the simplest way of forbidding supersymmetric terms in the Lagrangian that lead to proton decay that is experimentally excluded, by virtue of a Z_2 symmetry. In R parity violating models (RPV) either it must be accepted, that theoretically allowed terms are "accidentally" very small or additional symmetries are postulated, e.g. a Z_3 symmetry called "baryon triality" [34]. The RPV phenomenology is very different from the one with R parity conservation and it is not considered in this thesis.

[16] See Ref. [23] and references therein.

[17] String theory could be a candidate for the underlying fundamental theory, for which the SUSY Grand Unified Theory (GUT) could be the effective low energy theory.

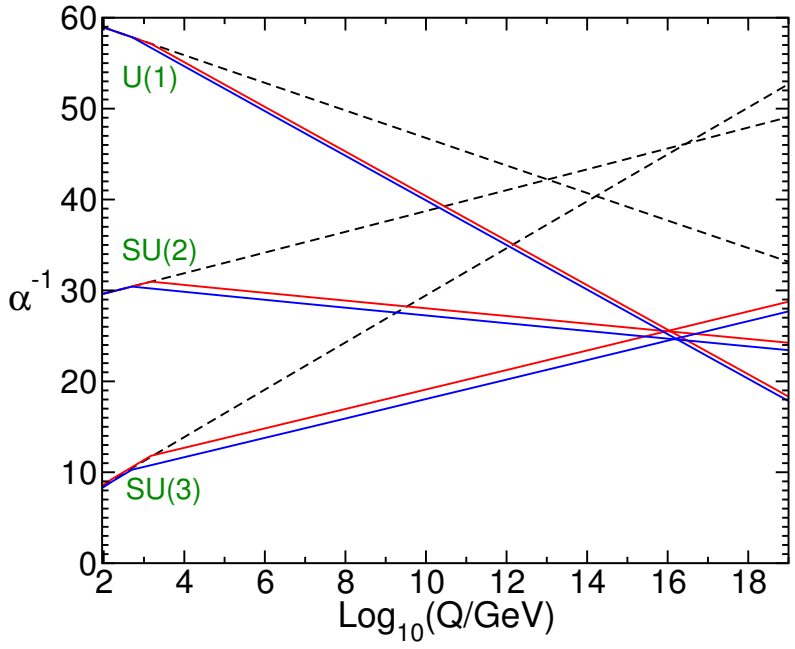

Figure 2.2.: Inverse coupling strength of the three interactions as a function of energy in the SM (dashed lines) and in the MSSM (solid lines). A SUSY mass scale of the order of 1 TeV is assumed, which leads to a change of slope in the energy dependence of the couplings. The gauge couplings unify in the MSSM at $\sim 2 \times 10^{16}$ GeV, while they do not in the SM [23].

Besides the unification of the gauge couplings, a SUSY GUT might additionally unify Yukawa couplings and provide an explanation for the observed charge quantization. Although there are still open theoretical questions and ongoing studies to formulate a complete GUT, there are viable models with predictions, that can be tested with the ATLAS detector.

In the GUT based on the group SO(10) [36], all MSSM gauge couplings are unified at the scale Λ_{GUT}. The parameters of SO(10) SUSY are [37]:

- common gaugino mass at Λ_{GUT} $m_{1/2}$,
- common mass of matter scalars m_{16},
- mass of Higgs soft terms m_{10},
- parametrization of potential splittings in the GUT scale Higgs soft terms M_D^2,
- trilinear coupling A_0,
- ratio of the two Higgs vacuum expectation values $\tan\beta$,
- sign of Higgs mass parameter, $\mathrm{sign}(\mu)$.

The SO(10) SUSY GUT allows not only for the unification of the gauge couplings, but also of the matter superfields in each generation [37]. To achieve this, an additional gauge singlet superfield has to be introduced compared to the MSSM. It is noteworthy, that this additional superfield also contains a right handed neutrino field, which is needed given the evidence for

neutrino oscillations. In the simplest SO(10) SUSY models also the Yukawa couplings in the third generation are expected to be unified $f_t = f_b = f_\tau$ at Λ_{GUT}. The phenomenological consequences of this are discussed in Section 3.3.4.

Supersymmetry Breaking

From theoretical motivations, SUSY is expected to be broken spontaneously. Analogously to the electroweak symmetry breaking, the Lagrangian of the theory is expected to be supersymmetric, whereas the ground state is not, thus hiding the supersymmetry at low energies. This results in the existence of a massless Goldstone particle, in this case a fermion usually referred to as the "goldstino".

To model the breaking of SUSY, two distinct sectors are often assumed. Besides the visible sector with observable particles, a hidden sector is postulated, in which the particles are neutral with respect to the SM gauge group. The breaking of SUSY is assumed to be caused in the hidden sector and communicated to the visible sector by some mechanism (or "messenger"). Examples are gauge- and gravity-mediated SUSY breaking.

Since the mechanism to spontaneously break supersymmetry is unknown, the effects of this breaking are parametrized by explicitly adding SUSY-breaking terms to the Lagrangian, denoted by $\mathcal{L}_{\mathrm{soft}}$

$$\mathcal{L} = \mathcal{L}_{\mathrm{SUSY}} + \mathcal{L}_{\mathrm{soft}}, \tag{2.54}$$

where only terms are included in $\mathcal{L}_{\mathrm{soft}}$, which preserve the solution to the hierarchy problem to all orders of perturbation theory. Introducing m_{soft} as the largest mass scale associated to the SUSY-breaking terms, the correction to the Higgs squared mass

$$\Delta m_H^2 = m_{\mathrm{soft}}^2 \left(\frac{\lambda}{16\pi^2} \ln(\Lambda_{\mathrm{UV}}/m_{\mathrm{soft}} + \dots \right) \tag{2.55}$$

with $\Lambda_{\mathrm{UV}} \sim M_P$ and $\lambda \sim 1$ does not need a high degree of cancellations provided the masses of some light SUSY partners are on the TeV scale. This gives reason to believe that new physics could be found at the LHC[18].

The terms introduced to the Lagrangian by $\mathcal{L}_{\mathrm{soft}}$ include gluino, wino and bino mass terms, contributions to the squark and slepton masses, Yukawa coupling terms and contributions to the Higgs potential. In fact, most of the 124 parameters of the MSSM are introduced by the SUSY-breaking, not by supersymmetry itself. Despite the large number of new parameters in the SUSY-breaking sectors, it is highly constrained by many observables from electroweak precision measurements (e.g. CP violation, FCNC).

2.3. Statistical Methods

In this chapter, the statistical concepts are introduced to test if any given hypothesis about an underlying physics model is compatible with the measured data or if it must be rejected. The interpretations presented in Section 5.4.2 are derived in the framework of the "frequentist-motivated" CLs method [38], which was also adopted by other particle physics experiments. In this way, interpretations from different experiments are easily comparable.

[18] A detailed treatment of SUSY breaking can be found in Ref. [23] and references therein.

2.3.1. Introduction of CLs Method

The level of agreement between observed data and a specific hypothesis H is expressed in terms of a p-value, which is defined as the probability, assuming hypothesis H is correct, to observe data with equal or lesser compatibility with H relative to the measured data. The hypotheses that have to be tested with the experimental data are the null hypothesis (background only, denoted as b) and the signal hypothesis (signal with background, denoted as s+b).

To derive the p-values, a test statistic is defined by $q = -2\ln(L(s+b)/L(b))$, where L stands for the likelihood function, which is explicitly defined in the next section. The probability density function f for the test statistic q is constructed from Monte Carlo pseudo-experiments for the hypotheses $s + b$ and b. The p-values are

$$p_{s+b} = P(q \geq q_{\text{obs}}|s+b) = \int_{q_{\text{obs}}}^{\infty} f(q|s+b)dq, \tag{2.56}$$

$$p_b = P(q \leq q_{\text{obs}}|b) = \int_{-\infty}^{q_{\text{obs}}} f(q|b)dq, \tag{2.57}$$

where q_{obs} stands for the observed test statistic.

For a meaningful exclusion of a possible signal, it is not necessarily sufficient to require p_{s+b} to be less than a certain threshold (e.g. $p_{s+b} < 0.05$). In case of limited experimental sensitivity, a downward fluctuation in the number of observed events can lead to a spurious exclusion if only p_{s+b} is taken into account. Two sets of distributions of the test statistic under the s and $s + b$ hypotheses and the corresponding p-values are shown in Fig. 2.3. On the left, the distributions of the test statistic $f(q|s + b)$ and $f(q|b)$ can be reasonably well separated. On the right this is not the case, corresponding to a lack of sensitivity of the measurement.

To prevent such a spurious exclusion instead of p_{s+b} the so-called CLs value is used, which is defined as the ratio

$$CLs = \frac{p_{s+b}}{1 - p_b}. \tag{2.58}$$

It additionally takes into account the compatibility with the background only hypothesis. The assumed signal model is then considered as excluded at 95% C.L., if $CLs < 0.05$.

2.3.2. Application of the CLs Method

To apply the CLs method, first an appropriate likelihood function has to be constructed. The fact that any real experiment is afflicted with systematic uncertainties has also be taken into account. These uncertainties are included in the form of nuisance parameters $\theta = \theta_1, \ldots, \theta_n$. The likelihood function L used reads as follows

$$L(\mathbf{n}|\mu, \mathbf{b}, \theta) = P(n_S|\lambda_S(\mu, \mathbf{b}, \theta)) \times P_{\text{Syst}}(\theta^0, \theta), \tag{2.59}$$

where the parameters are defined as follows:

- $\mathbf{n}$ stands for the measured distribution in the signal region.
- μ stands for the signal strength:
  $\mu = 1$ corresponds to the $s + b$ hypothesis with nominal signal strength and $\mu = 0$ corresponds to the background only hypothesis b.

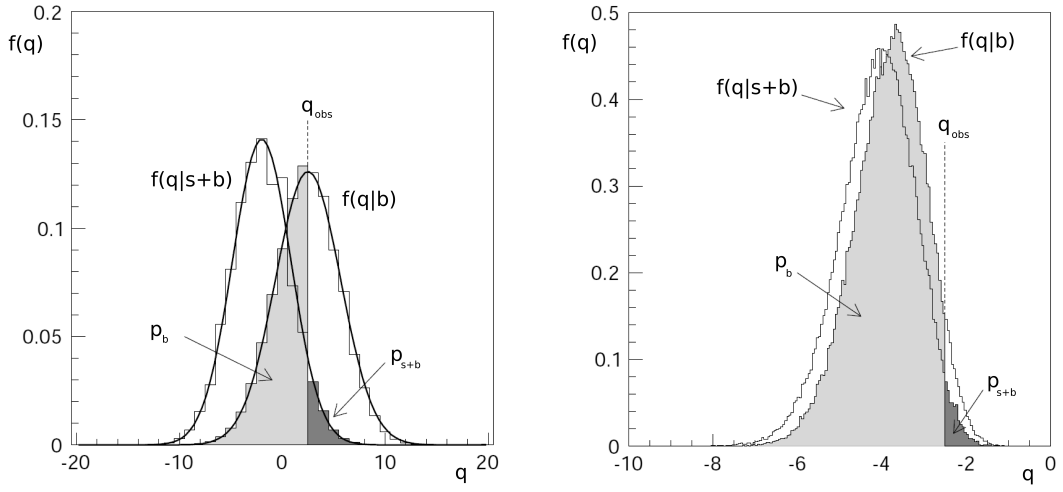

Figure 2.3.: Example distributions $f(q|s+b)$ and $f(q|b)$ of the test statistic q under the two hypotheses b (background only) and $s+b$ (signal and background) and the corresponding p-values [39] for observed test statistics q_{obs}. The figure shows an example of a low (right) and a larger separation power (left).

- **b** stands for the expected background distribution in the signal region.
- θ stands for systematic uncertainties (e.g. luminosity uncertainty).
- $\lambda_S(\mu, \mathbf{b}, \theta)$ is the number of expected events in the signal region given the signal strength μ and the expected background **b** considering correlated systematic uncertainties θ.
- n_S is the number of observed events in the signal region.
- $P(n_S|\lambda_S)$ is the Poissonian distribution of observing n_S events in the signal region given the expectation of λ_S events.
- P_{Syst} takes into account that the systematic uncertainties θ are allowed to vary around the nominal values θ^0.

From this likelihood function L, the test statistic $\tilde{q}_\mu$ is derived[19]:

$$\tilde{q}_\mu = -2 \ln \frac{L(\mu, \hat{\hat{\theta}}(\mu))}{L(\hat{\mu}, \hat{\theta})} \tag{2.60}$$

where $\hat{\mu}$ and $\hat{\theta}$ maximize the likelihood and $\hat{\hat{\theta}}(\mu)$ maximizes the likelihood for any given μ. In the previous expression, it is assumed that $0 \leq \hat{\mu} \leq \mu$ holds. The expression in Eq. 2.60 is called profile log likelihood ratio.

2.3.3. Setting Limits

If no significant excess over the SM expectation is observed in data, there is the possibility to constrain specific BSM model parameters using statistical methods. With the test statistic

[19] For simplicity of the notation, all parameters except μ and θ are suppressed.

given in Eq. 2.60 the p-values and hence the CLs value can be computed. Since the question of interest is if any given (nominal) signal model can be excluded, the signal strength for the limit setting is set to $\mu = 1$.

3 Phenomenology at Hadron Colliders

In this chapter, the main phenomenological aspects of hadron colliders in general and SUSY processes in particular are described.

3.1. Basic Principles of Hadron Collider Phenomenology

The total energy E_{cm} in the center-of-mass frame of two colliding particles of identical type with four-momenta p_1 and p_2 is usually written in terms of the Mandelstam variable $s = (p_1 + p_2)^2$. At a collider, both of the colliding particles are accelerated and collide with $\vec{p_1} = -\vec{p_2}$, resulting in

$$E_{\mathrm{cm}} = \sqrt{s} = E_1 + E_2 = 2E. \tag{3.1}$$

This is in contrast to a fixed target experiment, where the total energy scales approximately with $\sqrt{E}$. This makes collider experiments more efficient for high energy particle physics.

The acceleration of the particles is realized with electromagnetic fields, either in a linear (LINAC), or in a circular accelerator. In the latter, particles are injected and revolve around the ring many times, traversing the accelerating structures in each turn. In the last decades, circular colliders have played the dominant role in high energy particle physics. Both the Tevatron collider and the LHC are designed as circular accelerators.

The most important limitation of a circular e^+e^- collider is the energy loss ΔE due to synchrotron radiation, which scales as follows with the mass m and energy E of the colliding particles

$$\Delta E \sim \left(\frac{E}{m}\right)^4. \tag{3.2}$$

Due to these losses, the construction of a linear e^+e^- collider for high energy particle physics is presently under discussion. In the following, only circular colliders are discussed.

In a real experimental setup, not individual particles, but bunches of particles are accelerated and brought to collision. The interaction rate $\frac{dN}{dt}$ at a collider is given by

$$\frac{dN}{dt} = \mathcal{L}\sigma \tag{3.3}$$

with the cross section σ and the instantaneous luminosity $\mathcal{L}$. The cross section σ is determined by the underlying physics processes and independent of the experimental setup, whereas the luminosity $\mathcal{L}$ is determined by the parameters of the collider. For two colliding bunches with n_i particles per bunch i, revolving with a frequency f around the ring, the instantaneous luminosity is given by

$$\mathcal{L} = f\frac{n_1 n_2}{4\pi\sigma_x\sigma_y}, \tag{3.4}$$

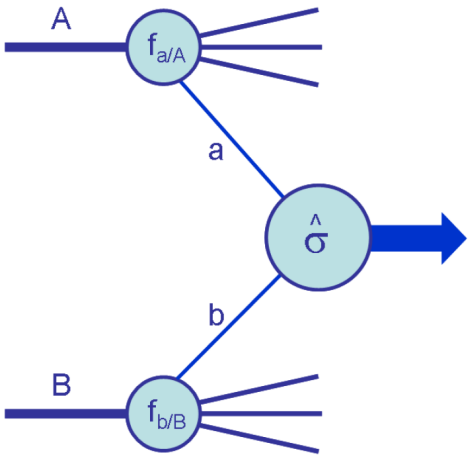

Figure 3.1.: Schematic illustration of the factorization theorem [40]. The constituents a and b of the incoming protons A and B, are characterized by the parton distribution functions $f_{a/A}$ and $f_{b/B}$, respectively. The partonic cross section is denoted by $\hat{\sigma}$.

where σ_x and σ_y are the root mean square (RMS) values of the beam profiles in x and y direction, respectively.

The amount of data that can be recorded and analyzed by the experiment is characterized by the time integrated luminosity L, given by

$$L = \int \mathcal{L} dt. \tag{3.5}$$

Conventionally, the unit $\mathrm{cm}^{-2}\mathrm{s}^{-1}$ is used for the instantaneous luminosity, and the inverse barn ($1\,\mathrm{b} = 10^{-24}\,\mathrm{cm}^2$) is used for the integrated luminosity, typically with prefixes used for SI units, e.g. pb^{-1}, fb^{-1}.

3.1.1. Parton Distribution Functions

Since hadrons are composite particles consisting of quarks and gluons ("partons"), the hard interaction will take place between the partons as they are the fundamental constituents.[1] Unlike the situation in an e^+e^- collider, the precise initial state of the colliding particles is unknown.

The collision of two hadrons A and B with momenta P_A and P_B, respectively, is illustrated in Fig. 3.1. The hard scattering involves the constituents a (of hadron A) and b (of hadron B) with momenta p_a and p_b, respectively. To describe the initial states of the colliding partons, Parton Distribution Functions (PDFs) are used. The function $f_{a/A}(x_a, Q^2)$ describes the probability at momentum transfer Q^2, to find a parton a with momentum fraction x_a inside the hadron A, where the momentum fraction x_a is defined via $p_a = x_a P_a$.

The PDFs are used to make the transition from the hadronic cross section σ to the partonic cross sections $\hat{\sigma}$, which can be calculated in perturbative QCD. For a pp collision with the

[1] For a didactic review see Ref. [40, 41].

final state f in the hard scattering, the cross section can be factorized according to

$$\sigma_{pp\to f+X} = \sum_{i_1,i_2} \int dx_{i_1} dx_{i_2} f_{i_1}(x_{i_1}, Q^2) f_{i_2}(x_{i_2}, Q^2) \hat{\sigma}_{i_1 i_2 \to f}, \tag{3.6}$$

where the sum includes all partons i_1 and i_2 of the two incoming protons.

For the scale Q^2 in the PDFs, the factorization scale μ_F^2 is introduced, which separates the long- and short range (also called "soft" and "hard") physics processes. The partonic cross section $\hat{\sigma}$ is calculated in a perturbative expansion using fixed orders[2] of the QCD coupling constant α_s, which is evaluated at the renormalization scale μ_R^2. Equation 3.6 can then be rewritten as

$$\sigma_{pp\to f+X} = \sum_{i_1,i_2} \int dx_1 dx_2 f_{i_1}(x_{i_1}, \mu_F^2) f_{i_2}(x_{i_2}, \mu_F^2) \left(\hat{\sigma}_0 + \alpha_s(\mu_R^2)\hat{\sigma}_1 + \dots\right)_{i_1 i_2 \to f}. \tag{3.7}$$

The scales μ_F and μ_R are usually chosen to match the typical momentum scale in the hard scattering process, e.g. in the production of a $t\bar{t}$ pair, the typical scale would be the mass of the top quark. If all orders of perturbation theory would be taken into account, the dependence of the cross section on these scales would vanish. Since this is not possible, the remaining dependence on these scales is treated as a theoretical systematic uncertainty.

The Q^2 dependencies of the PDFs are obtained by the so-called DGLAP equations [42–44]. For a quark q, the Q^2 evolution of $f_q(x, Q^2) \equiv q(x, Q^2)$ is given by

$$\frac{d}{d\log Q^2} q(x, Q^2) = \frac{\alpha_s}{2\pi} \int_x^1 \frac{d\xi}{\xi} q(\xi, Q^2) P_{qq}\left(\frac{x}{\xi}\right), \tag{3.8}$$

where P_{qq} is the so-called splitting function. The term $\alpha_s P_{qq}\left(\frac{x}{\xi}\right)$ is proportional to the probability, that a quark q with momentum fraction x originated from a parent quark with momentum fraction $\xi > x$, which has radiated a gluon. When all quarks, antiquarks and the gluon are included, the DGLAP equation shown in Eq. 3.8 becomes a $(2n_f + 1)$-dimensional matrix equation with splitting functions $P_{q_i q_j}$, P_{qg}, P_{gq} and P_{gg}, for $i, j = 1, \dots, n_f$.

The x dependence of the PDFs has to be obtained from experimental data, where a large variety of both collider and fixed-target experiments can be used. The structure of the proton can be probed with both leptons and hadrons. The kinematic reach (possible x and Q^2 values) of different experiments is shown in Fig. 3.2, together with the parton distributions, which they are mainly sensitive to. To a large extent, fixed target and collider experiments are complementary in their kinematic reach. Important contributions to the PDF determinations over a large range of x and Q^2 were made by the collider experiments at HERA [45] in high energy ep collisions (deep inelastic scattering).

As a result, a large number of physics processes are combined for the determination of the PDFs. Different groups have performed fits to the available experimental data, with different choices of input data sets and methodology. A recent review of the different PDF sets available and recommendations with respect to the usage at the LHC can be found in Refs. [46,47]. The parton density functions $f(x, Q^2)$ for quarks and gluons, obtained by the MSTW group [48], are shown in Fig. 3.3 for two values of Q^2.

[2] For perturbative calculations the order in the coupling constant is specified by the terms LO (leading order), NLO (next-to-leading order) and N^{n}LO (higher orders).

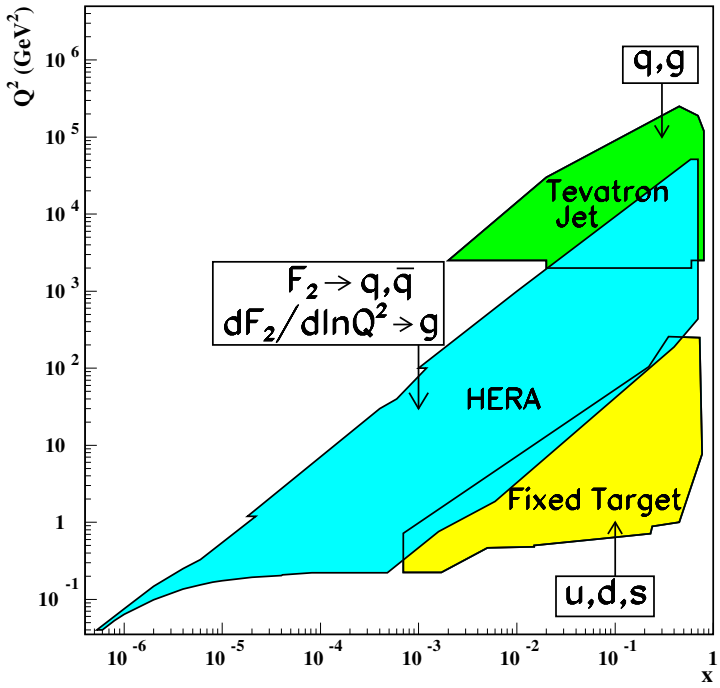

Figure 3.2.: Kinematic reach in x and Q^2 of fixed target experiments and the collider experiments at HERA (ep) and Tevatron ($p\bar{p}$). The insets show the parton distributions, which the experiments are mainly sensitive to (in case of the HERA experiment via the structure function F_2). The Figure is taken from Ref. [19].

3.1.2. Transition from Partons to Hadrons

Due to the confinement of quarks and gluons, a particle detector will detect hadrons instead of partons. Therefore, the connection between the hard scale of the parton interactions and the soft scale connected with hadrons has to be established. In contrast to the perturbative approach used in Eq. 3.7, which takes into account contributions up to a fixed order in α_s, non-perturbative effects have to be included. To a large extent, perturbative (fixed-order) and non-perturbative approaches are complementary and can therefore be combined. Special care has to be taken to avoid double-counting. A detailed review of the concepts presented here, can be found in Refs. [40, 41, 49].

Parton Showers

The evolution of the parton fragmentation is obtained by solving the DGLAP equation (Eq. 3.8). The solution is conventionally written in terms of the Sudakov form factor Δ, which for the initial state parton is defined as

$$\Delta(t) = \exp\left(-\int_{t_0}^{t} \frac{dt'}{t}\frac{\alpha_s}{2\pi}\int \frac{d\xi}{\xi}P(\xi)\frac{f(x/\xi,t)}{f(x,t)}\right), \tag{3.9}$$

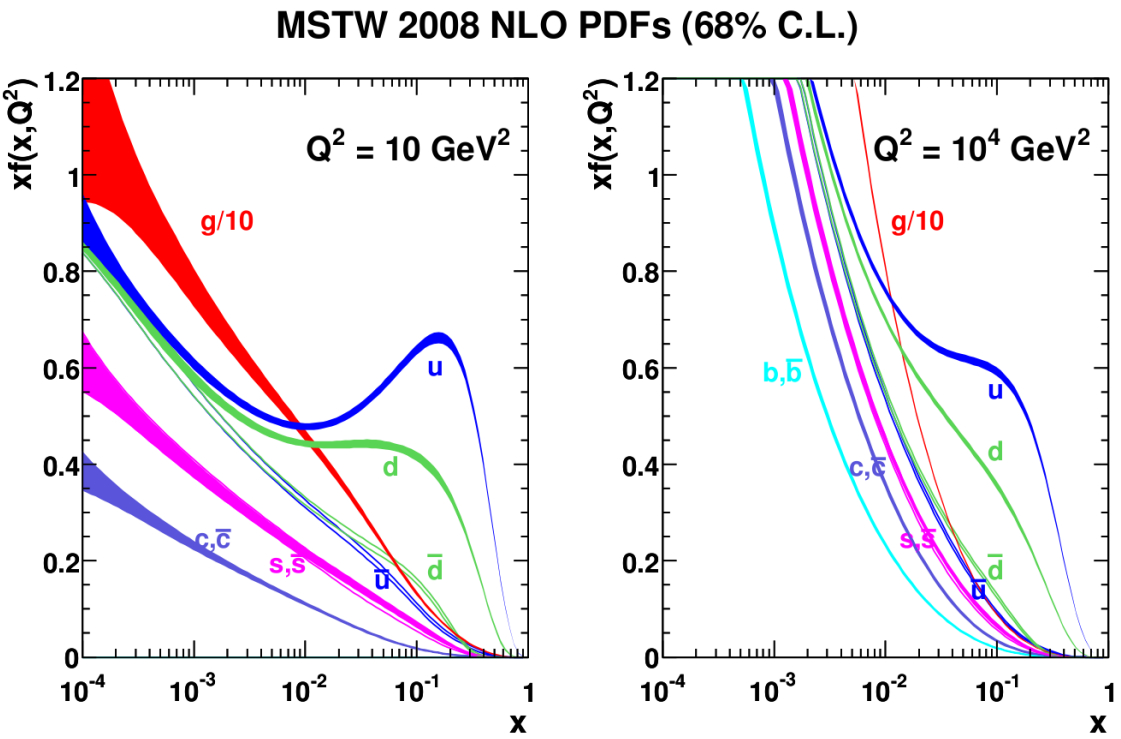

Figure 3.3.: Parton distribution functions $f(x, Q^2)$ for quarks and gluons (scaled by the momentum fraction x) as a function of x and for fixed values of Q^2. The PDFs are calculated at NLO for $Q^2 = 10$ GeV^2 (left) and $Q^2 = 10^4$ GeV^2 (right) [48].

where $t \equiv Q^2$ is the scale of the hard scattering, t_0 is the typical hadronic scale (cutoff scale) and P is the splitting function as introduced in Eq. 3.8. The Sudakov form factor gives the probability for a parton to evolve from a high scale t to the lower scale t_0, without emitting a gluon. To exclude contributions of arbitrarily soft gluons, an explicit infrared cutoff is introduced in the second integral of Eq. 3.9. The analogous expressions can be written down for the final state partons and generalized, including all $2n_f + 1$ splitting functions.

The Sudakov form factor includes the effects of real and virtual parton emission to all orders and is used in Monte Carlo simulation programs to simulate the evolution of partons. The evolution proceeds in steps, where the probability of no resolvable branching at the transition from scale t_i to t_{i+1} is given by

$$p^{\text{no branching}}_{t_i \to t_{i+1}} = \frac{\Delta(t_{i+1})}{\Delta(t_i)}. \tag{3.10}$$

A uniformly distributed random number R with $0 \leq R \leq 1$ is used to decide, if a branching is introduced. As a result, a cascade of partons is simulated. The fixed order calculations and parton showers are combined, using dedicated algorithms, such as CKKW [50] and MLM [51], to avoid double-counting.

Hadronization

For the final connection of the partons to hadronic final states, non-perturbative hadronization models are used. One class of models (string models) is based on the linear confinement of partons. A potential $V(r) = \kappa r$ between two partons is assumed, which depends linearly on the distance r. The so-called string constant κ is determined experimentally. The following example of the production of a $q\bar{q}$ pair illustrates the basic concept: as the $q\bar{q}$ pair moves apart, the potential energy rises and reaches the threshold to create an additional $q\bar{q}$ pair from the vacuum, resulting in two color singlet hadrons.

3.1.3. Underlying Event and Pile-Up

The hard scattering in a hadron-hadron collision involves individual partons inside the hadrons. The partons, that are not participating in this hard scattering ("spectator partons"), can interact on a lower scale, causing multiple "soft" interactions. These processes are summarized in the so-called underlying event. The different Monte Carlo programs include phenomenological models, which are fitted to experimental data, to describe the effects of the underlying event.

Due to the bunch structure of a hadron collider, there are further contributions to the event in addition to the hard scattering. Multiple hadrons can interact within one bunch-crossing ("in-time pile-up"), depending on the structure of the bunches. Due to long detector response times, the final state particles from the previous bunch-crossing can lead to overlapping signals in the detector ("out-of-time pile-up"), depending on the bunch spacing in the accelerator. Both effects are included in the simulated Monte Carlo events.

3.2. SUSY Phenomenology at the LHC

In pp collisions at the LHC, sparticles can be produced in the hard parton-parton interaction via the strong or electroweak interaction [23]. If R parity is conserved, the produced sparticles decay in cascades to SM particles and the LSP, usually the lightest neutralino $\tilde{\chi}_1^0$. The latter will leave the detector undetected and lead to large amounts of missing transverse energy $E_{\mathrm{T}}^{\mathrm{miss}}$, the primary signature in searches for R parity conserving SUSY. Leptons might appear in the final states of SUSY events, e.g. if charginos $\tilde{\chi}_1^{\pm}$ are produced in the cascades and decay via $\tilde{\chi}_1^{\pm} \to \tilde{\chi}_1^0 \ell^{\pm} \nu$ or if sleptons $\tilde{\ell}$ are produced and decay via $\tilde{\ell} \to \ell \tilde{\chi}_1^0$. The production of $\tilde{b}$ and $\tilde{t}$ squarks result in final states containing b and t-quarks. Experimental studies focusing on the third generation squarks use b-tagging to separate signal events from SM background processes.

3.2.1. Production Processes and Experimental Signatures

Typically the dominating SUSY production processes at the LHC proceed via gluon-gluon and gluon-quark interactions [23]. The cross sections for various SUSY processes are shown in Fig. 3.4 as a function of the average mass of the produced sparticles, calculated for $\sqrt{s} = 7\,\mathrm{TeV}$ with the program `PROSPINO` [52, 53]. The strong production results in either pairs of sparticles (e.g. squark-squark or gluino-gluino) or a squark in association with a gluino. For a given mass, the third generation squark production cross section is lower compared to the first and second generation squarks due to the flavor structure of the proton (taken into account by the PDFs). The squark mixing effects, described in Section 2.2.1, can lead to masses of the third

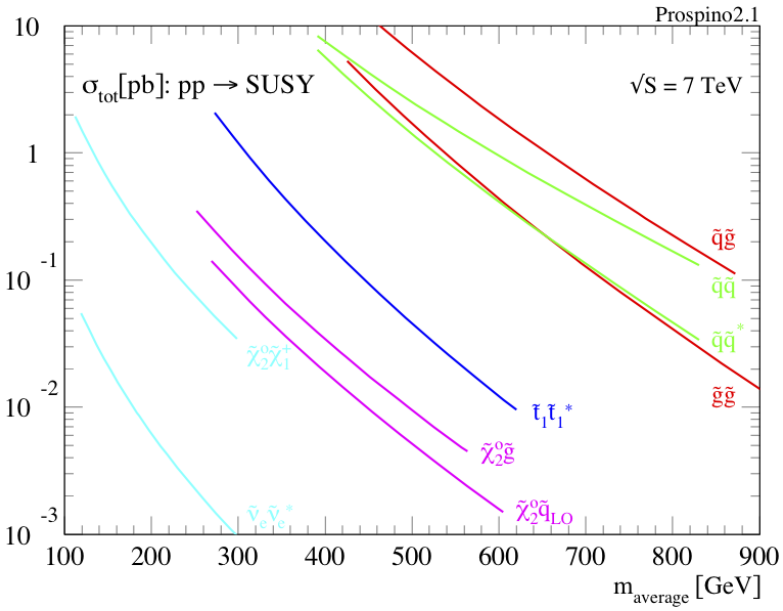

Figure 3.4.: Cross sections for various SUSY production processes as a function of the average mass of the produced particles, calculated with the program PROSPINO [52, 53].

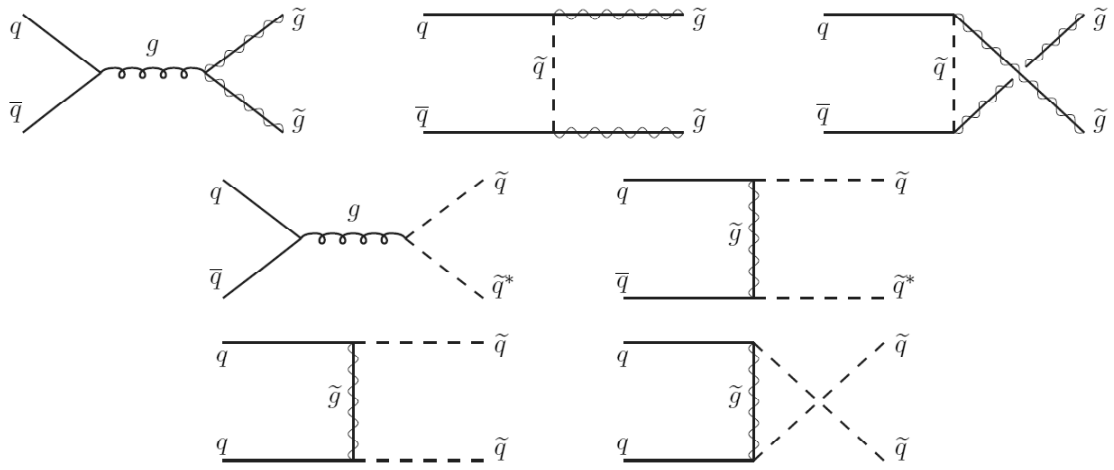

Figure 3.5.: Feynman diagrams for the production of SUSY particles via the strong interaction (quark-quark reactions) [23].

generation squarks that are significantly lighter compared to the first and second generation. As a result, the third generation production can be the dominant SUSY production process.

The Feynman diagrams for possible strong production SUSY processes are illustrated in Fig. 3.5 for quark-quark interactions and in Fig. 3.6 for gluon-gluon and quark-gluon processes.

The electroweak production processes result in pairs of charginos, neutralinos or sleptons

$$q\bar{q} \to \tilde{\chi}_i^+ \tilde{\chi}_j^-, \quad \tilde{\chi}_i^0 \tilde{\chi}_j^0, \quad \tilde{\ell}^+ \tilde{\ell}^-, \quad \tilde{\nu}_\ell \tilde{\nu}_\ell^*, \tag{3.11}$$

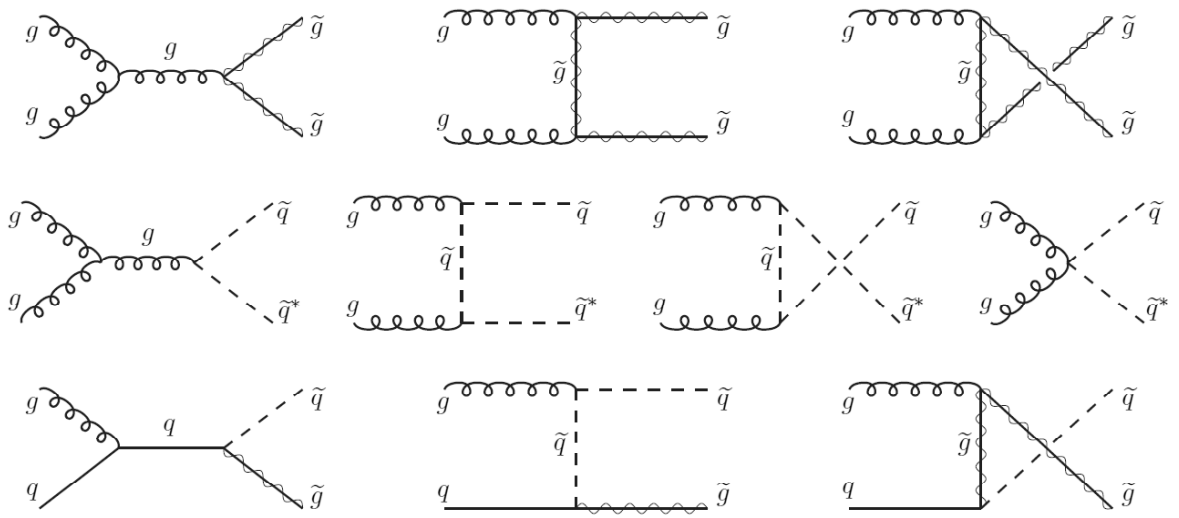

Figure 3.6.: Feynman diagrams for the production of SUSY particles via the strong interaction (gluon-gluon and quark-gluon reactions) [23].

a chargino in association with a neutralino or slepton plus sneutrino

$$u\bar{d} \to \tilde{\chi}_i^+ \tilde{\chi}_j^0, \quad \tilde{\ell}_L^+ \tilde{\nu}_\ell^*, \tag{3.12}$$

$$d\bar{u} \to \tilde{\chi}_i^- \tilde{\chi}_j^0, \quad \tilde{\ell}_L^- \tilde{\nu}_\ell^*, \tag{3.13}$$

where u and d stand for all "up-type" and "down-type" quarks, respectively. The electroweak production processes are expected to be subdominant with respect to the strong production and are therefore not in the focus of this thesis.

3.2.2. SUSY Mass Scale

Supersymmetry provides a rich phenomenology, introducing a variety of parameters that have to be measured experimentally. To facilitate the search for SUSY, many analyses are relying on inclusive quantities, sensitive to the scale of the new physics effects. Once evidence for physics beyond the SM is established, which is consistent with the expectations of SUSY, the underlying parameters have to be measured in detail. Before the discovery is made, it is useful to consider an average SUSY mass scale M_{SUSY} [54, 55]

$$M_{\mathrm{SUSY}} = \frac{\Sigma_i \sigma_i m_i}{\Sigma_i \sigma_i}, \tag{3.14}$$

where all new particles i are included and weighted with their respective inclusive production cross section σ_i. Taking into account the mass of the LSP an effective SUSY mass scale is defined as [55]

$$M_{\mathrm{SUSY}}^{\mathrm{eff}} = \left(M_{\mathrm{SUSY}} - \frac{m_{\mathrm{LSP}}}{M_{\mathrm{SUSY}}} \right). \tag{3.15}$$

This quantity reduces the complexity of the underlying physics model, it cannot be measured directly in the experiment, but well measurable quantities can be constructed that are highly correlated with $M_{\mathrm{SUSY}}^{\mathrm{eff}}$.

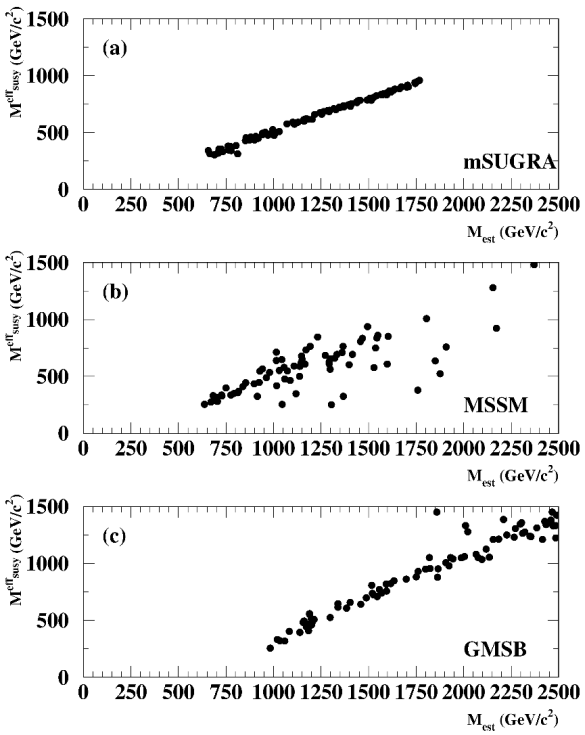

Figure 3.7.: Correlation between M_{est} and $M^{\text{eff}}_{\text{SUSY}}$ for three different SUSY models. Each point corresponds to the average M_{est} for a randomly chosen point in the parameter space of the respective model [55].

m_{eff} Variable

One class of inclusive quantities M_{est} is constructed from the scalar sum of reconstructed objects in the event

$$M_{\text{est}} = \sum_{i=1}^{N} {p_{\text{T}}}_i^{\text{jet}} + \sum_{j=1}^{L} {p_{\text{T}}}_j^{\ell} + aE_{\text{T}}^{\text{miss}} \tag{3.16}$$

where $N = \min\{N_{\text{jets}}, N_{\text{jets}}^{\max}\}$ is the maximum number of jets, $L = \min\{N_\ell, N_\ell^{\max}\}$ the maximum number of leptons taken into account and the parameter $a = 0, 1$. Figure 3.7 shows the correlation between M_{est} and $M^{\text{eff}}_{\text{SUSY}}$ for three different SUSY models, where $N_{\text{jets}}^{\max} = \infty$, ${N_\ell}^{\max} = 0$ and $a = 1$. In the optimization of the gluino mediated stop search the effective mass m_{eff} is used, which is defined as M_{est} with $N_{\text{jets}}^{\max} = 4$, ${N_\ell}^{\max} = 1$ and $a = 1$.

$\sqrt{s}^{(\text{sub})}_{\text{min}}$ Variable

The inclusive variable $\sqrt{s}^{(\text{sub})}_{\text{min}}$ [56, 57] is designed to be sensitive to the new physics mass scale, similar to the m_{eff} variable presented above. In contrast to m_{eff}, it is designed such, that the correlation to the new physics mass scale is mostly independent of model-specific assumptions. By construction, $\sqrt{s}^{(\text{sub})}_{\text{min}}$ is also mostly independent of effects from the underlying event, multiple interactions per bunch-crossing and initial state radiation.

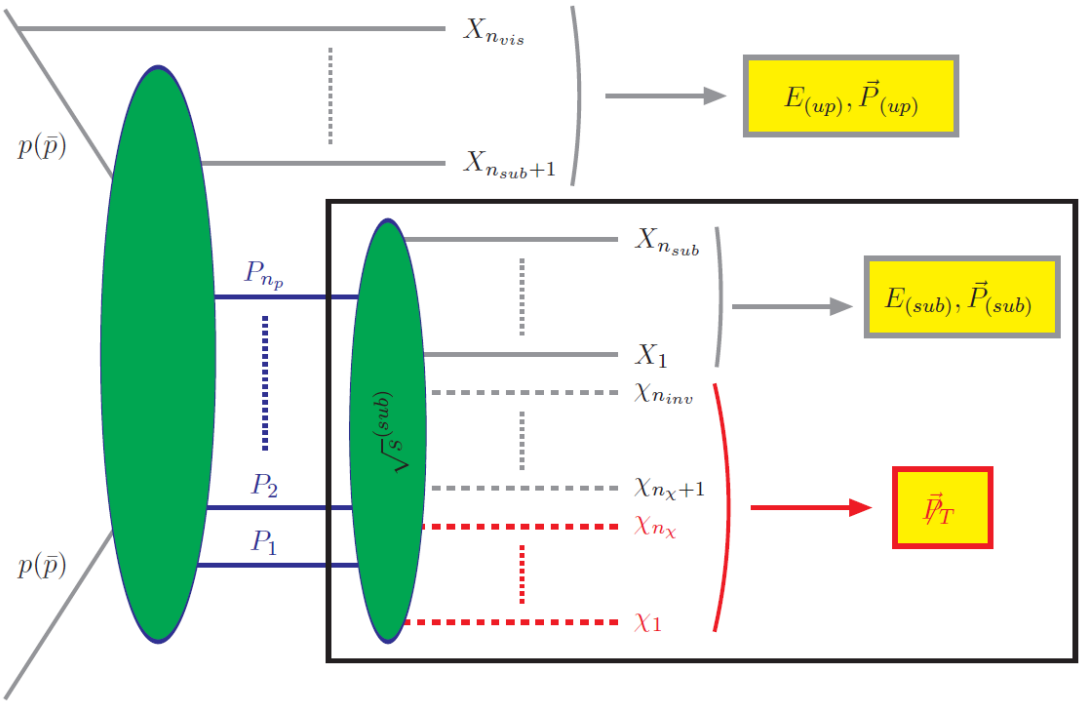

Figure 3.8.: Schematic view of the construction of the $\sqrt{s}^{(\mathrm{sub})}_{\mathrm{min}}$ variable [57]. The box indicates the relevant subsystem, separated from the underlying event.

In general, every event contains n_{vis} "visible" particles $X_1 \dots X_{n_{\mathrm{vis}}}$, which could be reconstructed with the detector (e.g. jets, leptons, photons) and n_{inv} "invisible" particles $\chi_1 \dots \chi_{n_{\mathrm{inv}}}$, which could be standard model particles (neutrinos) or unknown particles like the LSP. For the construction of $\sqrt{s}^{(\mathrm{sub})}_{\mathrm{min}}$, a subsystem is defined[3], which contains the complete event topology, excluding all objects from the underlying event, multiple parton interaction and initial state radiation. The total energy and transverse momentum of all visible particles in the subsystem $X_1 \dots X_{n_{\mathrm{sub}}}$ ($n_{\mathrm{sub}} \leq n_{\mathrm{vis}}$) can be computed, denoted by $E_{(\mathrm{sub})}$ and $\vec{P}_{T(\mathrm{sub})}$. All invisible particles are assumed to be part of the subsystem with missing transverse momentum $\not{\vec{P}}_T$. The construction of these quantities is illustrated schematically in Fig. 3.8. The $\sqrt{s}^{(\mathrm{sub})}_{\mathrm{min}}$ variable is then defined as

$$\sqrt{s}^{(\mathrm{sub})}_{\mathrm{min}}(\not{M}) = \left\{ \left(\sqrt{M^2_{(\mathrm{sub})} + P^2_{T(\mathrm{sub})}} + \sqrt{\not{M}^2 + \not{P}_T^2} \right)^2 - \left(\vec{P}_{T(\mathrm{sub})} + \not{\vec{P}}_T \right)^2 \right\}^{\frac{1}{2}}, \tag{3.17}$$

with

$$M^2_{(\mathrm{sub})} = E^2_{(\mathrm{sub})} - \vec{P}^2_{(\mathrm{sub})}, \tag{3.18}$$

$$\not{M} = \sum_{i=1}^{n_{\mathrm{inv}}} m_i, \tag{3.19}$$

where $\not{M}$ is identical to the sum of all non-SM invisible particles for vanishing neutrino masses. The distribution of $\sqrt{s}^{(\mathrm{sub})}_{\mathrm{min}}$ is expected to have a peak at the sum of the masses of the

[3] The actual construction of this subsystem is analysis dependent. The implementation used in the search for direct stop pair production is discussed in Section 6.1.3.

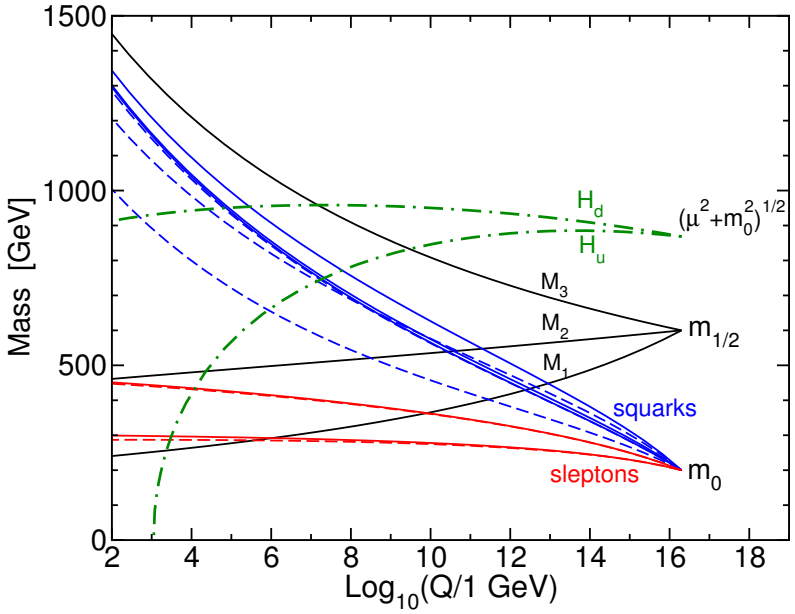

Figure 3.9.: Sparticle mass parameters as a function of the scale Q (renormalization group evolution) for MSUGRA boundary conditions. At $Q_0 = 2 \times 10^{16}$ GeV the unification of all scalar masses to m_0, all gaugino mass parameters M_1, M_2 and M_3 to $m_{1/2}$ and the Higgs mass parameters $(\mu^2 + m_{H_u}^2)^{1/2}$ and $(\mu^2 + m_{H_d}^2)^{1/2}$ to $(\mu^2 + m_0^2)^{1/2}$ is assumed. The value of $(\mu^2 + m_{H_u}^2)^{1/2}$ becomes negative at $Q \sim 1 \times 10^3$ GeV, resulting in electroweak symmetry breaking [23].

parent particles $P_1 \dots P_{n_\mathrm{p}}$ (as denoted in Fig. 3.8). The $\sqrt{s}_{\mathrm{min}}^{(\mathrm{sub})}$ variable is used as a main discriminating quantity in the direct stop pair production search presented in Chapter 6.

3.3. Phenomenological SUSY Models

In this chapter, the specific models that are used in the interpretation of the results are introduced.

3.3.1. Constrained MSSM

The number of parameters of the full MSSM can be reduced by a set of assumptions at a high scale, namely specific boundary conditions that are evolved down to the electroweak scale using renormalization group equations. In the Constrained Minimal Supersymmetric Standard Model (CMSSM) (or Minimal Supergravity (MSUGRA) model), it is assumed that all scalar masses unify to m_0 at the GUT scale. All gaugino masses are assumed to unify to $m_{1/2}$. The Higgs mass parameters $(\mu^2 + m_{H_u}^2)^{1/2}$ and $(\mu^2 + m_{H_d}^2)^{1/2}$ are assumed to unify to $(\mu^2 + m_0^2)^{1/2}$. The renormalization group evolution of the MSSM mass parameters with MSUGRA boundary conditions is shown in Fig. 3.9.

As a result, the reduced parameter space of the CMSSM/MSUGRA model contains

- the universal scalar mass m_0,

- the universal gaugino mass $m_{1/2}$,
- the universal trilinear scalar coupling A_0,
- the ratio of the vacuum expectation values of the two Higgs fields $\tan\beta$ and
- the sign of the higgsino mass parameter, $\mu = \pm 1$.

Many searches for SUSY are interpreted in the framework of CMSSM/MSUGRA scenario.

3.3.2. Simplified Models

The idea behind the concept of simplified models [58] is to construct scenarios with only a small number of additional particles and branching ratios, but each including some key phenomenological features. In that way the large number of possible realizations of SUSY can be grouped qualitatively.

Simplified models are in general not limited to SUSY, since also other BSM models with an additional R parity like discrete symmetry can yield similar experimental signatures, if the newly postulated particles share SM quantum numbers. In the context of this thesis, the focus lies on supersymmetric signatures, thus all quantities are formulated using the language of SUSY[4].

In case a SUSY-like excess is found in data, one possible strategy is to use that particular simplified model that describes the data best as a starting point to study more realistic (and thus more complex) models. This can be more efficient compared to a complete scan over the MSSM parameter space.

A typical strategy to construct a simplified model is to first define the main production mechanisms and decay channels. As discussed in Section 3.2, it is likely that the strong production processes dominates the production processes: $qq \to \tilde{g}\tilde{g}$, $qq \to \tilde{q}\tilde{q}$, $gg \to \tilde{g}\tilde{g}$ and $gg \to \tilde{q}\tilde{q}$. In the following, two specific simplified models are constructed, tailored to the third generation final states.

Gt Simplified Model

In the Gt model $\tilde{g}\tilde{g}$ production is assumed. The $\tilde{t}_1$ is assumed to be the lightest squark with $m_{\tilde{g}} < m_{\tilde{t}_1}$. The masses of all other sparticles are assumed to be above the TeV scale and thus out of reach. The three-body decay $\tilde{g} \to tt\tilde{\chi}_1^0$ of the gluino via an off-shell stop $\tilde{t}_1(*) \to t\tilde{\chi}_1^0$ is the only kinematically allowed process[5]. As a result, both gluinos decay via $\tilde{g} \to tt + \tilde{\chi}_1^0$ with a branching ratio of 100%, which is illustrated in Fig. 3.10.

Gtb Simplified Model

As in the Gt model, gluino pair production is considered as the main production process. Both $\tilde{b}_1$ and $\tilde{t}_1$ are assumed to be much lighter than the first and second generation squarks,

[4] To stress that this is in general not necessary, sometimes the phrase "SUSY-like models" is used.

[5] Intermediate highly virtual particles can always contribute, but are suppressed with respect to real particles, if kinematically allowed.

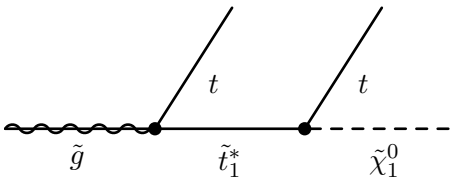

Figure 3.10.: Main gluino decay $\tilde{g} \to tt + E_{\mathrm{T}}^{\mathrm{miss}}$ in the Gt simplified model.

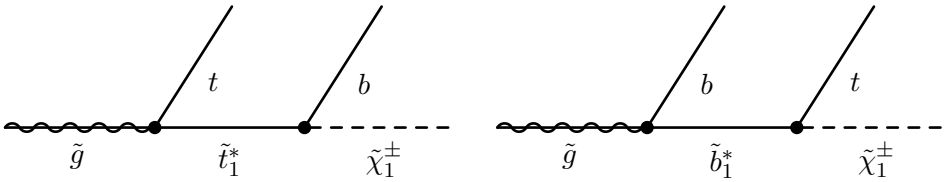

Figure 3.11.: Main gluino decays in the Gtb simplified model.

which are assumed to have masses above the TeV scale. For the gluino, $m_{\tilde{g}} < m_{\tilde{b}_1,\tilde{t}_1}$ is assumed. The main decays to consider are $\tilde{g} \to tb\tilde{\chi}_1^\pm$ via off-shell $\tilde{b}$ or $\tilde{t}$, which are illustrated in Fig. 3.11. The branching ratio of the virtual $\tilde{t}/\tilde{b}$ decay in $b/t + \tilde{\chi}_1^\pm$ is assumed to be 100% and the mass difference between $\tilde{\chi}_1^\pm$ and $\tilde{\chi}_1^0$ is assumed to be low. The charginos $\tilde{\chi}_1^\pm$ will decay further to SM particles and the lightest neutralino $\tilde{\chi}_1^0$ (LSP).

3.3.3. Phenomenological MSSM, Gluino-Stop Model

In the gluino-stop model, $\tilde{t}_1$ is assumed to be the lightest squark with $m_{\tilde{g}} > m_{\tilde{t}_1} + m_t$. All other squarks are assumed to be heavier than the gluino. The $\tilde{t}$ is assumed to be produced via $\tilde{g}\tilde{g}$[6] and $\tilde{t}_1\tilde{t}_1$ and assumed to decay exclusively via $\tilde{t}_1 \to b\tilde{\chi}_1^\pm$. Gaugino universality and thus $m_{\tilde{\chi}_1^\pm} \simeq 2m_{\tilde{\chi}_1^0}$ is assumed, with $m_{\tilde{\chi}_1^0} = 60\,\mathrm{GeV}$. The chargino is assumed to be a pure wino, resulting in a branching ratio of 11% for the process $\tilde{\chi}_1^\pm \to \tilde{\chi}_1^0 \ell^\pm \nu$. Figure 3.12 illustrates the direct production of stop pairs (right) and the production of stops via gluino pair production and decay (left).

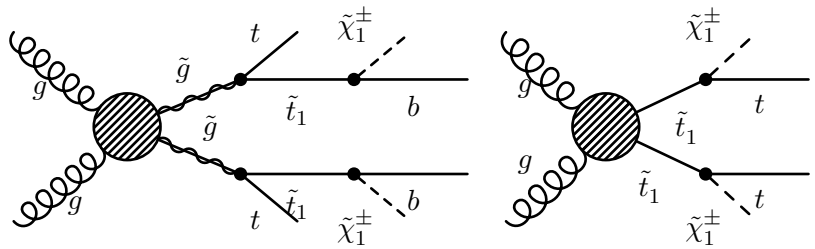

Figure 3.12.: Example diagrams for the gluino-stop model: Gluino pair production (left) and stop pair production (right).

[6]The Branching Ratio (BR) for $\tilde{g} \to \tilde{t}_1 t$ decays is assumed to be 100%.

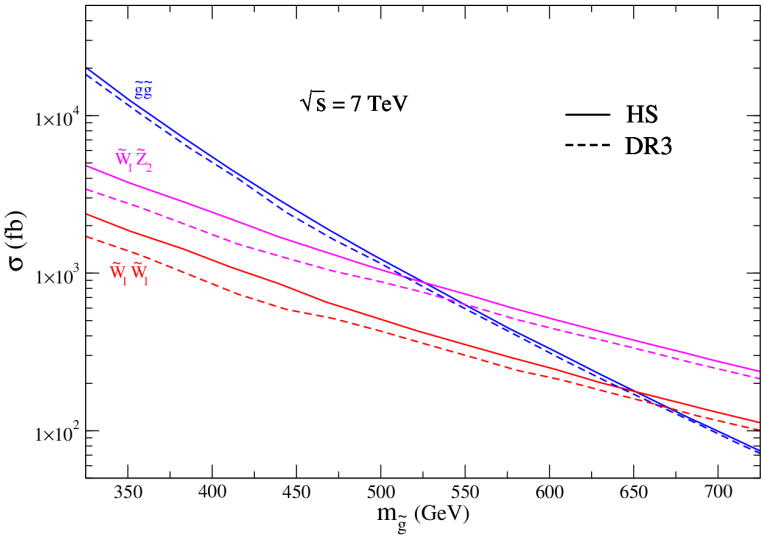

Figure 3.13.: Leading order cross sections as a function of the gluino mass for the production of gluino pairs, chargino pairs and a chargino in association with a neutralino in the DR3 and HS SO(10) SUSY GUT models [37]. The notation in the figure differs with respect to the notation in this thesis: Charginos (neutralinos) are denoted by $\tilde{W}_i$ ($\tilde{Z}_i$).

3.3.4. SO(10)

The SUSY GUT based on SO(10) with Yukawa coupling unification (introduced in Section 2.2.2) is expected to yield gluino masses of about 300 to 500 GeV [37]. Therefore, it can be expected that gluino pair production is the dominant production process with three-body decays into final states rich in b-jets. Two specific models that are used in the interpretation of the results are presented in the following.

To be consistent with radiative electroweak symmetry breaking, the Higgs mass terms must be split at Λ_{GUT}: $m^2_{H_u} < m^2_{H_d}$. This can be achieved by either the breaking of SO(10) affecting all scalar masses, or by splitting only the Higgs sector $m^2_{H_u,d} = m^2_{10} \mp 2M^2_D$. The latter is called "HS model", the former with a small mass splitting between the first and second generation compared to the third generation is called "DR3 model" [37]. The leading order cross sections for both models are shown in Fig. 3.13 as a function of the gluino mass. Up to about 525 GeV the gluino pair production dominates.

In both the DR3 and the HS model the mass spectra can be summarized as follows [37]:

- $m_{\tilde{q},\tilde{\ell}} \sim \begin{cases} 10\,\text{TeV} & \text{1st and 2nd generation;} \\ 1-3\,\text{TeV} & \text{3rd generation;} \end{cases}$
- $m_{\tilde{g}} \sim 300 - 500\,\text{GeV}$;
- $m_{\tilde{\chi}^\pm_1,\tilde{\chi}^0_2} \sim 100 - 180\,\text{GeV}$;
- $m_{\tilde{\chi}^0_1} \sim 50 - 90\,\text{GeV}$.

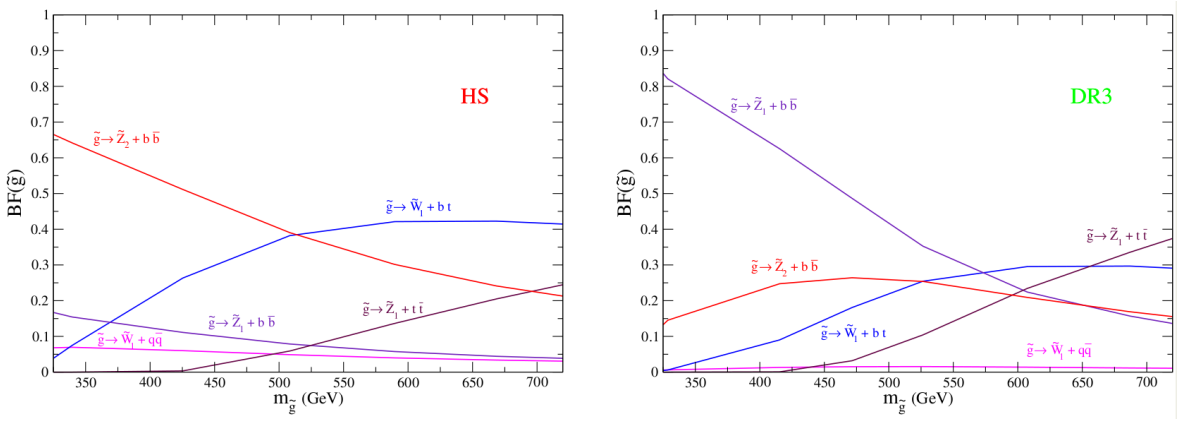

Figure 3.14.: Branching ratios of the gluino as a function of its mass benchmark points in the HS (left) and DR3 model (right) [37].

Due to the low gluino mass and the lighter third generation squarks, the dominant decay modes of the gluino are three-body decays to third generation quarks. Figure 3.14 shows for two benchmark scenarios the branching ratios of the gluino as a function of its mass. For gluino masses below 500-600 GeV, the decay $\tilde{g} \rightarrow \tilde{\chi}^0_{1(2)} + \bar{b}b$ is dominant for the DR3 (HS) model.

3.4. Overview of ATLAS Searches for Supersymmetry

Besides the SUSY searches presented in this thesis, there is a number of further searches being performed by the ATLAS Collaboration, in order to be sensitive to a large variety of SUSY scenarios. Figure 3.15 lists a representative selection of ATLAS searches for SUSY and provides an overview of their respective results. Depending on the analysis, the results are given as limits on a selected sparticle mass. The figure includes key assumptions of the individual analyses and basic experimental information (integrated luminosity, center-of-mass energy). For further details, the individual references are listed in the figure[7].

The listed ATLAS searches are grouped, according to the SUSY scenario they are designed to be sensitive to. Missing transverse momentum ($E_{\mathrm{T}}^{\mathrm{miss}}$) is one key observable used in all search channels, where the conservation of R parity is assumed, namely

- inclusive searches;
- third generation squark searches (direct and gluino mediated production of third generation squarks);
- electroweak production of SUSY particles.

The individual channels are characterized by the number of required jets, photons and leptons. The searches, focusing on the third generation of matter, use dedicated identification

[7] Fulltext access is provided to references labeled as "CONF" via the ATLAS public webpage [59] and to references labeled by an eight digit numerical code via the e-print service `arXiv.org`.

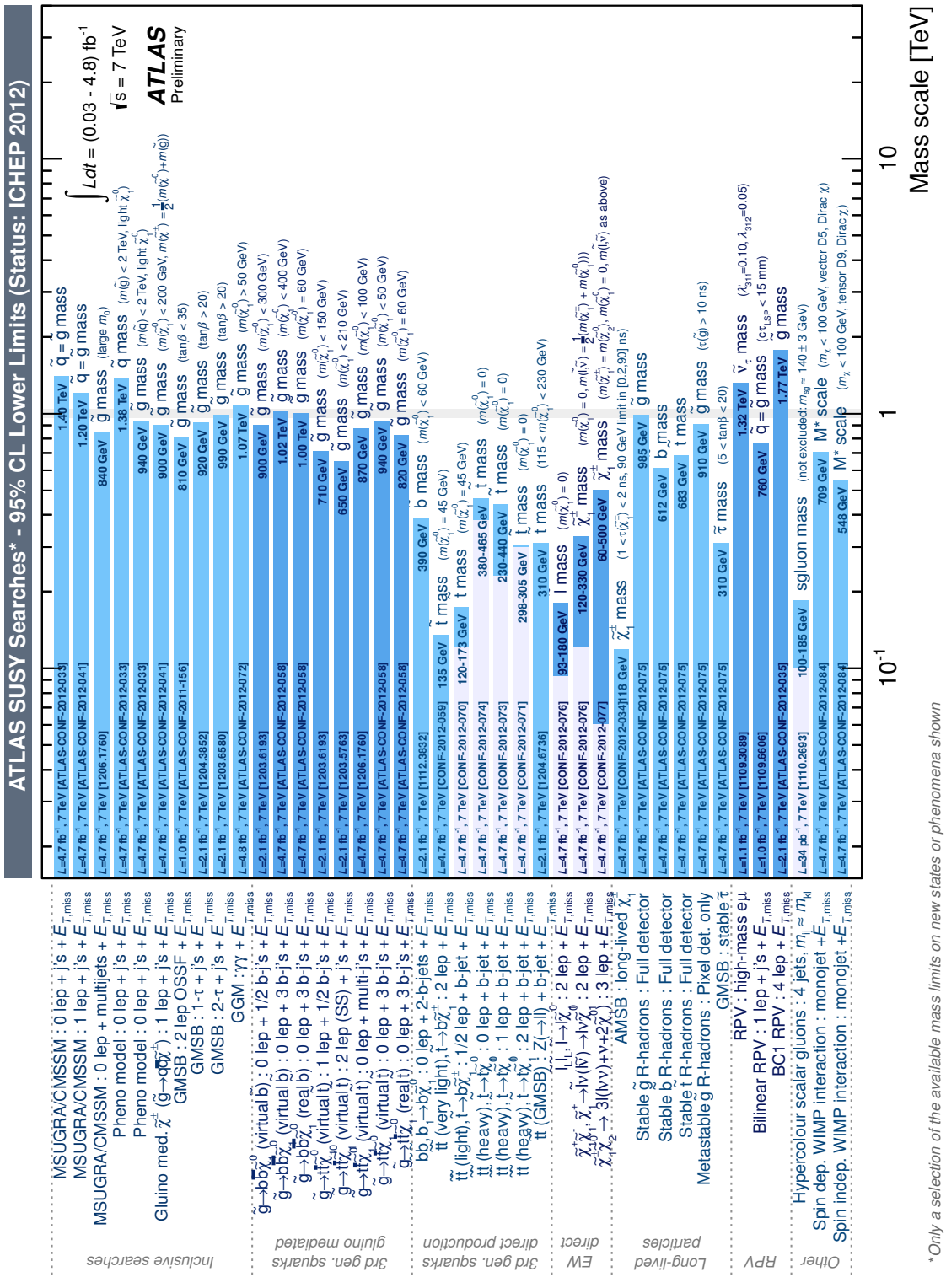

Figure 3.15.: Overview of limits at 95% C.L. for different SUSY mass parameters obtained by different ATLAS searches. The analyses are characterized by the considered model and the experimental signatures. Additional information (integrated luminosity, center-of-mass energy and the publication reference) is given for each analysis. Only a representative selection of the available results is shown [59].

algorithms for b-quarks or hadronically decaying τ-leptons.

Besides the "standard" searches for SUSY based on missing transverse momentum, there are additional analyses being performed in ATLAS targeting more "exotic" phenomenological scenarios. Two groups of searches are listed in Fig. 3.15:

- Under the assumption of R Parity Violation (RPV) the LSP is unstable and can decay to SM particles. Depending on the life time of the LSP, displaced vertices might be observed.
- The possibility to produce long-lived SUSY particles that hadronize inside the detector is studied with dedicated R-hadron analyses.

The remainder of this section presents a selection of ATLAS searches for SUSY with R parity conservation to illustrate the context of the main analyses performed in this thesis.

3.4.1. First and Second Generation Search

Due to the partonic structure of the proton (taken into account by the PDFs), the production cross section for $\tilde{g}\tilde{g}$ or $\tilde{q}\tilde{q}$ of the first and second generation is enhanced compared to the third generation squarks (e.g. $\tilde{t}\tilde{t}$). The cross sections are shown in Fig. 3.4 as a function of the produced sparticle mass.

This illustrates the fact that the first searches for SUSY with the ATLAS experiment were performed in the gluino pair production and first and second generation $\tilde{q}\tilde{q}$ search channels. The main analyses targeting these SUSY production modes were the inclusive 0-lepton search channel (subdivided in two sets of jet multiplicities) and the 1-lepton search channel.

In each analysis, a set of signal regions is defined, typically with different jet multiplicities and p_{T} thresholds. Key variables in these searches are the missing transverse momentum $E_{\mathrm{T}}^{\mathrm{miss}}$ (due to the conservation of R parity) and variables sensitive to the SUSY mass scale (as described in Section 3.2.2), namely

$$m_{\mathrm{eff}}^{N} = \sum_{i=1}^{N} {p_{\mathrm{T}}}_i^{\mathrm{jet}} + E_{\mathrm{T}}^{\mathrm{miss}}, \tag{3.20}$$

$$m_{\mathrm{eff}}^{\mathrm{inc}} = \sum_{i=1}^{N_{\mathrm{jet}}} {p_{\mathrm{T}}}_i^{\mathrm{jet}} + E_{\mathrm{T}}^{\mathrm{miss}} \quad \text{(used in Ref. [60])}, \tag{3.21}$$

$$H_{\mathrm{T}} = \sum_{i=1}^{N_{\mathrm{jet}}} {p_{\mathrm{T}}}_i^{\mathrm{jet}} \quad \text{(used in Ref. [61])}, \tag{3.22}$$

$$m_{\mathrm{eff}}^{\mathrm{inc}} = \sum_{i=1}^{N_{\mathrm{jet}}} {p_{\mathrm{T}}}_i^{\mathrm{jet}} + {p_{\mathrm{T}}}^{\ell} + E_{\mathrm{T}}^{\mathrm{miss}} \quad \text{(used in Ref. [62])}. \tag{3.23}$$

The main backgrounds are typically estimated (or validated) by using a set of dedicated control regions in data, that are kinematically close to the signal region, but dominated by SM background events. Detailed definitions of the individual signal and control regions can be found in Refs. [60–62].

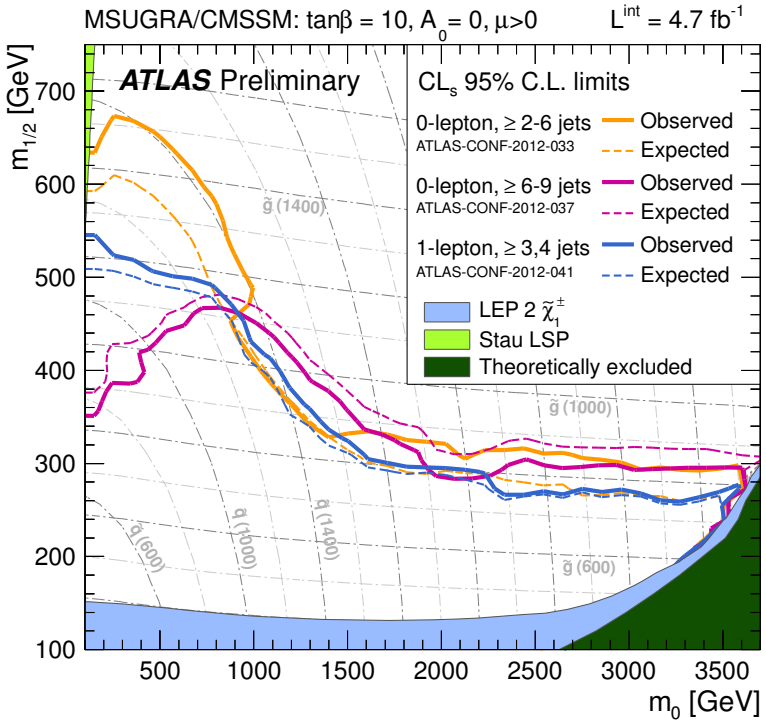

Figure 3.16.: Exclusion limits at 95% C.L. obtained with the zero and one lepton analyses in the $(m_0,m_{1/2})$-plane of MSUGRA/CMSSM for $\tan\beta = 10$, $A_0 = 0$ and $\mu > 0$. For zero leptons two different jet multiplicities are considered. The solid lines show the observed limits, the dashed lines show the expected limits. The individual analyses can be found in Refs. [60–62].

In both the zero and the one lepton analyses, no excess over the SM expectation has been observed. The results are interpreted in the framework of MSUGRA/CMSSM (introduced in Section 3.3.1), with the choice of parameters of $\tan\beta = 10$, $A_0 = 0$ and $\mu > 0$. The individual limits obtained with a dataset, corresponding to an integrated luminosity of $4.7\,\text{fb}^{-1}$, are shown in Fig. 3.16 in the $(m_0,m_{1/2})$-plane[8]. Equal masses of squarks and gluinos up to 1.4 TeV are excluded at 95% C.L., as well as gluino masses up to 840 GeV for high values of m_0.

3.4.2. Motivation for Third Generation Searches

The mixing effects, described in Section 2.2.1, can lead to masses of the third generation squarks, that are significantly lighter than the squarks of the first two families. This can overcompensate for the suppression due to the PDFs and lead to enhanced production cross section of stop and bottom particles. This is one key motivation for the search channels targeting the third generation of squarks.

In searches for SUSY that focus on third generation squarks, it is typically assumed, that the sbottom $\tilde{b}_1$ or the stop $\tilde{t}_1$ is the lightest squark and the neutralino $\tilde{\chi}_1^0$ is the LSP. All other squarks and sleptons are typically assumed to be heavier than 1 TeV. There are dedicated

[8] Additional interpretations in dedicated simplified model scenarios can be found in the references.

searches performed by the ATLAS Collaboration, both for the direct and gluino mediated production of sbottoms. Since the focus of this thesis lies on the search for stop particles, the following discussion concentrates on the stop phenomenology.

The stop is typically assumed to be produced by a gluino decay $\tilde{g} \to \tilde{t}_1 t$ or directly via $\tilde{t}_1\tilde{t}_1$ production. The possible decays of the stop define the experimental final states that can be searched for in the detector. Here, the mass of the $\tilde{t}$ is one essential parameter. Different analysis strategies have been developed to be sensitive to the different ranges of potential stop masses.

For low stop masses $(m_{\tilde{\chi}_1^\pm} + m_b) < m_{\tilde{t}_1} \leq m_t$, the stop will predominantly decay via $\tilde{t}_1 \to \tilde{\chi}_1^\pm + b$ with subsequent decay of the chargino via[9] $\tilde{\chi}_1^\pm \to W^\pm \tilde{\chi}_1^0$. For the direct stop pair production, this scenario is targeted by analyses based on the following final states

- two leptons and large missing transverse momentum [63];
- two b-jets, one or two leptons and large $E_{\mathrm{T}}^{\mathrm{miss}}$.

The latter analysis is presented in detail in Chapter 6. The experimental signatures in this case is similar to the top pair production, which makes this search challenging.

For higher stop masses $m_{\tilde{t}_1} > m_t + m_{\tilde{\chi}_0}$, the stop can additionally decay to a real top via $\tilde{t}_1 \to t + \tilde{\chi}_0$, with subsequent decay $t \to W + b$. For the direct stop pair production, this scenario is targeted by three analyses with b-jets, $E_{\mathrm{T}}^{\mathrm{miss}}$ and zero [64], one [65] or two leptons [66], respectively.

In the case of gluino pair production, where each stop is produced via $\tilde{g} \to \tilde{t}_1 t$, two additional top quarks appear in the final state resulting in four W bosons, four b-jets and $E_{\mathrm{T}}^{\mathrm{miss}}$ due to the neutralinos. The ATLAS search channels for this scenario require large $E_{\mathrm{T}}^{\mathrm{miss}}$ and either

- no leptons and multiple jets (b-jets);
- one lepton and one or two b-jets;
- two leptons and multiple jets.

The 1-lepton search for gluino mediated stop production is presented in detail in Chapter 5.

[9] Depending on the mass of the $\tilde{\chi}_1^\pm$, the produced W will be either real or virtual.

4 The LHC and the ATLAS Detector

This chapter serves as an introduction to the instrumental foundation of the analysis, namely the Large Hadron Collider (LHC) and the ATLAS detector. The section about the detector provides an overview of the individual detector components, needed to successfully reconstruct all final state objects used in the analysis, e.g. electrons, muons, b-jets and $E_{\mathrm{T}}^{\mathrm{miss}}$.

4.1. The Large Hadron Collider

The Large Hadron Collider, located at the European Laboratory for Particle Physics CERN in the vicinity of Geneva, Switzerland, is designed to accelerate and collide two proton or heavy ion beams in an underground ring with a circumference of 27 kilometers. For the presented analysis only data taken with proton beams are of interest. The designed proton energies are 7 TeV per beam. These beam energies could not be realized in the first phase of running due to technical limitations and safety precautions after an incident in 2008. Instead it was decided to run at an energy of 3.5 TeV per beam. After the restart of the LHC at the end of 2009, the LHC was successfully commissioned. In 2010, data corresponding to an integrated luminosity of $35\,\mathrm{pb}^{-1}$ were recorded by the ATLAS experiment which was fit to be used in a previous version of this analysis. The maximum stable instantaneous luminosity in 2010 was $2.07 \times 10^{32}\,\mathrm{cm}^{-1}\,\mathrm{s}^{-1}$. In 2011 it was already $3.65 \times 10^{33}\,\mathrm{cm}^{-1}\,\mathrm{s}^{-1}$ of peak instantaneous luminosity and $5.0\,\mathrm{fb}^{-1}$ of integrated luminosity were collected for analysis. This factor of ten in the instantaneous luminosity also posed new challenges in terms of data analysis, because of the possibility to have multiple interactions per bunch crossing and overlapping signals in the detector from previous bunch crossings (in-time and out-of-time pile-up respectively). The designed instantaneous luminosity for ATLAS is $10^{34}\,\mathrm{cm}^{-1}\,\mathrm{s}^{-1}$, which would bring 23 pile-up events for bunch crossings every 25 ns.

4.2. The ATLAS Detector

The ATLAS detector is a general purpose particle physics experiment located at one of the LHC collision points. As a classical general purpose detector, it is designed to achieve the maximum coverage in solid angle around the interaction point. This is realized by several layers of active detector components around the beam axis (barrel) and perpendicular to the beam axis in the forward regions (end-caps). Different detector technologies are used for the detection of the various particles [67–69]. Figure 4.1 shows an overview of the ATLAS detector, including all subdetectors and the magnet systems (one solenoid and three air-core toroids).

This section is organized as follows. After a brief introduction of the coordinate system used, the individual subdetectors, namely the inner tracker, the calorimeter system and the muon system, will be briefly described. The description of the trigger system and the Detector Control System (DCS), involving all the mentioned subdetectors, follows.

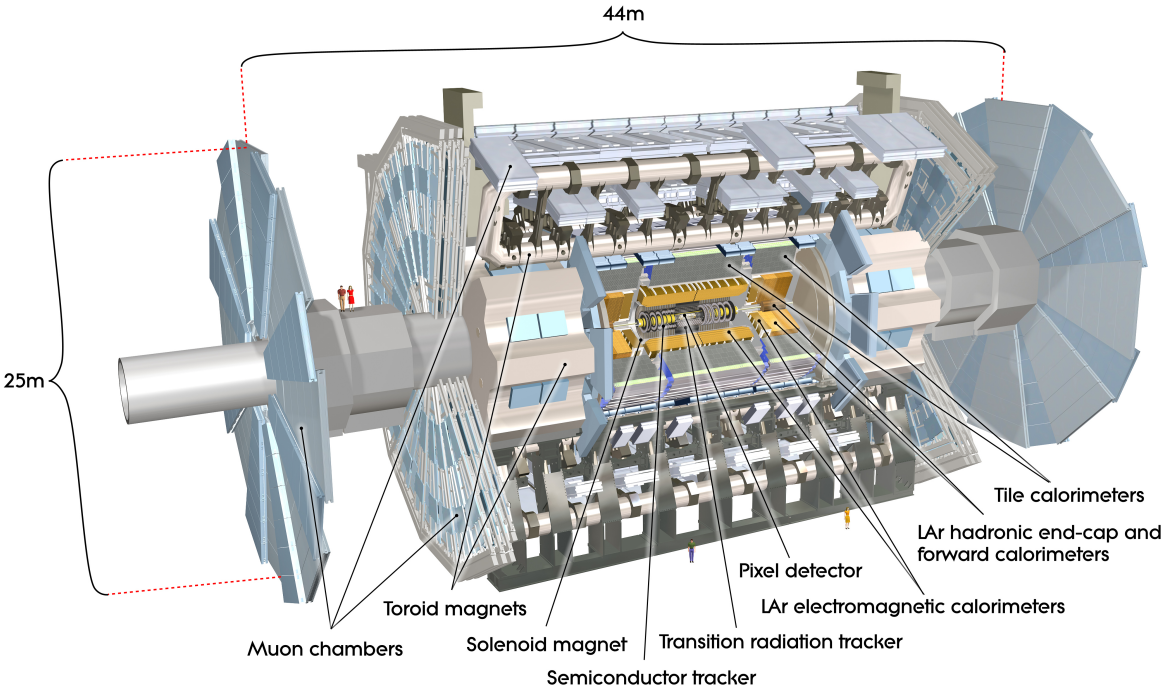

Figure 4.1.: Schematic layout of the ATLAS detector at the LHC, including all subdetectors and the magnet systems [70].

4.2.1. ATLAS Coordinate System and Definitions

A right-handed coordinate system with the origin at the nominal interaction point is used in the ATLAS experiment. The x-axis points to the center of the LHC ring and the z-axis is aligned with the beam axis (in the direction of the LHC beam 2)[1]. The polar angle θ is defined with respect to the LHC beam axis and the azimuthal angle ϕ around the beam axis in the x-y plane.

The pseudorapidity η is related to the polar angle θ by the following relation

$$\eta = -\ln(\tan\theta/2). \tag{4.1}$$

The distance of objects in the pseudorapidity-azimuthal angle space is defined as

$$\Delta R = \sqrt{\Delta\eta^2 + \Delta\phi^2}. \tag{4.2}$$

4.2.2. Inner Detector

The ATLAS inner tracker consists of silicon pixel layers, a Semiconductor Tracker (SCT) and a Transition Radiation Tracker (TRT). All components are arranged in barrel and end-cap segments in a solenoidal magnetic field of 2 T. The layout of the inner detector is shown schematically in Fig. 4.2. The pseudorapidity coverage extends up to $|\eta| < 2.5$. The barrel

[1] So the y-axis points upwards.

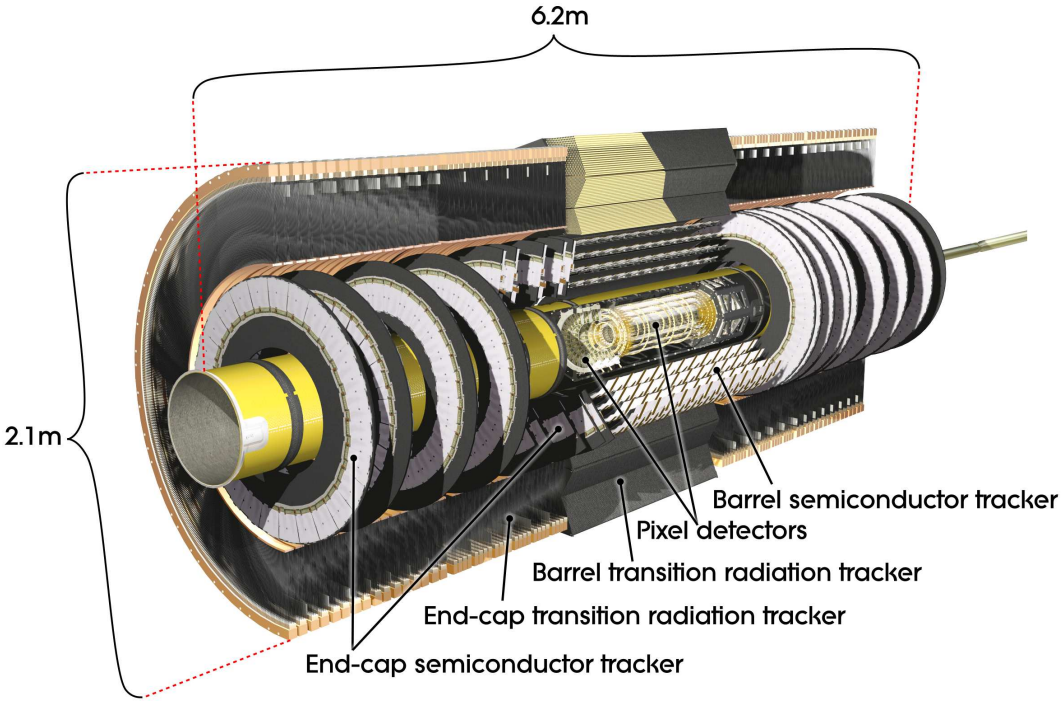

Figure 4.2.: Schematic layout of the ATLAS inner detector [69].

region is shown in detail in Fig. 4.3, including the radial positions of the inner detector components with respect to the beam axis.

The primary goals of the inner detector are to provide tracking information with high momentum resolution, reconstruction of primary and secondary vertices[2] and contribute to the electron identification.

Silicon Pixel Detector

The innermost component is the silicon pixel detector, which consists of three cylindrical layers and three disks (end-caps) perpendicular to the beam axis on each side in the forward direction. In total, the layers consist of 1744 identical silicon pixel sensor modules ($19\,\text{mm} \times 63\,\text{mm} \times 250\,\mu\text{m}$).

The dimensions of the individual pixels[3] is $50 \times 400\,\mu\text{m}^2$. The spatial resolution of the individual modules has been measured with test beam experiments and found to be $4.7\,\mu\text{m}$ for the optimal incident angle and no irradiation.

The total number of readout channels of the silicon pixel detector is 46 080.

[2] The secondary vertex information is essential especially when using b-tagging information.
[3] About 10% of the pixels have a larger size of $50 \times 600\,\mu\text{m}^2$.

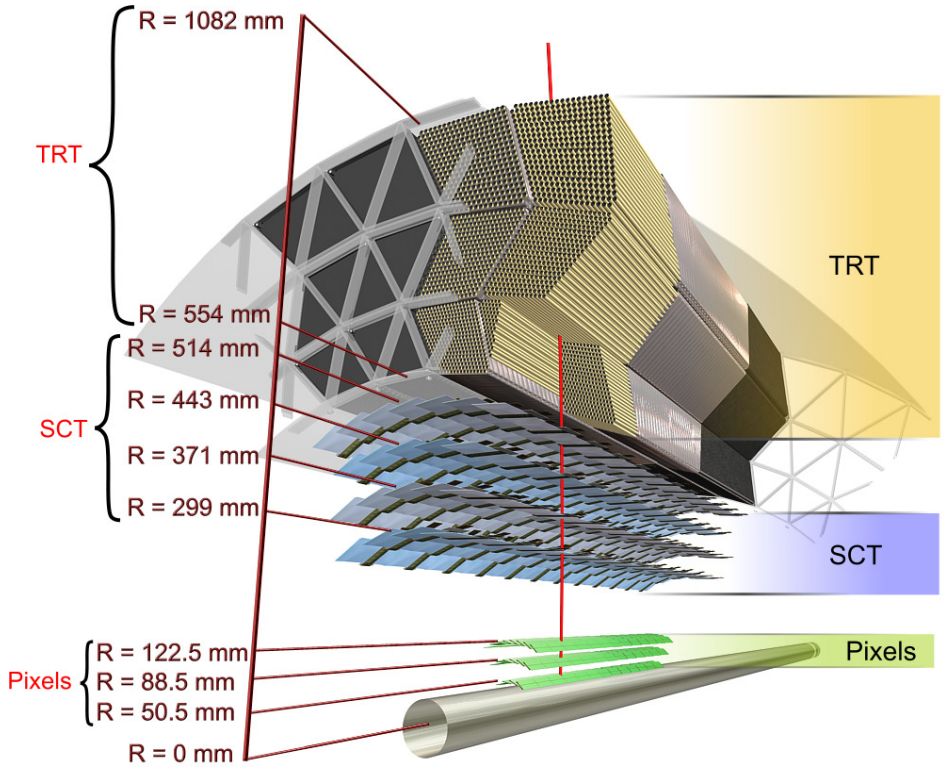

Figure 4.3.: Detailed view of the barrel region of the ATLAS inner detector, showing the radial positions of the detector components with respect to the beam axis [69].

Semiconductor Tracker (SCT)

Adjacent to the pixel detector is the SCT subdetector, which consists of four cylindrical layers and nine disks (end-caps) on each side, perpendicular to the beam axis in the forward direction. In total, there are 4088 individual modules with different dimensions, depending on the position of the module in the barrel or the end-cap.

The 2112 modules in the barrel are built out of two pairs of identical, single-sided silicon micro-strips sensors (768 strips per sensor of 126 mm length and 80 µm pitch), which are rotated around the center of the module by a relative angle of ±20 mrad. In the end-cap, there are 1976 individual modules of three different types. They consist of one sensor pair with a strip length between[4] 52 and 119 mm. The spatial resolution of the individual modules in the $R\phi$ plane is 17 µm and 580 µm in z direction.

The total number of readout channels of the SCT is approximately 6.3 million.

Transition Radiation Tracker (TRT)

The TRT consists of layers of polyimide straws tubes. There are up to 73 layers of tubes, which are parallel to the beam axis, in the barrel region and 160 layers arranged radially in wheels in the end-caps. The individual straw tubes are 4 mm in diameter and have a length

[4] A table with the detailed specifications of the different module types can be found in Ref. [69].

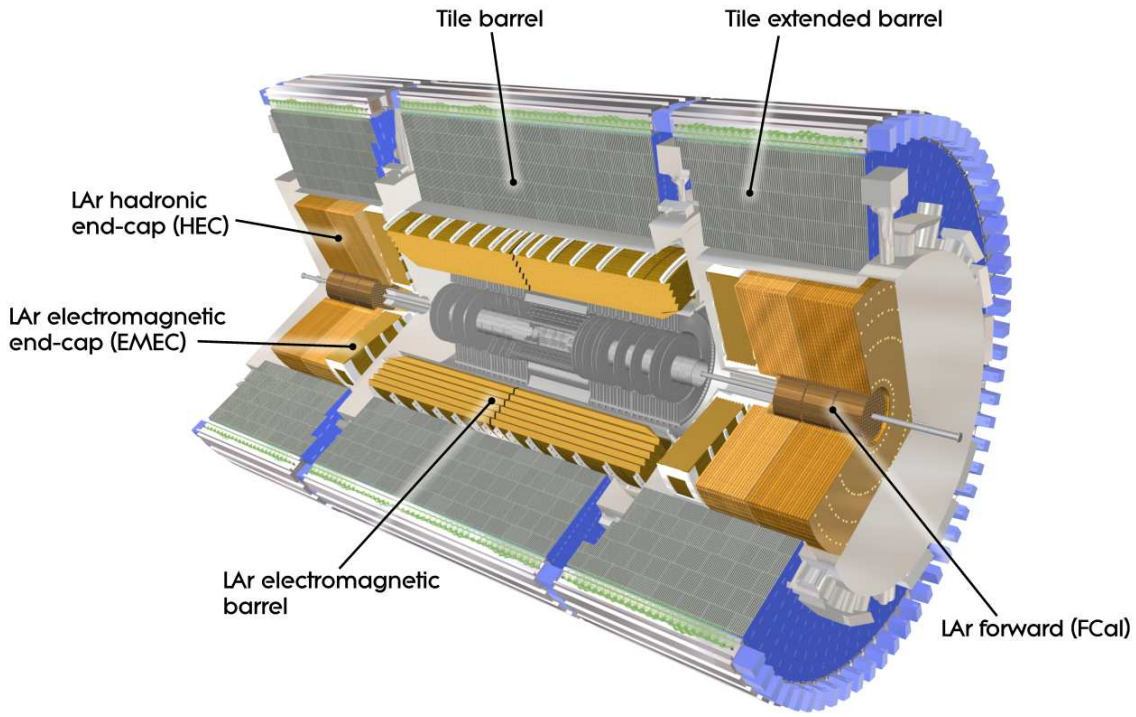

Figure 4.4.: Schematic layout of the ATLAS calorimeters [69].

of 144 cm in the barrel and 37 cm in the end-cap.

On average, the TRT provides two-dimensional measurement points with a $R\phi$ resolution better than 150 µm for charged particle tracks with $|\eta| < 2.5$ and $p_{\mathrm{T}} > 0.5\,\mathrm{GeV}$.

The total number of readout channels of the TRT is approximately 351000.

4.2.3. Calorimeter

The ATLAS calorimeters consist of an electromagnetic and a hadronic calorimeter. The individual components of the calorimeters are arranged in barrels and end-caps, with a total coverage of up to $|\eta| < 4.9$. They are designed to have a good containment of electromagnetic and hadronic showers, as well as a sufficient granularity. The layout of the ATLAS calorimeters is shown schematically in Fig. 4.4.

Electromagnetic Calorimeter

The electromagnetic calorimeter is realized as lead-Liquid Argon (LAr) sampling calorimeter covering a total pseudorapidity range of $|\eta| < 3.2$. It consists of one barrel with $|\eta| < 1.475$ and two end-caps with $1.375 < |\eta| < 3.2$. The granularities $\Delta\eta \times \Delta\phi$ vary, depending on $|\eta|$. The finest granularity is chosen in the central detector region to ensure good identification capabilities for electrons and photons[5].

[5] A detailed list of all used granularities of the EM calorimeter can be found in Ref. [69]

To ensure a good shower containment, the thickness of the electromagnetic calorimeter exceeds 22 radiation lengths X_0 in the barrel and 24 in the end-caps.

Hadronic Calorimeter

The hadronic calorimeter consists of three components: the tile barrel, the LAr hadronic end-cap and the LAr forward calorimeter.

The tile barrel consists of scintillator tiles with a total pseudorapidity coverage of $|\eta| < 1.7$. It is realized as a sampling calorimeter with steel as absorber material. It is segmented in three layers around the beam axis. The total thickness of the tile barrel at $\eta = 0$ is 9.7 interaction lengths λ, to ensure a good shower containment.

The calorimeter end-caps consist of four layers each, with a pseudorapidity coverage of $1.5 < |\eta| < 3.2$, and use LAr as active material. The total thickness is 10 interaction lengths λ.

A dedicated forward LAr calorimeter (both electromagnetic and hadronic) is installed in the extreme forward region $3.1 < |\eta| < 4.9$. It consists of one copper and two tungsten modules with LAr as the active medium and is approximately 10 interaction lengths λ thick.

4.2.4. Muon System

The muon system as the outermost sub-detector is designed to measure tracks of muons. The muon momentum is measured from the curvature of the track, created by magnetic fields. The magnetic field configuration is given by three large air-core toroid magnets and two smaller end-cap toroids. The resulting field is approximately orthogonal to the expected muon tracks.

The muon detectors for precision tracking are a combination of Monitored Drift Tubes (MDT) for $|\eta| < 2.7$ and Cathode Strip Chambers (CSC) for $2.0 < |\eta| < 2.7$. The former consists of tubes with mechanical isolation to the neighboring wires. The latter are multiwire proportional chambers with segmented cathode strips.

The detectors mainly used to trigger on muons are a combination of Resistive Plate Chambers (RPC) and Thin Gap Chambers (TGC) with a coverage of $|\eta| < 1.05$ and $1.05 < |\eta| < 2.7$, respectively.

The layout of the ATLAS muon system is shown schematically in Fig. 4.5.

4.2.5. Trigger System

At the LHC, the colliding particles are protons, non-elementary particles with a partonic substructure, that has to be taken into account. This results in experimental challenges, which are absent in leptonic collider experiments (e.g. e^+e^-, experiments at LEP). Though the center-of-mass energy of the colliding protons can be adjusted, the energy of the parton-parton interaction is not known. Therefore, many variables are measured in the plane perpendicular

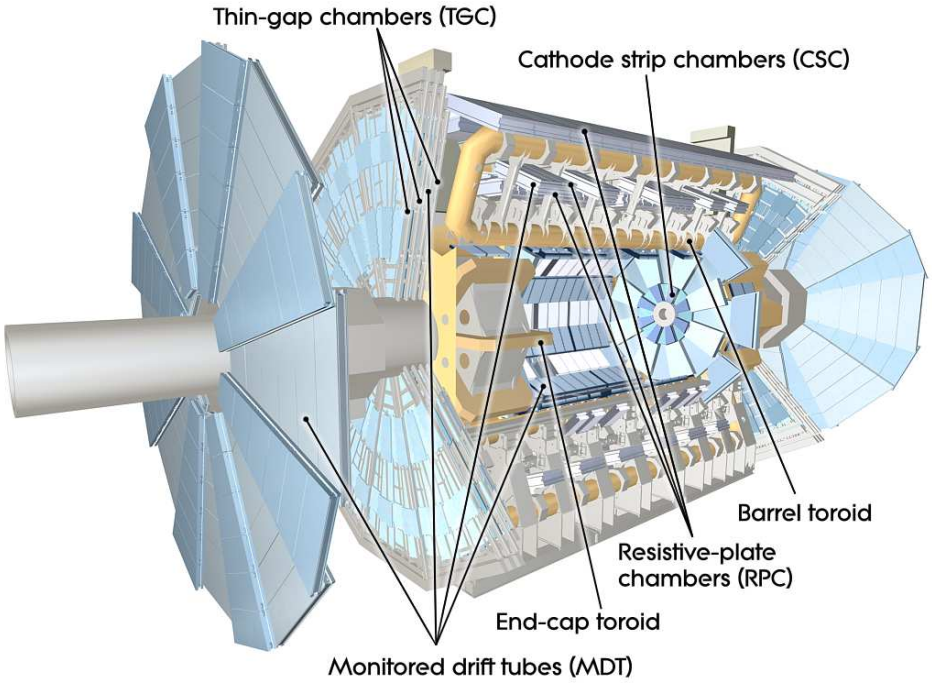

Figure 4.5.: Layout of the ATLAS muon system [69].

to the beam axis.

The hard scattering processes are accompanied by a large number of "soft" interactions, resulting in events with many soft hadronic jets. Figure 4.6 illustrates the cross sections of a set of production processes and the total cross section σ_{tot} as a function of the center-of-mass energy $\sqrt{s}$. At the LHC with $\sqrt{s} = 7\,\text{TeV}$ the cross section for the production of a W boson is six orders of magnitude below the total cross section, for the production of a top pair it is nine orders of magnitude below. To measure rare processes at a hadron collider, the experiments need to be able to reduce the amount of data, while keeping as many "interesting" events as possible.

The design bunch crossing rate at the LHC is 40 MHz. The designed rate of events that can be recorded is on average 200 Hz [67]. The reduction of events by a factor of about 200 000 is achieved with a layered trigger system.

The fastest and most basic trigger level (L1) has a design output rate of 75 kHz and a latency of 2.2 µs. It is realized as a hardware trigger and has not the full granularity of the detector as input. The High Level Trigger (HLT) consists of the Level 2 trigger (L2) and the Event Filter (EF), which are realized as software trigger. The L2 has a designed output rate of 3.5 kHz with a latency of 40 ms, the EF of 200 Hz and 4 s.

4.2.6. Detector Control System

From the description of the ATLAS detector above it is clear, that it consists of a number of sub-detectors and systems with different technologies. To ensure the safety and high quality

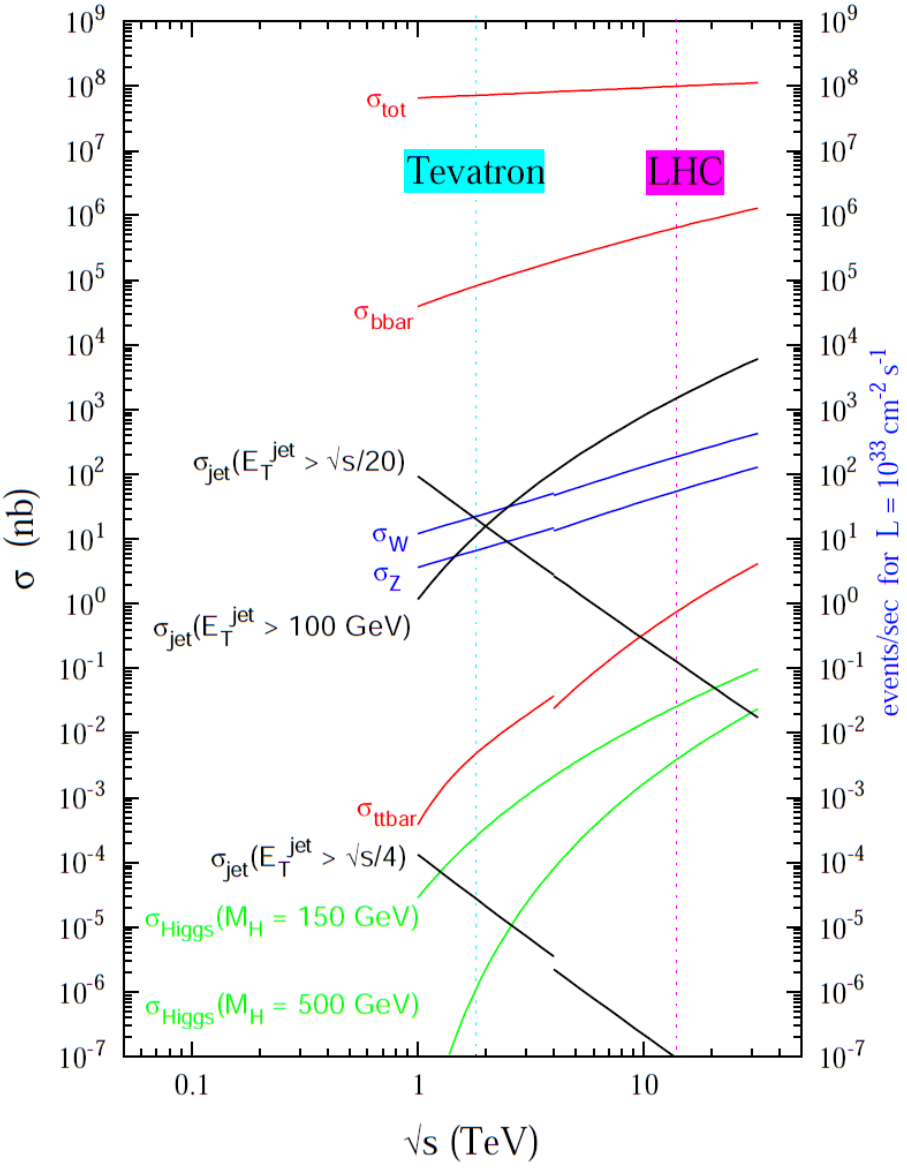

Figure 4.6.: Cross sections for various hard scattering processes as a function of the center-of-mass energy $\sqrt{s}$. To the left of the discontinuity the cross sections are shown for $p\bar{p}$, to the right for pp collisions. The vertical dashed lines indicate the design energies of the Tevatron (left) and the LHC (right) [71].

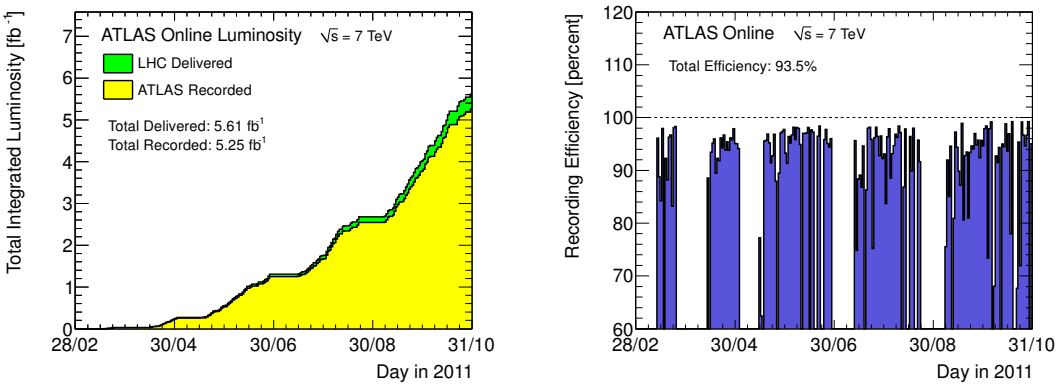

Figure 4.7.: Integrated luminosity delivered by the LHC and recorded with the ATLAS experiment as a function of time during the 2011 data-taking period (left), as well as the ATLAS data-taking efficiency (right).

of the data-taking throughout the detector there are in addition to the physics data (e.g. hits in the tracking detector) a large number of quantities (e.g. temperature sensors on detector modules) that have to be monitored permanently.

The ATLAS Detector Control System (DCS) offers the possibility to monitor and archive important parameters of the different detector components. For the monitoring that is needed while data-taking (online monitoring), a commercial Supervisory Control and Data Acquisition (SCADA) system (PVSS) is in place. To access, display and analyze historical meta data (offline monitoring) a tool was developed that facilitates the monitoring via a flexible and powerful user interface. The details are described in Appendix B.

4.3. Data-Taking and Reconstruction

The ATLAS detector has shown an outstanding performance. Due to the achievements on both the LHC accelerator and the ATLAS detector, it has been possible to deliver (record) a total integrated luminosity of $5.61\,\mathrm{fb}^{-1}$ ($5.25\,\mathrm{fb}^{-1}$) in 2011, resulting in a total data-taking efficiency[6] of 93.5%. Figure 4.7 shows the growth of integrated luminosity with time in 2011 (left) and the ATLAS data-taking efficiency (right). The large amount of collected data could only be achieved by high instantaneous luminosity. The growth of instantaneous luminosity at the ATLAS collision point is illustrated in Fig. 4.8. It shows the instantaneous luminosity per day (left) and the peak luminosity per fill (right).

The high instantaneous luminosity results in challenging data-taking conditions, caused by an increasing number of interactions per bunch crossing (pile-up). Figure 4.9 shows the distribution of the mean number of interactions (left) and the maximum mean number of interactions per bunch crossing (right). The resulting effects for physics analyses are carefully studied and taken into account.

[6]The data-taking efficiency is defined as the ratio between the integrated luminosity, delivered by the LHC and the recorded by the ATLAS experiment.

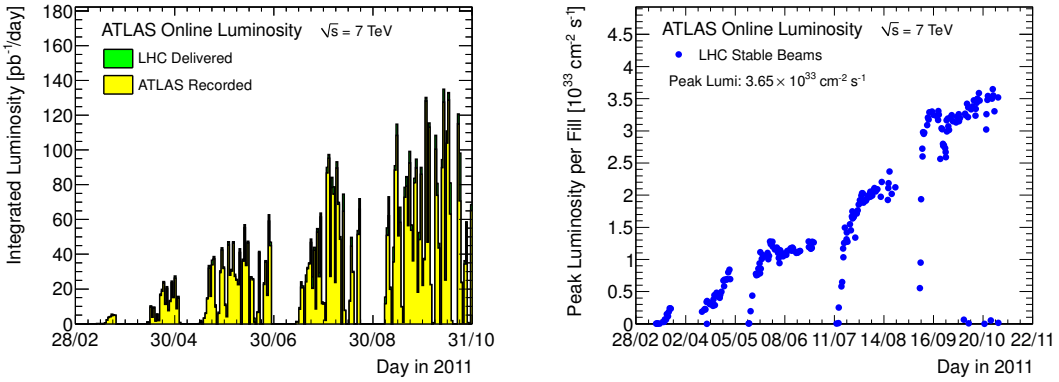

Figure 4.8.: Instantaneous luminosity per day during the 2011 data-taking period (left) and peak luminosity per fill (right).

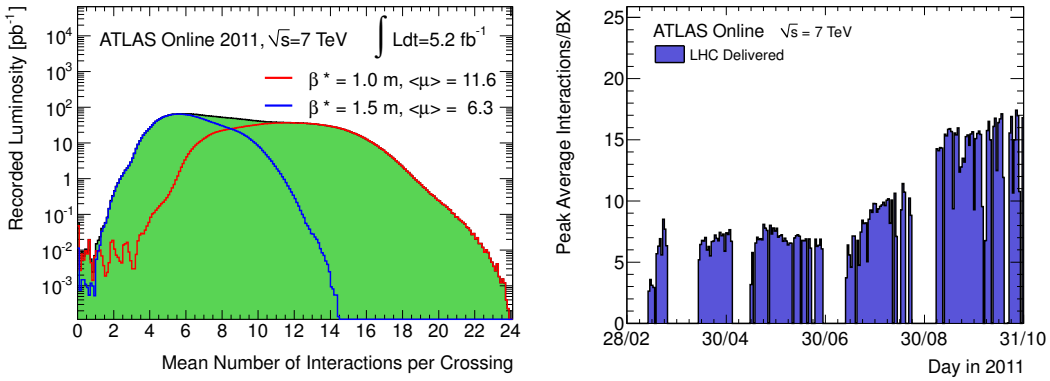

Figure 4.9.: Distribution of the mean number of interactions per bunch crossing for two running periods in 2011 with different beam parameter settings (left). Maximum average number of interactions per bunch crossing by day in 2011 (right).

4.3.1. Reconstruction of Electrons and Muons

This section serves as a summary of the important properties of the reconstruction of electrons and muons. This analysis is focused on a search for SUSY with light leptons, so the reconstruction of electrons and muons is a crucial ingredient, while no attempt is made to make use of hadronically decaying taus.

Electrons

The electrons in the central region of the detector $|\eta| < 2.47$ are reconstructed using clusters in the EM calorimeter matched to reconstructed charged particle tracks in the inner detector (track matching). The ATLAS Collaboration has defined three distinct sets of quality criteria referred to as "loose", "medium" and "tight" [72]. The loose and medium selections are based on information on the energy of the clusters, the showers shapes (lateral and total shower width), the quality of the tracks (hits in the tracking detectors) and the track matching. The tight selection additionally includes criteria to suppress photon conversions. The full list of variables used to define the quality criteria is given in Table 4.1.

Type	Description	Name
Loose selection		
Acceptance	$\|\eta\| < 2.47$	
Hadronic leakage	Ratio of E_T in the first layer of the hadronic calorimeter to E_T of the EM cluster (used over the range $\|\eta\| < 0.8$ and $\|\eta\| > 1.37$)	R_{had1}
	Ratio of E_T in the hadronic calorimeter to E_T of the EM cluster (used over the range $\|\eta\| > 0.8$ and $\|\eta\| < 1.37$)	R_{had}
Middle layer of EM calorimeter	Ratio of the energy in 3×7 cells over the energy in 7×7 cells centered at the electron cluster position	R_η
	Lateral width of the shower	$w_{\eta 2}$
Medium selection (includes loose)		
Strip layer of EM calorimeter	Total shower width	w_{stot}
	Ratio of the energy difference between the largest and second largest energy deposits in the cluster over the sum of these energies	E_{ratio}
Track quality	Number of hits in the pixel detector (≥ 1)	n_{pixel}
	Number of total hits in the pixel and SCT detectors (≥ 7)	n_{Si}
	Transverse impact parameter ($\|d_0\|$ <5 mm)	d_0
Track–cluster matching	$\Delta\eta$ between the cluster position in the strip layer and the extrapolated track ($\|\Delta\eta\| < 0.01$)	$\Delta\eta$
Tight selection (includes medium)		
Track–cluster matching	$\Delta\phi$ between the cluster position in the middle layer and the extrapolated track ($\|\Delta\phi\| < 0.02$)	$\Delta\phi$
	Ratio of the cluster energy to the track momentum	E/p
	Tighter $\Delta\eta$ requirement ($\|\Delta\eta\| < 0.005$)	$\Delta\eta$
Track quality	Tighter transverse impact parameter requirement ($\|d_0\|$ <1 mm)	d_0
TRT	Total number of hits in the TRT	n_{TRT}
	Ratio of the number of high-threshold hits to the total number of hits in the TRT	f_{HT}
Conversions	Number of hits in the b-layer (≥ 1)	n_{BL}
	Veto electron candidates matched to reconstructed photon conversions	

Table 4.1.: Definition of variables used for loose, medium and tight electron identification cuts for the central region of the detector with $|\eta| < 2.47$ [72] .

The energy scale of the electromagnetic calorimeter was obtained in test-beam measurements. The electron energy scale in the final ATLAS experimental setup, was calibrated with a combination of different techniques [72], including in-situ calibrations. The decays of well-known particles into an electron-positron pair are used, namely $Z \to ee$ and $J/\psi \to ee$. Alternatively, the ratio E/p of the energy E measured in the electromagnetic calorimeter and the momentum measured in the inner detector is used for calibration.

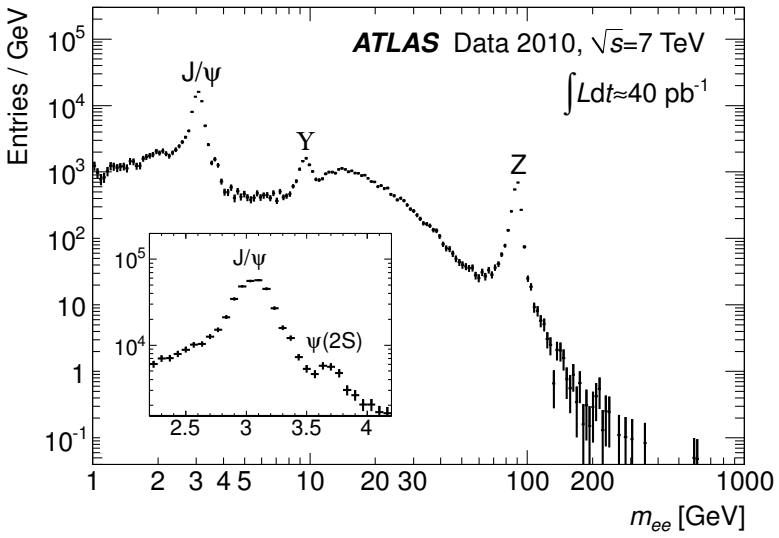

Figure 4.10.: Distribution of the reconstructed mass m_{ee} of electron candidate pairs passing the tight identification criteria for events selected by low E_{T} threshold dielectron triggers. The uncertainties are statistical only. The figure is taken from Ref. [72].

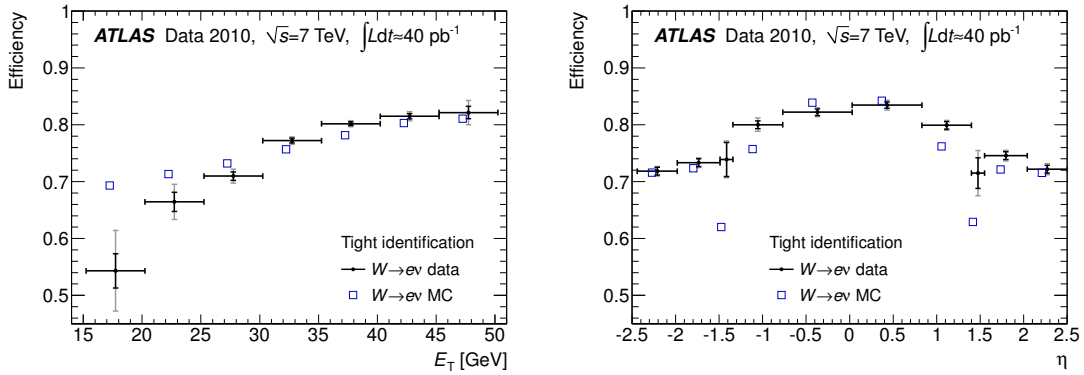

Figure 4.11.: Measured electron identification efficiencies depending on E_{T} (left) and η (right) [72]. The efficiencies are extracted for $W \to e\nu$ events.

To illustrate the performance of the electron reconstruction, the inclusive dielectron mass spectrum m_{ee} is shown in Fig. 4.10 for tight electrons with opposite sign, $E_T > 5\,\mathrm{GeV}$ and $|\eta| < 2.47$. The $c\bar{c}$ mesons J/ψ and $\psi(2S)$ (see inset), the $b\bar{b}$ meson Y and the Z boson are seen as peaks in the distribution.

The electron identification efficiency is studied using the processes $W \to e\nu$, $Z \to ee$ and $J\psi \to ee$. Figure 4.11 shows the measured electron efficiencies depending on E_{T} and η. The observed deviations in the electron identification efficiency in Monte Carlo (MC) and data are used to derive correction factors [72].

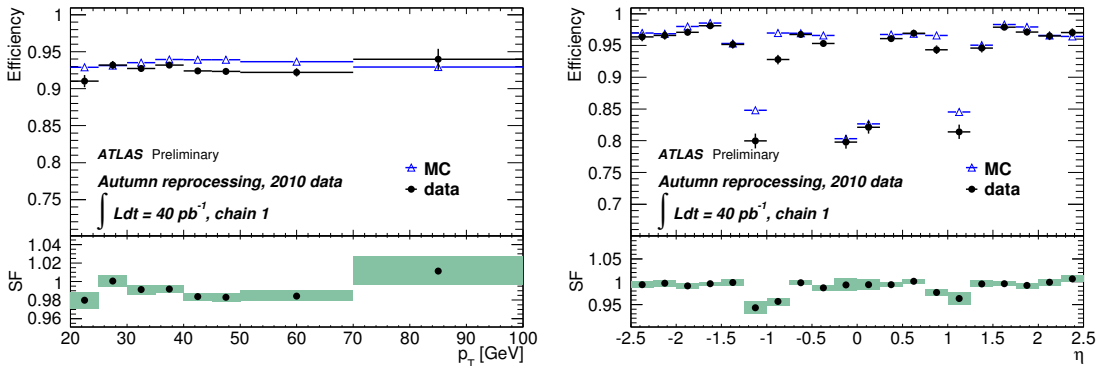

Figure 4.12.: Measured muon identification efficiencies and correction factors (SF) depending on p_{T} (left) and η (right) [74].

Muons

In the ATLAS detector, muons are independently measured in the inner detector and in the muon spectrometer. The STACO algorithm [73] is used to reconstruct the muons matching the information from the two subsystems. The muon momentum is a weighted average of the momentum measurement of the inner detector, which dominates for lower p_{T} values ($p_{\mathrm{T}} \sim 80\,\mathrm{GeV}$ for the barrel, $p_{\mathrm{T}} \sim 20\,\mathrm{GeV}$ for the end-caps) and the muon spectrometer measurement, which dominates for higher p_{T} values ($p_{\mathrm{T}} > 100\,\mathrm{GeV}$) [74].

To suppress background from cosmic muons, events with a muon with transverse (longitudinal) impact parameter with respect to the primary vertex exceeding 0.2(1) mm are rejected. As in the case of electrons a set of quality criteria has been defined:

- at least one hit in any pixel layer;
- at least 6 SCT hits;
- a successful TRT-extension where expected (i.e. within the acceptance of the TRT). An unsuccessful extension corresponds to either no associated TRT hits or a set of TRT hits classified as outliers. For $|\eta| < 1.9$, muons are required to have $N_{\mathrm{TRT}} = N_{\mathrm{TRT}}^{\mathrm{hits}} + N_{\mathrm{TRT}}^{\mathrm{outliers}} > 5$. Tracks with $N_{\mathrm{TRT}} > 5$ should satisfy $N_{\mathrm{TRT}}^{\mathrm{outliers}} < 0.9 N_{\mathrm{TRT}}$ ($N_{\mathrm{TRT}}^{\mathrm{hits}}$ is the number of hits in the TRT associated to the track and $N_{\mathrm{TRT}}^{\mathrm{outliers}}$ is the number of TRT outliers on the muon track).

The muon reconstruction efficiency is studied in data using the process $Z \to \mu\mu$. The observed deviations in MC and data are used to derive correction factors. Figure 4.12 shows the measured efficiencies as functions of η and p_{T}.

The momentum resolution of the muons is also studied in data using the processes $Z \to \mu\mu$ and $W \to \mu\nu_{\mu}$ [75]. In general the resolution was found to be worse compared to the simulation due to the imperfect knowledge of the detector alignment. Figure 4.13 shows the relative mass resolution of the dimuon mass in the $Z \to \mu\mu$ process in the muon spectrometer (MS) and the inner detector (ID).

The muon momentum resolutions were fitted in four different η ranges, separately for the muon spectrometer and the inner detector. As a result, the muon p_{T} is smeared to correct

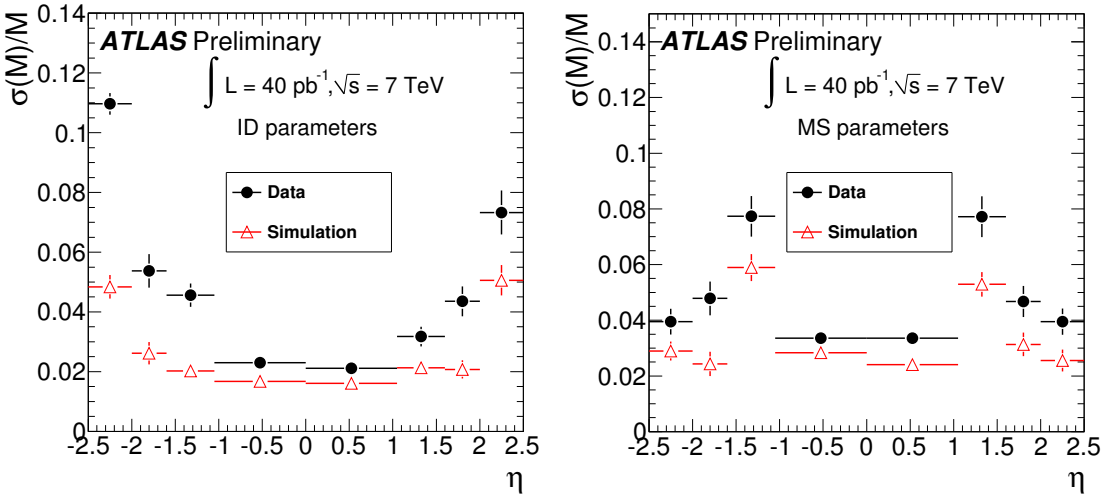

Figure 4.13.: Relative muon mass resolution depending on η for the inner detector (left) and the muon spectrometer (right) [75].

for the differences of the p_{T} resolution of the muon in MC and data.

4.3.2. Reconstruction of Hadronic Jets

Due to the nature of the strong interaction, quarks and gluons produced in the hard scattering process will hadronize and manifest themselves in the detector as collimated sprays of particles called hadronic jets. The algorithm employed in this analysis to reconstruct jets is called anti-k_t [76] and uses topological clusters in the calorimeter [77]. It belongs to a larger class of jet algorithms based on the distance measures

$$d_{ij} = \min\left(p_{Ti}^{2n}, p_{Tj}^{2n}\right) \frac{(y_i - y_j)^2 + (\phi_i - \phi_j)^2}{R^2}, \tag{4.3}$$

$$d_{iB} = p_{Ti}^{2n}, \tag{4.4}$$

with the definitions:

d_{iB}: distance between the particle i and the beam;

d_{ij}: distance between two particles i and j;

p_{Ti}: transverse momentum,

y_i: rapidity and

ϕ_i: azimuthal angle of particle i, respectively.

For the anti-k_t algorithm, n is set to -1. The distance parameter R is set to 0.4 in the jets used.

An important characteristic of the jet algorithm used is its collinear and infrared safety, which means, that jets are stable with respect to collinear and soft emission of partons inside a jet. This property is essential to be able to compare theoretical predictions with experimental

measurements.

The calibration of the jet energy [78] starts from the energy scale of the electromagnetic calorimeter. It has been obtained from test beam measurements and simulation. It is corrected, using $Z \to ee$ events from proton-proton collisions. Using this EM calibration, the energy of particles, that shower electromagnetically in the calorimeter (electrons, photons), is correctly measured.

The calorimeter response is defined as the average calorimeter signal divided by the energy of the incident particle. The ATLAS calorimeters are non-compensating, which means that the calorimeter response for hadrons h and electromagnetic particles e are different. The ratio e/h is a measure for the degree of non-compensation of the calorimeter. It was studied in test-beam experiments with electrons and pions [67]. To recover the correct hadronic energy scale, the EM scale energy of the jets is corrected with energy and pseudorapidity dependent factors, obtained with reconstructed and simulated jets. The influence of multiple interactions per bunch crossing is taken into account.

Spurious (or "fake") jet signals can be caused by non-collision background processes, which mainly consist of beam induced and cosmic muon induced effects [79]. A second source of fake jets is noise in the calorimeter, either noise bursts or coherent noise. A set of cleaning selections is applied to highly suppress fake jet events while preserving an efficiency for "real" jets close to 100%. These selections are based on the calorimeter pulse shapes and thresholds for fractions of energy coming from specific calorimeter regions to prevent noise induced background. Timing variables with respect to the bunch crossing are used to reduce cosmic and beam background effects. Events are rejected if at least one jet of $p_{\mathrm{T}} > 20\,\mathrm{GeV}$ fails the quality criteria.

4.3.3. Missing Transverse Momentum

In all searches for SUSY with R parity conservation, the missing transverse momentum plays an essential role. It is obtained by the negative vectorial sum of the transverse momenta of all reconstructed objects in the event. The unclustered energy, not used to reconstruct any object in the event, is also taken into account. Its modulus is referred to as $E_{\mathrm{T}}^{\mathrm{miss}}$.

The reconstruction of $E_{\mathrm{T}}^{\mathrm{miss}}$ [80] uses information from the calorimeter and the muon detector

$$E_{\mathrm{T}}^{\mathrm{miss}} = \sqrt{(E_x^{\mathrm{miss}})^2 + \left(E_y^{\mathrm{miss}}\right)^2} \tag{4.5}$$

$$E_{x(y)}^{\mathrm{miss}} = E_{x(y)}^{\mathrm{miss,calo}} + E_{x(y)}^{\mathrm{miss},\mu}. \tag{4.6}$$

Additional tracking information is used to account for low energy tracks.

The muon term in Eq. 4.6 is calculated using muons with reconstructed tracks within $|\eta| < 2.7$. The calorimeter term can be decomposed in the contributions of various reconstructed objects (electrons, photons, taus, jets, muons), which are calibrated individually

$$E_{x(y)}^{\mathrm{miss,calo}} = E_{x(y)}^{\mathrm{miss},e} + E_{x(y)}^{\mathrm{miss},\gamma} + E_{x(y)}^{\mathrm{miss},\tau} + E_{x(y)}^{\mathrm{miss,jets}} + E_{x(y)}^{\mathrm{miss,calo}-\mu} + E_{x(y)}^{\mathrm{miss,CellOut}}. \tag{4.7}$$

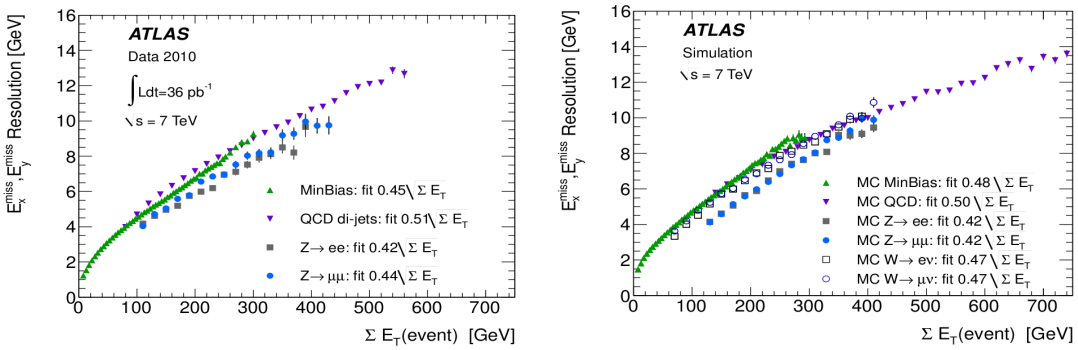

Figure 4.14.: Resolution of E_x^{miss} and E_y^{miss} as a function of ΣE_{T} for various physics processes for data taken at 7 TeV (left) and Monte Carlo simulated events (right). The fit values for the parameter k (see text) are given in the legend [80].

The last term $E_{x(y)}^{\text{miss,CellOut}}$ represents the energy clusters not used to reconstruct any physics object. It contains jets below a threshold which was chosen to be $p_{\text{T}} < 20\,\text{GeV}$[7].

The resolution $\sigma\left(E_{\text{T}}^{\text{miss}}\right)$ of $E_{\text{T}}^{\text{miss}}$ is parametrized using the total transverse energy ΣE_{T}

$$\Sigma E_{\text{T}} = \sum_{i=1}^{N_{\text{calocells}}} E_i \sin\theta_i. \tag{4.8}$$

It is found to be approximately

$$\sigma\left(E_{\text{T}}^{\text{miss}}\right) = k\sqrt{\Sigma E_{\text{T}}} \tag{4.9}$$

with deviations only for low (due to noise) and very high values of ΣE_{T} (due to the constant term in the resolution of the calorimetric energy[8]). Figure 4.14 shows the resolution of E_x^{miss} and E_y^{miss} as a function of ΣE_{T} for various physics processes for data taken at 7 TeV (left) and Monte Carlo simulated events (right). The fit values for the parameter k range between $0.42\,\text{GeV}^{1/2}$ and $0.51\,\text{GeV}^{1/2}$ and are given in the legend. Among the different physics processes, $Z \to \ell\ell$ shows a better resolution compared to dijet events. The comparison of the results from data and Monte Carlo simulated events shows a good agreement for both $Z \to \ell\ell$ and dijet events.

4.3.4. Flavor Tagging

Being able to distinguish b-jets from c-jets and light jets is one crucial aspect of this analysis. This sections gives first an overview of the properties of b-jets and the working principles of b-tagging algorithms. In the second part, the combination of b-tagging algorithms and its calibration is discussed.

[7] In Ref. [80] the treatment of low p_{T} objects for the $E_{\text{T}}^{\text{miss}}$ reconstruction is slightly different. An additional class "soft jets" is defined with $7\,\text{GeV} < p_{\text{T}} < 20\,\text{GeV}$. In addition, different calibration scales are used for the jets.

[8] The energy resolution $\sigma(E)$ of the calorimeter is by convention parametrized as $\sigma(E)/E = a/E \oplus b/\sqrt{E} \oplus c$, where a is the noise term, b is the sampling term and c the constant term.

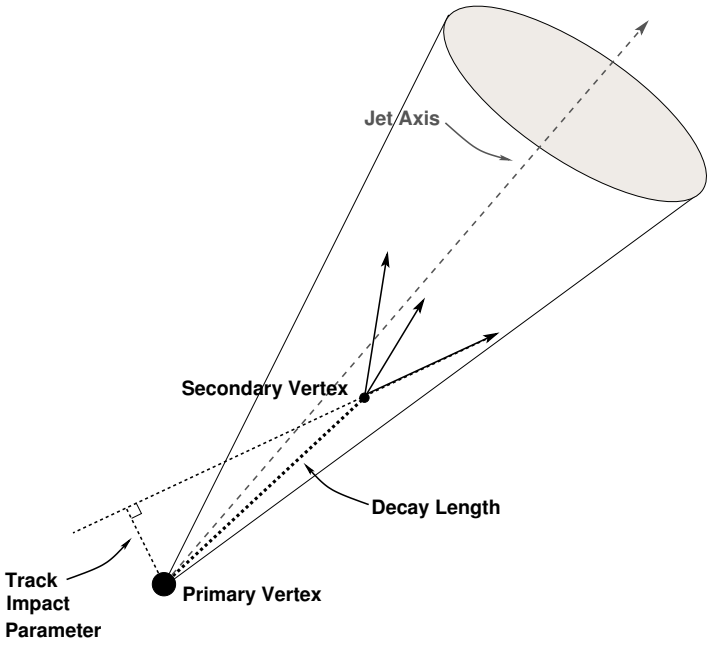

Figure 4.15.: Schematic view of a typical b-jet with a primary and a secondary vertex [81]. Important quantities used for b-tagging are sketched, namely the decay length and the track impact parameter.

The b-quarks produced in the hard interaction process form b-hadrons inside hadronic jets. The mean decay length of the b-hadron with lifetime τ is given by $\langle L \rangle = \beta\gamma c\tau$. For jets with p_{T} of the order of tens of GeV the b-hadrons will decay typically at the order of a few millimeters away from the primary vertex. Figure 4.15 illustrates the typical situation in a b-jet. Most b-tagging algorithms are based on the charged tracks associated to the reconstructed jets.

One class of b-tagging algorithms is based on the information about the impact parameter of tracks with respect to the primary vertex. Both the algorithms "JetProb" and "TrackCounting" use the signed transverse impact parameter[9], its modulus is defined as the distance of closest approach of a track to the primary vertex in the $r\phi$ projection and denoted as d_0 [82,83]. The sign of d_0 is defined by the angle between the jet axis and the line connecting the primary vertex and the point of closest approach. It is positive for angles below 90°, negative otherwise. Tracks from the decay of b or c-hadrons are expected to have positive values preferentially. A more advanced version of an impact parameter based algorithm ("IP3D") is based on a likelihood ratio technique using both the signed transverse impact parameter significance d_0/σ_{d_0} and signed longitudinal impact parameter significance z_0/σ_{z_0} of tracks associated to the jet [84], where z_0 is defined as the z-component of the point of closest approach.

Besides the impact parameter based taggers, there is a class of b-tagging algorithms based on explicitly reconstructing the b-hadron decay vertex. The important quantities in this case are the (signed) decay length L, which is also sketched in Fig. 4.15 and its significance L/σ_L [81] ("SV0"). A more advanced version of a secondary vertex based b-tagging algorithms was developed ("SV1"), which is also based on a likelihood ratio technique using more characteristics

[9] More specifically the signed transverse impact parameter significance $S_{d_0} = d_0/\sigma_{d_0}$ is used with the transverse impact parameter d_0.

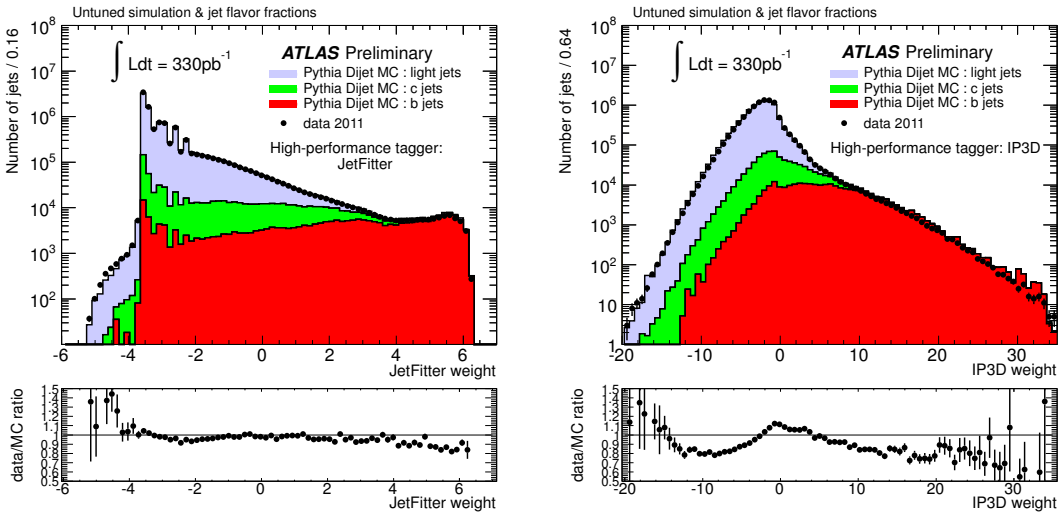

Figure 4.16.: Distributions of the number of jets as a function of the output weights of the high-performance b-tagging algorithms JetFitter (left) and IP3D (right) [84]. The lower parts of the figures show the ratio between the distributions obtained from data and Monte Carlo simulated events.

of the reconstructed secondary vertex [84]: the invariant mass of all associated tracks, the ratio of the sum of the energies of the tracks associated to the vertex to the total energy of all tracks in the jet, and the number of two-track vertices.

The tagging algorithm "JetFitter" [85] is conceptually different. It is based on the decay topology of b-hadrons inside jets. While the secondary vertex based b-tagging algorithms introduced above try to find one secondary vertex, JetFitter takes into account that b-hadrons can decay to c-hadrons, which in turn decay in a displaced vertex. The algorithm performs a multi-vertex fit relying on the assumption that the decay vertices of the b and c-hadron are aligned with the b-hadron flight path. The implementation is based on a Kalman filter using the impact parameters d_0 and z_0, the angular coordinates of the point of closest approach and the signed curvature of tracks q/p, with the charge q and the momentum p.

The high-performance b-tagging algorithms JetFitter and IP3D assign a numerical value ("weight") to each jet in the event, corresponding to how likely it is a b-jet. Figure 4.16 shows the respective output weight distributions, comparing the distributions in data with Monte Carlo simulated samples.

The aforementioned different b-tagging algorithms can be combined to yield a better result, either by adding the corresponding weights ("IP3D+SV1") or by using neural network techniques ("IP3D+JetFitter"). The latter is the combination which was used in the present analysis. Figure 4.17 shows the light-jet rejection as a function of the b-tagging efficiency for the different tagging algorithms, calculated using simulated top pair production events. It can be seen that the combined tagger used in this analysis yields the best rejection against light jets over a wide range of b-jet efficiencies.

For completeness it should be mentioned that due to the possible semi-leptonic decays of

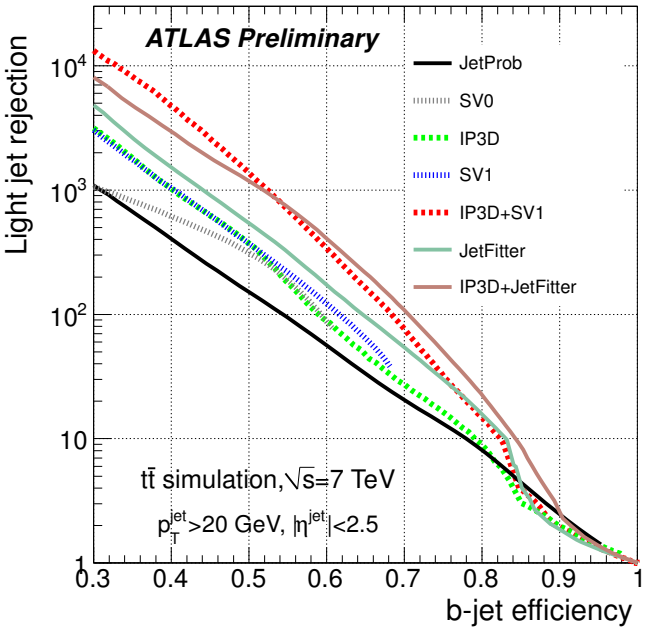

Figure 4.17.: Light-jet rejection as a function of the b-jet tagging efficiency for the basic tagging algorithms (JetProb and SV0) and for the high performance algorithms, estimated from simulated top-antitop events [84].

b-hadrons in jets, the detection of soft muons inside jets is also used for a b-tagging [86]. It was mainly used for calibrating purposes of the other b-tagging algorithms.

Combined Tagger IP3D+JetFitter

As it was the case for b-tagging algorithms used in the early phase of ATLAS data-taking periods, the combined IP3D+JetFitter tagging algorithm was studied in detail with ATLAS data [84].

For the b-tagging efficiencies and the mistag rates of light jets (and c-jets), corrections were derived. Since the performance depends on the transverse momentum, the corrections are given in the form of p_{T} dependent scale factors SF_b for b-jets and SF_{light} for light jets

$$SF_b(p_{\mathrm{T}}) = \frac{\epsilon_b^{\mathrm{data}}(p_{\mathrm{T}})}{\epsilon_b^{\mathrm{MC}}(p_{\mathrm{T}})}, \quad SF_{\mathrm{light}}(p_{\mathrm{T}}) = \frac{\epsilon_{\mathrm{light}}^{\mathrm{data}}(p_{\mathrm{T}})}{\epsilon_{\mathrm{light}}^{\mathrm{MC}}(p_{\mathrm{T}})}. \tag{4.10}$$

The efficiencies are obtained with the $p_{\mathrm{T}}^{\mathrm{rel}}$ method [87], which is based on the subset of b-jets containing reconstructed muons. The momentum of this muon transverse to the combined muon plus jet axis is called $p_{\mathrm{T}}^{\mathrm{rel}}$. Its distributions for light jets, b and c-jets are expected to be significantly different. Figure 4.18 shows an example of light, b and c-jet template shapes for $p_{\mathrm{T}}^{\mathrm{rel}}$ which can be used for a template fit of the spectrum of muons in data before and after b-tagging [87]. As an example, the efficiency $\epsilon_b^{\mathrm{data}}$ is then obtained by

$$\epsilon_b^{\mathrm{data}} = \frac{f_b^{\mathrm{tag}} N^{\mathrm{tag}}}{f_b N} C, \tag{4.11}$$

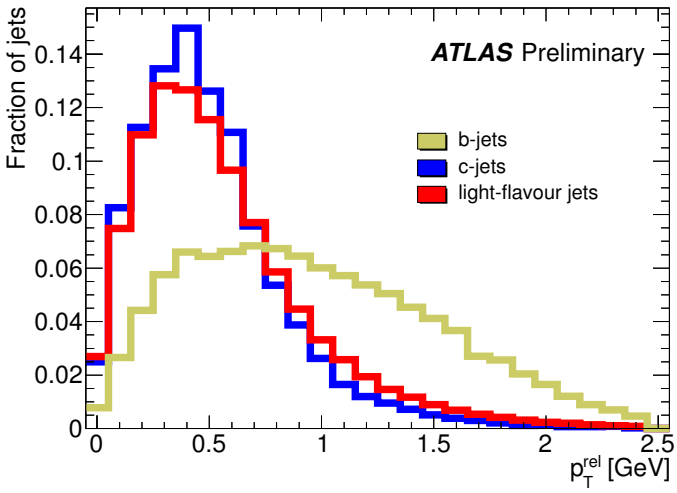

Figure 4.18.: Template shapes for $p_{\mathrm{T}}^{\mathrm{rel}}$ for light jets, b and c-jets [87].

with the fractions of b-jets f_b (f_b^{tag}) and the total number of jets N (N^{tag}) in the sample before (after) b-tagging. The factor C is a correction factor to take into account possible biases due to Monte Carlo modeling and heavy flavor contamination in the light jet template.

From the scale factors in Eq. 4.10, a weight factor w_{jet} is calculated for each jet in the event with $p_{\mathrm{T}} > 20\,\mathrm{GeV}$ and $|\eta| < 2.5$. For a b-tagged b-jet, the weight is given by

$$w_{\mathrm{jet}} = SF_b(p_{\mathrm{T}}) \tag{4.12}$$

and for a non b tagged b-jet[10]

$$w_{\mathrm{jet}} = \frac{1 - \epsilon_b^{\mathrm{data}}(p_{\mathrm{T}})}{1 - \epsilon_b^{\mathrm{MC}}(p_{\mathrm{T}})} = \frac{1 - SF_b(p_{\mathrm{T}})\epsilon_b^{\mathrm{MC}}}{1 - \epsilon_b^{\mathrm{MC}}(p_{\mathrm{T}})}. \tag{4.13}$$

In a final step, the weights of the individual jets are combined into a weight for the whole event

$$w_{\mathrm{event}} = \prod_{\mathrm{jet}} w_{\mathrm{jet}} \tag{4.14}$$

to correct for the observed deviations in data and the Monte Carlo simulation.

4.4. Monte Carlo Simulation

For the SM background processes, the theoretical predictions in form of Monte Carlo simulated events can be supplemented or even replaced by estimations obtained from measured data. The sensitivity studies considering different signal models and hence the design and optimization of a search rely on the simulated SUSY signal events.

The simulation process generally comprises the distinct steps of event generation, simulation of the detector response and reconstruction of physics objects. The individual steps

[10] These formulas are used for light jets analogously.

are technically achieved by dedicated computer programs. For every background process and for many different SUSY signals models, events were generated and processed with the same reconstruction software, also used to process measured data.

The remainder of this section serves as on overview of the Monte Carlo samples used for the SM background processes and the SUSY signal models.

4.4.1. Background Monte Carlo Simulation

Table 4.2 shows a list of the background samples studied with the respective cross section times BR, the order in perturbation theory to which it it was calculated [11] and the Monte Carlo generator used.

Production process	$\sigma\times$ BR in nb (pert. order)	Generator
$W \to \ell\nu$ (+jets)	31.4 (NNLO)	ALPGEN
$Z \to \nu\bar{\nu}$ (+jets)	5.82 (NNLO)	ALPGEN
$Z \to \ell^+\ell^-$ (+jets)	3.20 (NNLO)	ALPGEN
diboson (WW, WZ, ZZ)	7.1×10^{-2} (NLO)	HERWIG, ALPGEN
$t\bar{t}$	0.164 (NLO + NLL)	MC@NLO, POWHEG
		ALPGEN, ACERMC
single t	0.037 (NLO + NLL)	MC@NLO
$t\bar{t}$+$b\bar{b}$	0.9×10^{-3} (LO)	ALPGEN, ACERMC
$t\bar{t}$+W/Z	0.4×10^{-3} (LO)	Madgraph + PYTHIA

Table 4.2.: Standard Model background processes and respective cross sections times branching ratio. The ℓ here indicates all three lepton flavors (e,μ,τ).

For the QCD multijet production, simulated samples produced with PYTHIA [88] and ALPGEN [89] were used for intermediate studies, but not for the final result of the analyses. Rather a dedicated method based on control regions is used to estimate this background from data (see Section 5.2.3).

The boson (+jets) Monte Carlo samples are generated using the ALPGEN generator interfaced to JIMMY [90]. For the PDFs the CTEQ6L1 [91] set is used. The cross sections quoted at NNLO are calculated with the program FEWZ [92]. The diboson events are generated using HERWIG [93, 94]. The cross section quoted is calculated in NLO. For systematic studies, additional samples are generated with ALPGEN interfaced to HERWIG.

The default sample of Monte Carlo simulated events of the top pair and single top production were generated using the MC@NLO generator [95] interfaced to HERWIG and JIMMY for the parton showers and the underlying event respectively. A top mass of 172.5 GeV is assumed. The cross sections quoted are calculated in NLO in perturbation theory including corrections from Next to Leading Logarithm (NLL) resummation [96]. For the PDFs the CTEQ6.6 [97] set is used. For studying systematic uncertainties on the top pair production as the main background to the presented analysis, additional Monte Carlo samples are used,

[11] N^{n}LO stands for the n-th order of perturbation theory in the coupling constant, N^{n}LL stands for the n-th order of the leading logarithmic terms after resummation.

produced with POWHEG [98], ALPGEN and ACERMC [99]. Since the processes $t\bar{t}+b\bar{b}$ and $t\bar{t}+W/Z$ are not included in the default top pair production simulation, additional samples are used as cross checks, namely ALPGEN and ACERMC for $t\bar{t}+b\bar{b}$ and Madgraph + PYTHIA [100] for $t\bar{t}+W/Z$.

4.4.2. SUSY Signal Monte Carlo Simulation

The simulation of the signal samples is based on specific model assumptions.

Gluino Mediated Search

The signal models considered in this analysis are phenomenological MSSM, SO(10), and simplified models. For these signal models, the mass spectra and branching ratios are calculated using the following tools: SUSY-HIT [101] (phenomenological MSSM), ISAJET [102] (SO(10)) and Madgraph [100] (simplified models). For the latter, all masses are set to high values except those involved in the production and decay to effectively decouple the particle spectrum.

The SUSY events are generated using the generator HERWIG++ [103, 104]. The MRST 2007 LO* parton densities [105] are used. Samples are normalized to next-to-leading order (NLO) cross section predictions calculated using PROSPINO [52].

After the event generation, the detector response is simulated using the ATLAS full Geant4 simulation [106] and undergoes the exact same reconstruction as recorded data.

Table 4.3 shows a summary of the signal samples used for this analysis.

Model	Generator	Main parameters	Main processes
Pheno MSSM	SUSY-HIT	$m_{\tilde{g}}$, $m_{\tilde{t}}$	$\tilde{g}\tilde{g}$, $\tilde{t}\tilde{t}$
		$m_{\tilde{\chi}_1^0}$=60 GeV, $m_{\tilde{\chi}_1^\pm}$=120 GeV	$\tilde{t} \to b + \tilde{\chi}_1^\pm$ or $t + \tilde{\chi}_0^1$
Gtb Simplified Model	SUSY-HIT	$m_{\tilde{g}}$, $m_{\tilde{\chi}_1^0}$ (b/t final states)	$\tilde{g}\tilde{g}$
Gt Simplified Model	SUSY-HIT	$m_{\tilde{g}}$, $m_{\tilde{\chi}_1^0}$ (t-only final states)	$\tilde{g}\tilde{g}$
SO(10) HS	ISASUSY	R(Yukawa Unification), $m_{\tilde{g}}$	$\tilde{g}\tilde{g}$, $\tilde{\chi}_2^0\tilde{\chi}_1^\pm$
		tanβ=50.4, m_{16}=10 TeV, $\mu > 0$	$\tilde{g} \to b\bar{b} + \tilde{\chi}_2^0$
SO(10) DR3	ISASUSY	R(Yukawa Unification), $m_{\tilde{g}}$	$\tilde{g}\tilde{g}$, $\tilde{\chi}_2^0\tilde{\chi}_1^\pm$
		tanβ=50, m_{16}=11 TeV, $\mu > 0$	$\tilde{g} \to b\bar{b} + \tilde{\chi}_1^0$

Table 4.3.: Summary of SUSY signal samples considered in the gluino mediated stop search.

Direct Stop Search

The Monte Carlo simulated signal events used in the interpretation of the search for direct stop pair production are based on phenomenological MSSM models. It is assumed that the stop decays via $\tilde{t}_1 \to \tilde{\chi}_1^\pm + b$ only. Two different sparticle mass hierarchies are considered. The first set of signal samples is based on gaugino universality ($m_{\tilde{\chi}_1^\pm} \simeq 2m_{\tilde{\chi}_1^0}$) and forms a grid of points in the ($m_{\tilde{t}_1}$,$m_{\tilde{\chi}_1^0}$)-plane. The second set of signal samples constitutes a grid of points in the ($m_{\tilde{\chi}_1^\pm}$,$m_{\tilde{\chi}_1^0}$)-plane, where a fixed stop mass equal to 180 GeV has been assumed.

For all signal samples, the mass spectra were generated with `SUSY-HIT`. The event were generated with `HERWIG++` using MRST 2007 LO* parton densities. The samples are normalized to next-to-leading order (NLO) cross sections calculated with `PROSPINO` and corrected with next-to-leading logarithmic (NLL) accuracy.

5 Gluino Mediated Stop Production

Based on the general phenomenological introduction of the gluino mediated stop production presented in Section 3.4.2, this chapter is dedicated to the corresponding search performed with the ATLAS detector, namely SUSY signatures with exactly one electron or muon, b-jets and $E_{\mathrm{T}}^{\mathrm{miss}}$ [107]. Gluino mediated stop production is chosen as a first third generation SUSY search, since it has a high expected sensitivity with a relatively limited amount of integrated luminosity.

This chapter is organized as follows. In the first section, the selection criteria of the search are presented in depth. After the introduction of the data-taking conditions, the so-called baseline selection is presented, which is then used as a basis for the further optimization process to maximize the sensitivity for SUSY signatures of interest. The main background processes and the means to estimate them are presented in Section 5.2. After the discussion of the systematic uncertainties in Section 5.3, this chapter is concluded with the presentation of the results and their interpretation in Section 5.4.

5.1. Event Selection

5.1.1. Data-Taking Period and Trigger Selection

The ATLAS detector started data-taking at a center-of-mass energy of 7 TeV in 2010. Including all data taken in 2011, a total integrated luminosity of $5.25\,\mathrm{fb}^{-1}$ has been recorded. For the gluino mediated stop search, a total integrated luminosity of $2.05\,\mathrm{fb}^{-1}$ recorded in 2011 [108] has been analyzed. Data recorded in 2010 ($35\,\mathrm{pb}^{-1}$) is not included due to different data-taking conditions.

The set of available triggers with different criteria is constrained in each data-taking period by the total allowed trigger rate. The thresholds in transverse momentum for the used single light lepton triggers are chosen to be the lowest possible, given the constraints by rate limitations. The trigger reaches the maximum efficiency for electrons (muons) with $p_{\mathrm{T}} > 25(20)$ GeV[1].

5.1.2. Baseline Selection

A set of quality criteria is imposed to reduce non-collision background processes: Events are required to have at least four tracks associated to the primary vertex.

The selection starts with the requirement of exactly one[2] electron or muon. Based on the requirements described in Section 4.3.1 the following criteria are applied.

[1] For data-taking periods with high instantaneous luminosity the used muon trigger included an additional jet requirement. Its maximum efficiency is reached for a jet with $p_{\mathrm{T}} \geq 60\,\mathrm{GeV}$, a criterion which is taken into account by the choice of the final selection cuts.

[2] Events with more than one lepton are excluded, allowing for dedicated two or multilepton analyses.

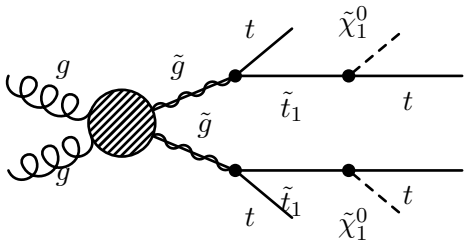

Figure 5.1.: Schematic view of the process $gg \to \tilde{g}\tilde{g} \to 4t + 2\tilde{\chi}_1^0$.

Electrons Electrons are preselected with $p_{\mathrm{T}} > 20\,\mathrm{GeV}$ and required to pass the "medium" quality criteria. Known problematic calorimeter regions are excluded and the electron p_{T} is smeared to correct for the differences of the electron scale resolution in MC and data. Electrons from the forward region of the detector $|\eta| > 2.5$ are not used. In the final selection, electrons are required to have $p_{\mathrm{T}} > 25\,\mathrm{GeV}$ and required to pass the "tight" quality criteria. Furthermore, they must be isolated in the detector: the scalar sum of the p_{T} of all tracks in a cone of $\Delta R = 0.2$ around the electron must not exceed 10% of the p_{T} of the electron.

Muons Muons are preselected with $p_{\mathrm{T}} > 10\,\mathrm{GeV}$ and $|\eta| < 2.4$. In the final selection, muons are required to have $p_{\mathrm{T}} > 20\,\mathrm{GeV}$ and are required to be isolated: the scalar sum of the p_{T} of all tracks in a cone of $\Delta R = 0.2$ must not exceed 1.8 GeV.

To avoid double-counting of reconstructed objects, a procedure is defined to remove preselected objects that fall into more than one category. A typical example is the fact, that isolated electrons are usually also reconstructed as jets. In a first step, jets are discarded that are close to a preselected electron with $\Delta R = \sqrt{\Delta\phi^2 + \Delta\eta^2} < 0.2$. Second, electrons and muons are discarded if a jet is found within a cone with $\Delta R < 0.4$.

The thresholds in p_{T} for the leptons are chosen to match the thresholds for the trigger plateau efficiencies.

Furthermore, at least four jets passing the following thresholds for their respective transverse momenta are required: $p_{\mathrm{T}} > 60\,\mathrm{GeV}$ for the leading jet and $p_{\mathrm{T}} > 50\,\mathrm{GeV}$ for the three subleading jets. The threshold for the leading jet is driven by the trigger requirements, the thresholds of the subleading jets are driven by pile-up considerations. The high jet multiplicity can be motivated as follows: If a gluino pair is produced and both gluinos decay to $t\tilde{t}$, each $\tilde{t}$ can decay to $t\tilde{\chi}_1^0$ or $b\tilde{\chi}_1^0\ell\nu$, depending on the specific model. The net result would be a final state containing several b-jets, light jets and leptons. Figure 5.1 illustrates the process $gg \to \tilde{g}\tilde{g} \to 4t + 2\tilde{\chi}_1^0$.

At least one of the selected jets with $p_{\mathrm{T}} > 50\,\mathrm{GeV}$ is required to be tagged as a b-jet. The combined tagger IP3D+JetFitter, described in Section 4.3.4, is used at the working point with a tagging efficiency of 60% on top Monte Carlo simulated events.

Furthermore, high values of missing transverse energy are expected in SUSY events due to the non-detection of the LSP. Therefore, $E_{\mathrm{T}}^{\mathrm{miss}} > 80\,\mathrm{GeV}$ is chosen to enhance the fraction of possible signal events. This threshold can be motivated by a typical top pair production event. In order to be selected, a top pair production event must contain exactly one lepton and at least four jets. In the simplest case, this is realized if one of the two W bosons produced

Cuts	≥ 4 jets	≥ 1 b jet	$E_{\mathrm{T}}^{\mathrm{miss}} > 80$ GeV	$m_{\mathrm{T}} > 100$ GeV
1-electron channel				
$t\bar{t}$ +single top	3697 ± 1361	2843 ± 1075	896 ± 379	109.1 ± 53.7
$t\bar{t}$ +X	194 ± 196	161 ± 164	53 ± 55	8.4 ± 8.7
W+jets	2027 ± 804	224 ± 142	65 ± 40	4.0 ± 3.7
others	572 ± 225	56 ± 31	4 ± 3	0.9 ± 0.5
1-muon channel				
$t\bar{t}$ +single top	3572 ± 1333	2757 ± 1040	862 ± 358	117.7 ± 65.3
$t\bar{t}$ +X	183 ± 185	153 ± 156	50 ± 51	8.1 ± 8.3
W+jets	1922 ± 771	214 ± 130	55 ± 39	6.1 ± 5.0
others	329 ± 135	32 ± 19	3 ± 3	0.2 ± 0.5

Table 5.1.: Expected SM event yields for the 1-muon and 1-electron channels normalized to $2.05\,\mathrm{fb}^{-1}$. The row labeled "others" contains the sum of Z and diboson production. Both the statistical uncertainties due to the low number of Monte Carlo simulated events and the systematic uncertainties described in Section 5.3 are taken into account.

in $t \to Wb$ decays to $\ell\nu$, the other one to two hadronic jets. Since the $E_{\mathrm{T}}^{\mathrm{miss}}$ is attributed to the non-detection of the neutrino, events with $E_{\mathrm{T}}^{\mathrm{miss}} > m_W$ are suppressed.

Finally, the transverse mass of the missing transverse momentum and the reconstructed lepton

$$m_{\mathrm{T}} = \sqrt{2p_{\mathrm{T}}^{\ell} E_{\mathrm{T}}^{\mathrm{miss}} - 2\vec{\mathbf{p}}_{\mathrm{T}} \cdot \vec{\mathbf{E}}_{\mathrm{T}}^{\mathrm{miss}}} \tag{5.1}$$

must exceed 100 GeV. This selection criterion suppresses events with real W bosons decaying to a light lepton and a neutrino. As a result, both the production of W bosons in association with jets and the top pair production processes are suppressed by this selection step.

The aforementioned analysis selection criteria comprise what is called the baseline selection. The expected numbers of events from MC after the different baseline selection steps are listed in Table 5.1. The top pair production is expected to be the dominant SM background process.

5.1.3. Optimization

The optimization of sensitivity of the analysis is performed using MC samples for the background processes, neglecting QCD multijet production, which is expected to be negligible after the baseline selection.

An important quantity connected to the mass scale of SUSY is the so-called effective mass m_{eff}, which is introduced in Section 3.2.2 and which in the context of this analysis is defined as

$$m_{\mathrm{eff}} = \sum_{i \leq n} ({p_{\mathrm{T}}}^{jet})_i + E_{\mathrm{T}}^{\mathrm{miss}} + {p_{\mathrm{T}}}^{\ell}. \tag{5.2}$$

The distribution of m_{eff} after the baseline selection is shown in Fig. 5.2 for the electron (left) and muon channel (right). In the following, the optimization of the m_{eff} selection threshold is

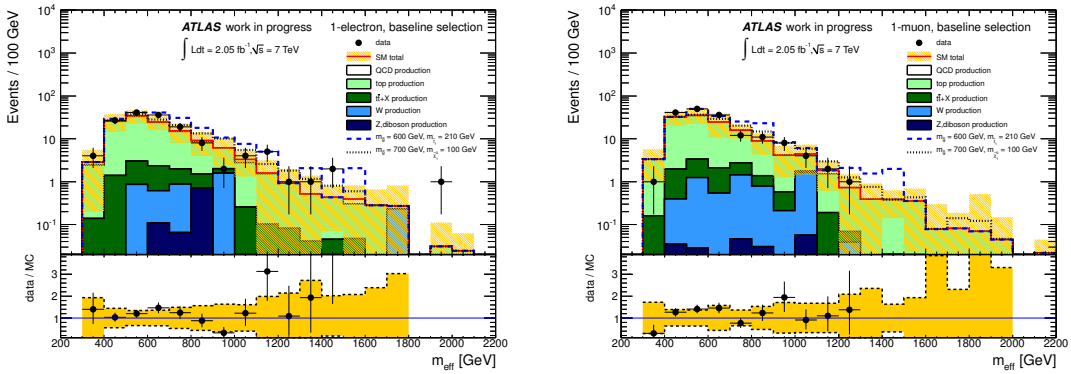

Figure 5.2.: Distributions of m_{eff} after the baseline selection for the electron (left) and muon channels (right). For reference, the contributions of two SUSY signals are superimposed, namely one signal point with $m_{\tilde{g}} = 600\,\text{GeV}$ and $m_{\tilde{t}_1} = 210\,\text{GeV}$ and one signal point with $m_{\tilde{g}} = 700\,\text{GeV}$ and $m_{\tilde{\chi}_1^0} = 100\,\text{GeV}$. The yellow band includes systematic uncertainties discussed in Section 5.3.

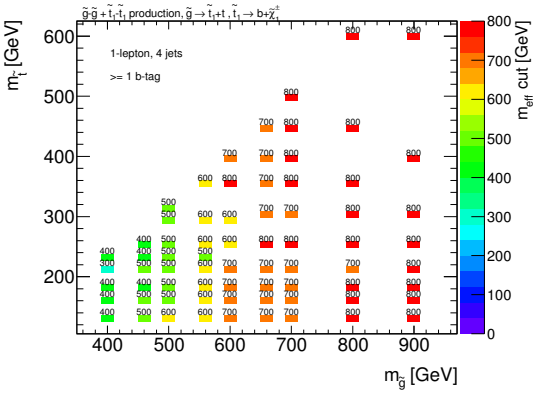

Figure 5.3.: Cut values for m_{eff} in GeV, which lead to the best significance $S/\sqrt{B}$ after the baseline selection in the gluino-stop mass plane, assuming $\tilde{g}\tilde{g}$ and $\tilde{t}_1\tilde{t}_1$ production with the decay modes $\tilde{g} \to \tilde{t}_1 + t$ and $\tilde{t}_1 \to b + \tilde{\chi}_1^{\pm}$.

presented in the gluino-stop mass plane, based on the following model assumptions: The stop $\tilde{t}_1$ is the lightest squark and is pair produced either directly or via the decay of a gluino, with the assumed BR($\tilde{g} \to \tilde{t}_1 t$)=100%. The produced $\tilde{t}_1$ will then decay as $\tilde{t}_1 \to b + \tilde{\chi}_1^{\pm}$. The mass of the chargino is assumed to be 120 GeV and twice the mass of the neutralino via gaugino universality.

The cut values of m_{eff}, which maximize the expected $S/\sqrt{B}$ ratio in the ($m_{\tilde{g}}$,$m_{\tilde{t}_1}$)-plane, are shown in Fig. 5.3. A cut value of 700 GeV is chosen, since it is the optimal choice in the region of the ($m_{\tilde{g}}$,$m_{\tilde{t}_1}$)-plane, which is targeted by the analysis, outside the region already excluded in previous analyses. This determines the first signal region, referred to as SR1-D.

The analogous plots are shown in Fig. 5.4 for the Gt (left) and Gtb (right) simplified models, respectively. To increase the sensitivity for these models, in addition to the first signal region,

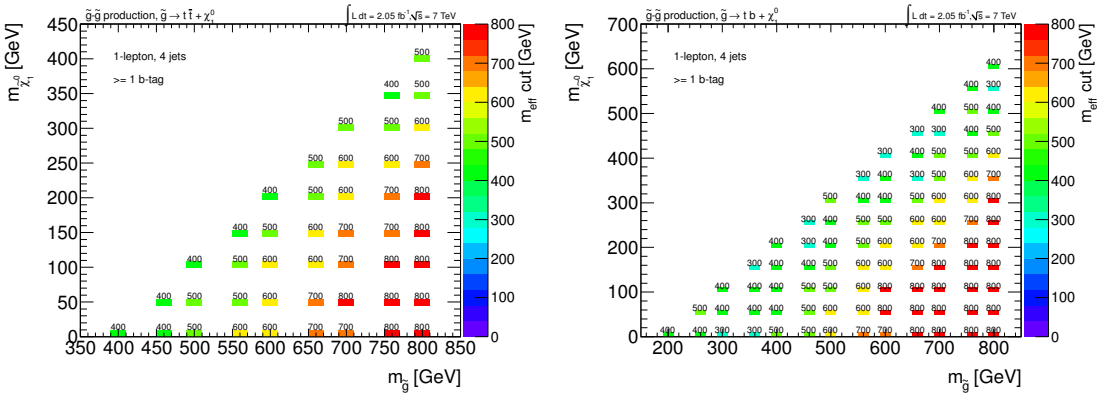

Figure 5.4.: Cut values for m_{eff} in GeV, which lead to the best significance $S/\sqrt{B}$ after the baseline selection in the ($m_{\tilde{g}}$,$m_{\tilde{\chi}_1^0}$)-plane for the Gt simplified model, assuming $\tilde{g}\tilde{g}$ production and gluino decay via $\tilde{g} \to t\bar{t}\tilde{\chi}_1^0$ (left) and for the Gtb simplified model, assuming $\tilde{g}\tilde{g}$ production and gluino decay via $\tilde{g} \to tb\tilde{\chi}_1^0$ (right).

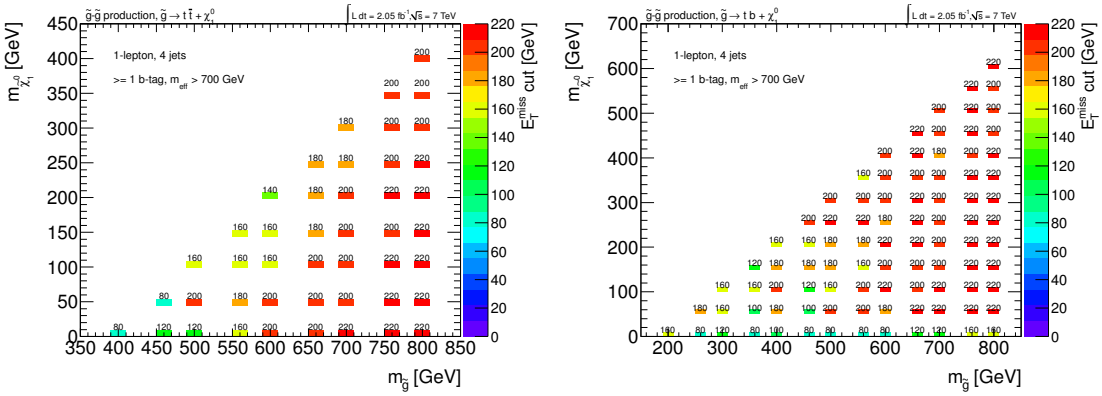

Figure 5.5.: Cut values for $E_{\text{T}}^{\text{miss}}$ in GeV which lead to the best significance $S/\sqrt{B}$ after the baseline selection in the ($m_{\tilde{g}}$,$m_{\tilde{\chi}_1^0}$)-plane for the Gt simplified model, assuming $\tilde{g}\tilde{g}$ production and gluino decay via $\tilde{g} \to t\bar{t}\tilde{\chi}_1^0$ (left) and for the Gtb simplified model, assuming $\tilde{g}\tilde{g}$ production and gluino decay via $\tilde{g} \to tb\tilde{\chi}_1^0$ (right).

a further optimization using a tighter $E_{\text{T}}^{\text{miss}}$ cut is performed. Figure 5.5 shows the result of this optimization. A selection criterion of $E_{\text{T}}^{\text{miss}} > 200\,\text{GeV}$ additionally to $m_{\text{eff}} > 700\,\text{GeV}$ is chosen to define the second signal region, referred to as SR1-E.

To summarize, two signal regions are defined. The first one via an effective mass cut of $m_{\text{eff}} > 700\,\text{GeV}$ only (SR1-D). The second one with an additional cut of $E_{\text{T}}^{\text{miss}} > 200\,\text{GeV}$ (SR1-E). The list of consecutive selection criteria both for the baseline selection and the two signal regions can be found in Table 5.2. The expected significance $S/\sqrt{B}$ in both signal regions in the gluino-stop plane is shown in Fig. 5.6. The Figures 5.7 and 5.8 show analogously the sensitivity for the Gt and Gtb simplified models, respectively.

Selection Step	Criteria
Baseline Selection	
leptons	exactly one e or μ
jets	four jets, $p_{\mathrm{T}}(j1) > 60\,\mathrm{GeV}$, $p_{\mathrm{T}}(j2, j3, j4) > 50\,\mathrm{GeV}$
b-tagging	at least one b-tagged jet
$E_{\mathrm{T}}^{\mathrm{miss}}$	$E_{\mathrm{T}}^{\mathrm{miss}} > 80\,\mathrm{GeV}$, $m_{\mathrm{T}} > 100\,\mathrm{GeV}$
Signal Region Selection	
SR1-D	$m_{\mathrm{eff}} > 700\,\mathrm{GeV}$
SR1-E	$E_{\mathrm{T}}^{\mathrm{miss}} > 200\,\mathrm{GeV}$

Table 5.2.: List of the consecutive selection criteria for the baseline selection and for the definition of the final signal regions SR1-D and SR1-E.

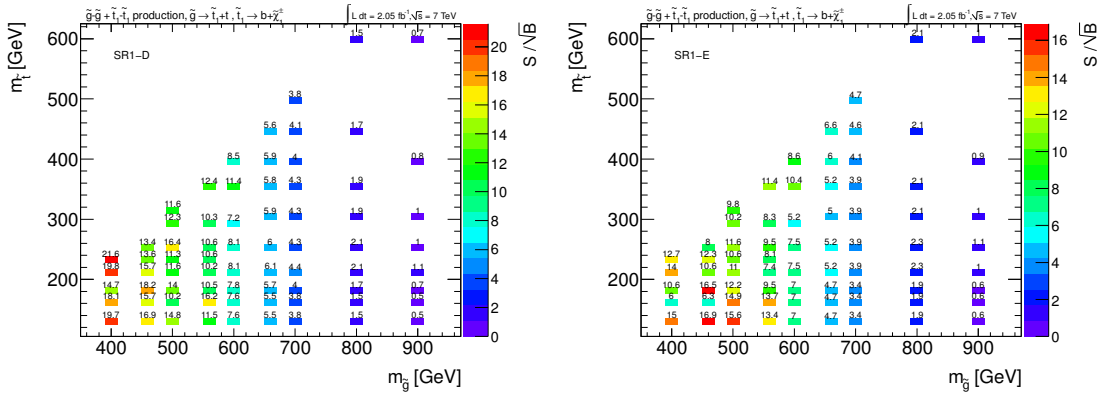

Figure 5.6.: Significance $S/\sqrt{B}$ in the $(m_{\tilde{g}}, m_{\tilde{t}_1})$-plane for SR1-D (left) and SR1-E (right), assuming $\tilde{g}\tilde{g}$ and $\tilde{t}_1\tilde{t}_1$ production with the decay modes $\tilde{g} \to \tilde{t}_1 + t$ and $\tilde{t}_1 \to b + \tilde{\chi}_1^{\pm}$.

5.2. Background Estimation

For every physics analysis, the understanding of the background processes is an essential ingredient. In the following, the main background processes are discussed with special emphasis on the estimation of the backgrounds from top and QCD multijet production.

5.2.1. Main Background Contributions

Various production processes from the SM have to be taken into account as potential contributions to background events in the analysis. The importance of the individual contributions is governed by the cross section and the efficiency of the selection criteria. The cross sections of various SM processes are illustrated in Fig. 5.9, which includes both the theoretical predictions and the measurements performed with the ATLAS detector. Although the cross sections of the production of the gauge bosons W and Z are almost three orders of magnitude higher than the top pair production cross section, the applied selections in this search result in the latter becoming the dominant background process.

In the following, two estimation techniques are presented. The first one is mainly tailored to estimate the dominant background contribution from $t\bar{t}$ production. The estimation of the contribution from QCD multijet production is based on a data-driven technique presented in Section 5.2.3.

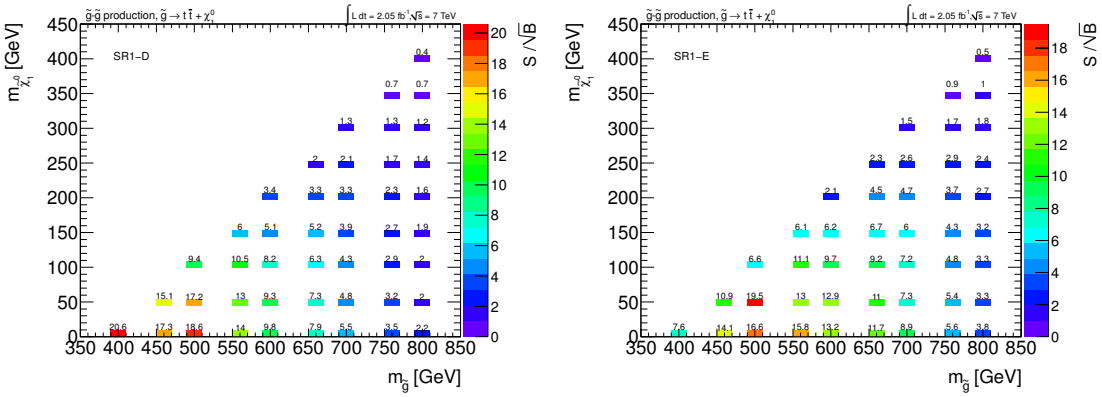

Figure 5.7.: Significance $S/\sqrt{B}$ in the ($m_{\tilde{g}}$,$m_{\tilde{\chi}_1^0}$)-plane of the Gt simplified model for SR1-D (left) and SR1-E (right), assuming $\tilde{g}\tilde{g}$ production and gluino decay via $\tilde{g} \to t\bar{t}\tilde{\chi}_1^0$.

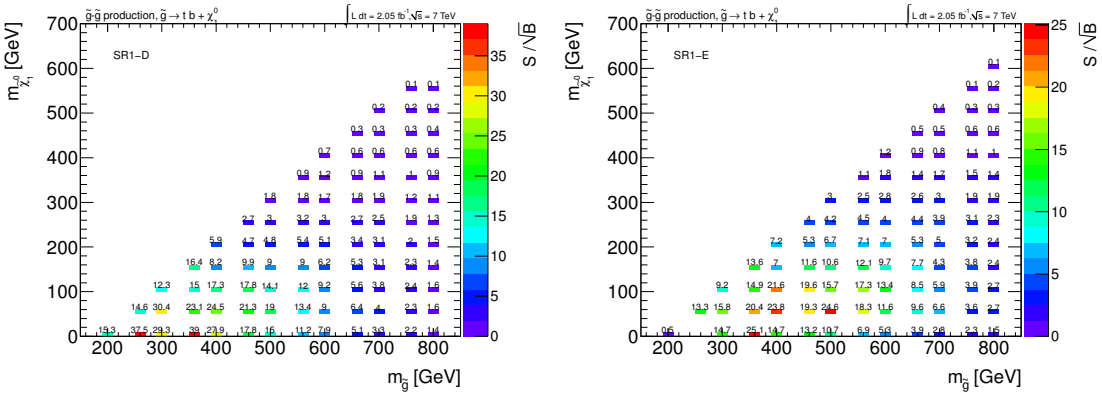

Figure 5.8.: Significance $S/\sqrt{B}$ in the ($m_{\tilde{g}}$,$m_{\tilde{\chi}_1^0}$)-plane of the Gtb simplified model for SR1-D (left) and SR1-E (right), assuming $\tilde{g}\tilde{g}$ production and gluino decay via $\tilde{g} \to tb\tilde{\chi}_1^0$.

5.2.2. Estimation of Top Pair Production Background

The production of top pairs is expected to be the dominant background in a SUSY search with multiple jets. Therefore, special care is taken to study this particular background and validate the expectation with measurements.

The estimation of the top pair production background uses both Monte Carlo simulated and data events in dedicated control regions. These control regions are constructed using the m_{eff} variable and the transverse mass m_{T} between the lepton and the $E_{\text{T}}^{\text{miss}}$. For low values of m_{T} the number of events with real W bosons is increased, thus enhancing the abundance of top pair (and W+jet) production events. The following set of control regions is studied[3]

CR1 : $40\,\text{GeV} < m_{\text{T}} < 100\,\text{GeV}$ and $m_{\text{eff}} > 500\,\text{GeV}$,

CR2 : $40\,\text{GeV} < m_{\text{T}} < 100\,\text{GeV}$ and $m_{\text{eff}} < 500\,\text{GeV}$,

CR3 : $m_{\text{T}} > 100\,\text{GeV}$ and $m_{\text{eff}} < 500\,\text{GeV}$.

The region labeled CR1 is close to the signal region due to the m_{eff} selection criterion and therefore used for the final estimation. The remaining control regions CR2 and CR3 are used

[3]The baseline selection criteria are also applied in the control regions unless stated otherwise.

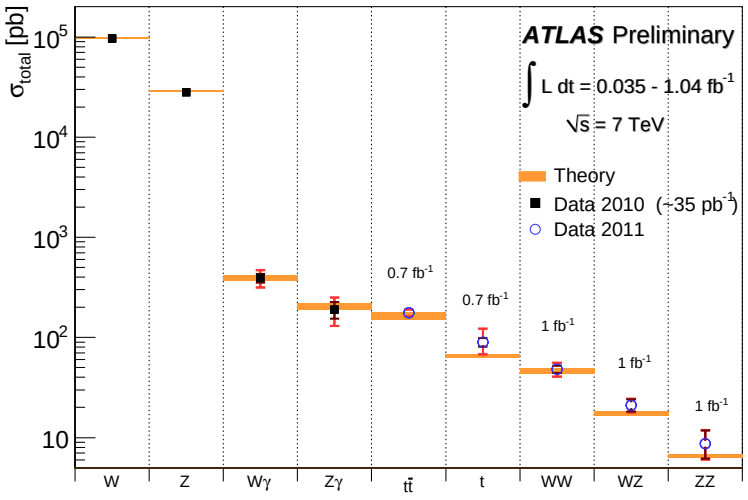

Figure 5.9.: Total cross sections σ_{total} for various SM processes. The theoretical predictions calculated at NLO or higher are shown as orange bands (including uncertainties). The experimental measurements performed with the ATLAS detector are shown as filled boxes for measurements using data taken in 2010 ($\sim 35\,\text{fb}^{-1}$ of integrated luminosity) and open circles for measurements using data taken in 2011 (up to $1\,\text{fb}^{-1}$ of integrated luminosity). The dark error bars represent the statistical uncertainties. The red error bars represent the full uncertainties, including systematic and luminosity uncertainties [59].

CR1	top	W/Z	others	SM	data ($2.05\,\text{fb}^{-1}$)
1-electron	414	40	4	458 ± 100	465
1-muon	377	25	5	407 ± 110	420

Table 5.3.: Expected background composition and comparison of the predicted total SM event yield to the measured event yield for $2.05\,\text{fb}^{-1}$ for CR1. The column "others" contains contributions from QCD multijet production and diboson production. The column "top" includes contributions from the single top, $t\bar{t}$, ttbb and $t\bar{t}+W/Z$ production processes. The quoted uncertainty on the SM prediction includes only detector-level systematic uncertainties, which are discussed in Section 5.3.

for consistency checks within the method. The expected background composition in CR1 from Monte Carlo simulation is shown in Table 5.3, together with the number of events measured in data. It can be seen that indeed the top pair production is the dominant background, with a non-negligible contribution from W and Z+jets events. The distributions of m_{eff} in the control region are shown in Fig. 5.10 for the electron (left) and muon channels (right).

Using the Monte Carlo simulated events, a so-called transfer factor T_f is defined relating the estimated number of events in the signal region N_{SR} to the observed number of events in control region CR1 ($N^{\text{obs}}_{\text{CR1}}$)

$$N_{\text{SR}} = \frac{N^{\text{MC}}_{\text{SR}}}{N^{\text{MC}}_{\text{CR1}}} N^{\text{obs}}_{\text{CR1}} = T_f N^{\text{obs}}_{\text{CR1}}. \tag{5.3}$$

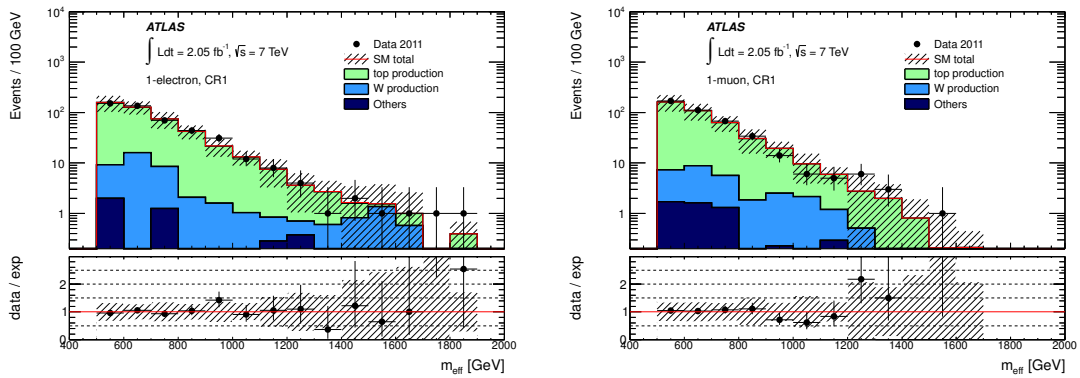

Figure 5.10.: Distributions of m_{eff} in the control region CR1 for the electron channel (left) and the muon channel (right). The hatched band represents the systematic uncertainties discussed in Section 5.3.

The results of the background estimation using the transfer factor are listed in Table 5.4.

SR	SM (MC estimate)	SM (estimated with T_f)
1-electron channel		
SR1-D	38.6 ± 18.7	39.2 ± 11.9
SR1-E	7.9 ± 4.2	8.1 ± 3.4
1-muon channel		
SR1-D	37.0 ± 20.5	38.2 ± 14.3
SR1-E	6.1 ± 4.8	6.3 ± 4.2

Table 5.4.: Estimation of N_{SR} for $2.05\,\text{fb}^{-1}$ with the total uncertainty. The results are presented separately for each channel. A detailed treatment of the systematic uncertainties is given in Section 5.3.

For the validation of the method, an analogous transfer factor $T_f^{\text{CR2}\to\text{CR3}}$ is defined to estimate the number of events in CR3 given the observed number of events in CR2

$$N_{\text{CR3}} = \frac{N_{\text{CR3}}^{\text{MC}}}{N_{\text{CR2}}^{\text{MC}}} N_{\text{CR2}}^{\text{obs}} = T_f^{\text{CR2}\to\text{CR3}} N_{\text{CR2}}^{\text{obs}}. \tag{5.4}$$

This estimate for N_{CR3} is compared to the expectation from Monte Carlo in Table 5.5. The observed agreement gives confidence in the reliability of the method.

5.2.3. Estimation of QCD Multijet Background

Due to the relatively high uncertainty on the cross section of QCD multijet production and the technical challenge of producing sufficiently large simulated samples, the need to estimate this background component from data becomes evident.

In events from QCD multijet production it is not expected that isolated light leptons ("real" leptons) are produced. Experimental signatures of light leptons can appear in the detector

CR	SM (MC estimate)	SM (estimated with T_f)	data
1-electron channel			
CR2	155.7 ± 67.3		151
CR3	28.9 ± 16.7	28.0 ± 10.0	31
1-muon channel			
CR2	191.5 ± 77.6		192
CR3	35.6 ± 17.4	35.7 ± 8.4	42

Table 5.5.: Validation of the method in predicting the non-QCD background in CR3 from CR2. The listed uncertainties include the systematic uncertainties discussed in Section 5.3.

either by non-prompt leptons produced in photon conversions or inside a heavy flavor jet by semileptonic b- or c-quark decays. Furthermore, other objects can be misreconstructed as leptons. In the following, these signatures are called "fake" leptons [109].

The estimation of the QCD multijet background used in this analysis is based on two distinct selection criteria for light leptons, called "loose" and "tight". The former selection imposes less constraints for the quality of the lepton, thus including more objects misreconstructed as leptons. The latter selection is identical to the signal selection. Based on these selections the number of events in each region can be decomposed in a real and a fake part

$$\begin{aligned} N^{\text{loose}} &= N^{\text{loose}}_{\text{real}} + N^{\text{loose}}_{\text{fake}}, \\ N^{\text{tight}} &= N^{\text{tight}}_{\text{real}} + N^{\text{tight}}_{\text{fake}}. \end{aligned} \tag{5.5}$$

If the efficiencies of real and fake leptons to also pass the tighter selection criteria

$$\varepsilon_{\text{real}} = \frac{N^{\text{tight}}_{\text{real}}}{N^{\text{loose}}_{\text{real}}}, \quad \varepsilon_{\text{fake}} = \frac{N^{\text{tight}}_{\text{fake}}}{N^{\text{loose}}_{\text{fake}}} \tag{5.6}$$

are known the system of equations

$$\begin{aligned} N^{\text{loose}} &= \frac{N^{\text{tight}}_{\text{real}}}{\varepsilon_{\text{real}}} + \frac{N^{\text{tight}}_{\text{fake}}}{\varepsilon_{\text{fake}}} \\ N^{\text{tight}} &= N^{\text{tight}}_{\text{real}} + N^{\text{tight}}_{\text{fake}}. \end{aligned} \tag{5.7}$$

can be solved for the number of events with a fake lepton in the tight selection

$$N^{\text{tight}}_{\text{fake}} = \frac{\varepsilon_{\text{fake}}}{\varepsilon_{\text{real}} - \varepsilon_{\text{fake}}}(N^{\text{loose}}\varepsilon_{\text{real}} - N^{\text{tight}}). \tag{5.8}$$

The estimation of the real and fake efficiencies from data are achieved in dedicated control regions enriched in real and fake leptons, respectively.

Estimation of $\varepsilon_{\text{fake}}$

The control region to measure the efficiency that a fake lepton also passes the tight lepton criteria is designed to be enriched in QCD multijet events. To avoid a possible bias of the estimation by contamination of real leptons in the control region, events for W/Z+jets and top production are subtracted. Their contribution is taken from Monte Carlo simulation.

The control region is then defined as follows:

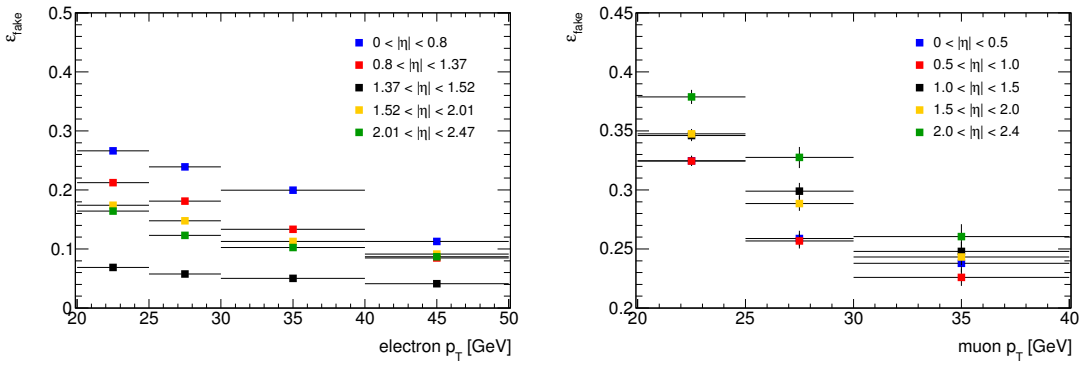

Figure 5.11.: The efficiencies ϵ_{fake} as functions of the p_{T} of the lepton in five η bins for the electron channel before (left) and for the muon channel (right).

- exactly one loose electron (muon) with $p_{\text{T}} > 25(20)\,\text{GeV}$,
- ≥ 1 b-jet with $p_{\text{T}} > 50\,\text{GeV}$,
- $E_{\text{T}}^{\text{miss}} < 30\,\text{GeV}$,
- $m_{\text{T}} < 40\,\text{GeV}$.

The resulting efficiencies $\varepsilon_{\text{fake}}$ are shown in Fig. 5.11 as functions of p_{T} for five different $|\eta|$ ranges, separately for the electron and muon channels.

At the same time, the control region must be checked against further biases (e.g. caused by different compositions in heavy flavor jets). For this reason, a second control region without the b-tagging requirement is defined, in which photon conversions and misreconstructed objects are expected to be enhanced:

- exactly one loose electron with $p_{\text{T}} > 20\,\text{GeV}$,
- ≥ 1 jet with $p_{\text{T}} > 50\,\text{GeV}$

and identical thresholds for $E_{\text{T}}^{\text{miss}}$ and m_{T}. The resulting efficiency for the electron channel $\varepsilon_{\text{fake}}$ is shown in Fig. 5.12 as a function of p_{T} for five different $|\eta|$ ranges. The observed differences are treated as an additional systematic uncertainty.

Estimation of $\varepsilon_{\text{real}}$

The estimation of the efficiency for a real lepton that passed the loose criteria to also pass the tight criteria is estimated from $Z \to \ell\ell$ Monte Carlo simulated events. The method relies on the fact that two real leptons are expected in the event, out of which one is required to satisfy tight quality criteria (called "tag" lepton). The second lepton ("probe") is used to calculate the efficiency. The control region in this case is defined as follows:

- exactly two loose electrons (muons) with $p_{\text{T}} > 25(20)$ GeV and opposite charges,
- the tag lepton satisfies the tight criteria,
- 81 GeV $< m_{\ell\ell} <$ 101 GeV.

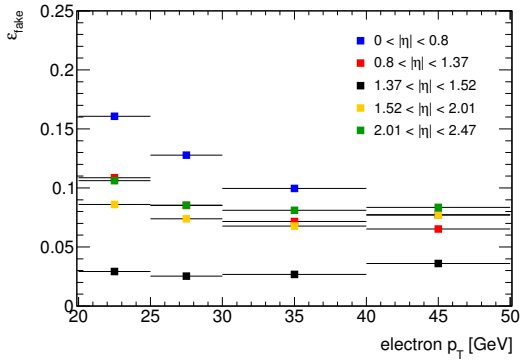

Figure 5.12.: The efficiency ϵ_{fake} as a function of the p_{T} of the electronlepton in five η bins for the electron channel before the b-tagging requirement.

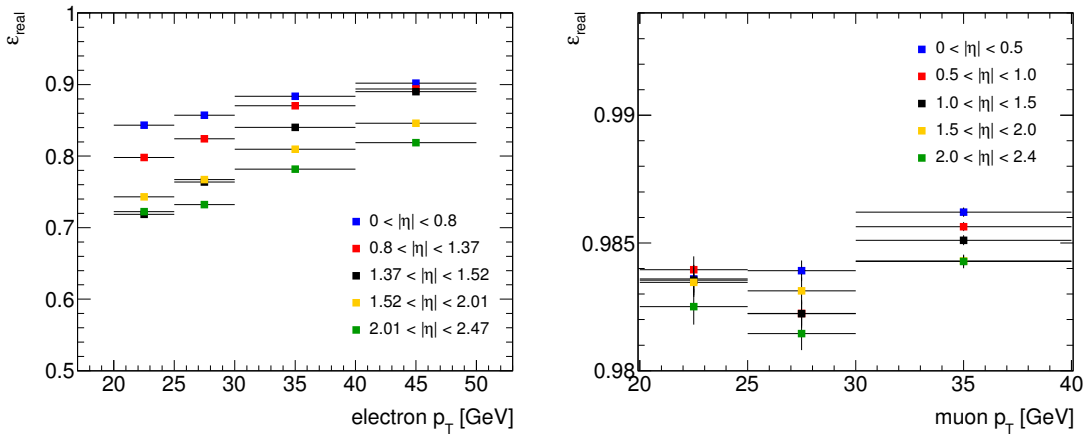

Figure 5.13.: The efficiency $\varepsilon_{\text{real}}$ as a function of the p_T in the five different $|\eta|$ bins for the electron channel (left) and the muon channel (right).

The resulting efficiencies $\varepsilon_{\text{real}}$ as a function of p_{T} are shown in Fig. 5.13 for five different $|\eta|$ ranges, separately for the electron (left) and muon channels (right).

Validation

The validity of the method described above is tested in the following control region

- exactly one tight electron (muon) with $p_{\text{T}} > 25(20)\,\text{GeV}$,
- ≥ 1 b-jet with $p_{\text{T}} > 50\,\text{GeV}$,
- $E_{\text{T}}^{\text{miss}} < 80\,\text{GeV}$.

The distributions of the p_{T} of the lepton, the p_{T} of the jets, $E_{\text{T}}^{\text{miss}}$ and m_{T} are shown in Figs. 5.14 and 5.15 after the application of the method, separately for the electron and muon channels. Further distributions are shown in Figs. 5.16 and 5.17, namely the number of jets, the number of b-jets and the η and ϕ of the lepton. All distributions show good agreement between the data and the SM expectation in this control region.

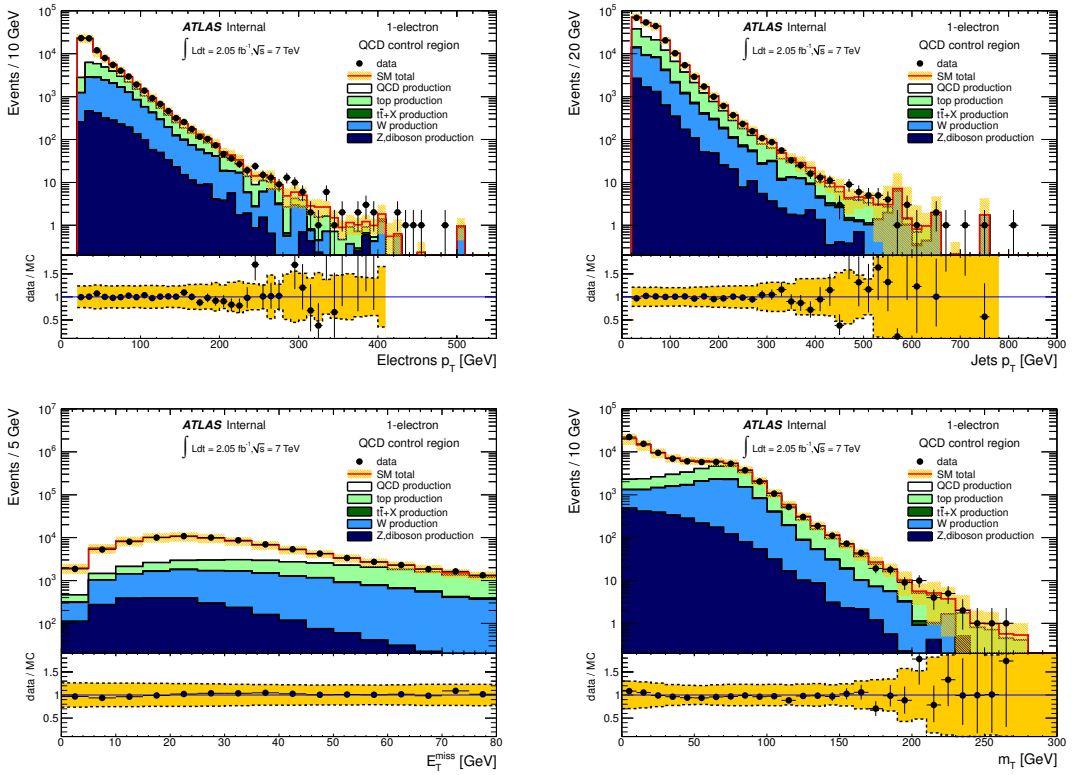

Figure 5.14.: Distributions of the lepton p_T, the p_T of the jets, $E_{\mathrm{T}}^{\mathrm{miss}}$ and m_{T} for the electron channel. The QCD multijet background is estimated from data. The yellow bands represent the uncertainty on the background prediction and include the uncertainty on the QCD prediction and all the uncertainties on the non-QCD background estimate from Monte Carlo, discussed in Section 5.3.

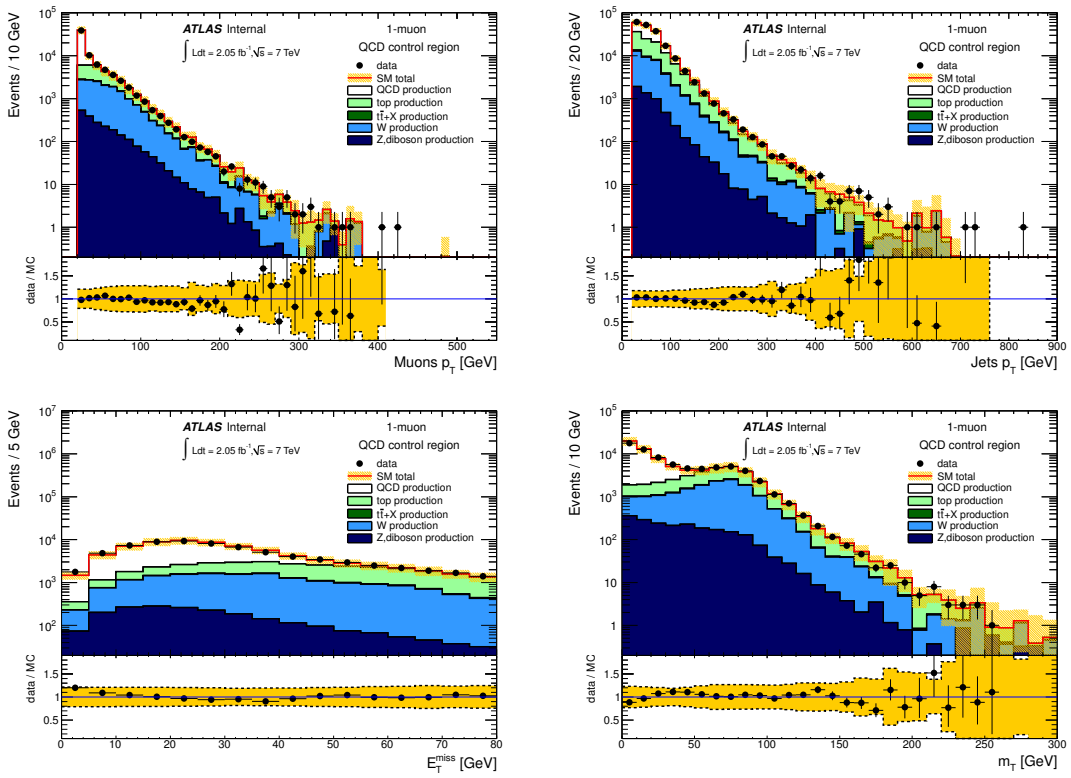

Figure 5.15.: Distributions of the lepton p_T, the p_T of the jets, $E_{\mathrm{T}}^{\mathrm{miss}}$ and m_{T} for the muon (right) channels. The QCD multijet background is estimated from data. The yellow bands represent the uncertainty on the background prediction and include the uncertainty on the QCD prediction and all the uncertainties on the non-QCD background estimate from Monte Carlo, discussed in Section 5.3.

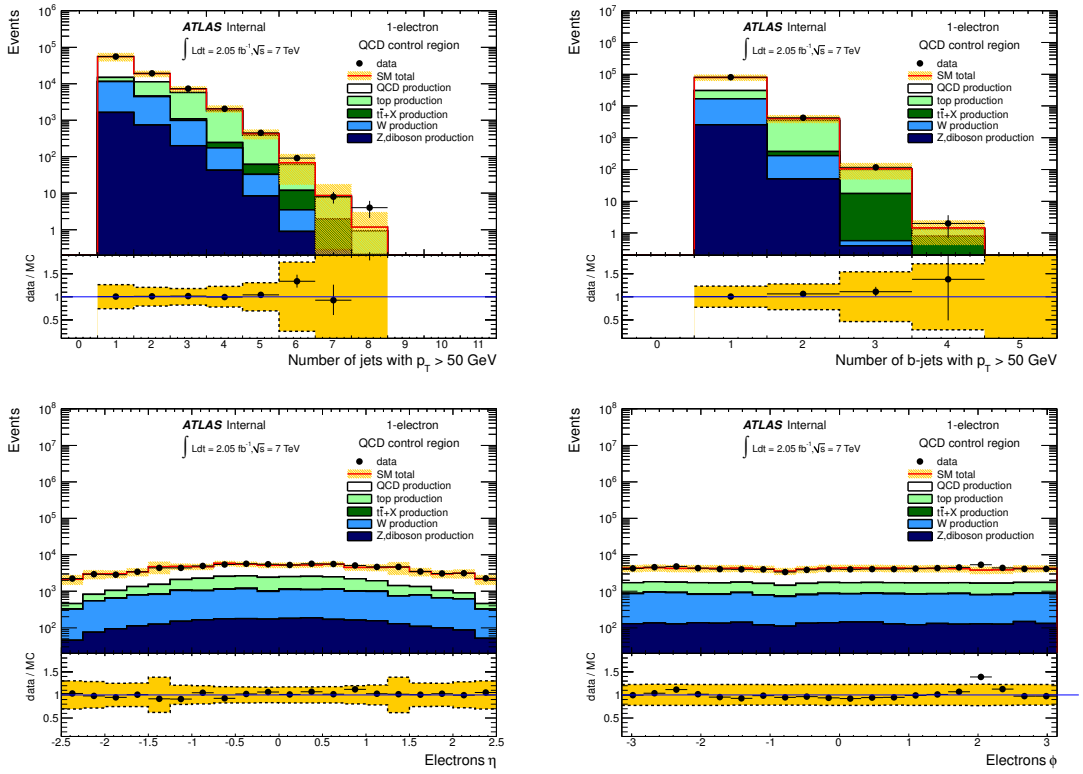

Figure 5.16.: Distributions of the number of jets, the number of b-jets, the lepton η and the lepton ϕ for the electron channel. The QCD multijet background is estimated from data. The yellow bands represent the uncertainty on the background prediction and include the uncertainty on the QCD multijet prediction and all the uncertainties on the non QCD background estimate from Monte Carlo, discussed in Section 5.3.

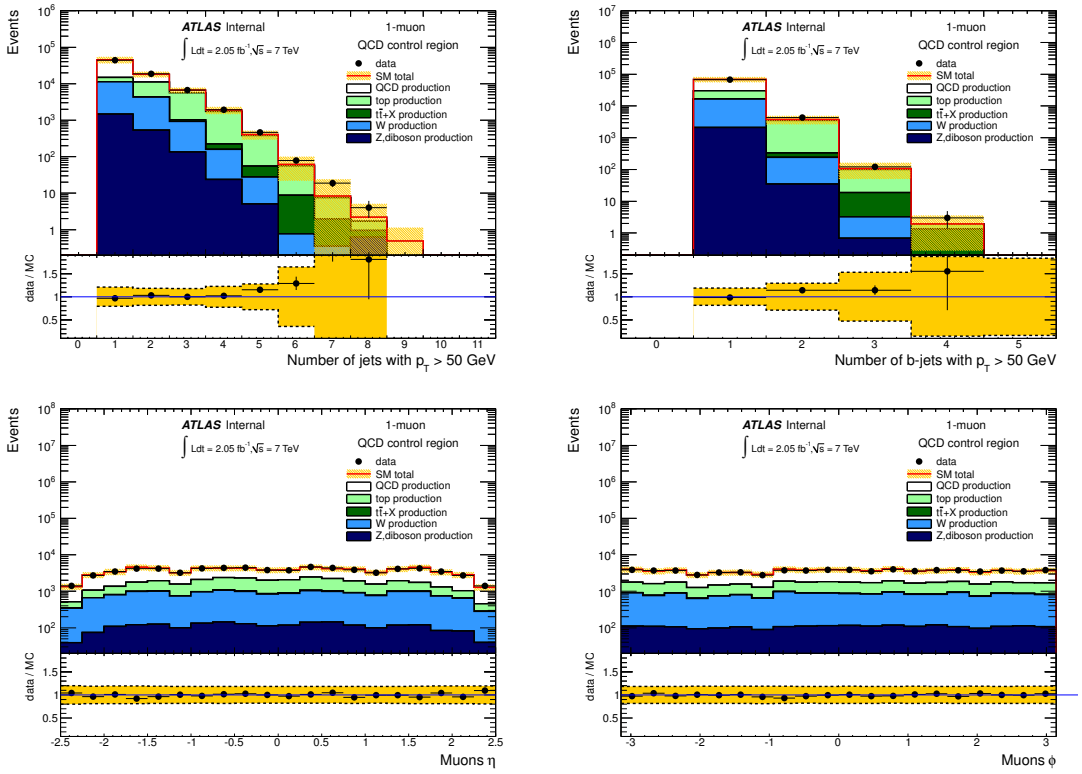

Figure 5.17.: Distributions of the number of jets, the number of b-jets, the lepton η and the lepton ϕ for the muon channel. The QCD background is estimated from data. The yellow bands represent the uncertainty on the background prediction and include the uncertainty on the QCD multijet prediction and all the uncertainties on the non QCD background estimate from Monte Carlo, discussed in Section 5.3.

5.3. Systematic Uncertainties

In the following, the systematic uncertainties are presented, split in experimental and theoretical uncertainties.

5.3.1. Experimental Uncertainties

The experimental systematic uncertainties include the uncertainties of the energy scale and resolution for jets, electrons and muons. For the leptons, additional uncertainties arise from the imprecise knowledge of the identification efficiency. The same is also true for b-jets, where the situation is even more complex. Additionally, the uncertainties on the measured luminosity and the effects of multiple interactions per bunch crossing ("pile-up") have to be taken into account. In the following, these experimental uncertainties are treated in more detail.

Luminosity For the integrated luminosity, an uncertainty of $\pm 3.7\%$ is assumed [108].

Pile-Up The high instantaneous luminosity in ATLAS is reached with a large number of protons per bunch, causing multiple collisions (primary vertices) per bunch crossing (called in-time pile-up). To take into account the effect of in-time pile-up, the Monte Carlo simulated events are produced with an average number of primary vertices per bunch crossings of $\langle \mu \rangle_{MC} = 8$. The Monte Carlo events are reweighted to match the distribution of primary vertices in data. The short time interval between two consecutive bunch crossings (50 ns) introduces an additional contribution to pile-up, called out-of-time pile-up. Especially in the calorimeters, signals from the previous bunch-crossings can overlap with the signals from the present one. As an example, the ATLAS LAr calorimeter has a signal shape with an approximate baseline of 500 ns [110]. The effect of out-of-time pile-up is taken into account, e.g. in the calibration of hadronic jets.

Jet Energy Scale (JES) The imperfect knowledge of the absolute energy scale of a hadronic jet is taken into account by varying the energy scale up and down by 1σ. The uncertainty consists of three parts, namely a term dependent on the p_{T} and η of the jet, a term dependent on the angular distance to the closest jet and finally a term dependent on the average quark-gluon composition of the sample. The influence of pile-up is included in the jet energy scale uncertainties. For the total uncertainty these terms are summed in quadrature. The resulting total uncertainty of the energy scale of a jet with $p_{\mathrm{T}} = 50\,\mathrm{GeV}$ for the central detector region is about $\pm 5\%$. Possible differences in the energy scale for b-jets compared to light jets are taken into account, by studying the calorimeter response for b-jets and performing systematic variations of the Monte Carlo simulation. As a results, an additional uncertainty of $\pm 2.5\%$ is obtained. Details on the methods can be found in Ref. [78]. The resulting uncertainty of the event yield is determined by rerunning the analysis with the jet energy scale varied up and down within the uncertainty. For the modified energy scale of the jets, the $E_{\mathrm{T}}^{\mathrm{miss}}$ in the event is recalculated accordingly.

Jet Energy Resolution (JER) The uncertainty on the jet energy resolution is based on the observed asymmetry between the p_{T} of the jets in dijet events. This asymmetry is used to construct the jet energy resolution, both in data and Monte Carlo simulated events. The observed difference is used as a systematic uncertainty. The fractional jet p_{T} resolution $\sigma(p_{\mathrm{T}})/p_{\mathrm{T}}$ is shown in Fig. 5.18 as a function of the average p_{T} of the jet in dijet events. The

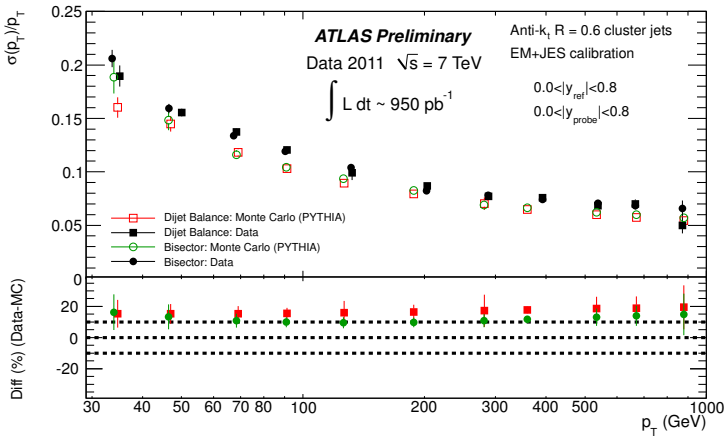

Figure 5.18.: Fractional jet p_{T} resolution $\sigma(p_{\mathrm{T}})/p_{\mathrm{T}}$ as a function of the average jet transverse momenta obtained from the dijet balance (squares) and the bisector method (circles) [59]. The lower part shows the relative difference between Monte Carlo simulation and data results. The dotted lines indicate a relative difference of ±10%. No pile-up corrections have been applied. For a detailed description of the methods and variables, see Ref. [111].

observed resolution in data is worse compared to the Monte Carlo simulation, therefore, the p_{T} of the jets in the simulation is smeared with a Gaussian distribution with unity as a mean value and a p_{T} and η dependent width. The effect of the smearing is evaluated by rerunning the analysis with the modified jets.

Lepton Identification Efficiency The uncertainty on the event yield, due to the uncertainty of the electron identification efficiency, is found to be all within ±3%. No scale factors are applied.

Lepton Energy Scale The lepton energy scale uncertainty is found to only have a sub percent influence on the final event yield and is therefore neglected.

***b*-Tagging** For the b-tagging algorithm introduced in Section 4.3.4 systematic studies [84] were conducted resulting in systematic uncertainties on the tagging efficiency of b-jets and the rejection of light and c-jets. These were transferred to uncertainties on the jet weight factors and ultimately on the event scaling factors. The effect of varying the event weight factors up and down by 1σ are assumed as systematic uncertainty.

5.3.2. Theoretical Uncertainties

The theoretical systematic uncertainties arise from the imperfect knowledge of physical quantities, e.g. the cross section of a specific physics process. Also the implementation of physical concepts in the Monte Carlo production play a role in this context, e.g. the modeling of the parton showers. The presentation of the theoretical systematic uncertainties below is organized in terms of specific physics processes.

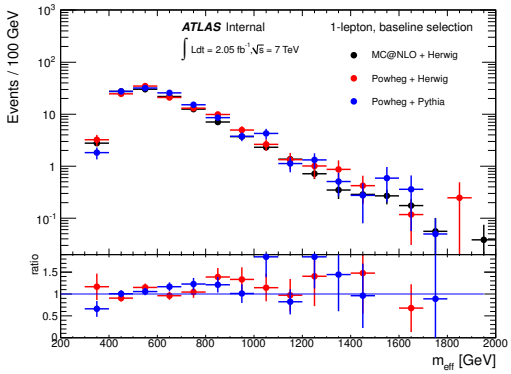

Figure 5.19.: Distribution of m_{eff} for $t\bar{t}$ events after the baseline selection as predicted by different generators and parton shower models.

Signal Uncertainties

For the theoretical systematic uncertainties on the signal cross sections, two sources are considered, namely PDF uncertainties of CTEQ6.6M [97] and uncertainties on the renormalization (μ_R) and factorization scale (μ_F).

The procedure to assess the scale uncertainties is defined as follows. Both scales are set to a scale μ, defined as the average of the masses of the particles that are produced, $\mu_F = \mu_R = \mu$. This scale μ is then varied up and down by a factor of two and the maximum difference is taken as systematic uncertainty.

The correlation between the PDF uncertainties and the scale uncertainties are neglected. The individual contributions are summed in quadrature.

Top Pair Production

As shown above, the production of top pairs is the dominant background in the presented analysis. Therefore, special care is taken in estimating the theoretical uncertainties on this particular background.

For the cross section of the top pair production, a value of $\sigma_{t\bar{t}} = 164.6^{+11.5}_{-15.8}$ pb is used. The uncertainty of this cross section is treated as systematic uncertainty. It has to be noted that this uncertainty is circumvented if control regions can be used to normalize the top pair production background.

For the top pair production background, different Monte Carlo generators are compared, namely the default program `MC@NLO` with `POWHEG` and `ALPGEN`. For the uncertainty connected to the modeling of the parton shower and fragmentation, comparisons are made between different Monte Carlo programs, namely `POWHEG` samples using either `HERWIG` or `PYTHIA` for fragmentation. The observed differences are treated as systematic uncertainties. Figure 5.19 shows the comparison of the m_{eff} distributions after the baseline selection defined in Section 5.1.2 with the different generators.

For the uncertainties due to the Initial State Radiation (ISR) and Final State Radia-

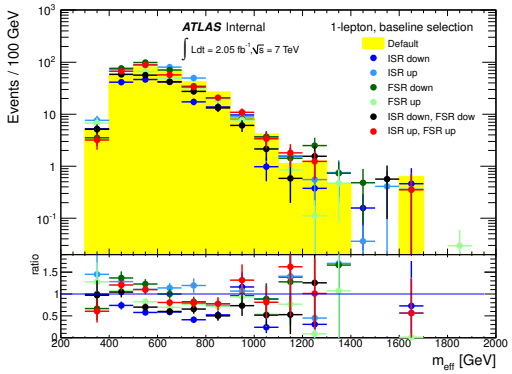

Figure 5.20.: Distribution of m_{eff} for $t\bar{t}$ events after the baseline selection as predicted by ACERMC interfaced to PYTHIA with different ISR and FSR parameters for $t\bar{t}$ production in the semi-leptonic channel.

tion (FSR), a study with simulated samples using ACERMC is performed. The envelope of the observed differences are treated as systematic uncertainties. Figure 5.20 illustrates these uncertainties in the m_{eff} distribution after the baseline selection.

Single Top Production

For the electroweak production of single top quarks, the following calculated cross sections are used: $\sigma(t) = 64.6^{+3.3}_{-2.3}$ pb, $\sigma(s) = 4.6 \pm 0.3$ pb and $\sigma(Wt) = 15.3^{+1.3}_{-1.4}$. Since the Wt process is found to have the largest relative uncertainty and is found to be dominant among the single top channels, the uncertainty of this channel is used as systematic uncertainty on the total single top cross section. In addition to this uncertainty, the same theoretical uncertainties as for the top pair production described above are applied also to the single top production.

Boson+Jets Production

For the W+jets and Z+jets contributions to the background, systematic uncertainties on the normalization are taken into account, assuming an uncertainty of ±24% per additional jet. For N additional jets $\sqrt{N} \times (\pm 24\%)$ is considered. The uncertainties for different values of N are treated as uncorrelated and summed in quadrature.

The uncertainties on the heavy flavor component for W+jets are taken into account, by using the uncertainties of the scale factors for Wbb/Wcc (1.63±0.76) and Wc (1.10±0.35) [112]. For Z+jets, the heavy flavor production cross section is in agreement with the theoretical prediction [113], therefore, no scale factors are applied. An uncertainty of 100% is assumed.

For the W+jets background, an additional uncertainty on the shapes based on a variation of ALPGEN parameters is added.

5.3.3. Uncertainty of the QCD Multijet Estimation

In the estimation of $\varepsilon_{\text{fake}}$, the uncertainty introduced by the subtraction of other background processes from Monte Carlo is taken into account by varying their normalization by ±20% in

each $(p_{\mathrm{T}}, |\eta|)$ bin. The dependence of the efficiency on the jet multiplicity in the event is also studied and found to be 1% (3%) in the electron channel before (after) the b-tagging requirement and 5% in the muon channel. These systematic uncertainties are added in quadrature with the statistical uncertainties in each $(p_{\mathrm{T}}, |\eta|)$ bin.

The procedure to determine the efficiency $\varepsilon_{\mathrm{real}}$ is done both with Monte Carlo simulated events and in data. The deviations are treated as systematic uncertainty.

5.3.4. Total Uncertainties

The total uncertainties are calculated taking into account all contributions introduced above. The estimate of the number of events in the two signal regions directly from Monte Carlo including all systematic uncertainties is given in Table 5.6. The uncertainties on the JES are found to be dominant among the experimental contributions to the uncertainty. The theory uncertainties are dominated by the contributions due to the uncertainties of the ISR/FSR and the variation of the Monte Carlo generators.

In contrast to the Monte Carlo based estimation, Table 5.7 contains the number of events in the two signal regions, estimated using the transfer factor. Besides estimating the number of background events in the signal region, one key feature of the data-driven approach via T_f is the reduction of systematic uncertainties. Most notably, the experimental uncertainties, e.g. the JES and b-tagging uncertainties, and the theory uncertainties are reduced to a large extend in the estimation. The additional uncertainty introduced by the use of the transfer factor, namely the statistical uncertainty in the control region, is found to be $\pm 5\%$.

5.4. Results and Interpretation

In the first part of this section, the observed distributions are shown and compared with the expectations from the SM. The contributions from SM background processes are determined using the estimation techniques described above. The second part of this chapter is dedicated to the interpretation of the results in the context of specific SUSY scenarios.

5.4.1. Measurements and Standard Model Expectation

The numbers of events for the electron and muon channels are listed in Table 5.8. For the consecutive selection steps, the MC expectation is given for the different physics processes separately. For the final signal regions, both the background expectation from MC and the expectation from data control regions are given.

In the following, a number of key distributions measured in data is compared with the SM expectation. The distributions are shown for the consecutive baseline selection criteria listed in Table 5.2 and for the two signal regions. For reference, two SUSY signals are superimposed, namely one signal point with $m_{\tilde{g}} = 600\,\mathrm{GeV}$ and $m_{\tilde{t}_1} = 210\,\mathrm{GeV}$ and one signal point with $m_{\tilde{g}} = 700\,\mathrm{GeV}$ and $m_{\tilde{\chi}_1^0} = 100\,\mathrm{GeV}$.

The number of jets with $p_{\mathrm{T}} > 50\,\mathrm{GeV}$ is shown in Fig. 5.21, the number of b-jets, both before and after the b-jet requirement, is shown in Fig. 5.22. The distributions of $E_{\mathrm{T}}^{\mathrm{miss}}$, m_{T}, m_{eff} and the p_{T} of the b-jets are shown in Figs. 5.23 and 5.24 for the electron and

Process	Number of Events (MC)	MC stat.	Experimental Uncertainties JES	JER	b-tag	Theory Uncertainties cross section	ISR/FSR	MC generator	Shower
SR1-D, electron channel									
$t\bar{t}$	28.7 ± 16.4	$\pm 4\%$	$\pm 28\%$	$\pm 3\%$	$\pm 10\%$	$\pm 8\%$	$\pm 41\%$	$\pm 21\%$	$\pm 13\%$
single top	1.6 ± 1.1	$\pm 26\%$	$\pm 36\%$	$\pm 14\%$	$\pm 7\%$	$\pm 8\%$	$\pm 50\%$		
W + jets	2.6 ± 2.8	$\pm 51\%$	$\pm 51\%$	$\pm 30\%$	$\pm 36\%$	$\pm 64\%$			
SR1-E, electron channel									
$t\bar{t}$	5.8 ± 3.7	$\pm 9\%$	$\pm 24\%$	$\pm 4\%$	$\pm 11\%$	$\pm 8\%$	$\pm 53\%$	$\pm 19\%$	$\pm 2\%$
single top	0.4 ± 0.5	$\pm 36\%$	$\pm 49\%$	$\pm 4\%$	$\pm 6\%$	$\pm 8\%$	$\pm 100\%$		
W + jets	1.1 ± 1.2	$\pm 81\%$	$\pm 0\%$	$\pm 0\%$	$\pm 42\%$	$\pm 76\%$			
SR1-D, muon channel									
$t\bar{t}$	28.4 ± 18.7	$\pm 4\%$	$\pm 30\%$	$\pm 2\%$	$\pm 9\%$	$\pm 8\%$	$\pm 54\%$	$\pm 18\%$	$\pm 4\%$
single top	1.7 ± 1.0	$\pm 23\%$	$\pm 16\%$	$\pm 11\%$	$\pm 12\%$	$\pm 8\%$	$\pm 47\%$		
W + jets	4.0 ± 3.8	$\pm 42\%$	$\pm 31\%$	$\pm 16\%$	$\pm 18\%$	$\pm 75\%$			
SR1-E, muon channel									
$t\bar{t}$	4.8 ± 4.4	$\pm 11\%$	$\pm 41\%$	$\pm 5\%$	$\pm 8\%$	$\pm 8\%$	$\pm 62\%$	$\pm 50\%$	$\pm 16\%$
single top	0.5 ± 0.6	$\pm 42\%$	$\pm 31\%$	$\pm 8\%$	$\pm 9\%$	$\pm 8\%$	$\pm 100\%$		
W + jets	0								

Table 5.6.: Monte Carlo based estimate of the main background contributions in SR1-D/E and associated systematic uncertainties for an integrated luminosity of $2.05\,\mathrm{fb}^{-1}$. The estimates are given separately for the electron and muon channel. The column "MC stat." refers to the uncertainties due to the limited number of Monte Carlo simulated events. The columns "MC generator" and "Shower" refer to the uncertainties of the top pair production, obtained by the comparison of different event generators and different modeling of parton showering and fragmentation (see text for details). The W+jets background is completely dominated by the W plus heavy flavor production.

Channel	SR Estimation	CR1 stat.	MC stat.	JES	JER	b-tag	lepton ID	QCD	theory	MC
SR1-D										
electron	39.2 ± 11.9	±5%	±4%	±3%	±6%	±1%	±1%	±1%	±29%	38.6 ± 18.7
muon	38.2 ± 14.3	±5%	±4%	±3%	±3%	±1%	±1%	±1%	±37%	37.0 ± 20.5
SR1-E										
electron	8.1 ± 3.4	±5%	±11%	±3%	±2%	±4%	±1%	±1%	±39%	7.9 ± 4.2
muon	6.3 ± 4.2	±5%	±8%	±8%	±2%	±2%	±1%	±1%	±65%	6.1 ± 4.8

Table 5.7.: Estimation of the number of events in the signal regions SR1-D and SR1-E, respectively. The event yields correspond to an integrated luminosity of $2.05\,\mathrm{fb}^{-1}$, they are presented separately for the electron and muon channels. The total uncertainty and the individual contributions to the total uncertainty are given. The column labeled "CR1 stat." represents the uncertainty due to the statistical uncertainty in the control region. The column labeled "MC stat." represents the uncertainty due to the limited number of Monte Carlo simulated events.

Selection	≥ 4 jets	≥ 1 b-jet	$E_{\mathrm{T}}^{\mathrm{miss}} > 80$ GeV	$m_{\mathrm{T}} > 100$ GeV	SR1-D	SR1-E
1-electron channel						
$t\bar{t}$ +single top	3697 ± 1361	2843 ± 1075	896 ± 379	109.1 ± 53.7	30.3 ± 16.8	6.3 ± 3.8
$t\bar{t}$ +X	194 ± 196	161 ± 164	53 ± 55	8.4 ± 8.7	3.0 ± 3.1	0.5 ± 0.6
W+jets	2027 ± 804	224 ± 142	65 ± 40	4.0 ± 3.7	2.6 ± 2.8	1.1 ± 1.2
others	572 ± 225	56 ± 31	4 ± 3	0.9 ± 0.5	0.8 ± 0.5	0
QCD (d-d)	1241 ± 303	320 ± 158	14 ± 21	4.1 ± 3.7	1.9 ± 1.4	0.1 ± 0.3
SM (MC)	7731 ± 2057	3603 ± 1190	1032 ± 412	126.5 ± 57.8	38.6 ± 18.7	7.9 ± 4.2
SM (d-d)					39.2 ± 11.9	8.1 ± 3.4
data ($2.05\,\mathrm{fb}^{-1}$)	7632	3648	1047	151	43	11
1-muon channel						
$t\bar{t}$ +single top	3572 ± 1333	2757 ± 1040	862 ± 358	117.7 ± 65.3	30.1 ± 18.7	5.3 ± 4.6
$t\bar{t}$ +X	183 ± 185	153 ± 156	50 ± 51	8.1 ± 8.3	2.7 ± 2.8	0.5 ± 0.6
W+jets	1922 ± 771	214 ± 130	55 ± 39	6.1 ± 5.0	4.0 ± 3.8	0
others	329 ± 135	32 ± 19	3 ± 3	0.2 ± 0.5	0.1 ± 0.5	< 0.1
QCD (d-d)	520 ± 167	188 ± 67	10 ± 9	0.7 ± 1.3	0.1 ± 0.4	0.3 ± 0.3
SM (MC)	6526 ± 1925	3344 ± 1131	980 ± 382	132.7 ± 68.4	37.0 ± 20.5	6.1 ± 4.8
SM (d-d)					38.2 ± 14.3	6.3 ± 4.2
data ($2.05\,\mathrm{fb}^{-1}$)	6524	3523	1031	166	38	6

Table 5.8.: Comparison between the expected SM event yields and the measured event yields for $2.05\,\mathrm{fb}^{-1}$ for muon and electron channels. The column labeled "others" corresponds to the sum of Z and diboson production. The QCD multijet background is estimated from data and the quoted uncertainties include both statistical and systematic uncertainties. The uncertainties on the non-QCD background processes include all systematic uncertainties as well as the uncertainty due to the limited number of Monte Carlo simulated events. QCD (d-d) refers to the estimate using the fully data driven technique, SM (d-d) refers to the semi-data driven technique.

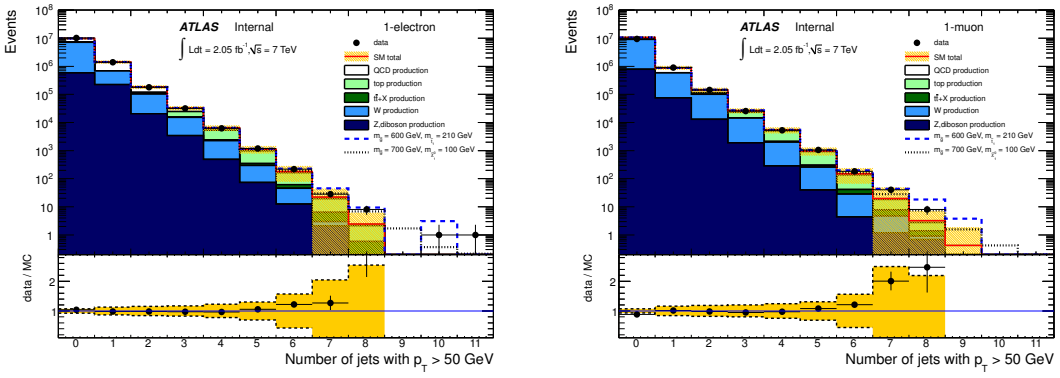

Figure 5.21.: Number of jets with $p_{\mathrm{T}} > 50$ GeV after lepton selection for the electron (left) and the muon (right) channels. The QCD multijet background is estimated from data. The uncertainty on the background prediction includes the uncertainty on the QCD multijet prediction and all the uncertainties on the non-QCD background estimate from Monte Carlo. For reference, two SUSY signals are superimposed, namely one signal point with $m_{\tilde{g}} = 600\,\mathrm{GeV}$ and $m_{\tilde{t}_1} = 210\,\mathrm{GeV}$ and one signal point with $m_{\tilde{g}} = 700\,\mathrm{GeV}$ and $m_{\tilde{\chi}_1^0} = 100\,\mathrm{GeV}$.

muon channel, respectively. The distribution of m_{T} after the $E_{\mathrm{T}}^{\mathrm{miss}}$ requirement is shown in Fig. 5.25. After the baseline selection, the m_{eff} distribution is shown in Fig. 5.26.

For the signal region SR1-D, the distributions of m_{eff}, $E_{\mathrm{T}}^{\mathrm{miss}}$, m_{T} and p_{T} of the lepton are shown in Figs. 5.27 and 5.28 for the electron and muon channel, respectively. The number of jets and b-jets, as well as the p_{T} of the jets and b-jets are shown in Figs. 5.29 and 5.30. The analogous distributions for SR1-E are shown in Figs. 5.31 to 5.34.

All distributions in Figs. 5.21 to 5.34 show good agreement and leave no room for significant contributions from physics beyond the SM. The measured numbers of events for $2.05\,\mathrm{fb}^{-1}$ of integrated luminosity are consistent with the SM expectation within the statistical and systematic uncertainties. No significant excess is observed.

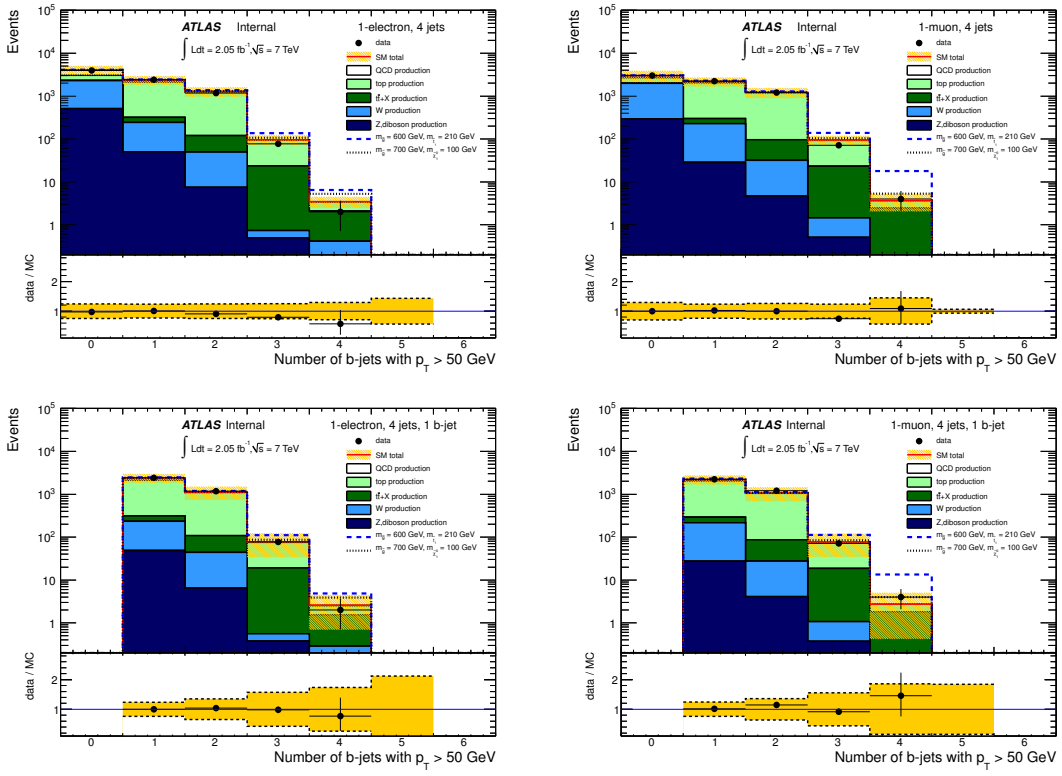

Figure 5.22.: Number of b-jets with $p_{\mathrm{T}} > 50$ GeV in events with exactly one lepton and at least four jets with $p_{\mathrm{T}} > 50$ GeV for the electron (left) and the muon (right) channels, before (top) and after (bottom) the b-tagging requirement. The QCD multijet background is estimated from data. The uncertainty on the background prediction includes the uncertainty on the QCD multijet prediction and all the uncertainties on the non-QCD background estimate from Monte Carlo. The b-tagging scale factors are applied only after the b-jet requirement. For reference, two SUSY signals are superimposed, namely one signal point with $m_{\tilde{g}} = 600\,\mathrm{GeV}$ and $m_{\tilde{t}_1} = 210\,\mathrm{GeV}$ and one signal point with $m_{\tilde{g}} = 700\,\mathrm{GeV}$ and $m_{\tilde{\chi}_1^0} = 100\,\mathrm{GeV}$.

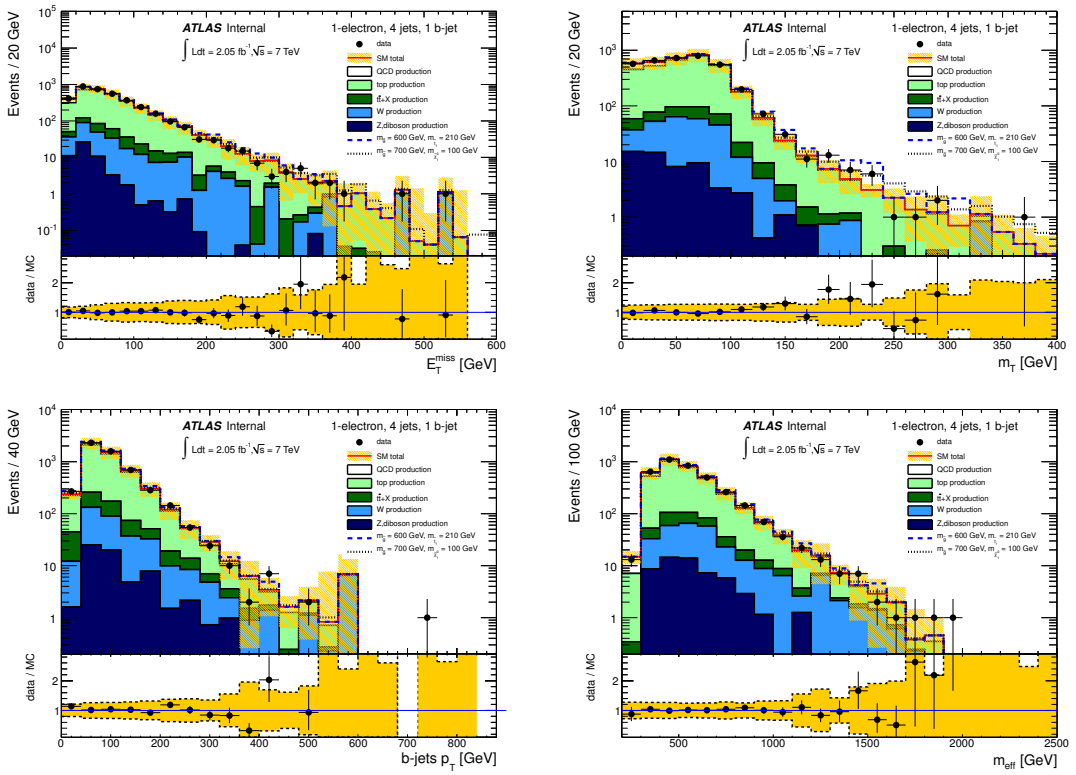

Figure 5.23.: Distributions of $E_{\mathrm{T}}^{\mathrm{miss}}$, m_{T}, p_{T} of b-jets and m_{eff} in events with exactly one lepton and at least four jets with $p_{\mathrm{T}} > 50$ GeV, one of which is a b-tagged jet, for the electron channel. The QCD multijet background is estimated from data. The uncertainty on the background prediction includes the uncertainty on the QCD multijet prediction and all the uncertainties on the non-QCD background estimate from Monte Carlo. For reference, two SUSY signals are superimposed, namely one signal point with $m_{\tilde{g}} = 600\,\mathrm{GeV}$ and $m_{\tilde{t}_1} = 210\,\mathrm{GeV}$ and one signal point with $m_{\tilde{g}} = 700\,\mathrm{GeV}$ and $m_{\tilde{\chi}_1^0} = 100\,\mathrm{GeV}$.

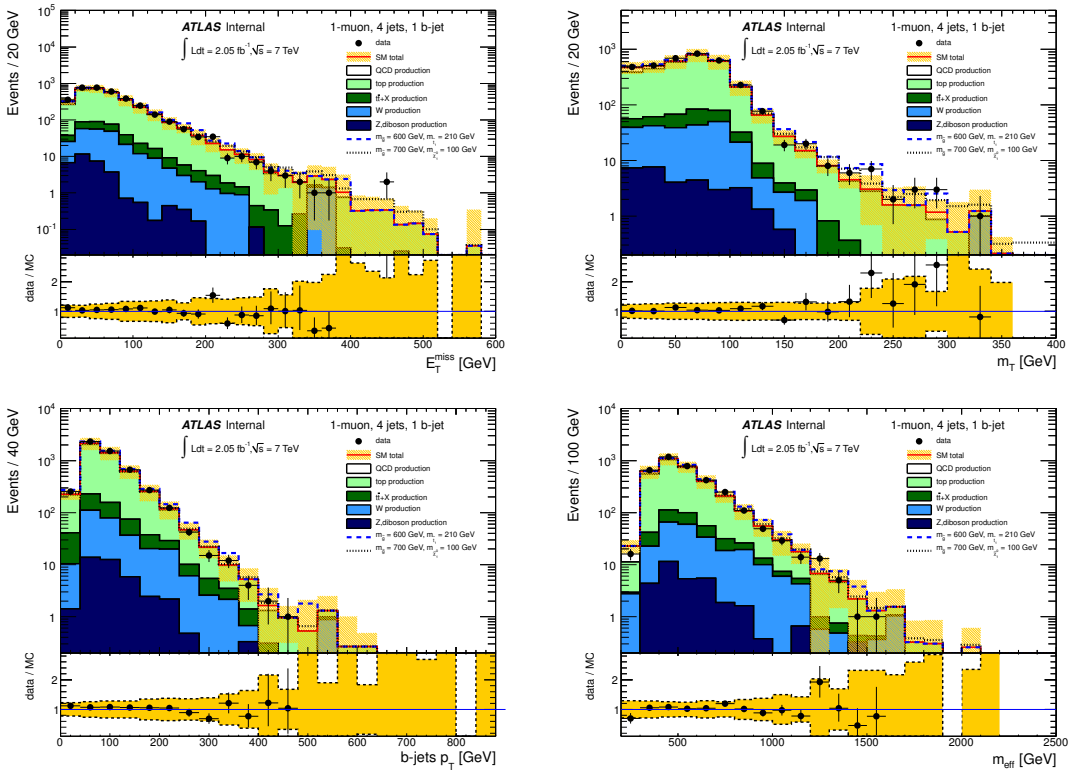

Figure 5.24.: Distributions of $E_{\mathrm{T}}^{\mathrm{miss}}$, m_{T}, p_{T} of b-jets and m_{eff} in events with exactly one lepton and at least four jets with $p_{\mathrm{T}} > 50$ GeV, one of which is a b-tagged jet, for the muon channel. The QCD multijet background is estimated from data. The uncertainty on the background prediction includes the uncertainty on the QCD multijet prediction and all the uncertainties on the non-QCD background estimate from Monte Carlo. For reference, two SUSY signals are superimposed, namely one signal point with $m_{\tilde{g}} = 600\,\mathrm{GeV}$ and $m_{\tilde{t}_1} = 210\,\mathrm{GeV}$ and one signal point with $m_{\tilde{g}} = 700\,\mathrm{GeV}$ and $m_{\tilde{\chi}_1^0} = 100\,\mathrm{GeV}$.

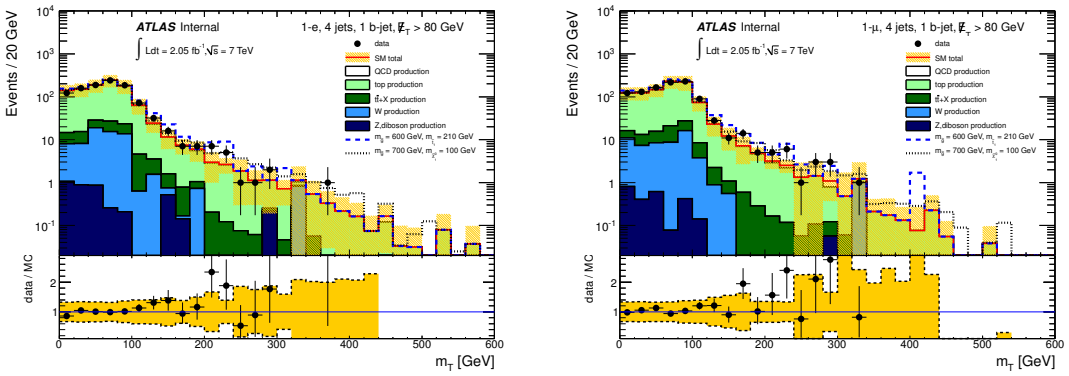

Figure 5.25.: Distributions of the transverse mass after the $E_{\mathrm{T}}^{\mathrm{miss}}$ cut for the electron (left) and the muon (right) channels. The QCD multijet background is estimated from data. The uncertainty on the background prediction includes the uncertainty on the QCD multijet prediction and all the uncertainties on the non-QCD background estimate from Monte Carlo. For reference, two SUSY signals are superimposed, namely one signal point with $m_{\tilde{g}} = 600\,\mathrm{GeV}$ and $m_{\tilde{t}_1} = 210\,\mathrm{GeV}$ and one signal point with $m_{\tilde{g}} = 700\,\mathrm{GeV}$ and $m_{\tilde{\chi}^0_1} = 100\,\mathrm{GeV}$.

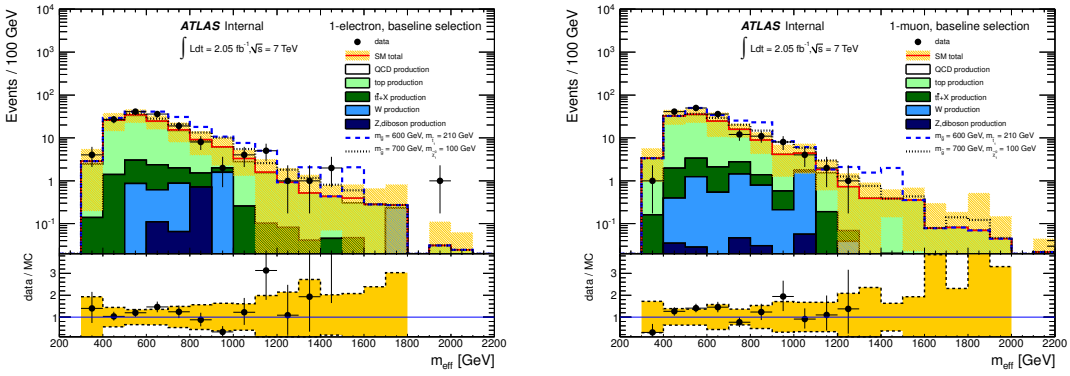

Figure 5.26.: Distributions of m_{eff} after the baseline selection for the electron (left) and the muon (right) channels. The QCD multijet background is estimated from data. The uncertainty on the background prediction includes the uncertainty on the QCD multijet prediction and all the uncertainties on the non-QCD background estimate from Monte Carlo. For reference, two SUSY signals are superimposed, namely one signal point with $m_{\tilde{g}} = 600\,\mathrm{GeV}$ and $m_{\tilde{t}_1} = 210\,\mathrm{GeV}$ and one signal point with $m_{\tilde{g}} = 700\,\mathrm{GeV}$ and $m_{\tilde{\chi}^0_1} = 100\,\mathrm{GeV}$.

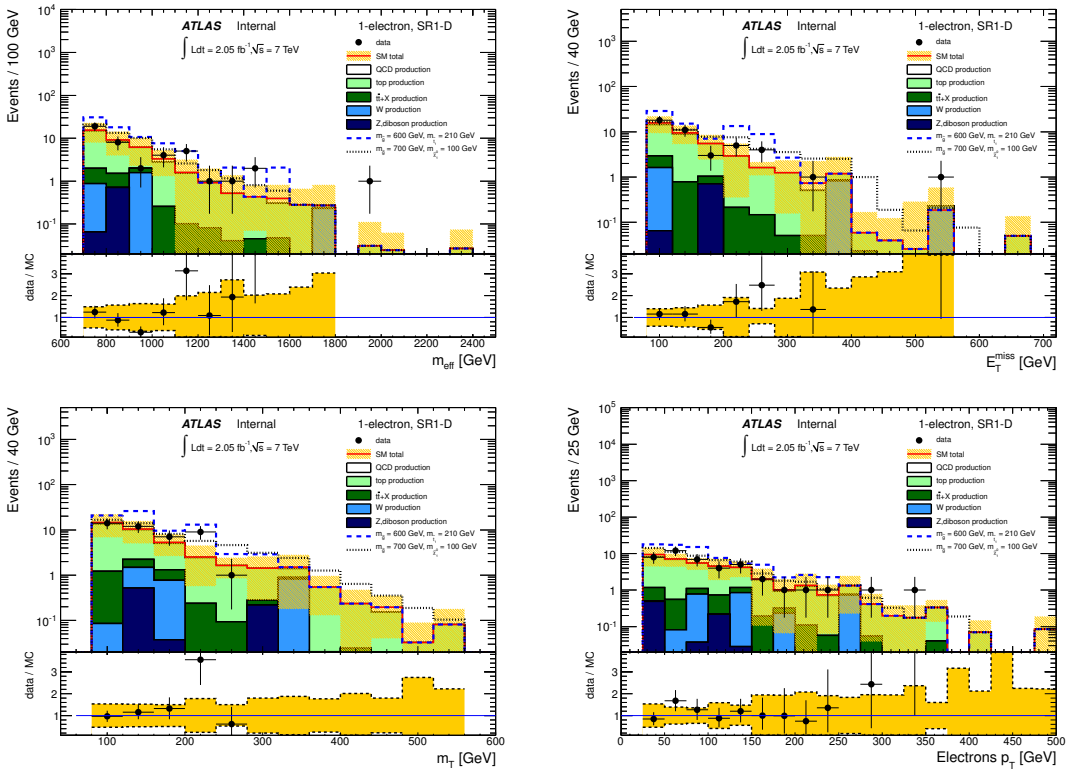

Figure 5.27.: Distributions of m_{eff}, $E_{\text{T}}^{\text{miss}}$, m_{T} and the lepton p_T in the SR1-D for the electron channel. The QCD multijet background is estimated from data. The uncertainty on the background prediction includes the uncertainty on the QCD multijet prediction and all the uncertainties on the non-QCD background estimate from Monte Carlo. For reference, two SUSY signals are superimposed, namely one signal point with $m_{\tilde{g}} = 600\,\text{GeV}$ and $m_{\tilde{t}_1} = 210\,\text{GeV}$ and one signal point with $m_{\tilde{g}} = 700\,\text{GeV}$ and $m_{\tilde{\chi}_1^0} = 100\,\text{GeV}$.

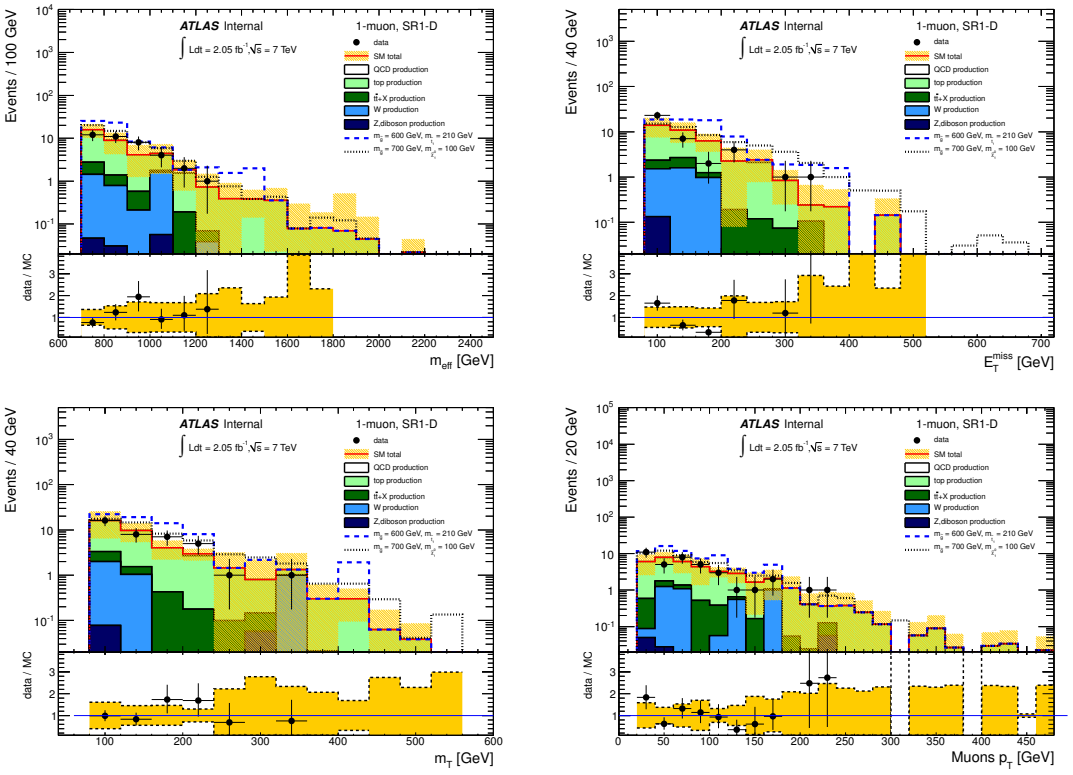

Figure 5.28.: Distributions of m_{eff}, $E_{\text{T}}^{\text{miss}}$, m_{T} and the p_{T} of the lepton in the SR1-D for the muon channel. The QCD multijet background is estimated from data. The uncertainty on the background prediction includes the uncertainty on the QCD multijet prediction and all the uncertainties on the non-QCD background estimate from Monte Carlo. For reference, two SUSY signals are superimposed, namely one signal point with $m_{\tilde{g}} = 600\,\text{GeV}$ and $m_{\tilde{t}_1} = 210\,\text{GeV}$ and one signal point with $m_{\tilde{g}} = 700\,\text{GeV}$ and $m_{\tilde{\chi}_1^0} = 100\,\text{GeV}$.

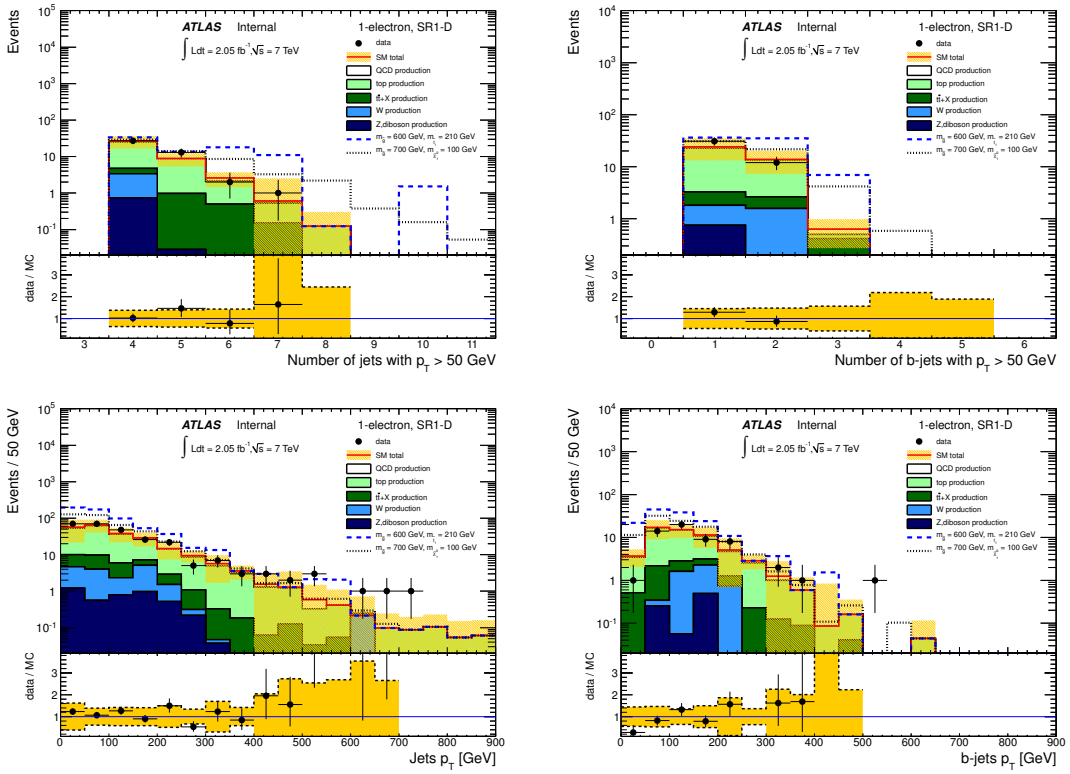

Figure 5.29.: Distributions of the number of jets, the number of b-jets, the jets p_T and the b-jets p_T in SR1-D for the electron channel. The QCD multijet background is estimated from data. The uncertainty on the background prediction includes the uncertainty on the QCD multijet prediction and all the uncertainties on the non-QCD background estimate from Monte Carlo. For reference, two SUSY signals are superimposed, namely one signal point with $m_{\tilde{g}} = 600\,\text{GeV}$ and $m_{\tilde{t}_1} = 210\,\text{GeV}$ and one signal point with $m_{\tilde{g}} = 700\,\text{GeV}$ and $m_{\tilde{\chi}_1^0} = 100\,\text{GeV}$.

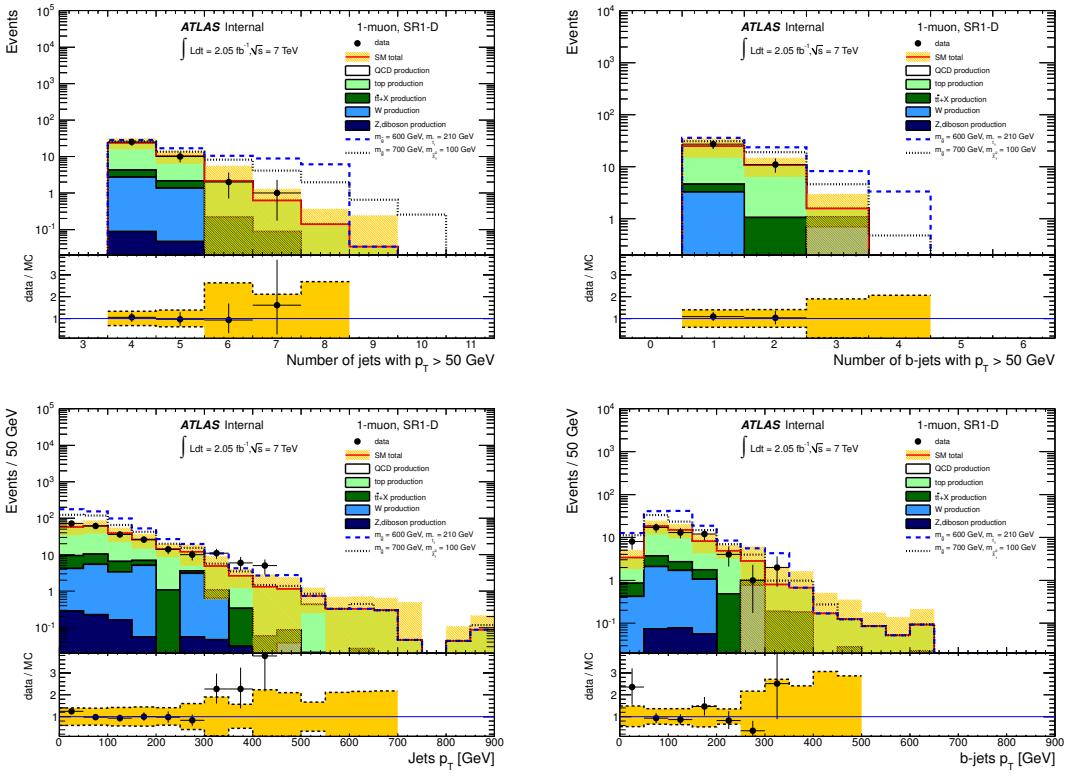

Figure 5.30.: Distributions of the number of jets, the number of b-jets, the jets p_T and the b-jets p_T in SR1-D for the muon channel. The QCD multijet background is estimated from data. The uncertainty on the background prediction includes the uncertainty on the QCD multijet prediction and all the uncertainties on the non-QCD background estimate from Monte Carlo. For reference, two SUSY signals are superimposed, namely one signal point with $m_{\tilde{g}} = 600\,\text{GeV}$ and $m_{\tilde{t}_1} = 210\,\text{GeV}$ and one signal point with $m_{\tilde{g}} = 700\,\text{GeV}$ and $m_{\tilde{\chi}_1^0} = 100\,\text{GeV}$.

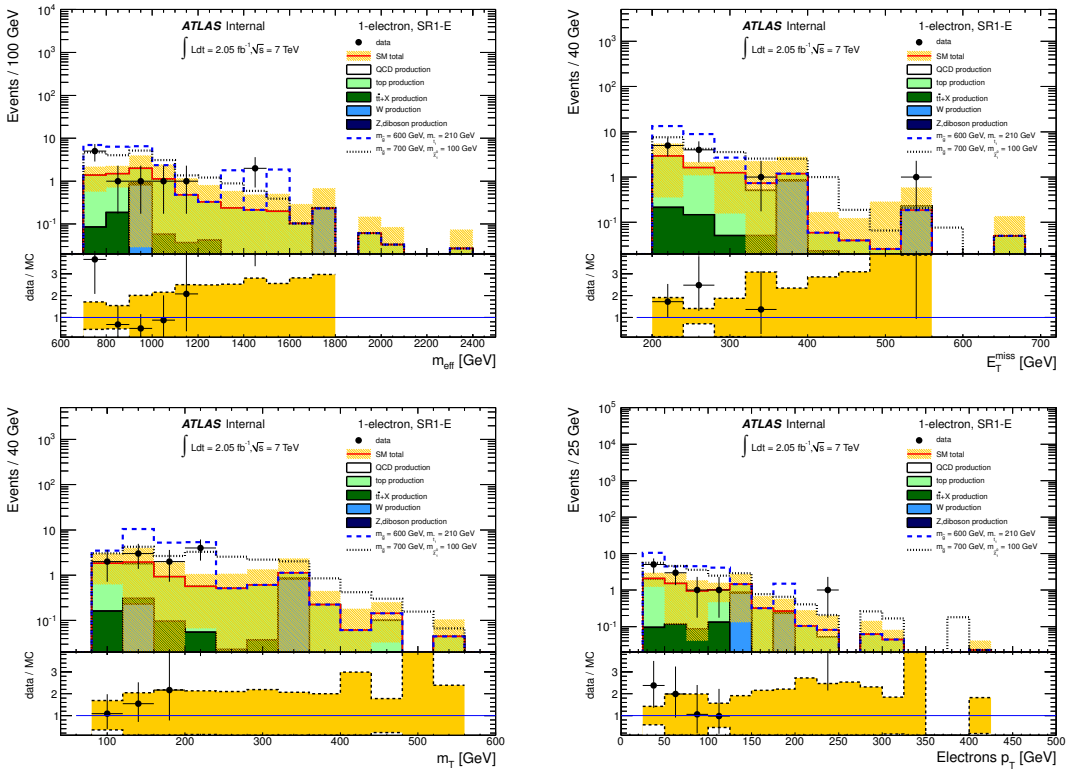

Figure 5.31.: Distribution of m_{eff}, $E_{\text{T}}^{\text{miss}}$, m_{T} and the lepton p_T in SR1-E for the electron channel. The QCD multijet background is estimated from data. The uncertainty on the background prediction includes the uncertainty on the QCD multijet prediction and all the uncertainties on the non-QCD background estimate from Monte Carlo. For reference, two SUSY signals are superimposed, namely one signal point with $m_{\tilde{g}} = 600\,\text{GeV}$ and $m_{\tilde{t}_1} = 210\,\text{GeV}$ and one signal point with $m_{\tilde{g}} = 700\,\text{GeV}$ and $m_{\tilde{\chi}_1^0} = 100\,\text{GeV}$.

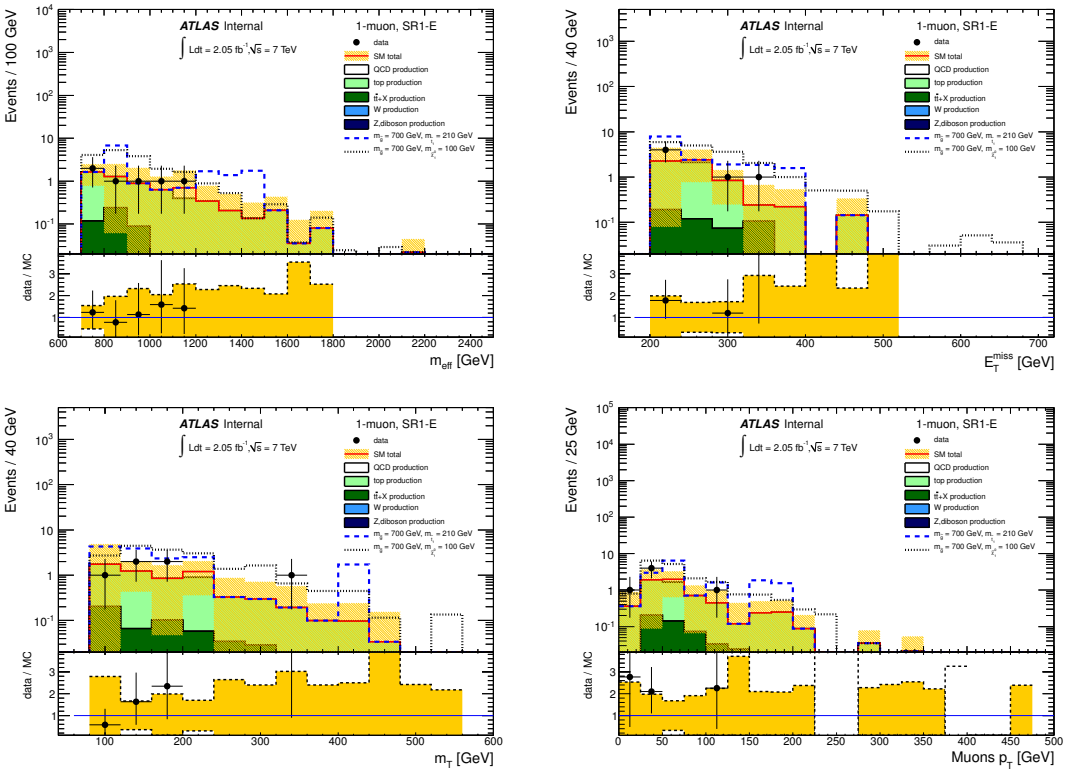

Figure 5.32.: Distribution of m_{eff}, $E_{\text{T}}^{\text{miss}}$, m_{T} and the lepton p_T in SR1-E for the muon channel. The QCD multijet background is estimated from data. The uncertainty on the background prediction includes the uncertainty on the QCD multijet prediction and all the uncertainties on the non-QCD background estimate from Monte Carlo. For reference, two SUSY signals are superimposed, namely one signal point with $m_{\tilde{g}} = 600\,\text{GeV}$ and $m_{\tilde{t}_1} = 210\,\text{GeV}$ and one signal point with $m_{\tilde{g}} = 700\,\text{GeV}$ and $m_{\tilde{\chi}_1^0} = 100\,\text{GeV}$.

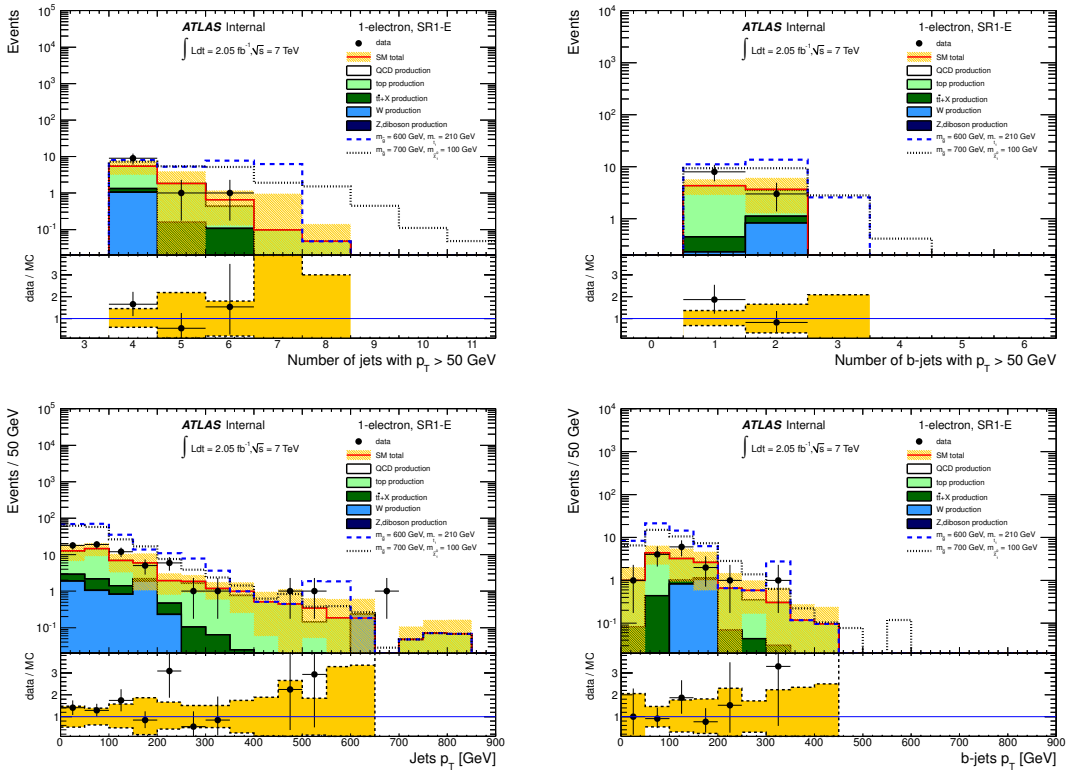

Figure 5.33.: Distribution of the number of jets, the number of b-jets, the jets p_T and the b-jets p_T in the SR1-E for the electron channel. The QCD multijet background is estimated from data. The uncertainty on the background prediction includes the uncertainty on the QCD multijet prediction and all the uncertainties on the non-QCD background estimate from Monte Carlo. For reference, two SUSY signals are superimposed, namely one signal point with $m_{\tilde{g}} = 600\,\text{GeV}$ and $m_{\tilde{t}_1} = 210\,\text{GeV}$ and one signal point with $m_{\tilde{g}} = 700\,\text{GeV}$ and $m_{\tilde{\chi}_1^0} = 100\,\text{GeV}$.

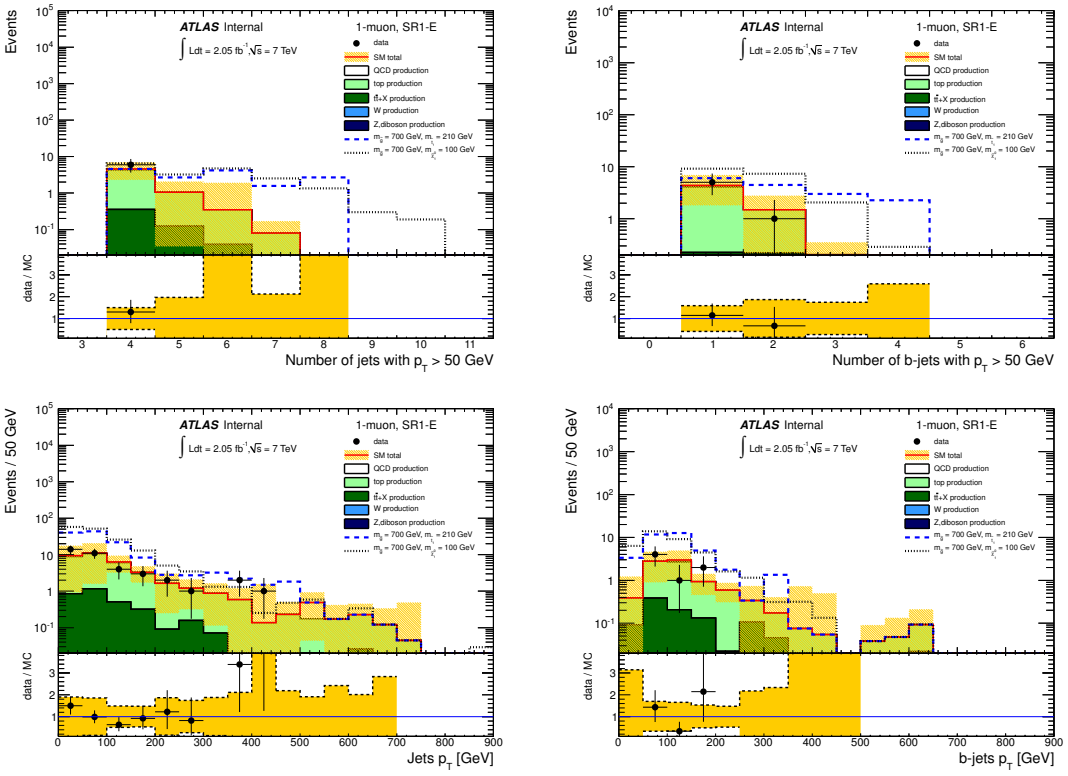

Figure 5.34.: Distribution of the number of jets, the number of b-jets, the jets p_T and the b-jets p_T in the SR1-E for the muon channel. The QCD multijet background is estimated from data. The uncertainty on the background prediction includes the uncertainty on the QCD multijet prediction and all the uncertainties on the non-QCD background estimate from Monte Carlo. For reference, two SUSY signals are superimposed, namely one signal point with $m_{\tilde{g}} = 600\,\text{GeV}$ and $m_{\tilde{t}_1} = 210\,\text{GeV}$ and one signal point with $m_{\tilde{g}} = 700\,\text{GeV}$ and $m_{\tilde{\chi}_1^0} = 100\,\text{GeV}$.

SR	95% CL upper limit	
	N events	σ_{vis}(fb)
	obs. (exp.)	obs. (exp.)
SR1-D	45.5 (42.1)	22.2 (20.5)
SR1-E	17.5 (15.3)	8.5 (7.5)

Table 5.9.: Observed and expected 95% C.L. upper limits on the non-SM contributions to the signal regions. The limits are given on the number of signal events and in terms of visible cross sections. The systematic uncertainties on the SM background estimation are included.

5.4.2. Exclusion Limits

Without assuming a specific SUSY model, the presented results are translated into 95% C.L. upper limits on the effective cross section[4] σ_{vis} and number of events from physics beyond the SM. Possible signal contamination in the control region are not taken into account.

The model independent interpretation is summarized in Table 5.9, separately for the signal regions SR1-D and SR1-E.

In the following, the results are interpreted in the context of specific SUSY scenarios and translated into exclusion limits based on the *CLs* procedure introduced in Section 2.3.1. The following models are taken into account: the SO(10) model, two simplified models and the gluino-stop model.

SO(10)

The SO(10) model in general has been introduced in Section 2.2.2 and 3.3.4. For the specific models used here, namely the D-term splitting model DR3 and the Higgs splitting model HS, the SUSY particle mass spectrum is found to be $m(\tilde{g})$=300-600 GeV, $m(\tilde{\chi}_1^{\pm})$=100-180 GeV, $m(\tilde{\chi}_1^0)$ =50-90 GeV and all other sparticles masses are beyond the TeV scale.

The expected and observed upper limit on the effective cross section, obtained using SR1-E, are shown in Fig. 5.35 for the DR3 (left) and HS (right) as a function of the gluino mass. The point of intersection of the observed limit line with the expected cross section (calculated with the program `PROSPINO` at NLO accuracy) yields the model dependent exclusion limit for the gluino mass. At 95% C.L. gluino masses $m_{\tilde{g}} < 650\,\text{GeV}$ are excluded in the DR3 model. For the HS model, gluino masses $m_{\tilde{g}} < 610\,\text{GeV}$ are excluded. The limits are significantly improved compared to the results of the previous ATLAS analysis [114], based on an integrated luminosity of $35\,\text{pb}^{-1}$, which are included in the figure[5].

[4]The effective cross section is defined as the cross section multiplied by the detector acceptance and the efficiency of the analysis.

[5]Only for low gluino masses, the observed limits are weaker compared to the previous analysis, due to the more restrictive selection criteria of the present analysis. At least two jets were required with p_{T} exceeding 60 GeV for the leading jet and 30 GeV for the subleading jet. The m_{eff} was required to exceed 500 GeV. The remaining selection criteria were analogous to the present analysis.

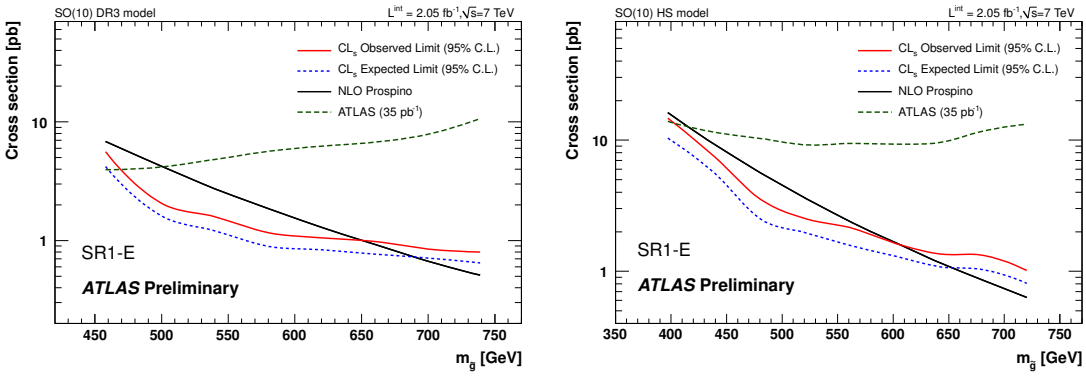

Figure 5.35.: Cross section for the SO(10) models as a function of the gluino mass, calculated with the program PROSPINO [52] at NLO (black). The D-term splitting model DR3 is shown on the left, the Higgs splitting model HS on the right. The observed (expected) upper limit on the cross section is shown as a red (blue dashed) line. For reference, the limit obtained with the previous analysis based on an integrated luminosity of $35\,\mathrm{pb}^{-1}$ is also included (black, dashed).

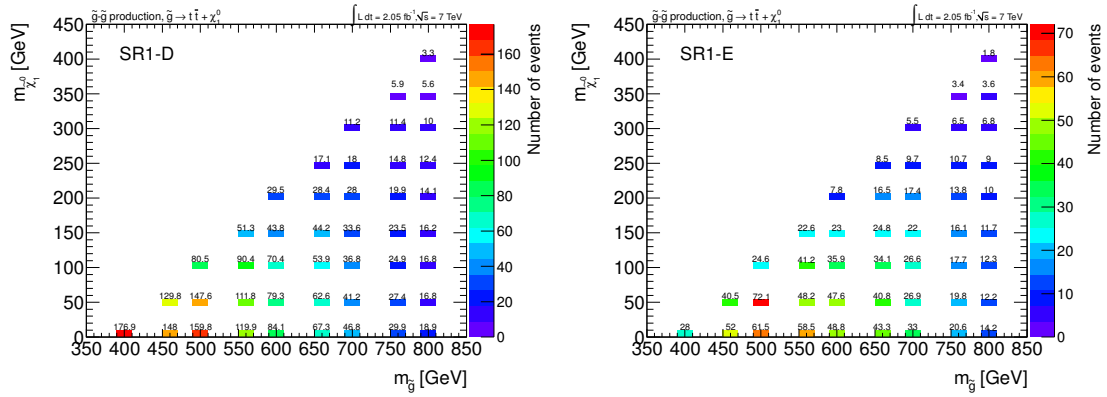

Figure 5.36.: Expected numbers of signal events in the $(m_{\tilde{g}},m_{\tilde{\chi}_1^0})$-plane of the Gt simplified model for an integrated luminosity of $2.05\,\mathrm{fb}^{-1}$ in SR1-D (left) and SR1-E (right).

Simplified Models

In this section, the results of the presented search are interpreted in the framework of the Gt and Gtb simplified models, introduced in Section 3.3.2. In both cases the production of SUSY particles is assumed to proceed via gluino pair production and subsequent decay.

The expected number of signal events assuming the Gt simplified model is shown in Fig. 5.36, for the signal regions SR1-D (left) and SR1-E (right). To prevent possible biases in the background estimation the expected numbers of signal events in the control region are also taken into account by subtracting the number of expected SUSY events in the control region

$$N_{\mathrm{data}}^{\mathrm{SR}} = (N_{\mathrm{data}}^{\mathrm{CR1}} - N_{\mathrm{SUSY}}^{\mathrm{CR1}})\frac{N_{\mathrm{MC}}^{\mathrm{SR}}}{N_{\mathrm{MC}}^{\mathrm{CR1}}}. \tag{5.9}$$

The expected and observed exclusion limits in the $(m_{\tilde{g}},m_{\tilde{\chi}_1^0})$-plane are shown in Fig. 5.37 as

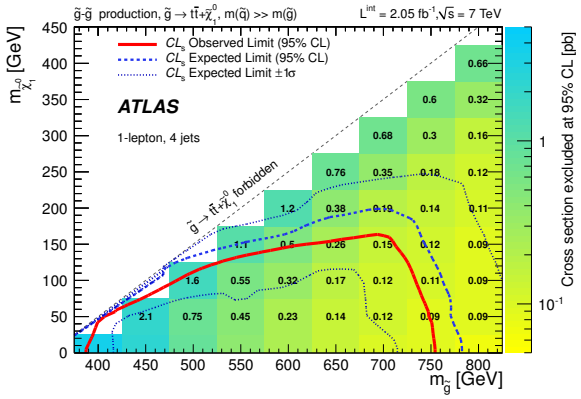

Figure 5.37.: Exclusion limit at 95% C.L. for the Gt simplified model in the ($m_{\tilde{g}}$,$m_{\tilde{\chi}_1^0}$)-plane. The observed limit is represented by the solid red line. The expected limit (dashed blue line) is shown with the $\pm 1\sigma$ variation of the uncertainties (dotted blue lines). The cross sections, which are excluded at 95% C.L., are given as numerical values and as color-coded bins in the gluino and neutralino mass.

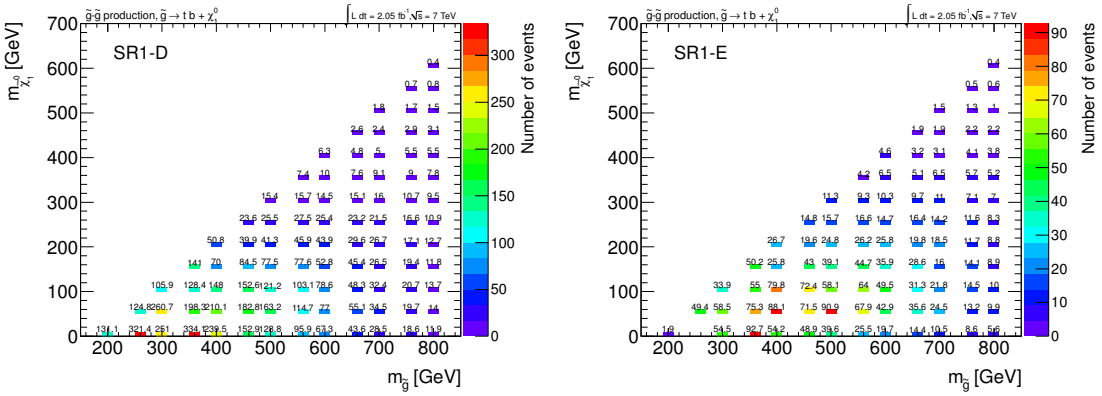

Figure 5.38.: Expected numbers of signal events in the ($m_{\tilde{g}}$,$m_{\tilde{\chi}_1^0}$)-plane of the Gtb simplified model for an integrated luminosity of 2.05 fb^{-1} in SR1-D (left) and SR1-E (right).

dashed blue and solid red line, respectively. In addition, the cross sections that are excluded at 95% C.L. are given in bins of the gluino and neutralino masses (color-coded bins and numerical values). For a neutralino mass of 50 GeV, gluino masses between 400 and 750 GeV are excluded at 95% C.L. with this analysis. For a gluino mass of 700 GeV, neutralino masses up to 160 GeV are excluded.

The expected numbers of signal events in the Gtb model are shown in Fig. 5.38 for SR1-D (left) and SR1-E (right). The resulting expected and observed exclusion limits in the ($m_{\tilde{g}}$,$m_{\tilde{\chi}_1^0}$)-plane are shown in Fig. 5.39. In this scenarios, gluino masses between 350 and 720 GeV are excluded at 95% C.L. for neutralino masses of 100 GeV. For a gluino mass of 600 GeV, neutralino masses below 200 GeV are excluded.

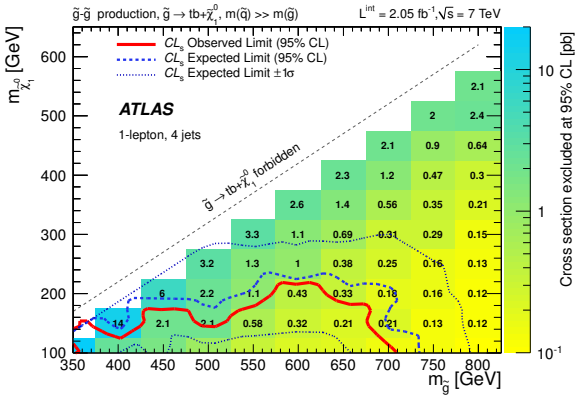

Figure 5.39.: Exclusion limit at 95% C.L. in the $(m_{\tilde{g}},m_{\tilde{\chi}_1^0})$-plane of the Gtb simplified model. The observed limit is represented by the solid red line. The expected limit (dashed blue line) is shown with the $\pm 1\sigma$ variation of the uncertainties (dotted blue lines). The cross sections, which are excluded at 95% C.L., are given as numerical values and as color-coded bins in the gluino and neutralino mass.

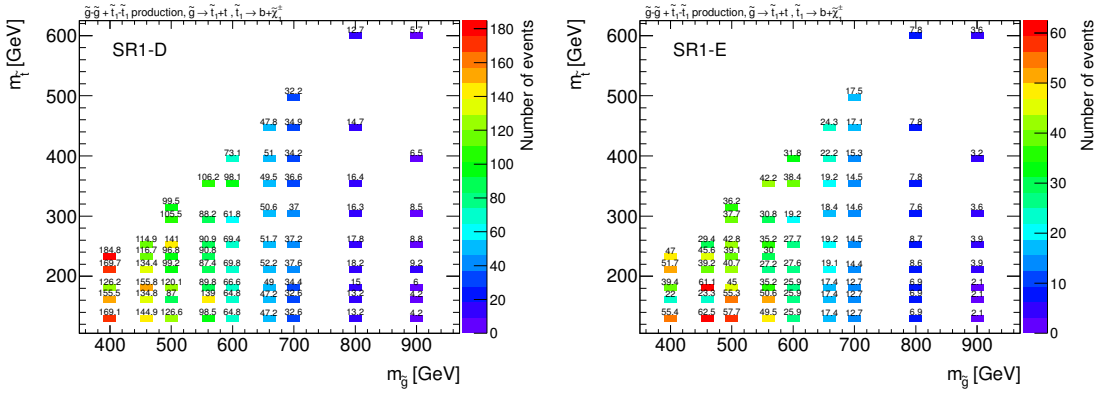

Figure 5.40.: Expected number of signal events in the $(m_{\tilde{g}},m_{\tilde{t}_1})$-plane of the gluino-stop model for an integrated luminosity of $2.05\,\mathrm{fb}^{-1}$ and for SR1-D (left) and SR1-E (right).

Gluino Stop Model

The number of expected signal events in the gluino-stop model are shown in Fig. 5.40 for SR1-D (left) and SR1-E (right). The fraction of signal events in the control region CR1 (signal contamination) are shown in Fig. 5.41. Since a non-negligible amount of signal events in the control region would lead to a bias in the background estimation, possible signal contamination is taken into account in the estimation for the non-QCD background. The number of expected SUSY signal events in the control region is subtracted from the number of observed events in the control region[6] (see Eq. 5.9).

The expected and observed exclusion limits in the $(m_{\tilde{g}},m_{\tilde{t}_1})$-plane of the gluino-stop model are shown in Fig. 5.42 as dashed blue and solid red line, respectively. For reference, the limit obtained with the previous analysis [114], based on an integrated luminosity of $35\,\mathrm{pb}^{-1}$, is

[6]For the low mass region the possible signal contamination becomes unreasonably large, so that conservatively the SM background was set to be half the MC based background estimation.

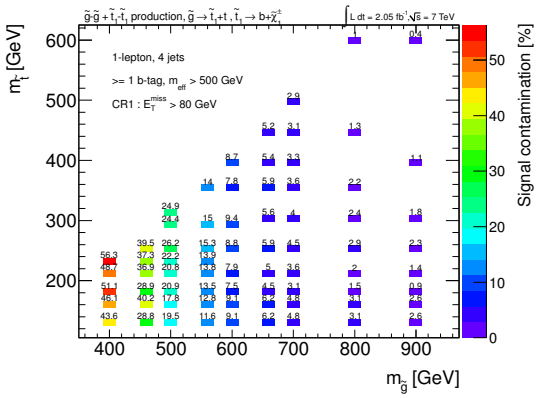

Figure 5.41.: Signal contamination (in percentage) in the control region CR1 in the ($m_{\tilde{g}}$,$m_{\tilde{t}_1}$)-plane of the gluino-stop model.

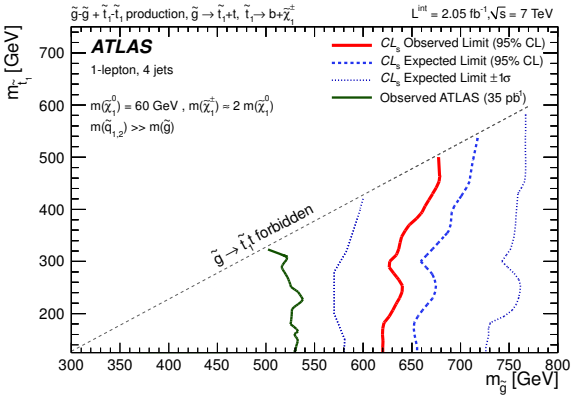

Figure 5.42.: Exclusion limit in the ($m_{\tilde{g}}$,$m_{\tilde{t}_1}$)-plane of the gluino-stop model. The observed limit is represented by the solid red line. The expected limit (dashed blue line) is shown with the $\pm 1\sigma$ variation of the uncertainties (dotted blue lines). For reference, the limit obtained with the previous analysis [114], based on an integrated luminosity of $35\,\mathrm{pb}^{-1}$, is included (solid dark line).

also included (solid dark line). The limit is obtained by taking into account for each point in the ($m_{\tilde{g}}$,$m_{\tilde{t}_1}$)-plane either SR1-D or SR1-E, depending on which signal region yields the best expected limit. Gluino masses below 620 GeV are excluded at 95% C.L. for stop masses below 440 GeV. This analysis significantly improves the limit obtained with the previous analysis.

5.5. Conclusions on Gluino Mediated Search

The presented measurements, based on an integrated luminosity of $2.05\,\text{fb}^{-1}$, are consistent within their uncertainties with the SM expectations. Besides a model independent limit on the number of events from physics beyond the SM and the effective cross sections, several model interpretations are given.

In models based on SO(10), gluinos with masses below 650 GeV and 610 GeV are excluded at 95% C.L. for DR3 and HS models, respectively. If the $\tilde{t}_1$ is produced via gluino decay, gluino masses are excluded at 95% C.L. in the range of 620-750 GeV depending on the specific model considered. If the gluino decay is $\tilde{g} \to bt\tilde{\chi}_1^0$ (100%) via off-shell stop or sbottom, gluino masses are excluded up to 720 GeV for a neutralino mass of 100 GeV.

The interpretations are summarized in Table 5.10. The table includes the model independent limit, given in terms of the visible cross section σ_{vis}, defined as the cross section multiplied by the detector acceptance and the efficiency of the analysis.

	Excluded Range at 95% C.L.	
model independent	$\sigma_{\text{vis}} > 8.5\,\text{fb}$	
SO(10) DR3 model	$m_{\tilde{g}} < 650\,\text{GeV}$	
SO(10) HS model	$m_{\tilde{g}} < 610\,\text{GeV}$	
Gt simplified model	$400\,\text{GeV} < m_{\tilde{g}} < 750\,\text{GeV}$ $m_{\tilde{\chi}_1^0} < 160\,\text{GeV}$	$m_{\tilde{\chi}_1^0} = 50\,\text{GeV}$ $m_{\tilde{g}} = 700\,\text{GeV}$
Gtb simplified model	$320\,\text{GeV} < m_{\tilde{g}} < 720\,\text{GeV}$ $m_{\tilde{\chi}_1^0} < 200\,\text{GeV}$	$m_{\tilde{\chi}_1^0} = 100\,\text{GeV}$ $m_{\tilde{g}} = 600\,\text{GeV}$
gluino-stop model	$m_{\tilde{g}} < 620\,\text{GeV}$	$m_{\tilde{t}_1} < 440\,\text{GeV}$

Table 5.10.: Summary of the observed limits at 95% C.L. obtained with the 1-lepton analysis. The model independent limit is given in terms of the visible cross section σ_{vis}, defined as the cross section multiplied by the detector acceptance and the efficiency of the analysis. The limits in the two considered SO(10) models are given in terms of the gluino mass. The limits for the simplified models are given for different assumptions of neutralino and gluino masses. For the gluino-stop model the combined limit is given for the gluino and stop mass.

The presented analysis significantly improves the previously published limits on the same subject by the ATLAS and CMS collaborations.

6 Direct Stop Production

This chapter presents the search for direct stop pair production performed with the ATLAS detector, considering events containing at least two b-quark jets, at least two light jets, missing transverse energy and exactly one electron or muon. The complementary and mutually exclusive stop search with exactly two leptons has also been performed by the ATLAS Collaboration [115, 116]. The results of the two analyses are combined and interpreted in common SUSY model scenarios.

The focus lies on the scenario, in which the mass of the stop is below or around the mass of the top quark ($m_{\tilde{t}_1} \leq m_t$ and $m_{\tilde{\chi}_1^\pm} < m_{\tilde{t}_1} - m_b$). The stop-chargino mass difference is assumed to be such, that sufficiently energetic b-jets from the decay $\tilde{t}_1 \to \tilde{\chi}_1^\pm b$ can be produced in the final state. To ensure a broad coverage of the SUSY parameter space, additional searches, targeting scenarios with different stop mass regions or low stop-chargino mass differences, are performed by the ATLAS Collaboration [63–66].

Under the assumption of direct stop pair production and subsequent decay of the stop via $\tilde{t}_1 \to \tilde{\chi}_1^\pm b$ and $\tilde{\chi}_1^\pm \to W^\pm \tilde{\chi}_1^0$, the event contains two b-jets, two W bosons and two neutralinos $\tilde{\chi}_1^0$. The neutralino is assumed to be the LSP, therefore a large amount of missing transverse momentum is expected in the event. This process is schematically shown in Fig. 6.1 (left), together with the top pair production for comparison (right). The decay of the W bosons can proceed hadronically or leptonically, leading to up to two additional leptons in the event.

The search is challenging because the signature of the signal resembles the signature of the top pair production. The strategy of the analysis is to exploit the fact, that the particles in the final state are in general softer compared to the top pair production, due to the relatively low stop mass and additional LSPs in the final state. The events are reconstructed under the assumption, that a top pair has been produced, so that top and W candidates can be constructed from the final state particles. These candidates are used to construct the main discriminating variable $\sqrt{s}_{\text{min}}^{(\text{sub})}$, introduced in Section 3.2.2.

This chapter is organized as follows. In the first section the selection criteria of the search

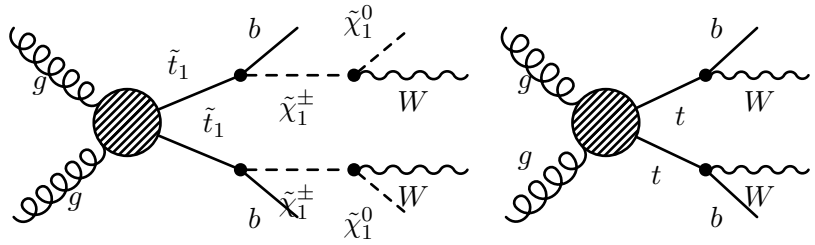

Figure 6.1.: Schematic view of the direct stop pair production with subsequent decay of the stop via $\tilde{t}_1 \to \tilde{\chi}_1^\pm b$ and $\tilde{\chi}_1^\pm \to W^\pm \tilde{\chi}_1^0$ (left). The top pair production is shown for comparison (right).

are presented. The main background processes and the means to estimate them are presented in Section 6.2. After the discussion of the systematic uncertainties in Section 6.3, the results and their interpretation are presented in Section 6.4. This chapter is concluded by summarizing remarks in Section 6.5.

6.1. Event Selection

6.1.1. Data-Taking Period and Trigger Selection

For the direct stop search presented, data corresponding to a total integrated luminosity of $4.7\,\mathrm{fb}^{-1}$, recorded in 2011, has been analyzed. Data recorded in 2010 ($35\,\mathrm{pb}^{-1}$) is not included due to different data-taking conditions. As it is the case for the gluino mediated search channel, single lepton triggers are used with the lowest p_T thresholds available depending on the data-taking conditions. Monte Carlo simulated events are re-weighted to match the trigger efficiency in data.

6.1.2. Baseline Selection

A set of quality criteria is imposed: Events are required to have at least five tracks associated to the primary vertex. No cosmic muon candidates are allowed. Reconstructed jets and muons are required to pass respective quality requirements (introduced in Section 4.3.2 for jets and Section 4.3.1 for leptons). If jets or muons that fail these criteria are found in the event, the event is rejected. The possible double-counting of reconstructed objects is resolved by using the procedure described in Section 5.1.2.

Events are required to contain exactly one electron or muon. The p_T thresholds are $p_\mathrm{T} > 25\,\mathrm{GeV}$ for electrons and $p_\mathrm{T} > 20\,\mathrm{GeV}$ for muons[1]. Furthermore at least four jets ($p_\mathrm{T} > 20$ GeV, $|\eta| < 2.5$) and $E_\mathrm{T}^\mathrm{miss} > 40\,\mathrm{GeV}$ are required. The low thresholds are chosen to ensure sensitivity of the analysis to the assumed stop mass around or below the top mass and a potentially small stop-chargino mass difference, resulting in relatively soft jets.

At least two jets in the event are required to be b-tagged, and at least two jets are required to be not b-tagged. The combined b-tagging algorithm (see Section 4.3.4) is used with a tagging efficiency of 60% and rejection factors of 380, 8 and 28 for light quarks, c-quarks and hadronically decaying taus, respectively. Both efficiency and rejection factors are obtained from simulated top events. The effect of the b-tagging scale factors is illustrated in Fig. 6.2: The number of b-tagged jets is shown without any b-tagging requirement (top) and after requiring at least one b-tag (bottom). Only after the b-tag requirement, the b-tagging scale factors are applied. There is an upward systematic shift introduced in the ratio "data / exp", also visible in further kinematic distributions, which are shown in Fig. 6.3 for the electron channel and Fig. 6.4 for the muon channel. Since the final normalization of the background processes is derived from control regions in data, this systematic shift is absorbed and corrected.

[1] Events with an additional signal electron (muon) with $p_\mathrm{T} > 20(10)$ GeV are rejected, to ensure that there is no overlap with the corresponding 2-lepton search channel.

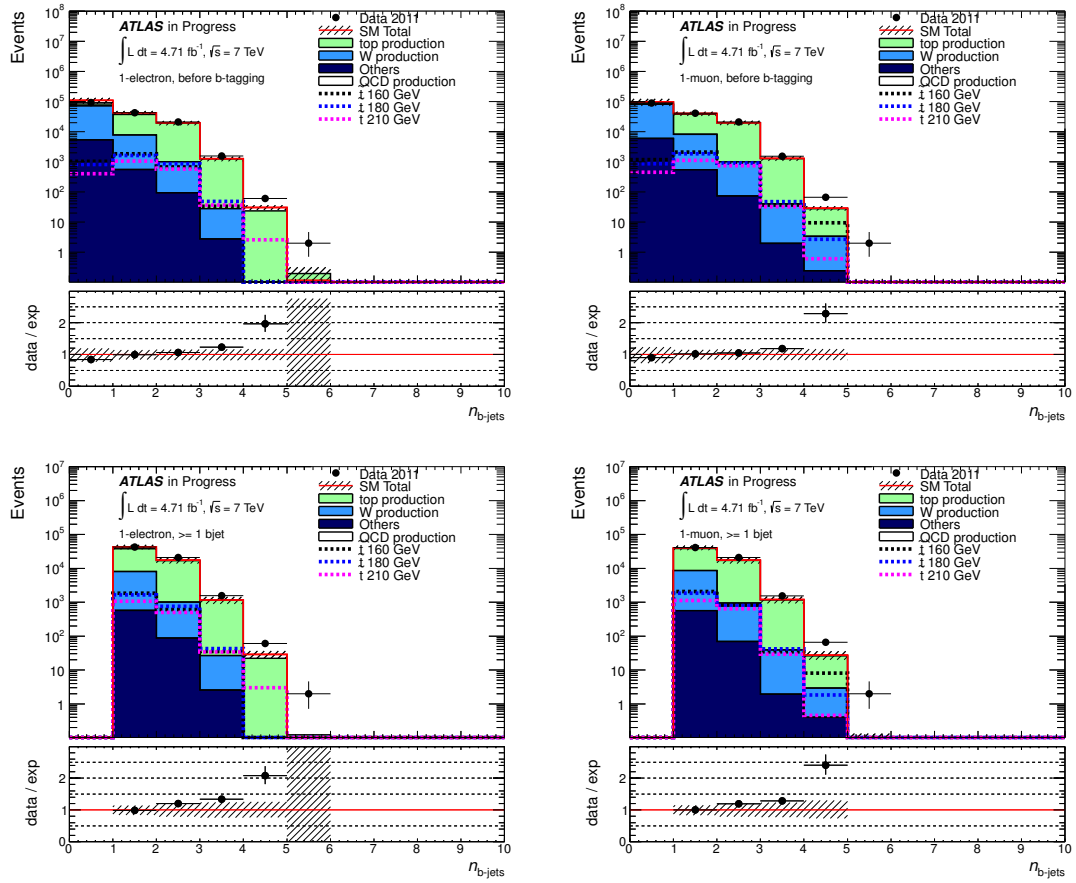

Figure 6.2.: Distributions of the number of b-tagged jets ($n_{b-\text{jets}}$) for the 1-electron (left) and the 1-muon channel (right) after the $E_{\text{T}}^{\text{miss}}$ selection and before (top) and after requiring at least one b-tagged jet (bottom). The top row plots do not include the b-tagging scale factors. For reference, the distributions of three different SUSY signals with stop masses of 160, 180 and 210 GeV, respectively, are superimposed (dashed lines). The hatched bands represent the systematic uncertainties (see Section 6.3).

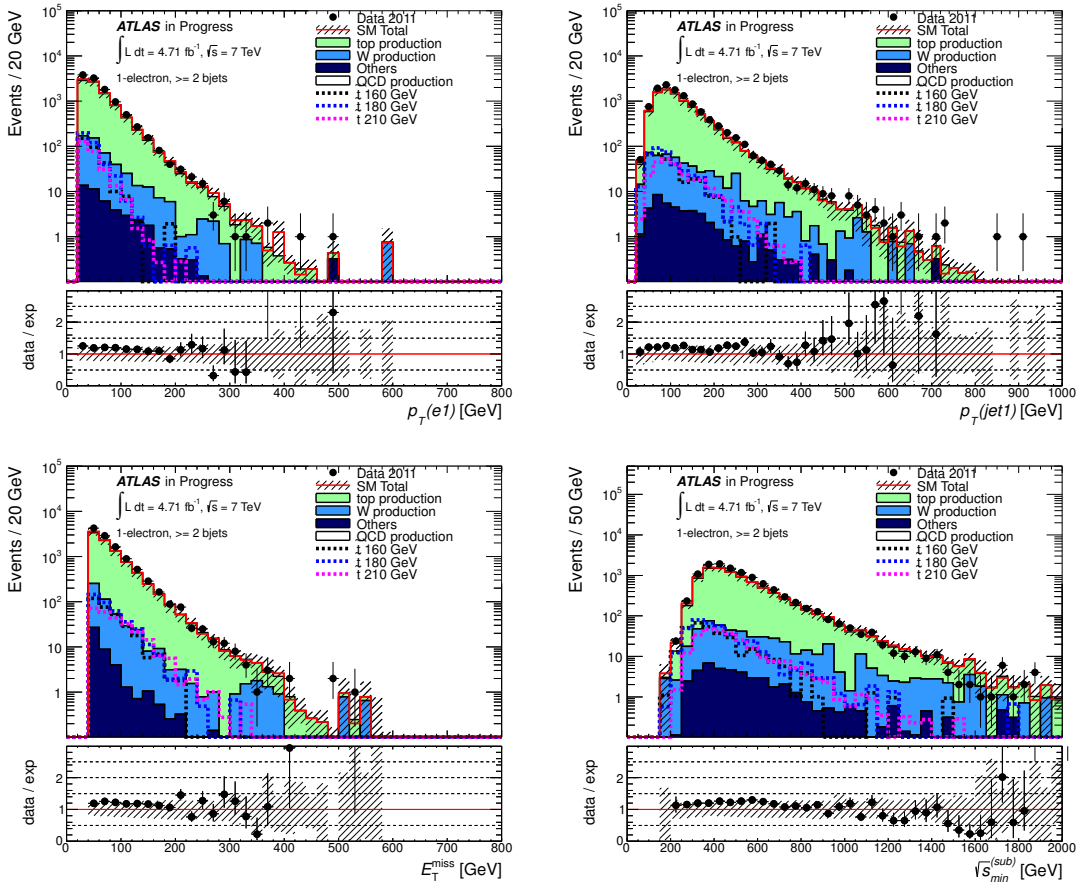

Figure 6.3.: Distributions of the p_{T} of the leading lepton (top left) and the leading jet (top right), the missing transverse momentum $E_{\mathrm{T}}^{\mathrm{miss}}$ (bottom left) and $\sqrt{s}_{\mathrm{min}}^{(\mathrm{sub})}$ (bottom right) in the 1-electron channel after the b-tagging requirement. For reference, the distributions of three different SUSY signals with stop masses of 160, 180 and 210 GeV, respectively, are superimposed (dashed lines). The hatched bands represent the systematic uncertainties (see Section 6.3).

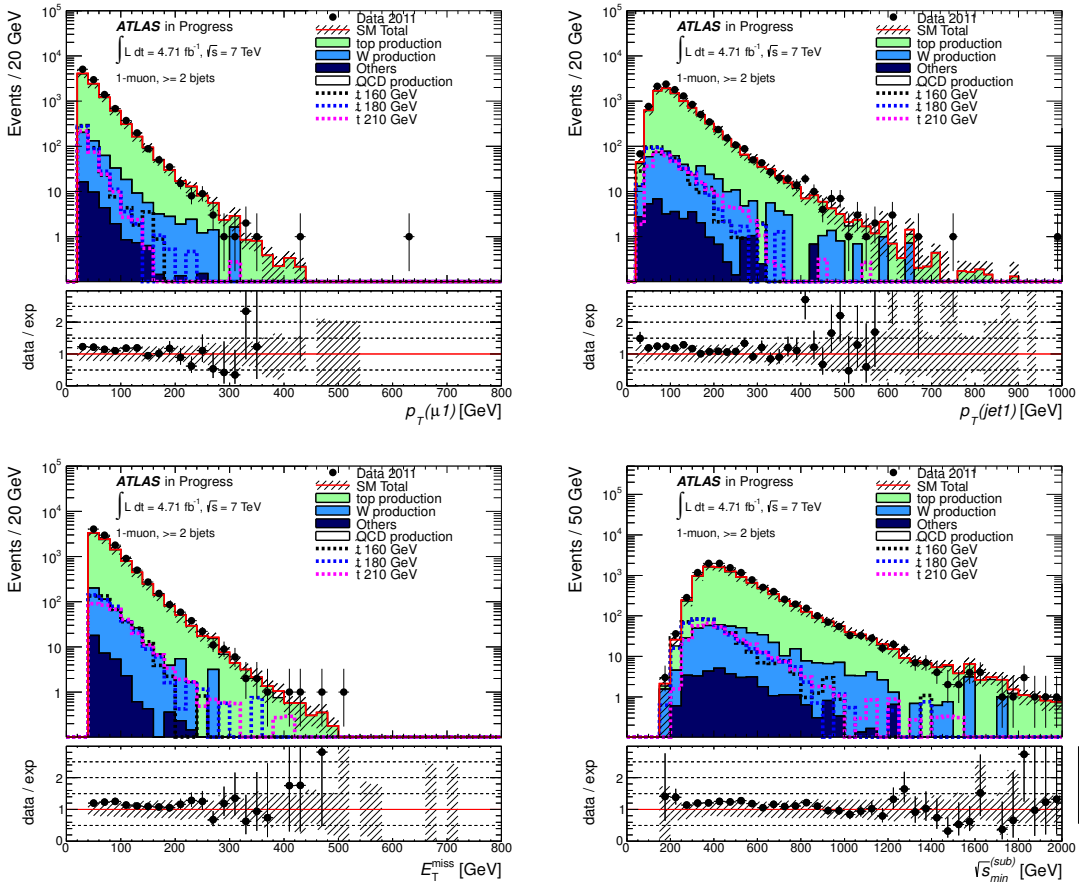

Figure 6.4.: Distributions of the p_{T} of the leading lepton (top left) and the leading jet (top right), the missing transverse momentum $E_{\mathrm{T}}^{\mathrm{miss}}$ (bottom left) and $\sqrt{s}_{\mathrm{min}}^{(\mathrm{sub})}$ (bottom right) in the 1-muon channel after the b-tagging requirement. For reference, the distributions of three different SUSY signals with stop masses of 160, 180 and 210 GeV, respectively, are superimposed (dashed lines). The hatched bands represent the systematic uncertainties (see Section 6.3).

Selection Step	Criteria
pre-selection	at least five tracks associated to the primary vertex cosmic muon veto jet and muon quality criteria
leptons	exactly one electron or muon $p_{\mathrm{T}} > 25\,\mathrm{GeV}$ and $\lvert\eta\rvert < 2.47$ for electrons $p_{\mathrm{T}} > 20\,\mathrm{GeV}$ and $\lvert\eta\rvert < 2.4$ for muons veto on additional leptons
jets	at least four jets $p_{\mathrm{T}} > 20$ GeV, $\lvert\eta\rvert < 2.5$
$E_{\mathrm{T}}^{\mathrm{miss}}$	$E_{\mathrm{T}}^{\mathrm{miss}} > 40\,\mathrm{GeV}$
b-tagging	at least two b-tagged jets at least two non b-tagged jets
QCD multijet reduction	transverse mass between lepton and $E_{\mathrm{T}}^{\mathrm{miss}}$: $m_{\mathrm{T}} > 30\,\mathrm{GeV}$

Table 6.1.: Summary of consecutive selection criteria comprising the "baseline" selection used in the direct stop search.

To reduce the abundance of events from QCD multijet production in the signal region the transverse mass m_{T} between the lepton and the missing transverse momentum is required to exceed 30 GeV. The baseline selection criteria are summarized in Table 6.1.

6.1.3. Explicit Reconstruction of the Top Pair Event Topology

The main discriminating variable in this analysis is the inclusive quantity $\sqrt{s}_{\mathrm{min}}^{(\mathrm{sub})}$. The construction of the variable (described in Section 3.2.2) in the analysis relies on the definition of the relevant subsystem and takes into account the top pair production as the main background. Using the hypothesis of a $t\bar{t}$ event, in which one W boson decays leptonically and the other one decays hadronically, top, W and neutrino candidates can be constructed for every event after the baseline selection.

Since the $E_{\mathrm{T}}^{\mathrm{miss}}$ is assumed to stem exclusively from the neutrino in the decay $W \to \ell\nu$, the transverse components of the neutrino candidates are uniquely defined, but two solutions are possible for the longitudinal component. The mass of a W candidate m_W^{lep} is constructed, by using the invariant mass of the lepton-neutrino system and the nominal W mass. For all combinations of two light jets in the event their invariant mass is computed and labeled m_W^{had}. All possible combinations of two light jets and one b-jet are used to calculate a top candidate mass m_t^{had} and all combinations of neutrino candidates, the lepton and one b-jet are used to calculate a second top candidate mass m_t^{lep}.

To find the combination of objects that best fits the $t\bar{t}$ hypothesis the probability

$$P_{\mathrm{tot}} = P(m_W^{\mathrm{lep}})P(m_t^{\mathrm{lep}})P(m_W^{\mathrm{had}})P(m_t^{\mathrm{had}}) \tag{6.1}$$

is calculated for each combination and the one with the highest value of P_{tot} is selected. The

	MC		data	
Channel	$\hat{\mu}$ [GeV]	$\hat{\sigma}$ [GeV]	$\hat{\mu}$ [GeV]	$\hat{\sigma}$ [GeV]
1-electron	168.4 ± 0.1	18.0 ± 0.2	168.6 ± 0.4	17.9 ± 0.8
1-muon	168.2 ± 0.1	18.6 ± 0.2	168.5 ± 0.5	18.9 ± 0.8

Table 6.2.: Results of the Gaussian fit to the peak of the m_t^{had} distribution after the reconstruction of the event (see text). The mean value $\hat{\mu}$ and the Gaussian width $\hat{\sigma}$ are listed for data and MC, separately for the 1-muon and 1-electron channel.

individual probabilities are constructed by

$$P(X) = 1 - \text{Erf}\left(\frac{|X - X_{\text{true}}|}{\sqrt{2}\Gamma_{\text{true}}}\right), \tag{6.2}$$

where Gaussian distributions are assumed with the true values X_{true} and Γ_{true} taken from Monte Carlo simulated events. Figure 6.5 shows the reconstructed W and top candidate mass distributions after the b-tagging selection step, separately for the electron (left) and muon (right) channels. The top candidate mass distributions show clear peaks around the nominal top mass coming from top pair production events, whereas the remaining background components exhibit broad distributions. Therefore, the reconstruction of the event is introducing no sizable bias for non-$t\bar{t}$ events. The distributions of three SUSY signals with stop masses of 160, 180 and 210 GeV, respectively, are superimposed for comparison. The signal distributions of the mass of the hadronic top candidate tend to be softer compared to the background.

As a result of this procedure, the relevant subsystem is uniquely defined and all quantities used in the definition of $\sqrt{s}_{\text{min}}^{(\text{sub})}$ (see Eq. 3.17) can be computed.

Besides $\sqrt{s}_{\text{min}}^{(\text{sub})}$, the distribution of the top candidate mass m_t^{had} is also used in the definition of the signal and control regions. Therefore, the peak position and width of the distribution is determined. At first, a Gaussian fit is performed to the distribution of m_t^{had} in the range 100 to 300 GeV, obtaining a value for the mean μ_{raw} and the width σ_{raw}. The Gaussian fit is then repeated in the range $[\mu_{\text{raw}} - \sigma_{\text{raw}}, \mu_{\text{raw}} + \sigma_{\text{raw}}]$, to obtain new values $\hat{\mu}$ and $\hat{\sigma}$. Table 6.2 shows the results of the fit in data and Monte Carlo, respectively.

After the baseline selection $m_t^{\text{had}} < \hat{\mu} - \hat{\sigma}$ is required. This selection criterion is motivated by the expected soft nature of the jets as compared to a $t\bar{t}$ event. A top control region CR_1^{top} is defined by $\hat{\mu} - 0.5\hat{\sigma} < m_t^{\text{had}} < \hat{\mu} + 0.5\hat{\sigma}$, which is dominated by top production. The background determination is described in detail in Section 6.2.

6.1.4. Optimization

For the SUSY signal under consideration the $\sqrt{s}_{\text{min}}^{(\text{sub})}$ distribution is expected to be softer than the one for $t\bar{t}$, due to the missing transverse momentum of the LSPs. In Figure 6.6 the distribution of $\sqrt{s}_{\text{min}}^{(\text{sub})}$ is shown in the 1-muon channel to illustrate the separation power. Only the top pair pair production background is shown, together with three SUSY signals with stop masses lower than or close to the top mass (130, 160 and 180 GeV).

An optimization is performed on the cut value for the $\sqrt{s}_{\text{min}}^{(\text{sub})}$ variable, using Monte Carlo simulated events for signal and background processes, where QCD multijet production is ne-

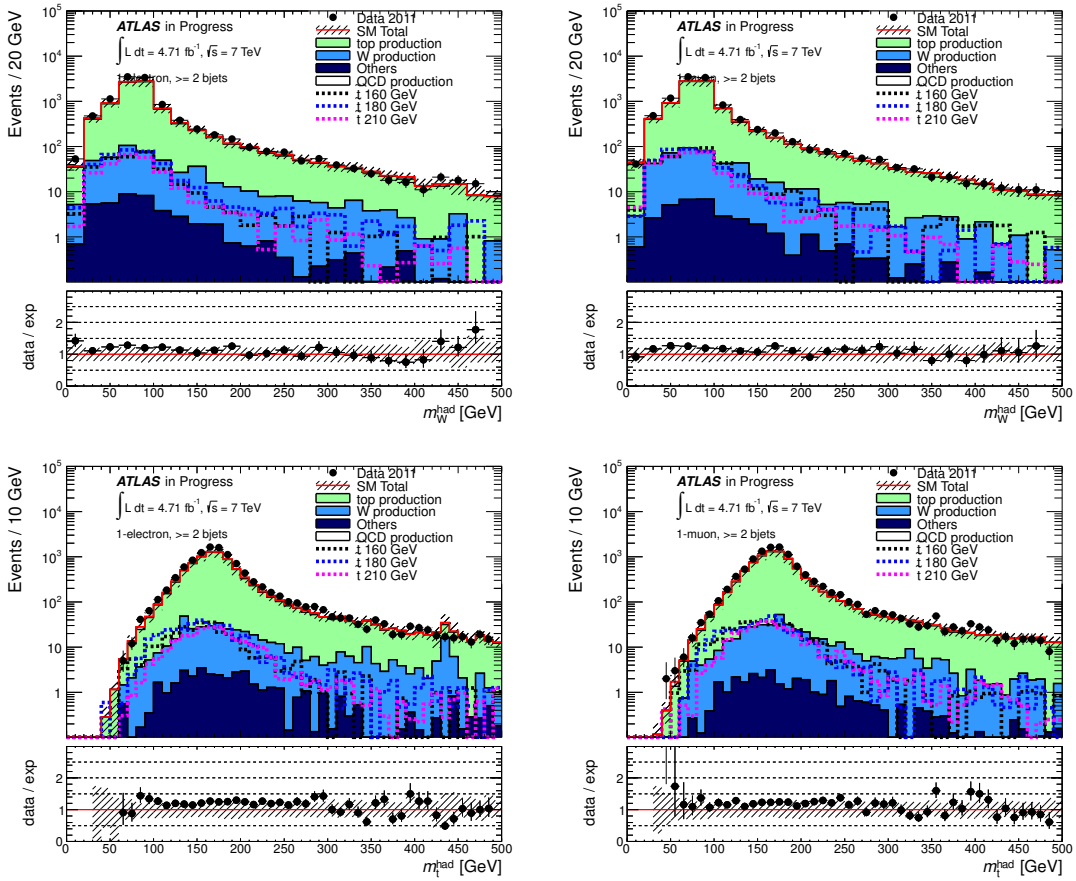

Figure 6.5.: Distributions of the W candidate mass m_W^{had} (top row) and the top candidate mass m_t^{had} (bottom row), obtained from the explicit reconstruction of the event under the assumption of $t\bar{t}$ production, where one top decays via $t \to Wb \to \ell\nu b$ and the other one via $t \to Wb \to qqb$. The particles used to construct the masses shown are matched to the decay products of the hadronic top decay. The distributions are obtained after the b-tagging and $E_{\text{T}}^{\text{miss}}$ requirements, separately for the 1-electron (left) and 1-muon (right) channel. For reference, the distributions of three different SUSY signals with stop masses of 160, 180 and 210 GeV, respectively, are superimposed (dashed lines). The hatched bands represent the systematic uncertainties (see Section 6.3).

glected. Table 6.3 summarizes the Monte Carlo estimates for the numbers of events from background processes for three different selection criteria: $\sqrt{s}_{\text{min}}^{(\text{sub})}$ <250 GeV, $\sqrt{s}_{\text{min}}^{(\text{sub})}$ <235 GeV and $\sqrt{s}_{\text{min}}^{(\text{sub})}$ <225 GeV. In Figures 6.7-6.9, the expected numbers of events in the signal region, the efficiency of the selection criteria and the significance are shown in the $(m_{\tilde{t}},m_{\tilde{\chi}_1^0})$-plane, assuming the gluino-stop signal model. The significance is approximated by

$$S/\sqrt{B + (B\delta B)^2}, \tag{6.3}$$

with the number of signal events S, background events B and the relative systematic uncertainty δB. For the three selections, the assumptions on the background uncertainties are:

- $\sqrt{s}_{\text{min}}^{(\text{sub})}$ <250 GeV: δB=30% uncertainty on the background;

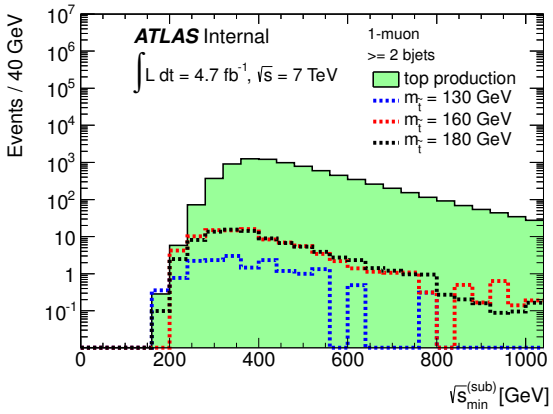

Figure 6.6.: Distribution of $\sqrt{s}_{\mathrm{min}}^{(\mathrm{sub})}$ in the 1-muon channel for the production of a top pair (solid, filled line) and three different SUSY signals with stop masses of 130, 160 and 180 GeV, respectively (dashed lines). The distributions are based on Monte Carlo simulated events, scaled to an integrated luminosity of $4.7\,\mathrm{fb}^{-1}$.

Process	$\sqrt{s}_{\mathrm{min}}^{(\mathrm{sub})}$ <250 GeV	$\sqrt{s}_{\mathrm{min}}^{(\mathrm{sub})}$ <235 GeV	$\sqrt{s}_{\mathrm{min}}^{(\mathrm{sub})}$ <225 GeV
$t\bar{t}$	17.9±1.0	5.0±0.5	1.5±0.3
W+HF	9.4±3.0	6.9±2.7	6.1±2.6
single top	2.4±0.6	0.7±0.3	0.3±0.2
Z+HF	0.3±0.2	0.1±0.1	0
diboson	0.3±0.1	0.1±0.1	0.1±0.1
total (non-QCD)	30.3±3.3	12.8±2.8	7.9±2.6

Table 6.3.: Estimated numbers of events from background processes for three different selection criteria using $\sqrt{s}_{\mathrm{min}}^{(\mathrm{sub})}$. The background estimation is based on Monte Carlo simulations and normalized to $4.7\,\mathrm{fb}^{-1}$. Events from QCD multijet production are neglected. The given uncertainties include the statistical components only.

- $\sqrt{s}_{\mathrm{min}}^{(\mathrm{sub})}$ <235 GeV: δB=35%;
- $\sqrt{s}_{\mathrm{min}}^{(\mathrm{sub})}$ <225 GeV: δB=40%.

The selection with $\sqrt{s}_{\mathrm{min}}^{(\mathrm{sub})} < 250\,\mathrm{GeV}$ is found to yield the best sensitivity and chosen to complete the signal region selection criteria, summarized in Table 6.4.

selection step	criteria
baseline selection	see Table 6.1
signal region (SR)	$m_t^{\text{had}} < \hat{\mu} - \hat{\sigma}$ $\sqrt{s}_{\text{min}}^{(\text{sub})} < 250\,\text{GeV}$

Table 6.4.: Summary of consecutive selection criteria comprising the final signal region selection used in the direct stop search.

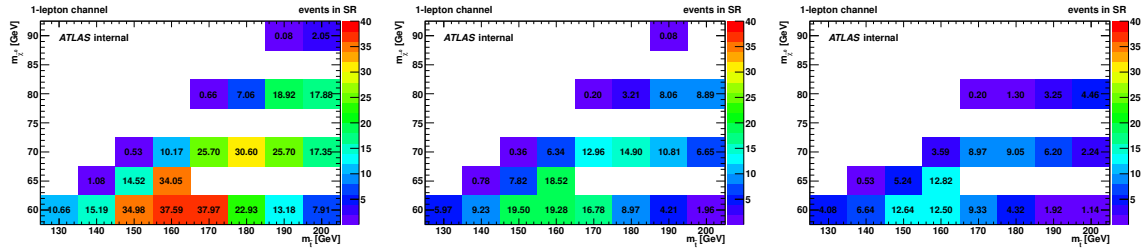

Figure 6.7.: Numbers of expected signal events in the ($m_{\tilde{t}}$,$m_{\tilde{\chi}_1^0}$)-plane for different selection criteria: $\sqrt{s}_{\text{min}}^{(\text{sub})}$ <250 GeV (left), $\sqrt{s}_{\text{min}}^{(\text{sub})}$ <235 GeV (middle) and $\sqrt{s}_{\text{min}}^{(\text{sub})}$ <225 GeV (right). The numbers of events are scaled to an integrated luminosity of 4.7 fb^{-1}.

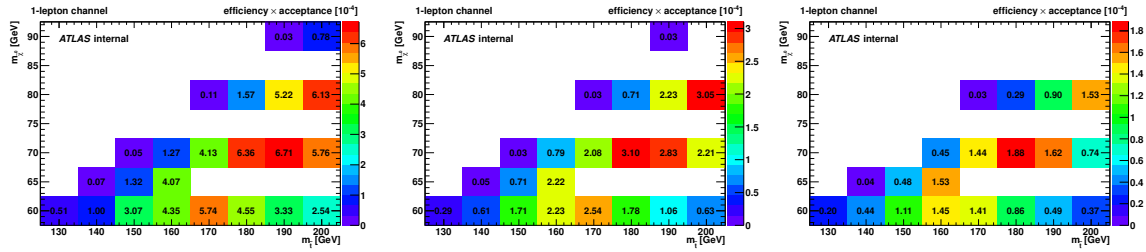

Figure 6.8.: Signal efficiency times acceptance in the ($m_{\tilde{t}}$,$m_{\tilde{\chi}_1^0}$)-plane for different selection criteria: $\sqrt{s}_{\text{min}}^{(\text{sub})}$ <250 GeV (left), $\sqrt{s}_{\text{min}}^{(\text{sub})}$ <235 GeV (middle) and $\sqrt{s}_{\text{min}}^{(\text{sub})}$ <225 GeV (right). The numbers are scaled to an integrated luminosity of 4.7 fb^{-1}.

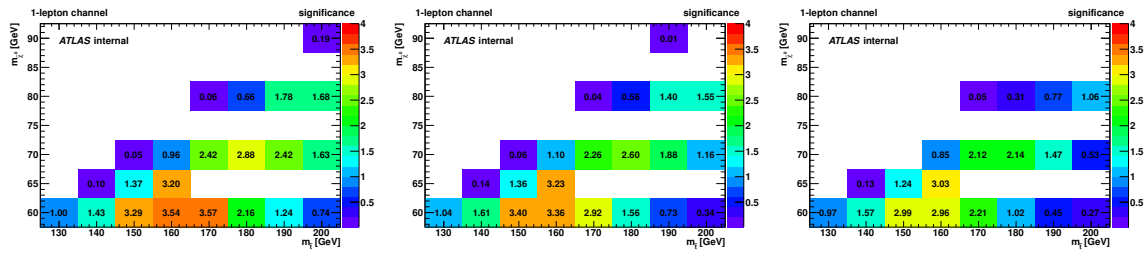

Figure 6.9.: Expected significance in the ($m_{\tilde{t}}$,$m_{\tilde{\chi}_1^0}$)-plane for three different selection criteria: $\sqrt{s}_{\text{min}}^{(\text{sub})}$ <250 GeV (left), $\sqrt{s}_{\text{min}}^{(\text{sub})}$ <235 GeV (middle) and $\sqrt{s}_{\text{min}}^{(\text{sub})}$ <225 GeV (right). The numbers are scaled to an integrated luminosity for 4.7 fb^{-1}.

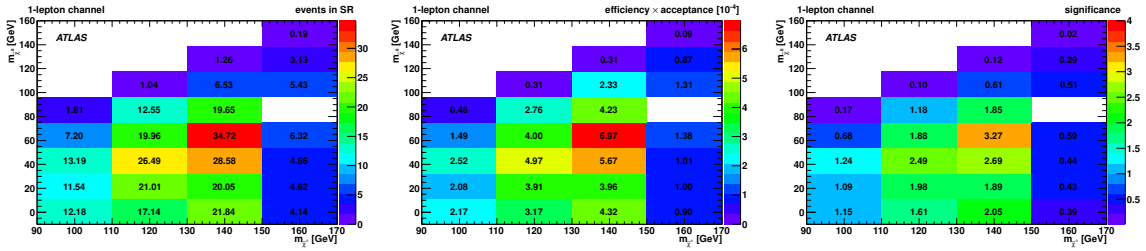

Figure 6.10.: Expected number of signal events in the ($m_{\tilde{\chi}_1^\pm}$,$m_{\tilde{\chi}_1^0}$)-plane (left), signal efficiency times acceptance (middle) and expected significance (right) for a fixed stop mass $m_{\tilde{t}} = 180\,\text{GeV}$. The numbers are scaled to an integrated luminosity of $4.7\,\text{fb}^{-1}$.

The selection criteria for the final signal region are optimized using the gluino-stop model scenario, but yield good results also for the signal scenario with a fixed stop mass of 180 GeV. The expected numbers of signal events (left), the signal efficiency times acceptance (middle) and the expected significance (right) for the chosen signal region are shown in the ($m_{\tilde{\chi}_1^\pm}$,$m_{\tilde{\chi}_1^0}$)-plane in Fig. 6.10.

6.2. Background Estimation

Due to the assumed stop masses close to the top mass there is a similarity of the signal event topology with the SM top pair production. Hence $t\bar{t}$ events are expected to contribute most to background events. Additionally, W+jets events and QCD multijet production are expected to give non-negligible contributions. In the following the estimation of these background components with control samples ($t\bar{t}$, W+jets) and a data-driven method (QCD multijet) are described. Further SM background processes, that are expected to be sub-dominant (single top, Z+jets, diboson production) are estimated from Monte Carlo simulation.

6.2.1. Estimation of W+Jets and Top Pair Production Background

Among the W+jets events, the heavy flavor component $Wb\bar{b}$+jets is expected to dominate, due to the b-jet selection criteria. Therefore, the estimation of this background component is based on a control sample enriched in $Wb\bar{b}$+jets events. For the construction of this control region, the distributions of the top candidate mass m_t^{had} and the invariant mass of the $b\bar{b}$ system m_{bb} are used. As it is shown in Fig. 6.5, the signal-to-background ratio is expected to be highest for $m_t^{\text{had}} < \hat{\mu} - \hat{\sigma}$ and the region around the top mass $\hat{\mu} - \hat{\sigma} < m_t^{\text{had}} < \hat{\mu} + \hat{\sigma}$ is dominated by top pair production. The region with $m_t^{\text{had}} > \hat{\mu} + \hat{\sigma}$ contains a higher fraction of W events. The distributions of m_{bb} are shown in Fig. 6.11 for the baseline selection with the additional criterion of $m_t^{\text{had}} > \hat{\mu} + \hat{\sigma}$ (top) and for the signal region (bottom). Since the $b\bar{b}$ pair is expected to be produced by gluon splitting in a significant fraction of the $Wb\bar{b}$ events, it is expected to have a low angular separation. The $b\bar{b}$ invariant mass is then expected to peak at lower values compared to $t\bar{t}$ events.

For the final definition of the W control region CR_1^W, a more restrictive selection criterion of $m_t^{\text{had}} > 250\,\text{GeV}$ is used to further increase the fraction of W+jets events. The selection criterion for the invariant mass of the $b\bar{b}$ system is chosen to be $m_{bb} < 50\,\text{GeV}$, which yields an increased fraction of W+jets events and a sufficiently high number of events. Figures 6.12 and

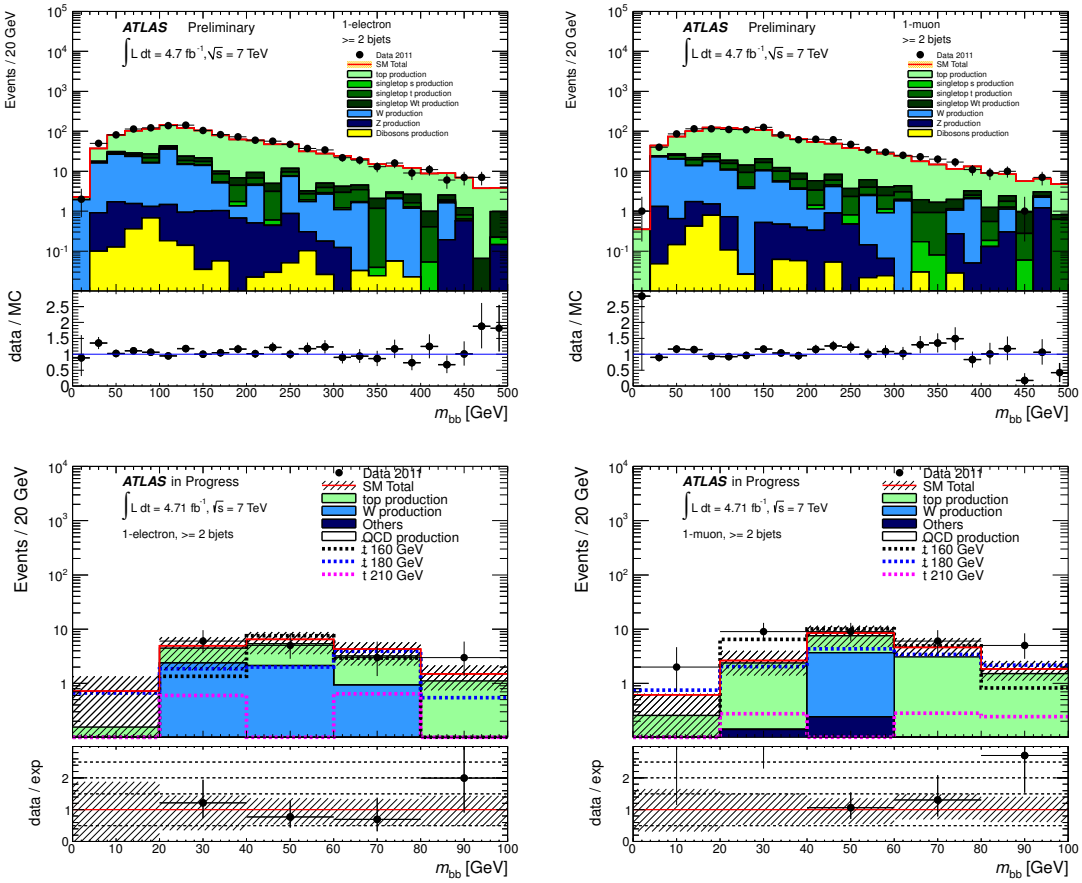

Figure 6.11.: Distributions of the invariant mass m_{bb} of the $b\bar{b}$ system for events with $m_t^{\mathrm{had}} > \hat{\mu}+\hat{\sigma}$ (top) and in the signal region (bottom) for the 1-electron (left) and 1-muon (right) channel. For reference, the distributions of three different SUSY signals with stop masses of 160, 180 and 210 GeV, respectively, are superimposed in the signal region (dashed lines).

6.13 show kinematic distributions in the W control region in the electron and muon channels, respectively.

Although the control region CR_1^W defined in this way is still dominated by $t\bar{t}$ events ($\sim 60\%$) the fraction of W events is significantly increased ($\sim 35\%$). Other SM backgrounds are expected to give a small contribution ($\sim 5\%$). The control regions CR_1^W and the $\mathrm{CR}_1^{\mathrm{top}}$ (defined in Section 6.1.3) are used to simultaneously determine normalization factors for the $t\bar{t}$ and W background components, denoted by w_t and w_W, respectively. Table 6.5 shows the composition of the control regions from Monte Carlo simulated events, the event yield in data and the resulting normalization factors. The listed uncertainties take into account both statistical uncertainties and the systematic uncertainties due to b-tagging, JES and JER. A detailed discussion of the systematic uncertainties is given in Section 6.3.

The consistency of the normalization factor w_t is tested in a dedicated control sample, which is enriched in top pair production events. For the construction of the control sample, the distribution of the reconstructed top mass m_t^{had} is used. To reduce the sensitivity to the JES

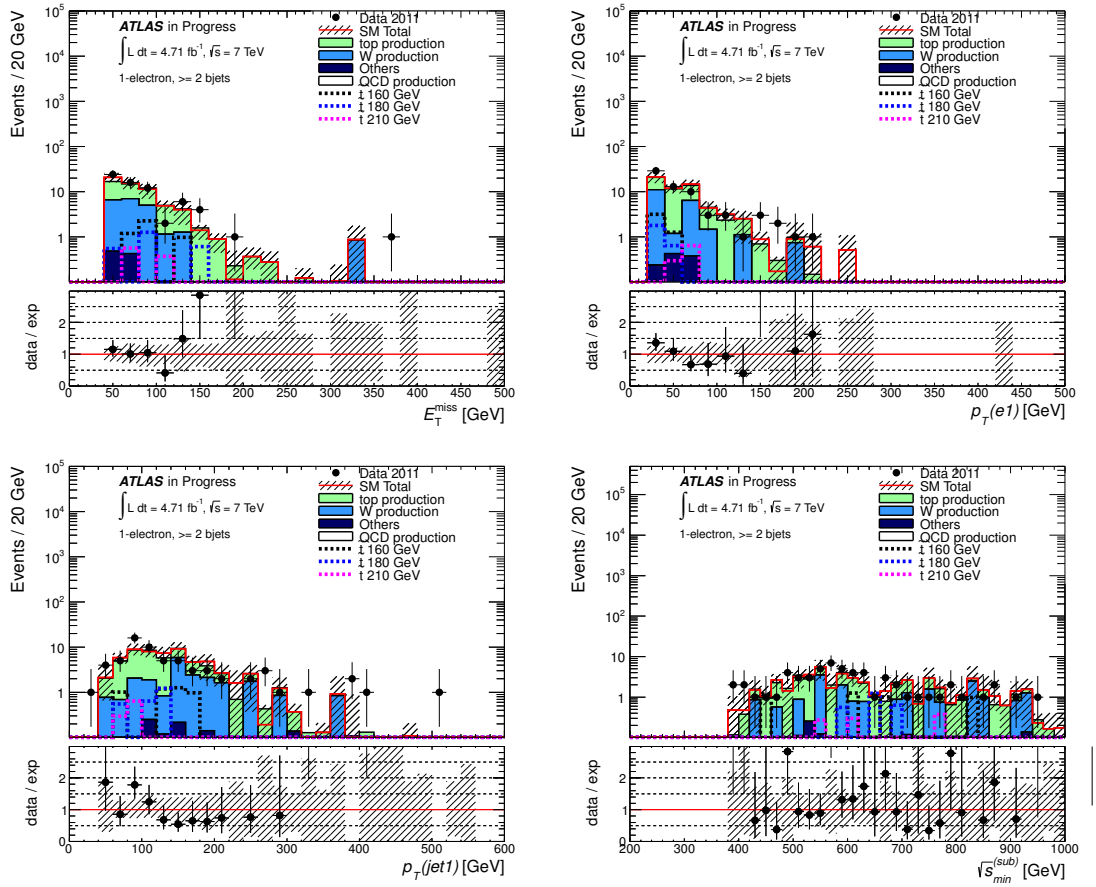

Figure 6.12.: Distributions of $E_{\mathrm{T}}^{\mathrm{miss}}$, leading lepton p_{T}, leading jet p_{T} and $\sqrt{s}_{\mathrm{min}}^{(\mathrm{sub})}$ in the W control region (1-electron channel). For reference, the distributions of three different SUSY signals with stop masses of 160, 180 and 210 GeV, respectively, are superimposed (dashed lines). The hatched bands represent the systematic uncertainties (see Section 6.3).

systematic uncertainty, the control region is defined using the fitted peak position $\hat{\mu}$ and width $\hat{\sigma}$ of the m_t^{had} distribution. The control region $\mathrm{CR}_2^{\mathrm{top}}$ is defined as $\hat{\mu}-0.5\hat{\sigma} < m_t^{\mathrm{had}} < \hat{\mu}+0.5\hat{\sigma}$, and $\sqrt{s}_{\mathrm{min}}^{(\mathrm{sub})} < 320\,\mathrm{GeV}$ to be close to the signal region.[2] The normalization factor ω for $t\bar{t}$ is defined as

$$\omega = \frac{N_{\mathrm{data}} - w_W N_W - a}{w_t N_t}, \tag{6.4}$$

with the following definitions:

N_{data}: number of measured events in $\mathrm{CR}_2^{\mathrm{top}}$,

w_W: normalization factor for W from the control region CR_1^W,

N_W: number of predicted W events in $\mathrm{CR}_2^{\mathrm{top}}$ from Monte Carlo,

N_t: number of predicted $t\bar{t}$ events in $\mathrm{CR}_2^{\mathrm{top}}$ from Monte Carlo,

[2] The selection on $\sqrt{s}_{\mathrm{min}}^{(\mathrm{sub})}$ is looser compared to the signal region to reduce the statistical uncertainties and the fractional signal contamination.

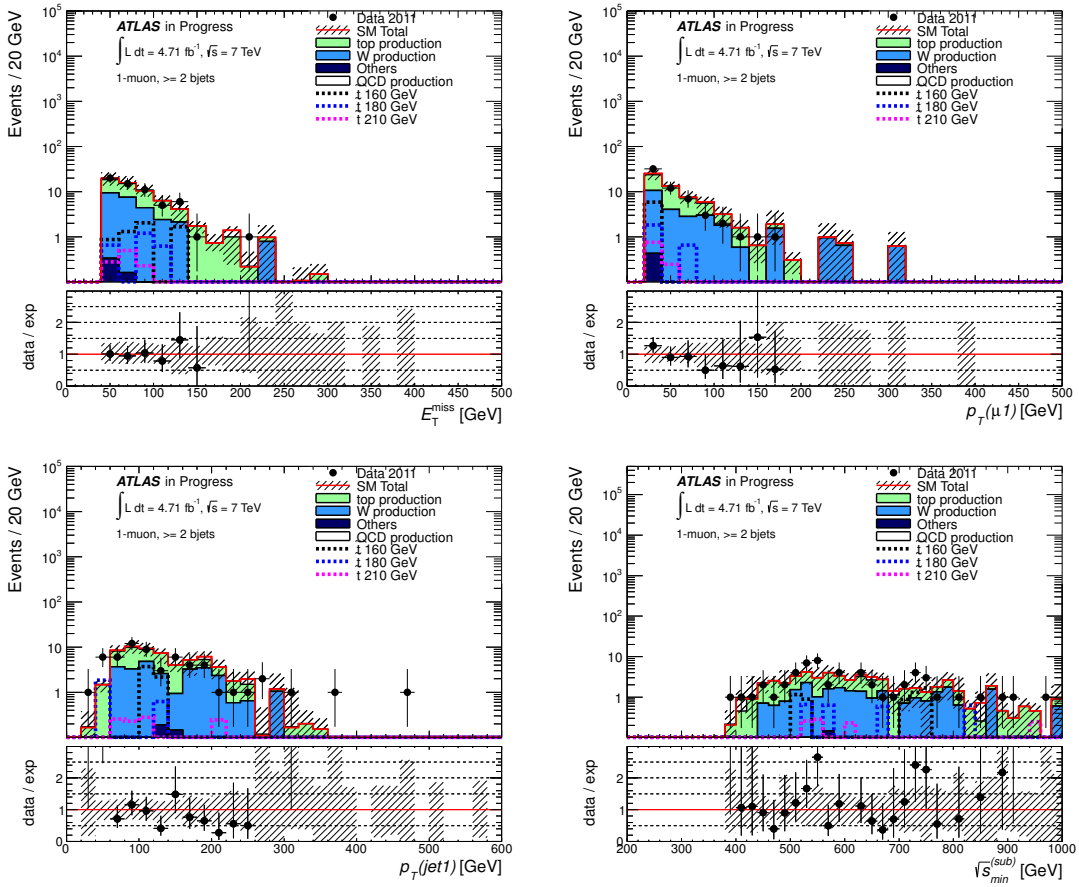

Figure 6.13.: Distributions of $E_{\mathrm{T}}^{\mathrm{miss}}$, leading lepton p_{T}, leading jet p_{T} and $\sqrt{s}_{\mathrm{min}}^{(\mathrm{sub})}$ distributions in the W control region (muon channel). For reference, the distributions of three different SUSY signals with stop masses of 160, 180 and 210 GeV, respectively, are superimposed (dashed lines). The hatched bands represent the systematic uncertainties (see Section 6.3).

a: predicted sum of single top, Z, diboson (all taken from Monte Carlo) and QCD multijet events (data driven) in $\mathrm{CR}_2^{\mathrm{top}}$.

The resulting value of $\omega = 0.95 \pm 0.07$ is consistent with unity within statistical uncertainties, which proves the consistency of the simultaneous normalization of the top pair production and W events in the previous section. Table 6.6 lists the event yields in data and Monte Carlo simulated events.

To ensure the validity of the background estimation, the fraction of events in the control regions from signal processes (signal contamination) is required to be low. In Figure 6.14, the signal contamination defined as $N_{\mathrm{CR}}^{\mathrm{signal}}/N_{\mathrm{CR}}^{\mathrm{totSM}}$ is shown for the control regions used. The maximum observed contamination is around 10%.

Process	1-electron		1-muon		1-lepton	
	CR_1^{top}	CR_1^W	CR_1^{top}	CR_1^W	CR_1^{top}	CR_1^W
$t\bar{t}$	2250	33	2300	30	4550	63
single top	55	2.8	52	3.8	107	6.6
W	52	21	71	26	123	46
Z	2.5	1	3.3	0.5	5.8	1.5
dibosons	1	0.1	1.3	0.3	2.3	0.4
QCD	49	3.5	33	1.1	82	4.6
total	2410 ± 480	61 ± 10	2460 ± 490	61 ± 10	4870 ± 930	122 ± 18
data	3014	66	3038	59	6052	125
$w_W = 0.7 \pm 0.1$, $w_t = 1.25 \pm 0.05$						

Table 6.5.: Event yields from data and MC in the control regions CR_1^{top} and CR_1^W for the 1-electron, 1-muon channel and for the sum of the two (1-lepton). The uncertainties on the total MC prediction include b-tagging, JES and JER uncertainties, and are dominated by b-tagging (about 20%).

Process	1-electron	1-muon	1-lepton
$t\bar{t}$	71	85	156
single top	2.9	3.2	6.1
W	4.1	6.4	10.5
Z	< 0.1	0.1	< 0.2
dibosons	0.05	0.1	0.15
QCD	1.6	1.9	3.5
total	80 ± 9	97 ± 10	177 ± 13
data	75	94	169
$\omega = 0.95 \pm 0.07$			

Table 6.6.: Event yields from data and MC in the CR_2^{top} control regions for the 1-electron, 1-muon channel and for the sum of the two (1-lepton). The W and $t\bar{t}$ predictions are based on Monte Carlo simulation with the factors w_W and w_t taken into account. Assuming that all systematics are fully correlated between CR_1^{top}, CR_1^W and CR_2^{top} (and therefore that any possible systematic shift in the event yield has been absorbed by the w_t and w_W factors), the uncertainties quoted on the total predictions are statistical only.

6.2.2. Estimation of QCD Multijet Background

Events from QCD multijet production can in principle contribute to the 1-lepton selection, if heavy flavor quark jets contain a lepton, through γ conversion or jet misidentification. The estimation of the QCD multijet background processes using Monte Carlo simulated events is not reliable, therefore, the data-driven method described in Section 5.2.3 is applied. The consistency of the method is illustrated in Figure 6.15, which shows the distribution of the transverse mass between the lepton and the missing transverse momentum after requiring one lepton, at least four jets, $E_T^{miss} > 40\,\text{GeV}$ and at least one b-jet. The contribution from QCD multijet production is concentrated at low m_T and is found to be in good agreement with the

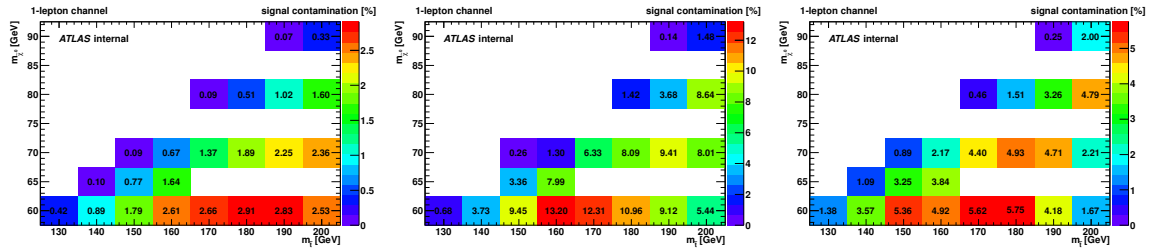

Figure 6.14.: Ratio of the number of expected signal and background events (signal contamination) in the $(m_{\tilde{t}},m_{\tilde{\chi}_1^0})$-plane for the control regions $\mathrm{CR}_1^{\mathrm{top}}$ (left), $\mathrm{CR}_2^{\mathrm{top}}$ (middle) and CR_1^{W} (right), respectively.

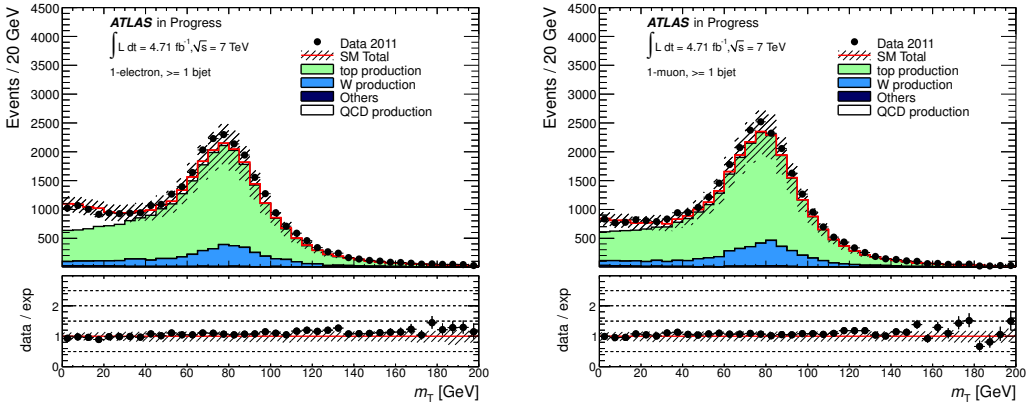

Figure 6.15.: Distributions of the transverse mass m_{T} between the electron (left) and muon (right) and the missing transverse momentum after requiring one lepton, at least four jets, $E_{\mathrm{T}}^{\mathrm{miss}} > 40\,\mathrm{GeV}$ and at least one b-jet. The hatched bands represent the systematic uncertainties (see Section 6.3).

observed distribution in data.

6.3. Systematic Uncertainties

Analogously to the treatment of the systematic uncertainties in Section 5.3 both experimental and theoretical uncertainties are considered. Furthermore the statistical uncertainties of the control regions and the uncertainties due to the limited number of Monte Carlo simulated events are taken into account.

6.3.1. Experimental Uncertainties

Luminosity For the integrated luminosity an uncertainty of ±3.7% is assumed [108].

Pile-Up To assess the systematic uncertainty due to pile-up, an uncertainty on the average number of interactions per bunch crossing μ is used. The comparison of two different implementations of soft QCD multijet production in `PYTHIA` leads to an uncertainty of μ of about

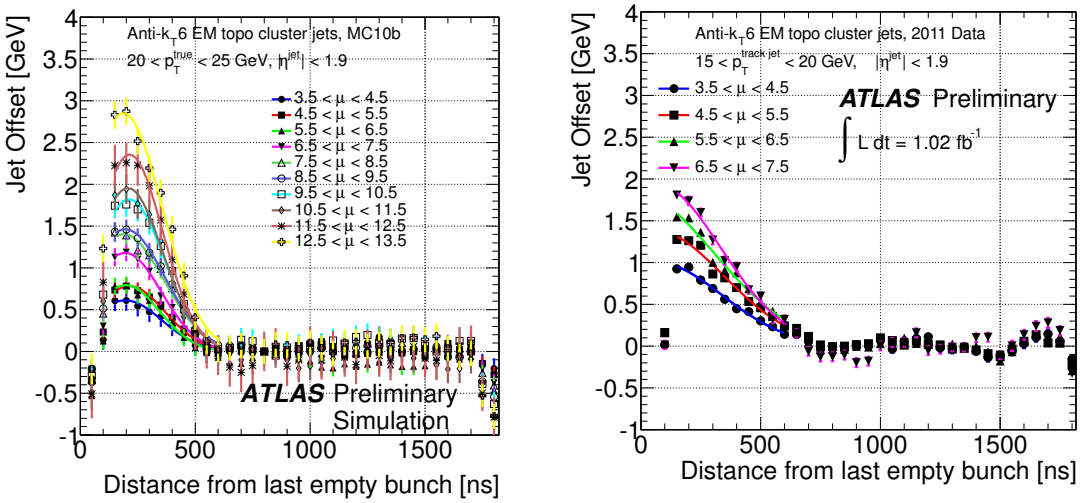

Figure 6.16.: Offset of the jet transverse energy E_T^{jet} in simulation (left) and data (right) as a function of the distance from the last empty bunch (DFE) in the current bunch train, binned in the average number of interactions per bunch crossing μ, for the central pseudo-rapidity region. Each point in the left (right) figure shows the mean (most probable) value of E_T^{jet} in a specific μ and DFE range, after subtracting the average transverse energy in the plateau region (DFE $>$ 600 ns) [59].

$\pm 10\%$. The analysis is rerun with μ scaled up and down to determine the effect on the event yield.

Jet Energy Scale (JES) To evaluate the uncertainty on the jet energy scale, jet energies are scaled up and down analogously to the treatment described in Section 5.3. The variation of the jet energies is propagated to the $E_{\text{T}}^{\text{miss}}$ by vectorially removing and re-adding the modified objects. The analysis is rerun to translate the jet energy scale uncertainty to an uncertainty on the event yield. Due to the significantly increased amount of out-of-time pile-up in 2011 one further contribution to the uncertainty is taken into account, namely the difference of the jet energy offset in data and Monte Carlo. The calorimeter signals from previous bunch crossings can overlap with in-time signals, but the signal shapes are designed such that the effects of out-of-time and in-time pile-up cancel on average for a constant bunch intensity. For the first bunches in a bunch train, there is an imbalance between in-time and out-of-time pile-up, causing a systematically higher calorimeter response. The same effect is seen, if not all bunches in a bunch train are filled and the time between the current bunch and the last empty bunch is less than the integration time of the calorimeter signal ($\sim$600 ns). The size of the imbalance depends on the amount of in-time pile-up. In Figure 6.16 the offset of the jet transverse energy E_T^{jet} is shown as a function of the distance to the last empty bunch (DFE) in the current bunch train in simulation (left) and data (right), binned in the number of primary vertices per bunch crossing μ. For example, for $5.5 < \mu < 6.5$ the maximum amplitude of the energy variation is 0.8 GeV in simulation and 1.5 GeV in data. The differences are used as an additional uncertainty.

Jet Energy Resolution (JER) The uncertainty on the jet energy resolution is taken into account (analogously to the treatment described in Section 5.3) by smearing the p_{T} of the

jets [111].

Lepton Identification Efficiency The reconstruction efficiency of electrons and muons is measured from the processes $Z \to ee$, $Z \to \mu\mu$, $W \to e\nu$ and $J/\psi \to ee$. The observed differences are used to derive scale factors [74, 117] with respective uncertainties. These uncertainties are translated to an uncertainty on the event yield by rerunning the analysis using scale factors that are varied up and down within their uncertainty.

Lepton Energy Scale The lepton energy scale uncertainty is found to only have a sub percent influence on the final event yield and is therefore neglected.

***b*-Tagging** The systematic uncertainty of the b-tagging algorithm is given as a systematic uncertainty of the b-tagging scale factors [84]. Analogously to Section 5.3, the analysis is rerun to evaluate the uncertainty on the event yield with scale factors varied up and down within the uncertainty.

$E_{\mathrm{T}}^{\mathrm{miss}}$ **Uncertainty** The calculation of the missing transverse momentum (see Eq. 4.7) introduces an uncertainty dominated by the term $E_T^{\mathrm{miss,CellOut}}$, which represents the missing transverse momentum from energy clusters not used to reconstruct any physics object in the final state. The uncertainty of $E_T^{\mathrm{miss,CellOut}}$ is calculated by shifting the topocluster energies up and down within the uncertainty and found to be $\pm 13\%$ [80]. The analysis is rerun to translate this uncertainty to an uncertainty of the event yield.

6.3.2. Theoretical Uncertainties

The theoretical uncertainties are evaluated individually for the SUSY signal and for the most important background processes.

Signal Uncertainties

For the theoretical systematic uncertainties on the signal cross sections, two sources are considered, namely PDF uncertainties and uncertainties on the renormalization scale μ_R and factorization scale μ_F.

The cross sections are calculated at next-to-leading order (NLO), taking into account next-to-leading logarithmic corrections. Lower and upper bounds of the cross section are constructed using the PDFs and the PDF uncertainties of the CTEQ6.6 [97] and MSTW2008 [48] PDF sets. For the CTEQ6.6 PDF set, the variation of α_s is taken into account. For the MSTW PDF set, the required information was not available at NLO+NLL precision, thus the α_s uncertainty is omitted for the MSTW PDF set. The scale uncertainties are taken into account by independently varying the scales μ_R and μ_F up and down by factors of two. The midpoint of the envelope is used as the nominal cross section, the half of the full width is used as uncertainty. Figure 6.17 shows the NLO+NLL stop cross section as a function of the stop mass, including the individual components of the uncertainties and the resulting total uncertainty.

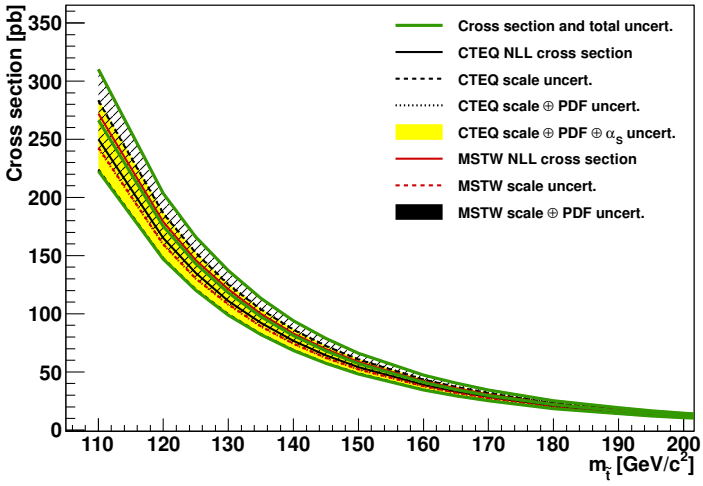

Figure 6.17.: Production cross section for stop pair production at next-to-leading order, including next-to-leading-logarithmic corrections, as a function of the stop mass. The solid black line correspond to the cross section predicted using the CTEQ PDF set. The dashed black line includes the CTEQ scale uncertainties, the dotted black line additionally includes the uncertainties on α_s. The yellow band corresponds to the cross section from the CTEQ PDFs including all uncertainties (quadratic sum). The solid red line corresponds to the MSTW prediction. The dashed red line includes scale uncertainties and the hatched black region corresponds to the quadratic sum of the scale and PDF uncertainties. The green solid lines corresponds to the final cross section used with the corresponding uncertainty.

Top Production

For the cross section of the top pair production, a value of $\sigma_{t\bar{t}} = 166.8^{+11.5}_{-15.8}$ pb is used. Since dedicated control regions are used to normalize the contribution from top pair production, the uncertainty on the cross section is reduced. Instead of the uncertainty quoted above, the uncertainty due to the limited number of Monte Carlo simulated events is taken into account, as well as the statistical uncertainty in the data control regions.

The residual shape uncertainties are considered as follows. The treatment of the top pair systematic uncertainties proceeds analogously to the method described in Section 5.3. The uncertainties on ISR and FSR are taken into account with dedicated `ACERMC` samples. The uncertainty connected to the modeling of the parton shower and fragmentation is obtained by comparing `POWHEG` samples using either `HERWIG` or `PYTHIA` for fragmentation.

The treatment of the single top production uncertainty is analogous to the method described in Section 5.3.

Boson+Jets Production

The contribution of the W+jets production background is dominated by Wbb production. The normalization is estimated from a dedicated control region. Therefore, only residual shape

uncertainties have to be considered. The following systematic effects have been studied:

- variation of factorization and normalization scale,
- different choices of the factorization and normalization scale, [3]
- parton shower matrix element matching scale.

Furthermore, the uncertainties on the W heavy flavor scale factors are taken into account (in analogy to the treatment used in Section 5.3): Wbb and Wcc: 1.63 ± 0.76. Wc: 1.10 ± 0.35 [112].

The uncertainties on the background from Z+jets production have been studied in analogy to W+jets. The Z+heavy flavor contribution is found to be in good agreement with the theoretical prediction [113], so no additional scale factor is applied.

6.3.3. Total Uncertainties

The total uncertainties are calculated, taking into account all contributions introduced above. The effect of the systematic uncertainties on the individual background processes, which are discussed in this section, is given in Table 6.7. The individual background components are estimated with the estimation techniques described in the previous chapter. The experimental uncertainties, e.g. the JES and b-tagging uncertainties, and the theory uncertainties are reduced to a large extent for the backgrounds, estimated with data-driven techniques.

[3] For the scales, generically denoted by Q, `ALPGEN` allows different parametrizations in terms of the final state partons: $Q^2 = m_W^2 + p_{\mathrm{T}W}^2$, $Q^2 = m_W^2$ or $Q^2 = m_W^2 + \sum m_T^2$, where the sum includes all final state partons. A detailed description of the input parameters is given in Ref. [89].

Process	CR	MC	Experimental Uncertainties						Theory Uncertainties	
	stat.	stat.	JES	JER	b-tag	lepton ID	$E_{\mathrm{T}}^{\mathrm{miss}}$	Pile-Up	$t\bar{t}$	W
$t\bar{t}$	±11%	±5%	$^{+2\%}_{-15\%}$	±10%	±1%	±1%	±9%	±3%	±13%	±2%
single top	-	±25%	±40%	±24%	±25%	±2%	±12%	±3%	±26%	-
W	±13%	±20%	$^{+13\%}_{-18\%}$	±7%	±1%	±1%	±25%	±3%	±8%	±15%
Z	-	±60%	±40%	±24%	±25%	±2%	±12%	±3%	-	-
dibosons	-	±35%	±30%	±40%	±30%	±3%	±30%	±3%	-	-
total (non-QCD multijet)	±11%	±5%	$^{+5\%}_{-15\%}$	±10%	±1%	±2%	±9%	±3%	±7%	±5%
QCD multijet	±45%									

Table 6.7.: Relative systematics uncertainties associated to the different background processes in the signal region. The column labeled as "CR stat." represents the statistical uncertainty due to the number of measured events in the control regions. The column "MC stat." represents the statistical uncertainty due to the limited number of Monte Carlo simulated events. The line labeled as "total" contains the relative uncertainty on the total SM background as obtained when rerunning the full analysis with each specific final state object reconstruction uncertainty. Note that the QCD multijet uncertainty is not included in the "total" row.

6.4. Results and Interpretation

In the first part of this section, the measured distributions of key observables are shown and compared with the expectations from the SM. The contributions from SM background processes are determined using the estimation techniques described above and are compared to the expectation from Monte Carlo simulation. The second part of this chapter is dedicated to the interpretation of the results in the context of specific SUSY scenarios.

6.4.1. Measurements and Standard Model Expectation

The numbers of events after the consecutive selection steps measured in data are listed in Table 6.8 and compared to the SM expectation using the Monte Carlo simulation to estimate the contributions from SM background processes. After the b-tagging selection step the top pair production is the dominant contribution to the SM background processes ($\sim 90\%$). After the signal region selection, the contributions from W and QCD multijet become non-negligible. For reference, three SUSY signals are included in the table with stop masses of 130, 180 and 210 GeV, respectively.

The event yield in the signal region is shown in detail in Table 6.9 for the electron and muon channels, as well as for the combination. The listed numbers for top pair production and W+jets events are calculated using the normalization factors w_W, w_t and ω introduced above. The estimation based on Monte Carlo simulation is given in parentheses. The estimation of the QCD multijet contribution is obtained using the data-driven approach. The systematic uncertainties for the combined channel are listed, split into two components: the first term represents the uncertainties from limited number of events in the Monte Carlo samples and the uncertainties on the scaling factors; the second term represents the systematic uncertainties. For the QCD multijet contribution, the total uncertainty is given.

The combination of the electron and muon channels yields 50 events in the signal region, while $38.2 \pm 3.3 \pm 7.3$ are expected from SM contributions. The difference in the expected and observed number of events is largest in the muon channel. However it is not significant and interpreted as a statistical fluctuation. The result is consistent with the background-only hypothesis within the uncertainties, hence no significant excess over the SM expectation is observed.

The distributions of important kinematic variables in the signal region, namely $E_{\mathrm{T}}^{\mathrm{miss}}$, the p_{T} of the leading lepton, the p_{T} of the leading jet and the $\sqrt{s}_{\mathrm{min}}^{(\mathrm{sub})}$ distribution, are shown in Fig. 6.18 for the 1-electron channel and in Fig. 6.19 for the 1-muon channel. For all distributions, the techniques described above are used to estimate the contributions of the individual SM background processes. For reference, the distributions of three different SUSY signals with stop masses of 160, 180 and 210 GeV, respectively, are superimposed.

1-electron	Top	W	QCD	Others	Total	Data	$m_{\tilde{t}_1} = 130$,	180,	210 GeV
pre-selection, lepton and jet requirements	43208	66985	119631	19180	249004	215632	2721	2333	1324
$E_{\mathrm{T}}^{\mathrm{miss}} > 40$ GeV	28703	37134	16369	4852	87058	78852	1810	1679	1033
two b-jets	7985	464	268	367	9084	10961	311	391	261
SR	8	5	4	1	18	18	12	9	1

1-muon	Top	W	QCD	Others	Total	Data	$m_{\tilde{t}_1} = 130$,	180,	210 GeV
pre-selection, lepton and jet requirements	41881	71082	36967	11597	161527	169507	3136	2639	1523
$E_{\mathrm{T}}^{\mathrm{miss}} > 40$ GeV	28918	41857	4262	5201	80238	76471	2127	1841	1167
two b-jets	8122	442	169	372	9105	10913	421	410	331
SR	10	4	3	2	19	32	23	13	1

Table 6.8.: Numbers of events after consecutive selection steps, comparing the SM background expectation, taken from Monte Carlo simulation, with data. For reference, the numbers for three signal models are included with stop masses of 130, 180 and 210 GeV, respectively, and $m_{\tilde{\chi}_1^0} = 60$ GeV. The column labeled 'Others' contains contributions from Z, single top and diboson production.

Process	SR yield		
	1-electron	1-muon	1-lepton
$t\bar{t}$	9.5 (8.0)	12.2 (9.9)	$21.7 \pm 2.6 \pm 5.2$ (17.9)
single top	1.1	1.3	$2.4 \pm 0.1 \pm 0.3$
W	4.2 (5.3)	2.4 (4.1)	$6.4 \pm 1.5 \pm 2.2$ (9.4)
Z	< 0.2	0.3	$0.5 \pm 0.3 \pm 0.3$
di-bosons	0.1	0.2	$0.3 \pm 0.1 \pm 0.1$
multi-jet	3.5	3.4	6.9 ± 2.0
total	18.5 (18.1)	19.7 (19.1)	$38.2 \pm 3.3 \pm 7.3$ (37.2)
data	18	32	50

Table 6.9.: Event yields in the signal region for the 1-electron, 1-muon and the combined 1-lepton channel. The contributions from SM background processes are estimated with the dedicated techniques described in the text. The prediction from Monte Carlo simulation is reported in parentheses, where applicable. The uncertainties are given for the combined 1-lepton channel. They are split into two components: the first term represents the uncertainties from the limited number of events in the Monte Carlo samples and the uncertainties on the scaling factors; the second term represents the systematic uncertainties. For the QCD multijet contribution, the total uncertainty is given.

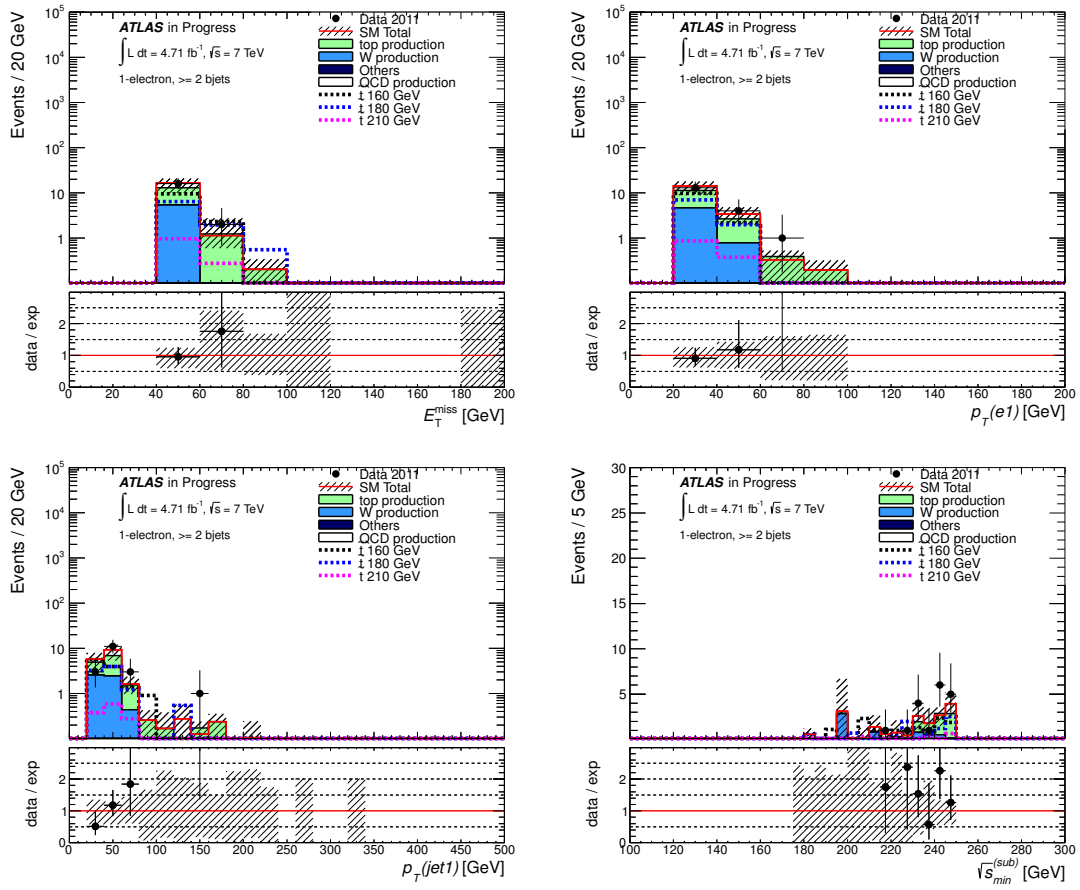

Figure 6.18.: Distributions of $E_{\mathrm{T}}^{\mathrm{miss}}$, the p_{T} of the leading lepton, the p_{T} of the leading jet and $\sqrt{s}_{\mathrm{min}}^{(\mathrm{sub})}$ in the signal region (1-electron channel). For reference, the distributions of three different SUSY signals with stop masses of 160, 180 and 210 GeV, respectively, are superimposed (dashed lines). The hatched bands represent the systematic uncertainties (see Section 6.3).

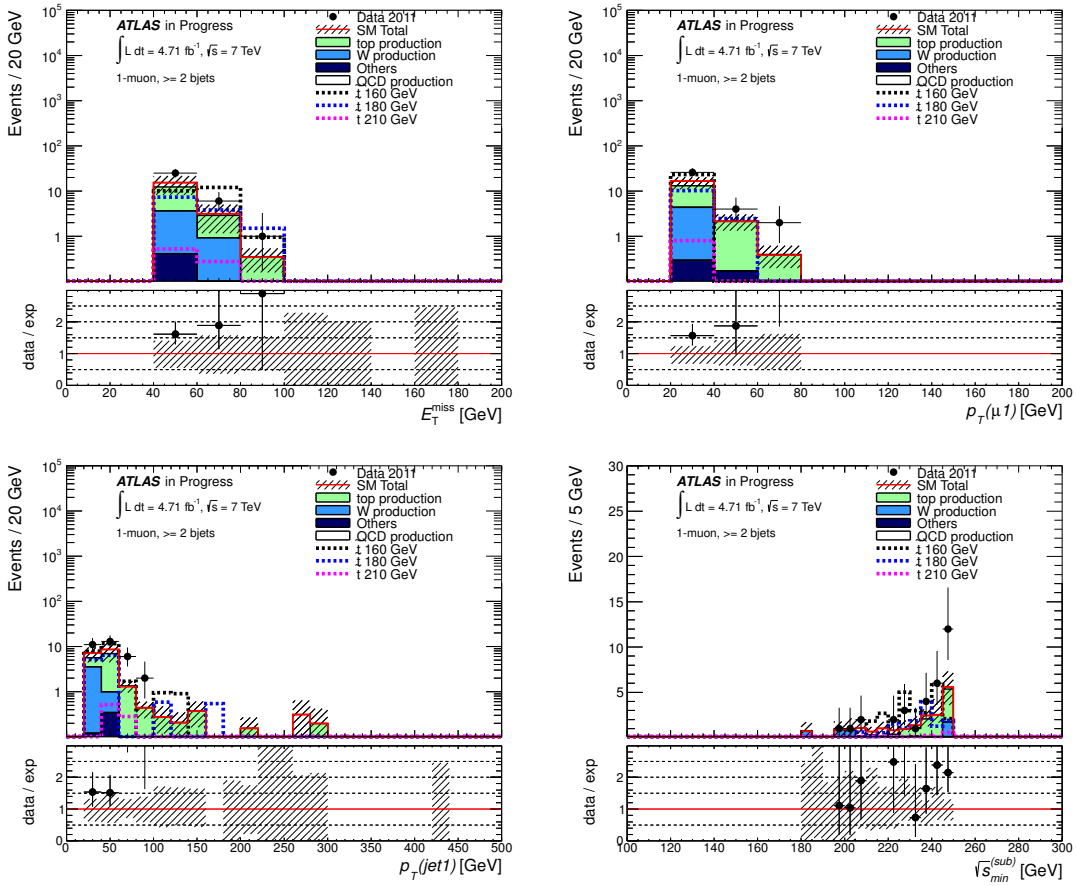

Figure 6.19.: Distributions of $E_{\mathrm{T}}^{\mathrm{miss}}$, leading lepton p_{T}, leading jet p_{T} and $\sqrt{s}_{\mathrm{min}}^{(\mathrm{sub})}$ in the signal region (1-muon channel). For reference, the distributions of three different SUSY signals with stop masses of 160, 180 and 210 GeV, respectively, are superimposed (dashed lines). The hatched bands represent the systematic uncertainties (see Section 6.3).

6.4.2. Exclusion Limits

The results are used to derive a model-independent 95% C.L. upper limit on the number of events and the effective cross section σ_{vis} of physics processes beyond the SM. The observed upper limit on the number of events is found to be 31, while the expected upper limit is 20. The observed upper limit on the effective cross section is found to be 6.6 fb, by dividing out the integrated luminosity and taking into account the uncertainty. The expected upper limit on the effective cross section is 4.2 fb.

In the following, interpretations in the form of 95% C.L. limits in specific model scenarios are presented. All models considered assume 100% BR for $\tilde{t}_1 \to \tilde{\chi}_1^{\pm} + b$ and heavy first and second generation squarks and sleptons (> 3 TeV). All systematic uncertainties described in Section 6.3 are included in the derivation of the limits.

Gluino Stop Model

The expected and observed limits in the ($m_{\tilde{t}_1}$,$m_{\tilde{\chi}_1^0}$)-plane of the gluino-stop model with assumed gaugino universality $m_{\tilde{\chi}_1^{\pm}} = 2m_{\tilde{\chi}_1^0}$ are shown in Figure 6.20. Possible signal contamination (assuming nominal signal strength) is taken into account in the right part of the figure and neglected in the left part. The region of stop masses that is expected to be excluded (dashed black line) is between ∼150 and ∼180 GeV for $m_{\tilde{\chi}_1^0} \approx 60$ GeV. Neutralino masses up to 73 GeV are expected to be excluded for a stop mass close to the top mass. The yellow band represents the experimental uncertainty on the expected limit ($\pm 1\sigma_{\text{exp}}$). For the construction of the limit, a variation of the theoretical signal uncertainties $\pm 1\sigma_{\text{theory}}^{\text{SUSY}}$ is performed. No exclusion limit could be set for the nominal signal model, only the limit obtained by the $+1\sigma_{\text{theory}}^{\text{SUSY}}$ variation (red dotted line) is shown in the figure.

Fixed Stop Mass

The expected and observed limits in the ($m_{\tilde{\chi}_1^{\pm}}$,$m_{\tilde{\chi}_1^0}$)-plane of the signal model with an assumed stop mass of 180 GeV is shown in Fig. 6.21, without (left) and with (right) signal contamination taken into account. The expected region of exclusion lies between chargino masses of ∼125 and ∼145 GeV for a neutralino mass of 50 GeV. The expected limit is denoted by the black dashed line and the $\pm 1\sigma_{\text{exp}}$ variation by the yellow band. No limit could be derived in this case.

6.4.3. Combination with Dilepton Search

Besides the 1-lepton search channel presented in this thesis, a complementary and mutually exclusive dilepton search has been performed [115, 116]. It is based on identical preselection criteria and the analogously defined quantity $\sqrt{s}_{\text{min}}^{(\text{sub})}$. The event selection in the dilepton search requires

- at least two jets with $p_{\text{T}} > 20$ GeV and $|\eta| < 2.5$;
- exactly two leptons with opposite charge:

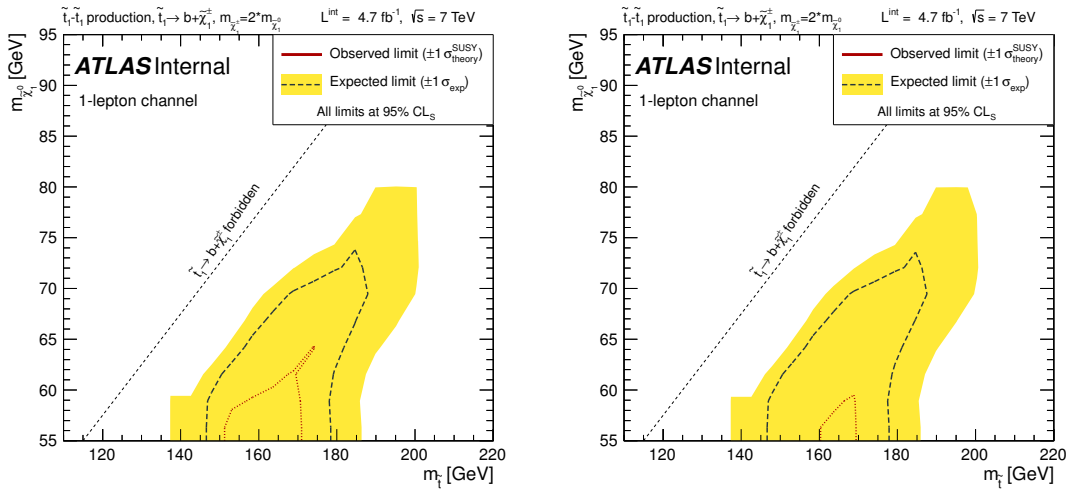

Figure 6.20.: Exclusion limits at 95% C.L. in the ($m_{\tilde{t}_1}$,$m_{\tilde{\chi}_1^0}$)-plane assuming direct stop pair production, where the stop decays exclusively via $\tilde{t}_1 \to b\tilde{\chi}_1^{\pm}$. A fixed chargino-neutralino mass ratio is assumed ($m_{\tilde{\chi}_1^{\pm}} = 2m_{\tilde{\chi}_1^0}$). The limits are obtained without (left) and with (right) signal contamination taken into account. The expected limit (dashed line) is shown with a $\pm 1\sigma_{\text{exp}}$ variation of the experimental uncertainties (yellow band). The theoretical uncertainties of the signal are taken into account in the calculation of the observed limit by a $\pm 1\sigma_{\text{theory}}^{\text{SUSY}}$ variation. No limit could be set in the nominal signal model. The observed limit with a $+1\sigma_{\text{theory}}^{\text{SUSY}}$ variation of the signal is given by the dotted line.

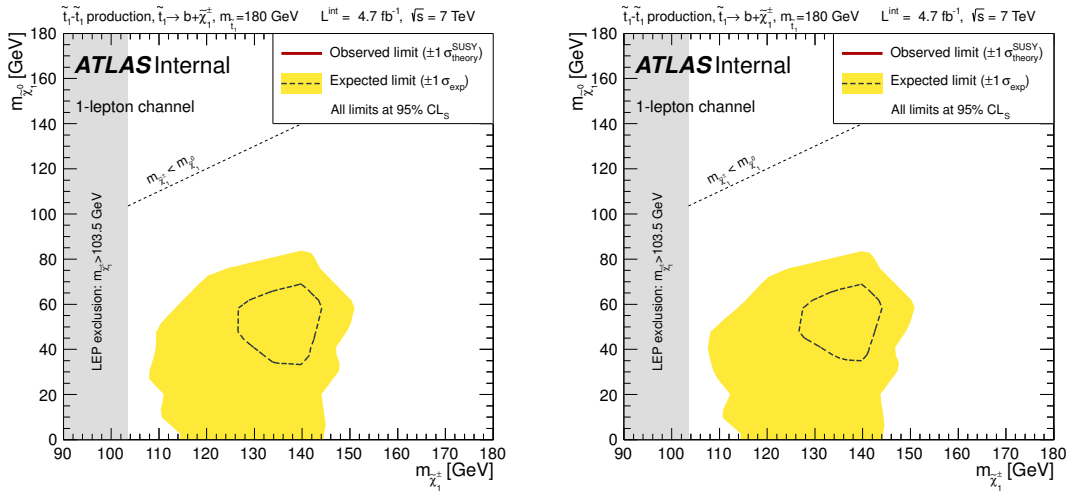

Figure 6.21.: Exclusion limits at 95% C.L. in the ($m_{\tilde{\chi}_1^{\pm}}$,$m_{\tilde{\chi}_1^0}$)-plane assuming $m_{\tilde{t}_1} = 180$ GeV without (left) and with (right) signal contamination taken into account. The expected limit (dashed line) is shown with a $\pm 1\sigma_{\text{exp}}$ variation of the experimental uncertainties (yellow band). No limit could be set.

– two electrons:
the p_{T} of the leading and the subleading electron is required to exceed 25 and 20 GeV, respectively;

  - two muons:
    the p_{T} of the leading and subleading muon is required to exceed 20 and 10 GeV, respectively;
  - electron + muon:
    the p_{T} of the electron is required to exceed 25 GeV, the p_{T} of the muon is required to exceed 20 GeV;

- minimum $E_{\mathrm{T}}^{\mathrm{miss}}$ of 40 GeV;
- at least one jet in the leading two jets must be b-tagged.

The invariant mass of the lepton pair $m_{\ell\ell}$ is used to distinguish the signal region and dedicated control regions:

- signal region: 30 GeV $< m_{\ell\ell} <$ 81 GeV;
- Z control region: 81 GeV $< m_{\ell\ell} <$ 101 GeV with same-flavor leptons;
- $t\bar{t}$ control region: $m_{\ell\ell} >$ 101 GeV.

In the control regions normalization factors are derived for the corresponding background contributions. The QCD multijet background contribution is estimated with a data-driven method analogous to the 1-lepton search channel. Further background contributions are expected to be small and are taken from Monte Carlo simulation.

A similar optimization as in Section 6.1.4 is performed for the definition of the $\sqrt{s}_{\mathrm{min}}^{(\mathrm{sub})}$ selection criterion. In addition, the total invariant mass of the two leptons and the two leading jets $m_{\ell\ell jj}$ is considered. As a result, two signal regions are defined:

SR1: $\sqrt{s}_{\mathrm{min}}^{(\mathrm{sub})} < 225\,\mathrm{GeV}$,

SR2: $\sqrt{s}_{\mathrm{min}}^{(\mathrm{sub})} < 235\,\mathrm{GeV}$ and $m(\ell\ell jj) < 140\,\mathrm{GeV}$,

which are found to perform best for a variety of signal models.

The expected and observed exclusion limits at 95% C.L. obtained with the dilepton search in the $(m_{\tilde{t}_1}, m_{\tilde{\chi}_1^0})$-plane, assuming the direct production of stop pairs, where the stop decays exclusively via $\tilde{t}_1 \to b\tilde{\chi}_1^{\pm}$, are shown in Fig. 6.22. A fixed mass ratio for the chargino and the neutralino is assumed ($m_{\tilde{\chi}_1^{\pm}} \simeq 2m_{\tilde{\chi}_1^0}$). The figure includes the limits considering the signal region SR1 (top) and SR2 (bottom), without (left) and with (right) signal contamination taken into account. Stop masses close to the top mass are excluded up to neutralino masses of about 75 GeV. In the region close to the kinematic boundary of $m_{\tilde{t}_1} = m_b + m_{\tilde{\chi}_1^{\pm}}$, the sensitivity is limited due to soft b-jets that cannot be identified as such.

The respective limits in the $(m_{\tilde{\chi}_1^{\pm}}, m_{\tilde{\chi}_1^0})$-plane, assuming $m_{\tilde{t}_1} = 180\,\mathrm{GeV}$, are shown in Fig. 6.23. It includes the limits considering the signal region SR1 (top) and SR2 (bottom), without (left) and with (right) signal contamination taken into account. The excluded region is around the combination of $m_{\tilde{\chi}_1^0} = 60\,\mathrm{GeV}$ and $m_{\tilde{\chi}_1^{\pm}} = 135\,\mathrm{GeV}$.

Since the one and two lepton selection criteria are mutually exclusive, a combined limit including both analyses can be derived. The resulting combined 95% C.L. exclusion limit in the

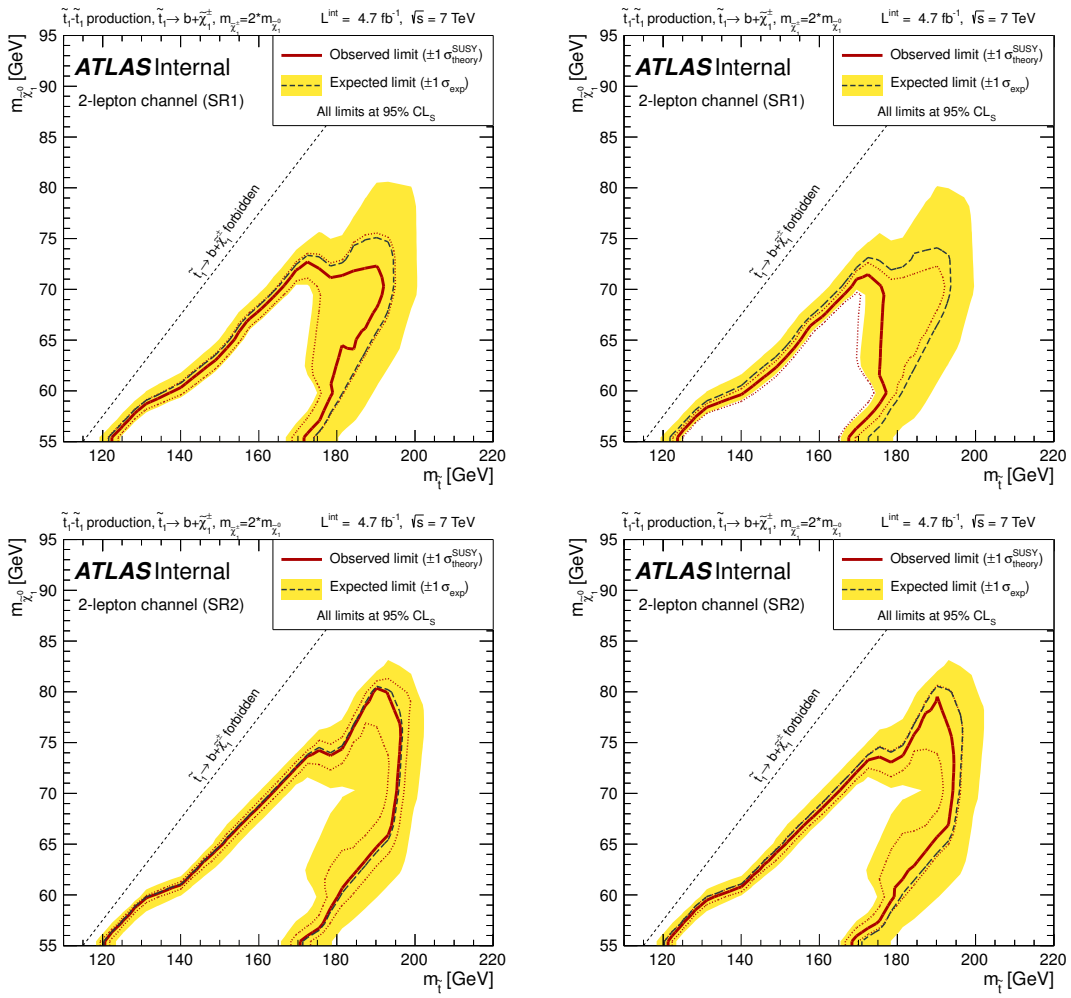

Figure 6.22.: Exclusion limits at 95% C.L. obtained with the 2-lepton analysis on the $(m_{\tilde{t}_1}, m_{\tilde{\chi}_1^0})$-plane assuming direct stop pair production, where the stop decays exclusively via $\tilde{t}_1 \rightarrow b\tilde{\chi}_1^{\pm}$. A fixed chargino-neutralino mass ratio is assumed $(m_{\tilde{\chi}_1^{\pm}} = 2m_{\tilde{\chi}_1^0})$. The expected limit (dashed line) is shown with a $\pm 1\sigma_{\text{exp}}$ variation of the experimental uncertainties (yellow band). The observed limit (red line) is shown with a $\pm 1\sigma_{\text{theory}}^{\text{SUSY}}$ variation of the theoretical uncertainties of the signal (red dotted lines). The top (bottom) figures show the limits in the case of considering the signal region SR1 (SR2). The left (right) figures show the different limits without (with) signal contamination taken into account [115].

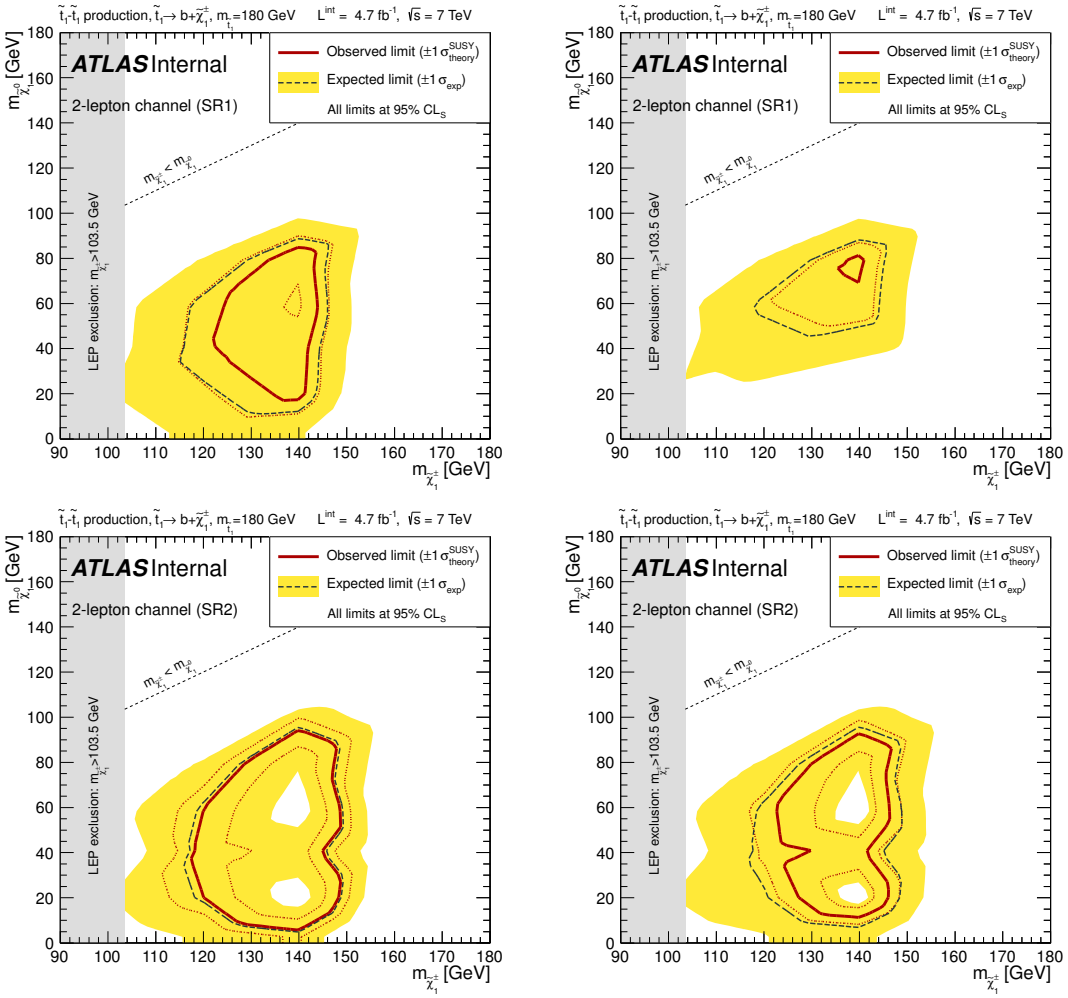

Figure 6.23.: Exclusion limits at 95% C.L. obtained with the 2-lepton analysis on the $(m_{\tilde{\chi}_1^\pm}, m_{\tilde{\chi}_1^0})$-plane assuming direct stop pair production, where the stop decays exclusively via $\tilde{t}_1 \to b\tilde{\chi}_1^\pm$. A fixed chargino-neutralino mass ratio is assumed $(m_{\tilde{\chi}_1^\pm} = 2m_{\tilde{\chi}_1^0})$. The expected limit (dashed line) is shown with a $\pm 1\sigma_{\text{exp}}$ variation of the experimental uncertainties (yellow band). The observed limit (red line) is shown with a $\pm 1\sigma_{\text{theory}}^{\text{SUSY}}$ variation of the theoretical uncertainties of the signal (red dotted lines). The top (bottom) figures show the limits obtained using the signal region SR1 (SR2). The left (right) figures show the different limits without (with) signal contamination taken into account [115].

($m_{\tilde{t}_1}$,$m_{\tilde{\chi}_1^0}$)-plane, assuming direct stop pair production with stop decay via $\tilde{t}_1 \to b\tilde{\chi}_1^\pm$ and a fixed chargino-neutralino mass ratio ($m_{\tilde{\chi}_1^\pm} = 2m_{\tilde{\chi}_1^0}$), is shown Fig. 6.24. The combinations for SR1 (left) and SR2 (right) are given separately, as well as the best combination in each point (bottom). Stop masses between ∼130 GeV and ∼170 GeV can be excluded for a neutralino mass of 60 GeV. Stop masses close to the top mass are excluded up to neutralino masses of about 75 GeV.

The combined limit of the one and 2-lepton search channel in the ($m_{\tilde{\chi}_1^\pm}$,$m_{\tilde{\chi}_1^0}$)-plane, assuming $m_{\tilde{t}_1} = 180$ GeV, is shown in Fig. 6.25. The combinations with SR1 (left) and SR2 (right) are given separately, as well as the best combination in each point[4]. Chargino masses between 120 and 145 GeV are excluded for a neutralino mass of 60 GeV. For a chargino mass of 140 GeV, the excluded neutralino masses range from 45 to 95 GeV.

[4]In Figure 6.25 the limit with the best point-by-point combination of the one and 2-lepton channel (bottom) is based on an enlarged set of Monte Carlo simulated signal events compared to the upper plots. The exclusion around $m_{\tilde{\chi}_1^\pm} = 140$ GeV and $m_{\tilde{\chi}_1^0} = 20$ GeV visible in the upper right plot is found to be caused by a statistical fluctuation and no longer visible in the combination with enlarged signal sample (bottom).

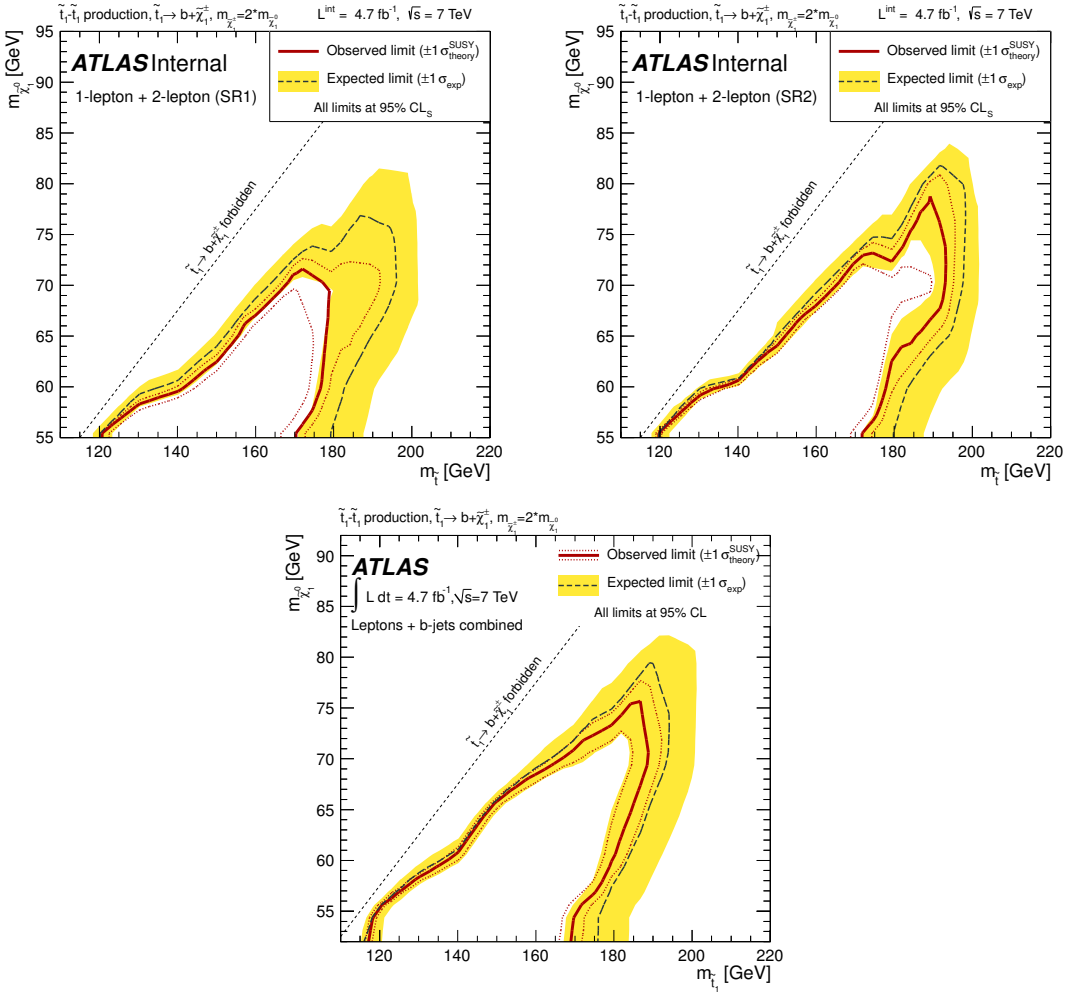

Figure 6.24.: Combined exclusion limits at 95% C.L. in the $(m_{\tilde{t}_1}, m_{\tilde{\chi}_1^0})$-plane assuming direct stop pair production, where the stop decays exclusively via $\tilde{t}_1 \to b\tilde{\chi}_1^{\pm}$. A fixed chargino-neutralino mass ratio is assumed ($m_{\tilde{\chi}_1^{\pm}} = 2m_{\tilde{\chi}_1^0}$). The expected limit (dashed line) is shown with a $\pm 1\sigma_{\text{exp}}$ variation of the experimental uncertainties (yellow band). The observed limit (red line) is shown with a $\pm 1\sigma_{\text{theory}}^{\text{SUSY}}$ variation of the theoretical uncertainties of the signal (red dotted lines). The top-left (top-right) figure shows the combined limit of the 1-lepton channel and the signal region SR1 (SR2) of the 2-lepton analysis. For the final limit the best expected limit from SR1 and SR2 is used for the combination (bottom).

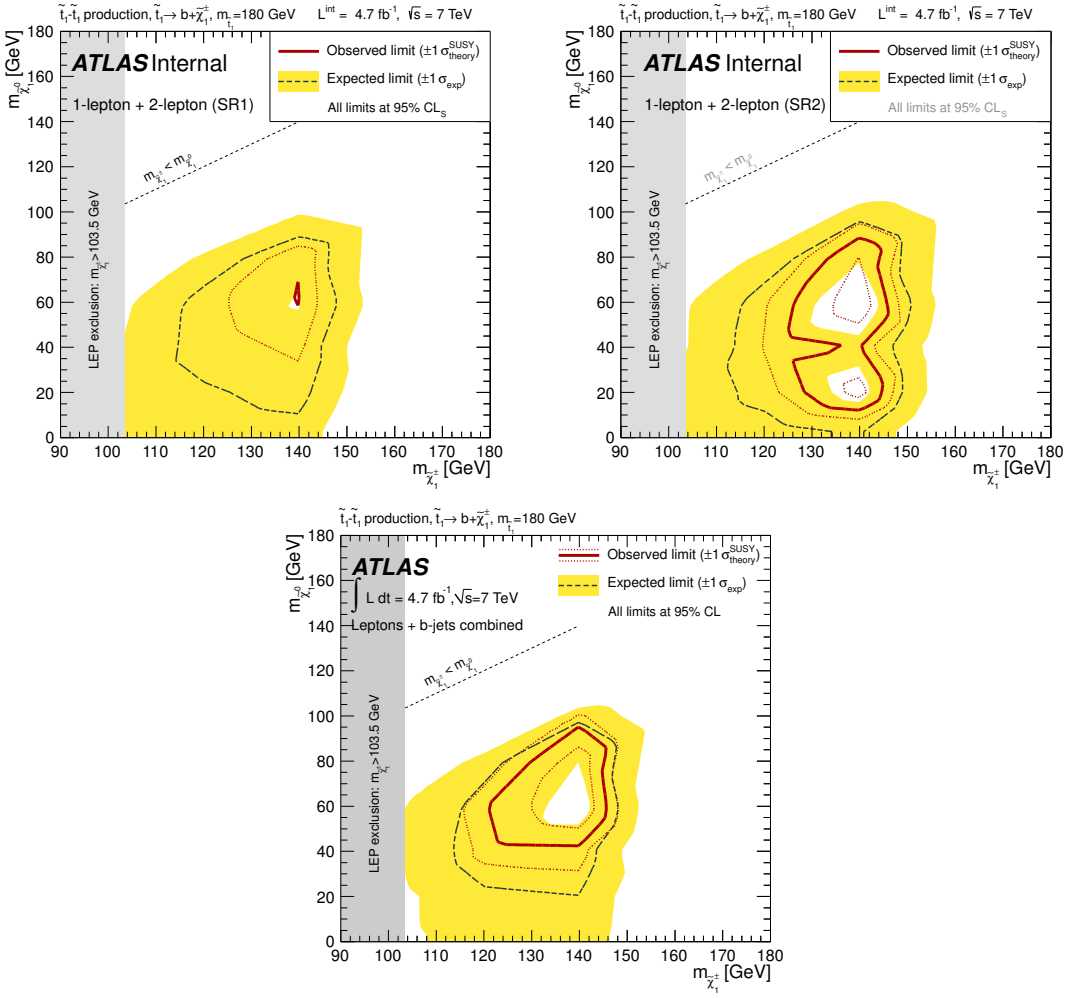

Figure 6.25.: Combined exclusion limits at 95% C.L. in the $(m_{\tilde{\chi}_1^\pm}, m_{\tilde{\chi}_1^0})$-plane assuming direct stop pair production, where the stop decays exclusively via $\tilde{t}_1 \to b\tilde{\chi}_1^\pm$. A fixed stop mass of $m_{\tilde{t}_1} = 180$ GeV is assumed. The expected limit (dashed line) is shown with a $\pm 1\sigma_{\text{exp}}$ variation of the experimental uncertainties (yellow band). The observed limit (red line) is shown with a $\pm 1\sigma_{\text{theory}}^{\text{SUSY}}$ variation of the theoretical uncertainties of the signal (red dotted lines). The top-left (top-right) figure shows the limit for the combination of the 1-lepton analysis and signal region SR1 (SR2) of the 2-lepton analysis. For the final limit the best expected limit from SR1 and SR2 is used for the combination (bottom).

6.5. Conclusions on the Direct Stop Pair Production Search

The search for direct stop pair production with the ATLAS detector is presented under the assumption of stop masses around or below the top mass using a dataset corresponding to an integrated luminosity of $4.7\,\text{fb}^{-1}$. No significant excess over the SM expectation is observed. Therefore, limits at 95% C.L. are derived.

The sensitivity of the 1-lepton search for direct stop production is reflected by the shown expected exclusion limits. Assuming direct stop production with a decay of the stop via $\tilde{t}_1 \to b\tilde{\chi}_1^{\pm}$ and gaugino universality $m_{\tilde{\chi}_1^{\pm}} = 2m_{\tilde{\chi}_1^0}$, stop masses between ∼150 and ∼180 GeV for $m_{\tilde{\chi}_1^0} \approx 60\,\text{GeV}$ are expected to be excluded. Neutralino masses up to ∼73 GeV are expected to be excluded for a stop mass close to the top mass. The expected exclusion in the signal model with an assumed stop mass of 180 GeV ranges from chargino masses of ∼125 to ∼145 GeV for a neutralino mass of ∼50 GeV. The 1-lepton analysis alone does not lead to an experimental limit. The observed number of events in the signal region is consistent with an upward fluctuation of the SM background contributions within the uncertainties. No significant excess is observed.

In combination with the 2-lepton search, stop masses between ∼130 and ∼170 GeV are excluded for $m_{\tilde{\chi}_1^0} = 60\,\text{GeV}$ in SUSY scenarios with direct stop pair production, stop decay exclusively via $\tilde{t}_1 \to b\tilde{\chi}_1^{\pm}$ and gaugino universality $m_{\tilde{\chi}_1^{\pm}} = 2m_{\tilde{\chi}_1^0}$. Furthermore, stop masses around the top mass are excluded for $m_{\tilde{\chi}_1^0} < 75\,\text{GeV}$. In SUSY scenarios with a fixed stop mass of $m_{\tilde{t}_1} = 180$ GeV, chargino masses between ∼120 and ∼145 GeV are excluded for a neutralino mass of 60 GeV. Neutralino masses between ∼45 and ∼95 GeV are excluded for a chargino mass of 140 GeV.

The sensitivity and performance of the presented analyses are illustrated in Fig. 6.26 within the context of the five dedicated stop searches performed with the ATLAS detector [63–66, 116]. The observed and expected exclusion limits are shown for the individual search channels. For $m_{\tilde{t}_1} > 200\,\text{GeV}$ the stop is assumed to decay exclusively via $\tilde{t}_1 \to t+\tilde{\chi}_1^0$, for $m_{\tilde{t}_1} < 200\,\text{GeV}$ via $\tilde{t}_1 \to b + \tilde{\chi}_1^{\pm}$. The different analyses are complementary, since they are targeting different regions in the $(m_{\tilde{t}_1}, m_{\tilde{\chi}_1^0})$-plane. For light neutralino masses $m_{\tilde{\chi}_1^0} < 10\,\text{GeV}$, stop masses between $120\,\text{GeV} < m_{\tilde{t}_1} < 155\,\text{GeV}$ and $230\,\text{GeV} < m_{\tilde{t}_1} < 500\,\text{GeV}$ are excluded at 95% C.L. The lower exclusion range is valid up to neutralino masses of about 75 GeV, the upper exclusion range reaches a neutralino mass of about 160 GeV for a stop mass of about 400 GeV. Both the region with $m_{\tilde{t}_1} \approx m_t + m_{\tilde{\chi}_1^0}$ and with $m_{\tilde{t}_1} \approx m_t + m_{\tilde{\chi}_1^0}$ are experimentally challenging, due to very soft objects in the final state. Only with future data-taking and analyses, it will be possible to extend the sensitivity to the full $(m_{\tilde{t}_1}, m_{\tilde{\chi}_1^0})$-plane shown in Fig. 6.26.

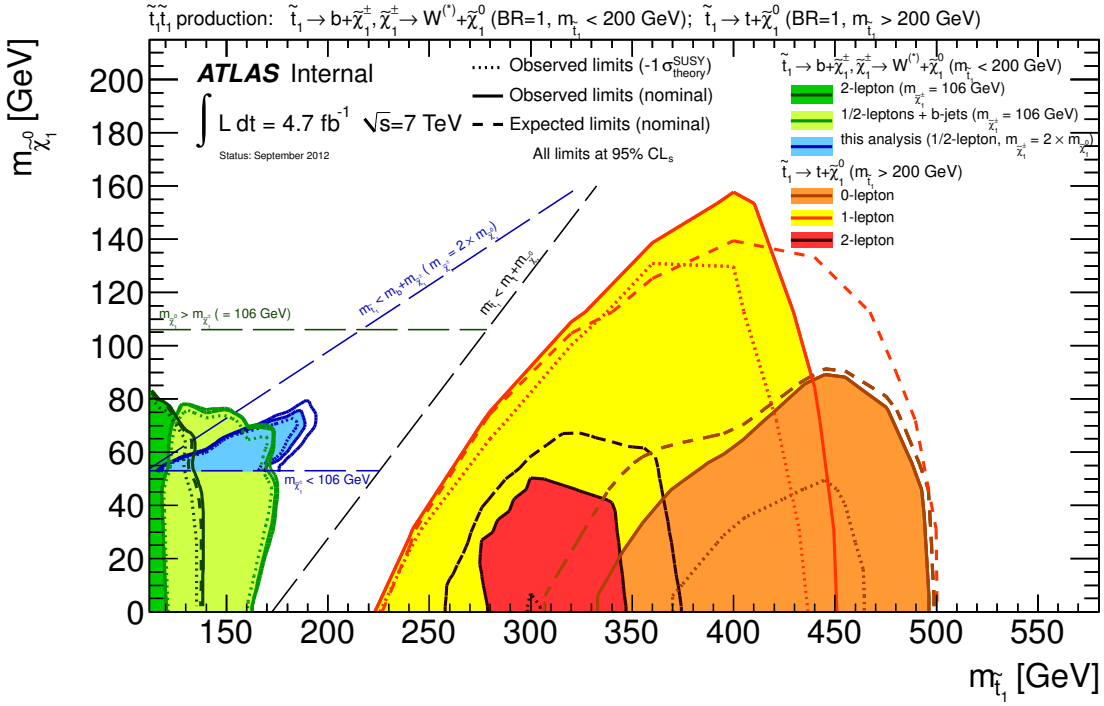

Figure 6.26.: Summary of exclusion limits at 95% C.L. in the ($m_{\tilde{t}_1}$,$m_{\tilde{\chi}_1^0}$)-plane for five ATLAS searches for SUSY [59], assuming direct stop pair production. In the analyses contributing to the exclusion limit for $m_{\tilde{t}_1} < 200\,\text{GeV}$ ($m_{\tilde{t}_1} > 200\,\text{GeV}$), the stop is assumed to decay exclusively via $\tilde{t}_1 \to b + \tilde{\chi}_1^{\pm}$ and $\tilde{\chi}_1^{\pm} \to W^{(*)}\tilde{\chi}_1^0$ ($\tilde{t}_1 \to t + \tilde{\chi}_1^0$). Different assumptions are used for the $\tilde{\chi}_1^{\pm}$-$\tilde{\chi}_1^0$ mass hierarchy as listed in the legend. The observed (expected) limits are shown as continuous (dashed) lines. The dotted lines represent the results obtained when reducing the nominal signal cross section by 1σ of the theoretical uncertainty.

7 Summary

Although the Standard Model of Particle Physics (SM) is very successful in the description of nature, there are still many open questions, e.g. the hierarchy problem or the explanation of dark matter. Supersymmetry (SUSY) is a theoretically well-motivated theory of physics beyond the SM, that can provide solutions to some of these open questions. For every fermion in the SM, supersymmetry postulates a new boson and vice versa. The hierarchy problem is solved due to the cancelation of loop contributions between the SM particles and the SUSY partners to physical quantities, e.g. the Higgs boson mass. With the assumption of a new conserved quantum number, named R parity, supersymmetry yields a candidate for a dark matter particle, namely the Lightest Supersymmetric Particle (LSP). If SUSY is realized in nature, it must be a broken symmetry, since no SUSY partners to the SM particles with equal masses have been observed. The solution of the hierarchy problem can be preserved even for broken supersymmetry, provided that there exist at least some SUSY partners at the TeV scale. With the LHC collider experiments, this TeV scale can be explored to search for signatures of SUSY.

The ATLAS detector started data-taking at a center-of-mass energy of 7 TeV in March 2010 and since then, a variety of searches for SUSY signatures has been performed. With conserved R parity, the experimental signature contains a large amount of missing transverse momentum, due to the non-detection of the LSP. Due to the light quarks in the initial state of the colliding protons, the search for the production of first and second generation partners of quarks (squarks) had the largest sensitivity in the early stage of data-taking, resulting in strong limits on the first and second generation squark masses. The solution of the hierarchy problem can be preserved for heavy first and second generation squarks, if the third generation squarks are light. In many scenarios, the squarks of the third generation are lighter than their first and second generation counterparts, due to mixing effects that are proportional to the SM quark masses. As a result, the third generation squarks can be produced with enhanced cross sections and their decay products include t and b-quarks. The experimental signatures in these scenarios contain b-jets.

This thesis focuses on two distinct searches for squarks of the third generation, specifically the direct production of stop pairs and the production of stop via the decay of gluinos. Both searches are based on experimental signatures with large missing transverse momentum, b-jets and one electron or muon. Inclusive variables, which are sensitive to the mass scale of SUSY are used to discriminate the signal from the SM background processes. The determination of the expected background is one essential aspect of every physics analysis. In both analyses, dedicated background estimation techniques are used. Control samples in data are used to supplement or replace the background expectation from Monte Carlo simulation.

The search for the gluino mediated production of stops is based on a dataset corresponding to an integrated luminosity of $2.05\,\mathrm{fb}^{-1}$. No significant excess beyond the Standard Model expectation is found. Therefore, both model independent upper limits on physics beyond the SM and specific model interpretations are derived.

In the gluino-stop model, which was used in the optimization of the analysis, the stop is assumed to be the lightest squark and all other squarks are assumed to be heavier than the gluino. The stop and the gluino are assumed to fulfill the mass relation $m_{\tilde{g}} > m_{\tilde{t}_1} + m_t$. The following limits at 95% C.L. on the gluino and stop masses are obtained:

$$m_{\tilde{g}} < 620\,\text{GeV}, \quad m_{\tilde{t}_1} < 440\,\text{GeV}. \tag{7.1}$$

Additional interpretations are derived in the context of two model scenarios with SO(10) unification. In these models the Higgs mass terms must be split at the unification scale Λ_{GUT} to be consistent with radiative electroweak symmetry breaking. In the so-called DR3 and HS models, this is achieved by the breaking of SO(10) affecting all scalar masses (DR3) and by only splitting the Higgs sector (HS). Gluino masses of 650 GeV and 610 GeV are excluded within the DR3 and HS model, respectively.

Simplified model scenarios are used to search for key phenomenological features within a model including only a limited number of new parameters. Two simplified models focusing on the production of third generation squarks are used, namely the Gt and Gtb models. In both models, the gluino pair production is the main production process and the third generation squarks are assumed to be the lightest squarks. The exclusion limits are given in a $(m_{\tilde{g}},m_{\tilde{\chi}_1^0})$-plane. To illustrate the extent of the exclusion limits, the following gluino masses are excluded for fixed values of neutralino masses

$$\text{Gt:} \quad 400\,\text{GeV} < m_{\tilde{g}} < 750\,\text{GeV} \quad \text{for } m_{\tilde{\chi}_1^0} = 50\,\text{GeV}, \tag{7.2}$$

$$\text{Gtb:} \quad 320\,\text{GeV} < m_{\tilde{g}} < 720\,\text{GeV} \quad \text{for } m_{\tilde{\chi}_1^0} = 100\,\text{GeV}. \tag{7.3}$$

The exclusion limits from previous analyses are significantly extended.

The search for the direct production of stop pairs is based on a dataset corresponding to an integrated luminosity of $4.7\,\text{fb}^{-1}$, collected during the year 2011. No significant excess beyond the Standard Model expectation is found. Therefore, both model independent upper limits on physics beyond the SM and limits using specific models are derived. Although the expected exclusion limits prove the sensitivity of the analysis in these scenarios, no limits could be set. The results are consistent with an upward fluctuation of the background within the uncertainty.

An additional search for the direct production of stop pairs with two leptons in the final state has been performed by the ATLAS Collaboration. The two search channels are complementary and mutually exclusive, therefore they are used to derive combined exclusion limits.

Two model interpretations are given, namely within the gluino-stop model and a fixed stop mass model. In the gluino-stop model, the combined exclusion limits are determined in the $(m_{\tilde{t}_1},m_{\tilde{\chi}_1^0})$-plane. To illustrate the extent of the exclusion, the following limits are given for the mass of the stop with a fixed value of the neutralino mass and vice versa

$$130\,\text{GeV} < m_{\tilde{t}_1} < 170\,\text{GeV} \quad \text{for} \quad m_{\tilde{\chi}_1^0} = 60\,\text{GeV}, \tag{7.4}$$

$$m_{\tilde{\chi}_1^0} < 75\,\text{GeV} \quad \text{for} \quad m_{\tilde{t}_1} \sim m_t. \tag{7.5}$$

In SUSY scenarios with a fixed stop mass of $m_{\tilde{t}_1} = 180$ GeV, the exclusion limits are determined in the $(m_{\tilde{\chi}_1^\pm},m_{\tilde{\chi}_1^0})$-plane. The following limits illustrate the exclusion for the mass

of the chargino with a fixed mass of the neutralino and vice versa

$$120\,\text{GeV} < m_{\tilde{\chi}_1^\pm} < 145\,\text{GeV} \quad \text{for} \quad m_{\tilde{\chi}_1^0} = 60\,\text{GeV}, \tag{7.6}$$

$$45\,\text{GeV} < m_{\tilde{\chi}_1^0} < 95\,\text{GeV} \quad \text{for} \quad m_{\tilde{\chi}_1^\pm} = 140\,\text{GeV}. \tag{7.7}$$

Additional searches for the direct production of stop pairs are performed by the ATLAS Collaboration, targeting different mass ranges and different decay modes of the stop. In combination with these searches, large areas in the $(m_{\tilde{t}_1}, m_{\tilde{\chi}_1^0})$-plane are excluded. The excluded region is divided into two parts by a corridor, in which the mass of the stop is close to the sum of the masses of the top and the neutralino. This region is experimentally challenging, due to very soft objects in the final state. To illustrate the extent of the exclusion the following stop masses are excluded for a fixed value of $m_{\tilde{\chi}_1^0} = 10\,\text{GeV}$

$$120\,\text{GeV} < m_{\tilde{t}_1} < 155\,\text{GeV}, \tag{7.8}$$

$$230\,\text{GeV} < m_{\tilde{t}_1} < 500\,\text{GeV}. \tag{7.9}$$

Neutralino masses up to 75 GeV are excluded for the lower exclusion range of the stop, the upper exclusion range reaches a neutralino mass of about 160 GeV for a stop mass of about 400 GeV.

By excluding the existence of relatively light third generation squarks, the searches presented strongly constrain low fine-tuning SUSY scenarios. Together with the complementary SUSY searches for gluinos, first and second generation squarks, and gauginos, and with the results on the mass and properties of the newly discovered boson, they constitute unprecedented severe constraints on the MSSM.

At present, the LHC is already operating at an increased center-of-mass energy of 8 TeV. At the end of 2012, a dataset corresponding to an integrated luminosity of about $25\,\text{fb}^{-1}$ is expected to be recorded, which will enlarge the region of sensitivity for the searches for supersymmetry. Ultimately, the center-of-mass energy is planned to be increased up to the design value of 14 TeV. With these energies and about three years of data-taking, the discovery reach in the $(m_{\tilde{t}_1}, m_{\tilde{\chi}_1^0})$-plane is significantly extended. For a center-of-mass energy of 14 TeV and a dataset corresponding to an integrated luminosity of $300\,\text{fb}^{-1}$, the discovery reach extends to stop masses of the order of 800 GeV [118], putting low fine-tuning supersymmetry to a critical and possibly final test.

A Conventions

Units It is common in particle physics to express physical quantities in units of the reduced Planck constant $\hbar$ and velocity of light c. This is equivalent to setting $\hbar = c = 1$ in any physics formulas. This results in the following relations

$$[\text{energy}] = [\text{mass}] = [\text{momentum}] = [\text{length}]^{-1}. \tag{A.1}$$

Energies, momenta and masses are usually given in units of 10^9 electron volts (GeV). For cross sections it is common to use units of cm^2 or barn ($1\,\text{b} = 10 \times 10^{-28}\,\text{cm}^2$). Luminosities are usually given in terms of inverse femtobarn (fb^{-1}).

Indices Lorentz indeces (ranging from 0 to 3) are denoted by greek letters (μ, ν, ...). A sum over repeated indeces is implicit.

B ATLAS DCS Data Viewer

In this chapter, the concept and development of the ATLAS collaboration tool ATLAS DCS Data Viewer (DDV) [119] is presented, which was part of the service effort for the collaboration.

B.1. Introduction

The ATLAS Detector Control System (DCS), which was briefly introduced in Section 4.2.6, is responsible for the supervision of the detector components. It produces a large amount of data during the operation of the ATLAS detector, mainly consisting of operational parameters of the detector and its components. The data is stored in an offline database and can be used for offline monitoring.

The aim of the DDV project is to provide a flexible tool for the ATLAS community to access and visualize historical ATLAS DCS data.

B.2. DDV Overview and Architecture

After having recorded physics data from collisions in the ATLAS detector, it is essential to be able to get to know as many details as possible about the state of the detector at any given point in time (e.g. in case of problems with data quality). For this case there is an offline database (complete replica of the online database) which archieves this information. The aim of the DDV is to facilitate the access and visualization of the stored operational parameters for any user in the ATLAS community. Figure B.1 illustrates the relation and communication between the ATLAS DCS and the end user via DDV.

The design specifications of the tool include the following aspects:

- platform and browser independence,
- reasonable application startup time (less than 10sec),
- short response time to requests (order of seconds),
- multiple data selection methods,
- multiple output formats (chart, table, ascii, ROOT),
- reproducible configuration in XML format,
- database protection mechanisms.

The architecture was designed in a highly modular fashion and is based on a server client concept, which is illustrated in Fig. B.2. In this way it is possible to combine the concept of centralization in the server part as well as flexibility in the client part.

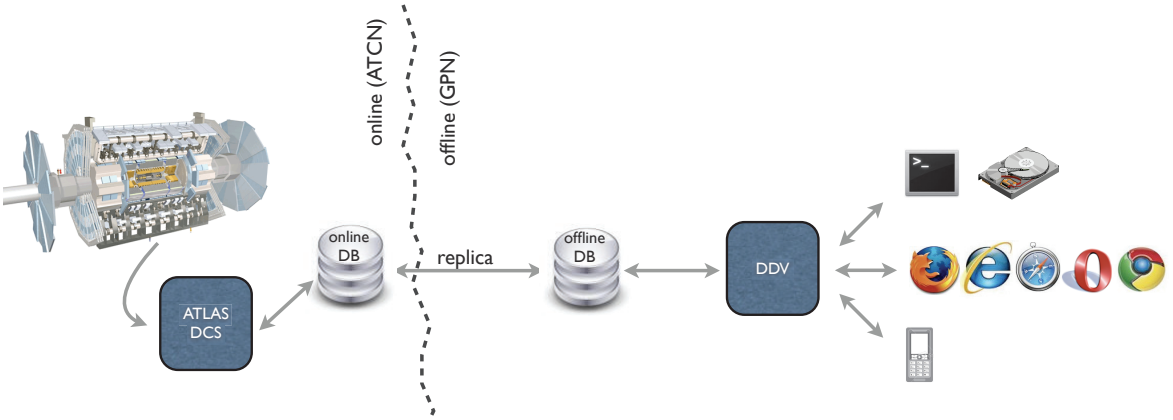

Figure B.1.: Schematic view of the communication between the ATLAS DCS and the end user via DDV [119].

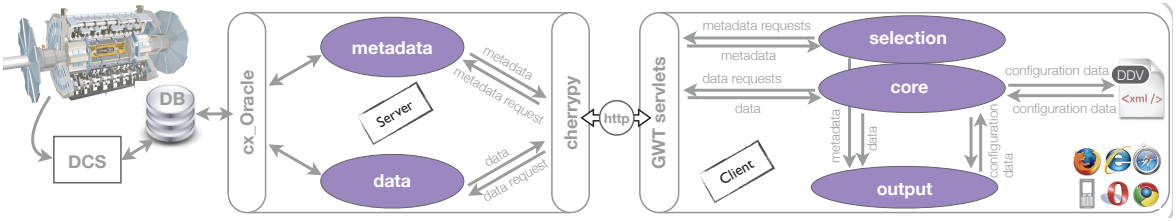

Figure B.2.: The DDV server-client architecture [119].

B.3. Server

The server part of DDV is written in Python and it is designed to communicate with the database and transfers the results to the clients. The focus of the development within the context of the service work for the ATLAS collaboration was on the client side.

B.4. Client

The client side of DDV is written in Java and is transferred to browser independent AJAX-based web application. The architecture of the client allows the modular and independent development of plugins for specific tasks like visualization.

Different methods are implemented to select the data that should be visualized, namely a column-based browsing tool and a search engine. The configuration of the visualization is defined in a configuration tool and can saved in xml format. The definition of the dataset and configuration are transferred to the chosen output plugin in a standardized format.

The default output plugin is in form of a Java Applet. The configuration of the visualization can be changed interactively.

Bibliography

[1] UA1 Collaboration, *Experimental observation of isolated large transverse energy electrons with associated missing energy at* $\sqrt{s} = 540\,\text{GeV}$, Phys. Lett. **B122** no. 1, (1983) 103–116.

[2] UA2 Collaboration, *Observation of Single Isolated Electrons of High Transverse Momentum in Events with Missing Transverse Energy at the CERN* $\bar{p}p$ *Collider*, Phys. Lett. **B122** (1983) 476–485.

[3] UA1 Collaboration, *Experimental Observation of Lepton Pairs of Invariant Mass Around 95* GeV/c^2 *at the CERN SPS Collider*, Phys. Lett. **B126** (1983) 398–410.

[4] UA2 Collaboration, *Evidence for* $Z_0 \to e^+e^-$ *at the CERN* $\bar{p}p$ *Collider*, Phys. Lett. **B129** (1983) 130–140.

[5] D0 Collaboration, *Observation of the Top Quark*, Phys. Rev. Lett. **74** no. 14, (Apr, 1995) 2632–2637.

[6] CDF Collaboration, *Observation of Top Quark Production in* $p\bar{p}$ *Collisions with the Collider Detector at Fermilab*, Phys. Rev. Lett. **74** no. 14, (Apr, 1995) 2626–2631.

[7] ATLAS Collaboration, *Observation of a new particle in the search for the Standard Model Higgs boson with the ATLAS detector at the LHC*, Phys. Lett. **B716** (2012) 1–29.

[8] CMS Collaboration, *Observation of a new boson at a mass of 125 GeV with the CMS experiment at the LHC*, Phys. Lett. **B716** (2012) 30–61.

[9] S. Glashow, *Partial Symmetries of Weak Interactions*, Nucl. Phys. **22** (1961) 579–588.

[10] S. Weinberg, *A Model of Leptons*, Phys. Rev. Lett. **19** (1967) 1264–1266.

[11] A. Salam, *Weak and Electromagnetic Interactions*, Originally printed in Svartholm: Elementary Particle Theory, Proceedings Of The Nobel Symposium Held 1968 At Lerum, Sweden, Stockholm 1968, 367-377.

[12] F. Halzen and A. D. Martin, *Quarks and Leptons*. Wiley, 1984.

[13] F. Englert and R. Brout, *Broken Symmetry and the Mass of Gauge Vector Mesons*, Phys. Rev. Lett. **13** (Aug, 1964) 321–323.

[14] P. Higgs, *Broken symmetries, massless particles and gauge fields*, Phys. Lett. **12** no. 2, (1964) 132–133.

[15] P. W. Higgs, *Broken Symmetries and the Masses of Gauge Bosons*, Phys. Rev. Lett. **13** (Oct, 1964) 508–509.

[16] G. S. Guralnik, C. R. Hagen, and T. W. B. Kibble, *Global Conservation Laws and Massless Particles*, Phys. Rev. Lett. **13** (Nov, 1964) 585–587.

[17] P. W. Higgs, *Spontaneous Symmetry Breakdown without Massless Bosons*, Phys. Rev. **145** (May, 1966) 1156–1163.

[18] T. W. B. Kibble, *Symmetry Breaking in Non-Abelian Gauge Theories*, Phys. Rev. **155** (Mar, 1967) 1554–1561.

[19] Particle Data Group, J. Beringer *et al.*, *Review of particle physics*, Phys. Rev. **D86** (2012) 010001.

[20] S. Kanemitsu and K. Tobe, *New physics for muon anomalous magnetic moment and its electroweak precision analysis*, `arXiv:1207.1313 [hep-ph]`.

[21] K. Ishiwata, N. Nagata, and N. Yokozaki, *Natural supersymmetry and $b \to s\gamma$ constraints*, Phys. Lett. **B710** (Mar., 2012) 145–148, `arXiv:1112.1944 [hep-ph]`.

[22] D. Chung, L. Everett, G. Kane, S. King, J. D. Lykken, *et al.*, *The Soft supersymmetry breaking Lagrangian: Theory and applications*, Phys. Rept. **407** (2005) 1–203, `arXiv:hep-ph/0312378 [hep-ph]`.

[23] S. P. Martin, *A Supersymmetry Primer*, `arXiv:hep-ph/9709356`.

[24] I. Aitchison, *Supersymmetry in Particle Physics*. Cambridge University Press, 2007.

[25] H. Baer and X. Tata, *Weak Scale Supersymmetry*. Cambridge University Press, 2006.

[26] S. Dimopoulos and D. W. Sutter, *The Supersymmetric flavor problem*, Nucl. Phys. **B452** (1995) 496–512, `arXiv:hep-ph/9504415`.

[27] A. Djouadi, *The Anatomy of electro-weak symmetry breaking. II. The Higgs bosons in the minimal supersymmetric model*, Phys. Rept. **459** (2008) 1–241, `arXiv:hep-ph/0503173 [hep-ph]`.

[28] G. Degrassi, S. Heinemeyer, W. Hollik, P. Slavich, and G. Weiglein, *Towards high precision predictions for the MSSM Higgs sector*, Eur. Phys. J. **C28** (2003) 133–143, `arXiv:hep-ph/0212020 [hep-ph]`.

[29] S. Heinemeyer, V. A. Khoze, M. Tasevsky, and G. Weiglein, *Exclusive Production of the MSSM Higgs Bosons at the LHC*, `arXiv:1206.0183 [hep-ph]`.

[30] R. Haag, J. T. Lopuszanski, and M. Sohnius, *All possible generators of supersymmetries of the S-matrix*, Nucl. Phys. **B88** no. 2, (1975) 257–274.

[31] V. Rubin, N. Thonnard, and J. Ford, W.K., *Rotational properties of 21 SC galaxies with a large range of luminosities and radii, from NGC 4605 ($R = 4$ kpc) to UGC 2885 ($R = 122$ kpc)*, Astrophys. J. **238** (1980) 471.

[32] D. Clowe, M. Bradac, A. H. Gonzalez, M. Markevitch, S. W. Randall, C. Jones, and D. Zaritsky, *A Direct Empirical Proof of the Existence of Dark Matter*, Astrophys. J. Lett. **648** no. 2, (2006) L109.

[33] D. B. Cline, *Recent results on the low mass dark matter WIMP controversy: 2011*, `arXiv:1109.1799 [astro-ph.CO]`.

[34] L. E. Ibanez and G. G. Ross, *Discrete gauge symmetries and the origin of baryon and lepton number conservation in supersymmetric versions of the standard model*, Nucl. Phys. **B368** no. 1, (1992) 3–37.

[35] H. Georgi and S. L. Glashow, *Unity of All Elementary-Particle Forces*, Phys. Rev. Lett. **32** (Feb, 1974) 438–441.

[36] H. Fritzsch and P. Minkowski, *Unified Interactions of Leptons and Hadrons*, Ann. Phys. **93** (1975) 193–266.

[37] H. Baer, S. Kraml, A. Lessa, and S. Sekmen, *Testing Yukawa-unified SUSY during year 1 of LHC: the role of multiple b-jets, dileptons and missing E_{T}*, JHEP **02** (2010) 055, arXiv:0911.4739 [hep-ph].

[38] A. L. Read, *Presentation of search results: The CL(s) technique*, J. Phys. **G28** (2002) 2693–2704.

[39] ATLAS Statistics Forum, *The CLs method: information for conference speakers.*

[40] J. M. Campbell, J. W. Huston, and W. J. Stirling, *Hard Interactions of Quarks and Gluons: A Primer for LHC Physics*, Rept. Prog. Phys. **70** (2007) 89, arXiv:hep-ph/0611148.

[41] R. K. Ellis, W. J. Stirling, and B. R. Webber, *QCD and Collider Physics*. Cambridge University Press, 1996.

[42] Y. L. Dokshitzer, *Calculation of the Structure Functions for Deep Inelastic Scattering and e+ e- Annihilation by Perturbation Theory in Quantum Chromodynamics.*, Sov. Phys. JETP **46** (1977) 641–653.

[43] V. Gribov and L. Lipatov, *Deep inelastic e p scattering in perturbation theory*, Sov. J. Nucl. Phys. **15** (1972) 438–450.

[44] G. Altarelli and G. Parisi, *Asymptotic Freedom in Parton Language*, Nucl. Phys. **B126** (1977) 298.

[45] H1 and ZEUS, F. D. Aaron *et al.*, *Combined Measurement and QCD Analysis of the Inclusive ep Scattering Cross Sections at HERA*, JHEP **01** (2010) 109, arXiv:0911.0884 [hep-ex].

[46] S. Alekhin, S. Alioli, R. D. Ball, V. Bertone, J. Blumlein, *et al.*, *The PDF4LHC Working Group Interim Report*, arXiv:1101.0536 [hep-ph].

[47] M. Botje, J. Butterworth, A. Cooper-Sarkar, A. de Roeck, J. Feltesse, *et al.*, *The PDF4LHC Working Group Interim Recommendations*, arXiv:1101.0538 [hep-ph].

[48] A. Martin, W. Stirling, R. Thorne, and G. Watt, *Parton distributions for the LHC*, Eur. Phys. J. **C63** (2009) 189–285, arXiv:0901.0002 [hep-ph].

[49] A. Buckley, J. Butterworth, S. Gieseke, D. Grellscheid, S. Hoche, *et al.*, *General-purpose event generators for LHC physics*, Phys. Rept. **504** (2011) 145–233, arXiv:1101.2599 [hep-ph].

[50] S. Catani, F. Krauss, R. Kuhn, and B. Webber, *QCD matrix elements + parton showers*, JHEP **0111** (2001) 063, arXiv:hep-ph/0109231 [hep-ph].

[51] M. L. Mangano, M. Moretti, F. Piccinini, and M. Treccani, *Matching matrix elements and shower evolution for top-quark production in hadronic collisions*, JHEP **0701** (2007) 013, arXiv:hep-ph/0611129 [hep-ph].

[52] W. Beenakker, R. Hopker, and M. Spira, *PROSPINO: A program for the production of supersymmetric particles In next-to-leading order QCD, hep-ph/9611232*, arXiv:hep-ph/9611232.

[53] *PROSPINO2*, http://www.ph.ed.ac.uk/~tplehn/prospino/.

[54] F. E. Paige, *Determining SUSY particle masses at LHC*, arXiv:hep-ph/9609373.

[55] D. R. Tovey, *Measuring the SUSY mass scale at the LHC*, Phys. Lett. **B498** (2001) 1–10, arXiv:hep-ph/0006276.

[56] P. Konar, K. Kong, and K. T. Matchev, $\sqrt{\hat{s}}_{\rm min}$ *: a global inclusive variable for determining the mass scale of new physics in events with missing energy at hadron colliders*, JHEP **2009** no. 03, (2009) 085.

[57] P. Konar, K. Kong, K. Matchev, and M. Park, *RECO level* $\sqrt{s}_{\rm min}$ *and subsystem improved* $\sqrt{s}_{\rm min}$*: global inclusive variables for measuring the new physics mass scale in events at hadron colliders*, JHEP **2011** (2011) 1–35, 10.1007/JHEP06(2011)041.

[58] J. Alwall, P. C. Schuster, and N. Toro, *Simplified models for a first characterization of new physics at the LHC*, Phys. Rev. **D79** (Apr, 2009) 075020.

[59] ATLAS Collaboration, *ATLAS Public Results*. https://twiki.cern.ch/twiki/bin/view/AtlasPublic.

[60] ATLAS Collaboration, *Search for squarks and gluinos using final states with jets and missing transverse momentum with the ATLAS detector in* $\sqrt{s} = 7\,\text{TeV}$ *proton-proton collisions* Public Note ATLAS-CONF-2012-033, CERN, Geneva, Mar, 2012.

[61] ATLAS Collaboration, *Hunt for new phenomena using large jet multiplicities and missing transverse momentum with ATLAS in* $L = 4.7\ fb^{-1}$ *of* $\sqrt{s} = 7\,\text{TeV}$ *proton-proton collisions* Public Note ATLAS-CONF-2012-037, CERN, Geneva, Mar, 2012.

[62] ATLAS Collaboration, *Further search for supersymmetry at* $\sqrt{s} = 7\,\text{TeV}$ *in final states with jets, missing transverse momentum and one isolated lepton* Public Note ATLAS-CONF-2012-041, CERN, Geneva, Mar, 2012.

[63] ATLAS Collaboration, *Search for light scalar top quark pair production in final states with two leptons with the ATLAS detector in* $\sqrt{s} = 7\,\text{TeV}$ *proton–proton collisions* Public Note ATLAS-CONF-2012-059, CERN, Geneva, Jun, 2012.

[64] ATLAS Collaboration, *Search for a supersymmetric partner of the top quark in final states with jets and missing transverse momentum at* $\sqrt{s} = 7\,\text{TeV}$ *with the ATLAS detector* Public Note ATLAS-CONF-2012-074, CERN, Geneva, Jul, 2012.

[65] ATLAS Collaboration, *Search for direct top squark pair production in final states with one isolated lepton, jets, and missing transverse momentum in* $\sqrt{s} = 7\,\text{TeV}$ *pp collisions using* $4.7\,\text{fb}^{-1}$ *of ATLAS data* Public Note ATLAS-CONF-2012-073, CERN, Geneva, Jul, 2012.

[66] ATLAS Collaboration, *Search for a heavy top partner in final states with two leptons with the ATLAS detector* Public Note ATLAS-CONF-2012-071, CERN, Geneva, Jul, 2012.

[67] ATLAS Collaboration, *ATLAS: Detector and physics performance technical design report. Volume 1*, CERN-LHCC-99-14.

[68] ATLAS Collaboration, *ATLAS: Detector and physics performance technical design report. Volume 2*, CERN-LHCC-99-15.

[69] ATLAS Collaboration, *The ATLAS Experiment at the CERN Large Hadron Collider*, JINST **3** no. 08, (2008) S08003.

[70] CERN.

[71] F. Gianotti, *Physics at the LHC*, Phys. Repts. **403–404** no. 0, (2004) 379–399.

[72] ATLAS Collaboration, *Electron performance measurements with the ATLAS detector using the 2010 LHC proton-proton collision data*, Eur. Phys. J. **C72** (2012) 1–46, 10.1140/epjc/s10052-012-1909-1.

[73] ATLAS Collaboration, *Expected Performance of the ATLAS Experiment: Detector, Trigger and Physics*, CERN-OPEN-2008-020, page 335-342, 2008.

[74] ATLAS Collaboration, *Muon reconstruction efficiency in reprocessed 2010 LHC proton-proton collision data recorded with the ATLAS detector* Public Note ATLAS-CONF-2011-063, CERN, Geneva, Apr, 2011.

[75] ATLAS Collaboration, *Muon Momentum Resolution in First Pass Reconstruction of pp Collision Data Recorded by ATLAS in 2010* Public Note ATLAS-CONF-2011-046, CERN, Geneva, Mar, 2011.

[76] M. Cacciari, G. P. Salam, and G. Soyez, *The Anti-k(t) jet clustering algorithm*, JHEP **0804** (2008) 063, `arXiv:0802.1189 [hep-ph]`.

[77] W. Lampl, S. Laplace, D. Lelas, P. Loch, H. Ma, S. Menke, S. Rajagopalan, D. Rousseau, S. Snyder, and G. Unal, *Calorimeter Clustering Algorithms: Description and Performance* Public Note ATL-LARG-PUB-2008-002. ATL-COM-LARG-2008-003, CERN, Geneva, Apr, 2008.

[78] ATLAS Collaboration, *Jet energy measurement with the ATLAS detector in proton-proton collisions at* $\sqrt{s} = 7\,\text{TeV}$, `arXiv:1112.6426 [hep-ex]`.

[79] ATLAS Collaboration, *Non-collision backgrounds as measured by the ATLAS detector during the 2010 proton-proton run* Public Note ATLAS-CONF-2011-137, CERN, Geneva, Sep, 2011.

[80] ATLAS Collaboration, *Performance of Missing Transverse Momentum Reconstruction in Proton-Proton Collisions at* 7 TeV *with ATLAS*, Eur. Phys. J. **C72** (2012) 1844, `arXiv:1108.5602 [hep-ex]`.

[81] ATLAS Collaboration, *Performance of the ATLAS Secondary Vertex b-tagging Algorithm in* 7 TeV *Collision Data* Public Note ATLAS-CONF-2010-042, CERN, Geneva, Jul, 2010.

[82] ATLAS Collaboration, *Impact parameter-based b-tagging algorithms in the* 7 TeV *collision data with the ATLAS detector: the TrackCounting and JetProb algorithms* Public Note ATLAS-CONF-2010-041, CERN, Geneva, Jul, 2010.

[83] ATLAS Collaboration, *Performance of Impact Parameter-Based b-tagging Algorithms with the ATLAS Detector using Proton-Proton Collisions at* $\sqrt{s} = 7$ TeV Public Note ATLAS-CONF-2010-091, CERN, Geneva, Oct, 2010.

[84] ATLAS Collaboration, *Commissioning of the ATLAS high-performance b-tagging algorithms in the* 7 TeV *collision data* Public Note ATLAS-CONF-2011-102, CERN, Geneva, Jul, 2011.

[85] G. Piacquadio and C. Weiser, *A new inclusive secondary vertex algorithm for b-jet tagging in ATLAS*, JPCS **119** no. 3, (2008) 032032.

[86] ATLAS Collaboration, *Soft muon tagging and Dstar/mu correlations in* 7 TeV *collisions with ATLAS* Public Note ATLAS-CONF-2010-100, CERN, Geneva, Dec, 2010.

[87] ATLAS Collaboration, *Calibrating the b-Tag Efficiency and Mistag Rate in* $35\,\mathrm{pb}^{-1}$ *of Data with the ATLAS Detector* Public Note ATLAS-CONF-2011-089, CERN, Geneva, Jun, 2011.

[88] T. Sjostrand, S. Mrenna, and P. Skands, *PYTHIA 6.4 physics and manual*, JHEP **05** (2006) 026, `arXiv:hep-ph/0603175`.

[89] M. L. Mangano, M. Moretti, F. Piccinini, R. Pittau, and A. D. Polosa, *ALPGEN, a generator for hard multiparton processes in hadronic collisions*, JHEP **07** (2003) 001, `arXiv:hep-ph/0206293`.

[90] J. M. Butterworth, J. R. Forshaw, and M. H. Seymour, *Multiparton interactions in photoproduction at HERA*, Z. Phys. **C72** (1996) 637–646, `arXiv:hep-ph/9601371`.

[91] J. Pumplin, D. R. Stump, J. Huston, H.-L. Lai, P. Nadolsky, and W.-K. Tung, *New Generation of Parton Distributions with Uncertainties from Global QCD Analysis*, JHEP **2002** no. 07, (2002) 012.

[92] F. P. K. Melnikov, *Electroweak gauge boson production at hadron colliders through* $O(\alpha_s^2)$, Phys. Rev. **D74** (2006) 114017, `arXiv:hep-ph/0609070`.

[93] G. Marchesini and B. Webber, *Simulation of QCD Jets Including Soft Gluon Interference*, Nucl. Phys. **B238** (1984) 1.

[94] G. Marchesini and B. Webber, *Monte Carlo Simulation of General Hard Processes with Coherent QCD Radiation*, Nucl. Phys. **B310** (1988) 461.

[95] S. Frixione and B. R. Webber, *Matching NLO QCD computations and parton shower simulations*, JHEP **06** (2002) 029, `arXiv:hep-ph/0204244`.

[96] S. Moch and P. Uwer, Nucl. Phys. Proc. Suppl. **183** (2008) 75–80.

[97] P. M. Nadolsky *et al.*, *Implications of CTEQ global analysis for collider observables*, Phys. Rev. **D78** (2008) 013004, `arXiv:0802.0007 [hep-ph]`.

[98] S. Frixione, P. Nason, and C. Oleari, *Matching NLO QCD computations with Parton Shower simulations: the POWHEG method*, JHEP **0711** (2007) 070, `arXiv:0709.2092 [hep-ph]`.

[99] B. P. Kersevan and E. Richter-Was, *The Monte Carlo event generator AcerMC version 2.0 with interfaces to PYTHIA 6.2 and HERWIG 6.5, hep-ph/0405247*, arXiv:hep-ph/0405247.

[100] J. Alwall *et al.*, *MadGraph/MadEvent v4: The New Web Generation*, JHEP **09** (2007) 028, arXiv:0706.2334 [hep-ph].

[101] A. Djouadi, M. M. Muhlleitner, and M. Spira, *Decays of Supersymmetric Particles: the program SUSY-HIT (SUspect-SdecaY-Hdecay-InTerface)*, Acta Phys. Polon. **B38** (2007) 635–644, arXiv:hep-ph/0609292.

[102] F. Paige, S. Protopopescu, H. Baer, and X. Tata, *ISAJET 7.69: A Monte Carlo event generator for p p, anti-p p, and e+ e- reactions, hep-ph/0312045*, arXiv:hep-ph/0312045.

[103] M. Bahr *et al.*, *Herwig++ Physics and Manual*, Eur. Phys. J. **C58** (2008) 639–707, arXiv:0803.0883 [hep-ph].

[104] M. Bahr *et al.*, *Herwig++ 2.3 release note, arXiv:0812.0529*, 2008.

[105] A. Sherstnev and R. Thorne, *Parton Distributions for LO Generators*, Eur. Phys. J. **C55** (2008) 553–575, arXiv:0711.2473 [hep-ph].

[106] ATLAS Collaboration, *The ATLAS Simulation Infrastructure*, Eur. Phys. J. **C70** (2010) 823–874, arXiv:1005.4568 [physics.ins-det].

[107] ATLAS Collaboration, *Search for supersymmetry in pp collisions at* $\sqrt{s} = 7\,\text{TeV}$ *in final states with missing transverse momentum and b-jets with the ATLAS detector*, Phys. Rev. **D85** (2012) 112006.

[108] ATLAS Collaboration, *Luminosity Determination in pp Collisions at* $\sqrt{s} = 7\,\text{TeV}$ *using the ATLAS Detector in 2011* Public Note ATLAS-CONF-2011-116, CERN, 2011.

[109] ATLAS Collaboration, *Measurement of the* $W \to \ell\nu$ *and* $Z/\gamma* \to \ell\ell$ *production cross sections in proton-proton collisions at* $\sqrt{s} = 7\,\text{TeV}$ *with the ATLAS detector*, JHEP **1012** (2010) 060, arXiv:1010.2130 [hep-ex].

[110] ATLAS Collaboration, *Readiness of the ATLAS liquid argon calorimeter for LHC collisions*, Eur. Phys. J. **C70** (Dec., 2010) 723–753.

[111] ATLAS Collaboration, *Jet energy resolution and reconstruction efficiencies from in-situ techniques with the ATLAS Detector Using Proton-Proton Collisions at a Center of Mass Energy* $\sqrt{s} = 7\,\text{TeV}$ Public Note ATLAS-CONF-2010-054, CERN, 2010.

[112] ATLAS Collaboration, *Measurement of the cross section for the production of a W boson in association with b-jets in pp collisions at with the ATLAS detector*, Phys. Lett. **B707** no. 5, (2012) 418–437.

[113] ATLAS Collaboration, *Measurement of the cross-section for b-jets produced in association with a Z boson at with the ATLAS detector*, Phys. Lett. **B706** no. 4–5, (2012) 295–313.

[114] ATLAS Collaboration, *Search for supersymmetry in pp collisions at* $\sqrt{s} = 7\,\text{TeV}$ *in final states with missing transverse momentum and b-jets*, Phys. Lett. **B701** no. 4, (2011) 398–416.

[115] ATLAS Collaboration, *Search for light scalar top pair production in final states with leptons and b-jets with the ATLAS detector in* $\sqrt{s} = 7\,\text{TeV}$ *proton-proton collisions*, to be submitted .

[116] ATLAS Collaboration, *Search for light top squark pair production in final states with leptons and b-jets with the ATLAS detector in* $\sqrt{s} = 7\,\text{TeV}$ *proton–proton collisions* Public Note ATLAS-CONF-2012-070, CERN, Geneva, Jul, 2012.

[117] ATLAS Collaboration, *Improved electron reconstruction in ATLAS using the Gaussian Sum Filter-based model for bremsstrahlung* Public Note ATLAS-CONF-2012-047, CERN, Geneva, May, 2012.

[118] ATLAS Collaboration, *Physics at a High-Luminosity LHC with ATLAS* Public Note ATL-PHYS-PUB-2012-001, CERN, Geneva, Aug, 2012.

[119] U. Bitenc, S. D'Auria, M. Fehling-Kaschek, D. Hoffmann, O. Pisano, S. Roe, S. Schlenker, C. Tsarouchas, and S. Winkelmann, *ATLAS Detector Control System Data Viewer*, internal communication.

Acknowledgments

First of all, I would like to thank Prof. Karl Jakobs for accepting me as a PhD student and giving me the opportunity to work both on such a rich and interesting topic and in such a pleasant environment as the Freiburg ATLAS group and the Graduiertenkolleg. I also would like to thank JProf. Harald Ita and Prof. Gregor Herten that they agreed to be available for the oral examination.

Thanks to Xavier Portell and Iacopo Vivarelli for the guidance and many interesting discussions during the different stages of the PhD.

Thanks to Michael Dührssen, Giacinto Piacquadio, Julian Glatzer, Christian Weiser, Iacopo Vivarelli, Felix Bührer, Vakhtang Tsiskaridze for supporting the local computing.

Thanks to my office mates Mirjam and Leonas, Julian, Felix, Liv and Sascha for the pleasant atmosphere in the office and many valuable discussions.

Thanks to all members of the Jakobs and Schumacher group and the members of the ATLAS SUSY subgroup for gluino mediated third generation and sbottom pair production and the members of the ATLAS SUSY subgroup for direct stop production.

I would like to thank my family and friends who were supporting me.

Last, but not least, thanks to Christina Skorek for the support on all administrative tasks.